An evaluation of flood modelling techniques on a stretch of the River Devon, Clackmannanshire.

BY

Scott Barclay

in partial fulfilment of the requirement for the

Honours Degree of BSc Environmental Management

at

SRUC

and

THE UNIVERSITY OF EDINBURGH

March 2025

Word count: 11999

Abstract

Earths weather patterns are changing at a rapid rate due to anthropogenic induced climate change, which could see a variation and intensification of water cycles. With these changes there is an enormous challenge in adapting and mitigating against the severe threat of flooding which could be achieved via river flood modelling, and the subsequent correct implementation of natural flood management practices.

LiDAR terrain mapping is a key tool in the fight against flooding, however Scotland has fallen behind other regions in Great Britian achieving only 40% LiDAR coverage compared to partners in England and Wales with 100% coverage. Therefore this study seeks to ascertain, via an evaluation of flood modelling techniques, if that in the 60% of Scotland were LiDAR blackspots occur, is UAV-SfM/Photogrammetry a viable alternative for flood modelling.

Via a range of models and flood simulations completed the study found the importance of using the correct cell size and N-values within HEC-RAS 2D modelling for the most accurate results. Through a comparison of 1D modelling and 2D modelling, if computing processing power and time allows, models should be run as 2D with the smallest cell size (catchment size dependant) to ensure the most accurate outputs.

Through a continuation of varied flood modelling simulations, the study also concludes that currently Photogrammetry derived DTMs aren’t a viable alternative to LiDAR derived DTMs due to the varied and also inconsistent differences in flood results, such as Photogrammetry models often having less flooded area and flood volume, but also having a far greater depth of flood for every HEC-RAS model conducted. The study also concludes that the ArcGIS Pro Flood Simulation isn’t a viable alternative to HEC-RAS, and while it may be useful for short rainfall flood events in small areas, it isn’t an engineering tool that is comparable to the accuracy of HEC-RAS produced results.

Please note: Due to the variation and number of methods applied to this project, and the number of Figures and Tables created, this report deviates slightly from the traditional layout of an Honours project. To make the report and its findings easier to read, follow and understand, a decision was made to combine some of the methods, results and discussions together into their own sections.

Acknowledgements

I'd like to pass my thanks on to Forth Rivers Trust for allowing me the opportunity to work on this project and thanks to Laura McGowan for sharing the potential opportunities and setting up the initial meeting with Amy Ferguson and Michiel Voermans. I'd also like to further my gratitude to Michiel Voermans for taking the time out to attend online Teams chats and getting necessary data shared with me often at short notice.

I'd like to offer a huge thank you to Simon Gibson-Poole and Alistair Hamilton for first introducing me to GIS in second and third year, and for also agreeing to my primary and secondary project supervisors and for all of your advice and support through-out this Honours project.

A huge thank you to absolutely everyone at SRUC (staff and students) who have gotten me to this stage. After being made redundant during the COVID-19 pandemic in Spring 2020, I initially applied for the HNC in Environmental Management to give me some structure to my week during the uncertain covid-pandemic times. I never thought for one-minute I'd still be here all these years later completing an Honours degree.

And a final and biggest thanks to my favourite wee guy in the world, my son Arthur. He's no doubt had to witness my increased stress levels and moans (even more so than normal!) not to mention not being around as often due to the early starts and late finishes in the library. Thanks for your patience mate and I promise I'll make it up to you.

Table of Contents

List of Figures

List of Tables

Abbreviations

1D	One-dimensional
2D	Two-dimensional
3D	Three-dimensional
CAA	Civil Aviation Authority
CH_4	Methane
CO2	Carbon Dioxide
CSV	Comma Separated Values
DEFRA	Department for Environment Food and Rural Affairs
DEM	Digital Elevation Model
DSM	Digital Surface Model
DTM	Digital Terrain Model
ESRI	Environmental Systems Research Institute, Inc.
EXIF	Exchangeable Image File Format
FRT	Forth Rivers Trust
GCP	Ground Control Point
GIS	Geographic Information System
GNSS	Global Navigation Satellite System
GPS	Global Positioning System
GPU	Graphics Processing Unit
HEC-RAS	Hydrologic Engineering Center - River Analysis System
IPCC	Intergovernmental Panel on Climate Change
km	Kilometre
kph	kilometre per hour
LiDAR	Light Detection and Ranging
MSP	Member of Scottish Parliament
NASA	National Aeronautics and Space Administration
NFM	Natural Flood Management
ppb	Parts Per Billion
ppm	Parts Per Million
QGIS	(Name of Geographic Information System application)
RGB	Red, Green and Blue
SAR	Synthetic Aperture Radar
SEPA	Scottish Environment Protection Agency
SfM	Structure from Motion
UAV	Unmanned Aerial Vehicle
UK	United Kingdom of Great Britain and Northern Ireland
USA	United States of America
USGS	United States Geological Survey
WSE	Water surface elevation

1 – Introduction

Flooding can be some of the worst natural disasters to occur, accounting for around one-third of all natural disasters globally affecting millions of people worldwide. Of all of the people affected by natural disasters, half comes at the expense of flooding, which could get worse (Lee *et al.*, 2020). According to the Intergovernmental Panel on Climate Change (IPCC) AR6 report, global warming of 1.5ºC is likely to occur in the period between 2021-2040, bringing with it extremities in weather patterns and greater variability and intensity of the water cycle (Ranasinghe, 2022).

With changes in levels of precipitation likely, along with historic and current changes in land use like draining of wetlands for agricultural and urban development (Hoskins, 1955), the challenges posed by flooding are likely to be exacerbated. To overcome this previously we have relied up on physical infrastructure for flood mitigation, building things such as dams, levees and seawalls. While physical defences can offer protection, it has also been found they can increase the extent of flooding and damages (Breen *et al*., 2022) which is why more recently there has been a gradual shift towards natural flood management (NFM) techniques.

NFM aims to work with natural hydrological and morphological processes to reduce the risk of flooding. It aims to achieve this via restoration of floodplains and wetlands, re-meandering rivers to their natural state and the creation of riparian woodlands, all with the aim to increase water storage capacity and slow down the flow of water naturally (SEPA, 2016). However, before NFM systems can be considered, the vulnerability and capability of the river and wider catchment needs to be assessed.

One way of accessing a river and catchment is through remote sensing techniques such as satellite imagery, Light Detection and Ranging (LiDAR) and Photogrammetry with each having its own advantages and limitations. Satellite imagery can capture broad areas but can lack resolution and be affected by weather (Avila-Aceves *et al.*, 2023). Aerial LiDAR is unaffected by weather and can be highly accurate, offering detailed topographical information, which is critical for flood modelling (Khanal *et al.*, 2020), but can also be expensive and availability of data can be limited, with 60% of Scotland lacking coverage with no immediate plans to rectify this (Scottish Government, 2024a). Where LiDAR data blackspots exist, an alternative to it can be Photogrammetry.

Photogrammetry is the process of turning overlapping two-dimensional (2D) photographs that can be captured by an unmanned aerial vehicle (UAV), into a three-dimensional (3D) model using specialised computer applications (Schenk, 2005). A benefit of photogrammetry can be reduced costs compared to acquiring aerial LiDAR and greater flexibility and manoeuvrability' of small UAV (Jouav, 2024). Like the LiDAR data, these finished datasets can be exported as a digital elevation model (DEM) and subsequently used for flood modelling in applications such as HEC-RAS

(USACE, 2024b) and ArcGIS (ESRI, n.d a). Further analysis of the DEMs and flood modelling results can then be conducted in geographic information system (GIS) applications such as QGIS (QGIS, n.d).

Therefore, the project seeks to ascertain any differences in the flood modelling results between a Scottish Government LiDAR derived DEM, and a Photogrammetry derived DEM on a 2.5km section of the River Devon, Clackmannanshire (Scotland). This is to establish the feasibility of using UAV imagery and photogrammetry processes in locations that lack LiDAR coverage. Furthermore, the project also seeks to identify any differences between two flood modelling applications, the dedicated hydrological application HEC-RAS (USACE, 2024b), and a Flood Simulation tool that is part of the suite of tools within ArcGIS (Esri, 2024b). The computer applications, DEM’s and results are therefore crucial for assisting with the implementation of flood mitigation measures through natural flood management techniques, especially during these times of climate change and the potential increased risks that it poses.

2 - Literature Review

2.1 - Flood Management

Floods are one of the most threatening natural hazards and pose a significant challenge to human populations across the globe (Schanze, 2006). In the period of 1900-2006 it is estimated that one-third of natural disasters were floods. Furthermore, during that same period, of all the people affected by all natural disasters, almost half of them were affected solely by floods (Lee *et al.*, 2020)

While floods have posed a significant challenge historically, that challenge could be set to be escalate due to the increase in frequence of flood events and the increase in the amount of damage floods could cause (Lee *et al.*, 2020) . Due to the threats of flooding historically and in the future, human societies all across the world have attempted to mitigate against flooding via the implementation of structural flood management and natural flood management techniques.

2.1.1 – Structural Flood Management

With the Industrial Revolution and a growing population, the United Kingdom had to bring more of its lands into production. This resulted in the draining of various wetlands and floodplains so they could be used for agricultural purposes (Hoskins, 1955). In addition to this, due to population pressures in coastal and urban areas (post WW2), saltmarshes had begun to be reclaimed for further agricultural purposes (common agricultural policy) and human settlements (Purseglove, 1988). The drainage of saltmarshes, wetlands and floodplains, with urbanisation and increases in impermeable surfaces greatly increased the risk of flooding across many areas of Britian (Werritty, 2006).

With the severe altering of Britian’s natural landscape and subsequent increased risk of flooding, national and local authorities sought to reduce these risks via the implementation of physical flood defence systems across rivers and coastlines (Werritty, 2006). Examples of these manmade flood defence systems include dams, levees, weirs, embankments, seawalls, gabions and moveable gates and barriers.

While there are benefits to these man-made flood defence systems, they can be very expensive for the initial installation and ongoing maintenance. Additionally, by withholding water and not allowing it to spill out into natural floodplains and wetlands, the natural storage capacity of the landscape has decreased. Therefore, manmade infrastructure in the rivers along with the straightened sections of river will simply hold the vast quantities of the fast-moving water before the defence systems eventually break and the water spills over, greatly increasing the risk of flooding downstream (Chiu *et al*., 2022). This is why there has been a gradual shift from physical flood defence systems towards nature-based flood solutions.

2.1.2 – Natural Flood Management

According to the Scottish Environment Protection Agency (SEPA) Natural Flood Management handbook, NFM "involves techniques that aim to work with natural hydrological and morphological processes, features and characteristics to manage the sources and pathways of flood waters" (SEPA, 2016), examples of which are demonstrated in Figure 1.

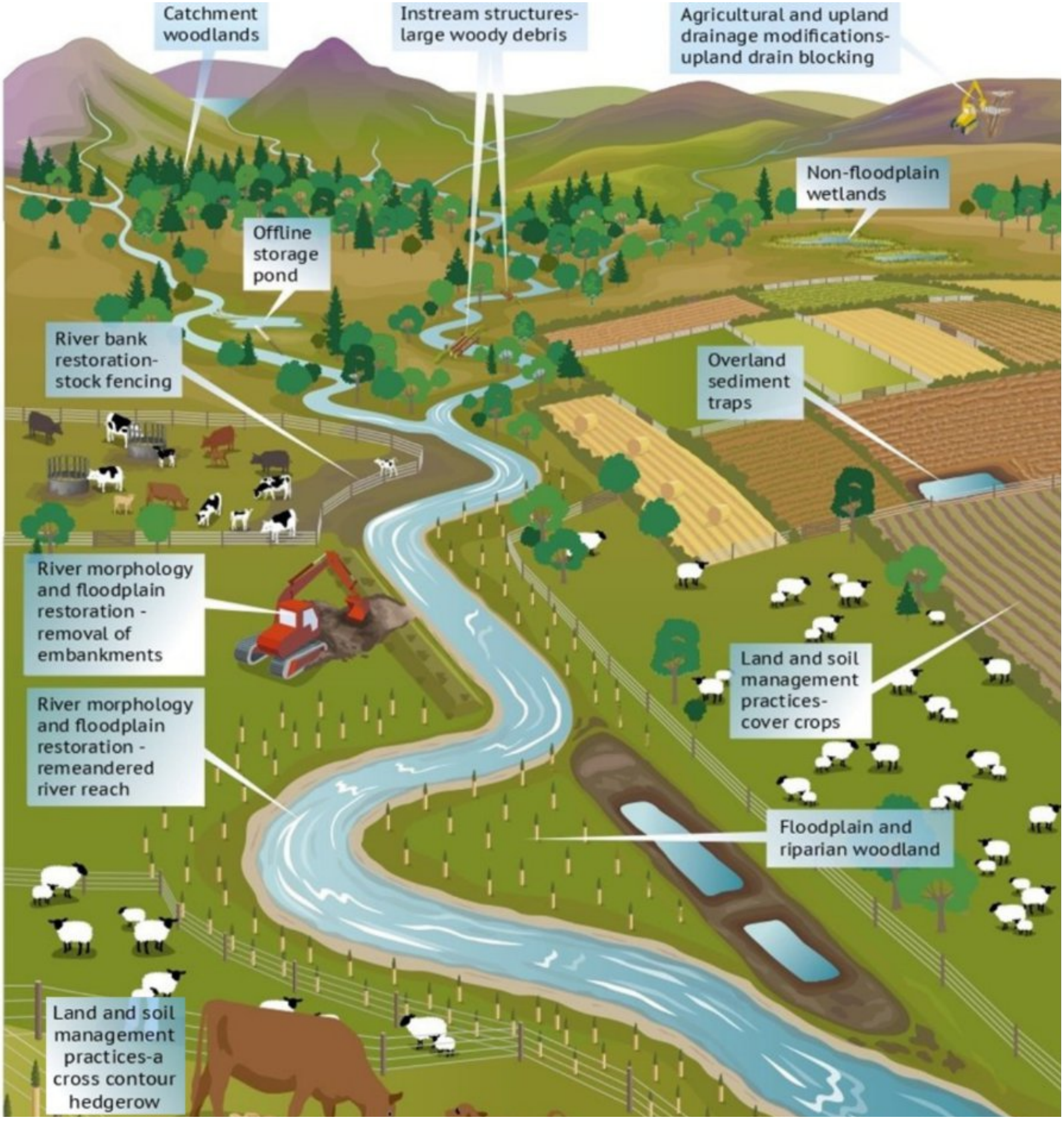

Figure 1 - Examples of NFM techniques from SEPA NFM handbook (SEPA, 2016)

The processes can slow the flow and increase water storage by mimicking natural functions of the catchment, floodplains and coast. Some of the techniques include restoring, altering and enhancing natural features and processes and can include: soil and land management, river management, floodplain management, woodland management, run-off management as well as coastal and estuary management (Environment Agency, 2024b).

The concepts of working with natural processes and natural flood management are enshrined in Scots Law under the Flood Risk Management (Scotland) Act 2009 (Wingfield *et al.*, 2019). Under the act, SEPA are legally required work with local and other responsible authorities to establish sustainable ways to manage the risk of floods, including the implementation of natural flood management systems.

As well as the initial purpose of water infiltration and attenuation, NFM can be more economically feasible by reducing costs associated with building traditional structural flood defences, while reducing the reliance and thus increasing the lifespan of existing structural flood defences (University of Reading, 2019). Furthermore, NFM can also increase species richness and habitat diversity and sequester carbon (CIWEM, 2022).

As a result of this, the Department for Environment Food and Rural Affairs (DEFRA) and the Environment Agency (England) recently announced joint funding of £25m to assist with the creation and implementation of 38 separate natural flood management projects covering a range of habitats including urban and rural, inland and coastal, upland and lowland (Environment Agency, 2024b), while the Scottish Government, SEPA and associated partners have completed implementation of natural flood management techniques as part of the Eddleston Water Project. Some of the techniques implemented included riparian woodland planting, river re-meandering, floodplain restoration, off-line storage pond creation and the placement of instream structures (Tweed Forum, 2022).

Despite current and future NFM projects in the pipeline across Britian, there still remains some minor criticism of natural flood management systems and its low adoption. One of the key factors behind slow implementation of NFM could be the lack of evidence beyond small scale local benefits, due to the lack of monitoring and evidence of how it affects larger catchments, in addition to the added complexity of implementing NFM systems due to the fragmentation of lands, and different uses people have for these resources across Scotland (Wingfield *et al.*, 2019). With further funding and increasing threats from climate change there could be a sharp increase in the number of NFM projects implemented (Thaler *et al.*, 2023).

2.2 Climate Change

Earth's climate has been subject to change over hundreds of thousands of years both naturally and anthropogenically. Natural climate change can be caused by things like changes from incoming solar radiation from the sun, the Milankovitch cycle (the eccentricity, axial tilt and precession of earth's orbit of the sun), ocean currents and atmospheric circulation as well volcanic activity (British Geological Survey, 2019). As a result of these natural changes, Earth has altered between periods of warming (interglacial) and cooling (glacial) consistently over the last 800,000 years (Snyder *et al*., 2011)

However, recent data has shown that human activities has started to alter Earth's climate on a much faster scale. From isotopic data from ice cores, some reaching a depth of 3km, British Antarctic Survey has 120,000 years' worth of continuous ice core data from Greenland and 800,000 years from Antarctica (Bauska, 2022)

What these datasets have established is that for 800,000 years, Earth's CO_2 (carbon dioxide) concentration levels never breached 300ppm (parts per million) until around the start of the 20th century where they have risen steadily since (Snyder *et al*, 2011). CH_4 (methane) has had similar changes. For 800,000 years CH_4 levels never breached 800ppb, again until around late 19th/early 20th century where they too have risen consistently since (Bauska, 2022).

Today, CO_2 levels are over 50% higher compared to pre-industrialisation levels at over 415ppm (Hashimoto, 2019), while CH_4 levels have doubled in the same time period to over 1600ppb (Bauska, 2022) with the he rapid increases in vast quantities of greenhouse gases in the atmosphere alter Earth's climate and natural cycles.

With the anthropogenic increases of greenhouse gases into the atmosphere, as well as further changes to Earth's surface such as loss of vegetation, this is altering the radiative balance of Earth and the atmosphere which has resulted in increases of Earth's global surface temperature. These changes can result in altering earth's natural water cycles, weather patterns and further distribution of water across the surface and atmosphere of Earth (Dilmore *et al*., 2018).

2.2.1 – Increases of flooding

Due to climate change and land-use change (Hall *et al.*, 2014), there is a risk of increased extreme weather events and flooding across the globe. (Calvin *et al.,* 2023). Flooding can be caused by more intense rainfall and changes in precipitation patterns, intensification and altering of water cycles (Huntington, 2006) as well as rising sea levels (Vitousek *et al.*, 2017) and snow and glacier melt (James *et al*., 2016).

In the IPCC "Climate Change 2023" report, it is stated that over the continent of Europe, heavy precipitation has likely increased and that heavy precipitation will become both more intense and frequent with additional global warming (Calvin *et al.*, 2023). The same IPCC report also states with high confidence that there have been significant trends in peak streamflow and that more land areas will see an increase of being affected by river floods (medium confidence) (Calvin *et al.*, 2023).

These sentiments were shared by the official Meteorological Office of the United Kingdom who concluded that storms over Autumn and Winter are becoming wetter due to climate change. The same report also states on average, precipitation on stormy days is now 30% greater than it was compared to the pre-industrialised climate (Kew *et al*., 2024). With the changes in weather and increased threat of flooding, a range of remote sensing techniques have been created to help plan, adapt and mitigate against flood events (Leitão, 2016).

2.3 – Remote Sensing

Remote sensing is a technique used to gather information on an area or object from a distance. This is useful for flood modelling and helping implement natural flood management systems as it allows for faster data collection of large areas, which is particularly useful if the area is remote and physical access is limited. Remote sensing data is typically acquired using either satellite or aircraft-based recording instruments and can be passive or active (Munawar *et al*, 2022).

Passive remote sensing requires energy from the sun. This is reflected or absorbed and re-emitted and passive instruments, typically in the form of a satellite with an optical sensor, can detect electromagnetic radiation then measure and process the spectral information within the captured content (Amani *et al.*, 2022). Active sensing doesn't require radiation from the sun as it can generate and emit its own energy usually in the form of laser beams and microwaves. This energy is then backscattered or reflected and the active instrument (satellite or moving aircraft) processes and measures the captured data within the microwave band of the electromagnetic spectrum (NASA, 2021).

Active remote sensing has advantages over passive in that it can capture data 24/7 as it uses its own energy source and doesn't really on sunlight. Furthermore, active remote sensing has all weather capability as the microwaves can penetrate fog and cloud (Gupta, 2018). This is particularly useful for data capture of areas that have high cloud cover.

2.3.1 – Satellite Remote Sensing

There are a range remote sensing instruments available to assist with flood modelling and natural flood management implementation and one of these is satellite imagery. Satellite imagery can be both passive and active and is an invaluable tool due to the different data collection methods and datasets satellites can provide, which are depending on the types of sensors the satellite uses.

Synthetic Aperture Radar (SAR) and Light Detection and Ranging (LiDAR) are both examples of active satellite remote sensing technologies. SAR sensors operate by transmitting highly powered radio waves at over 1000Hz from spaceborne instruments towards Earth. In a sequential way the instruments then receive the backscatter from Earth and can calculate the time and distance from each point before creating a 2D image of Earth's surface (Moreira *et al.*, 2013).

LiDAR operates in a similar way but emits laser pulses instead of radio waves before calculating the time for the reflected laser to return to the sensor. It too, based on that distance and time calculation can create an image of Earth's surface using 3D point cloud data (Wandinger, 2005).

SAR has an advantage over LiDAR as its independent from sunlight and cloud cover (Moreira *et al.*, 2013) and can also provide near real time data on flood events (Wu *et al.*, 2023), whereas LiDAR can be affected by fog and cloud (Davis *et al.*, 1999), however LiDAR can offer higher resolution than SAR. Either way both technologies can be vital in flood modelling due to the produced datasets such as digital elevation model (DEM), digital surface model (DSM) and digital terrain models (DTM) that can then be used to predict the extent of floods (Avila-Aceves *et al.*, 2023).

Another satellite remote sensing technology is satellite image processing. This is a passive remote sensing technique and involves satellites orbiting Earth that then capture images of Earth's surface. Images captured by satellite play a vital role in flood management as they can capture large areas of land and show land cover characteristics and changes like increasing urbanisation and deforestation. The images along with daily rainfall and rainfall intensity are usually used in hydrological flood modelling (Avila-Aceves *et al.*, 2023).

In addition, scientists from Massachusetts Institute of Technology (MIT) have developed a new tool that integrates satellite imagery and a physics-based flood model along with A.I/machine learning to generate satellite photographs of future flooding events (Chu, 2024). While satellite imagery will continue to play a role in flood modelling it does have some limitations, such as being affected by weather conditions like cloud cover (Davis *et al.*, 1999). Satellite remote sensing can also be expensive with the total cost of NASA's Landsat8 satellite to cost around $1billion for its 5-year programme (NASA, 2015). Furthermore, there are also limitations on resolution, with Landsat8's maximum resolution being 30m for all bar one of the 9 Bands (PAN being 15m) (Acharya *et al*., 2015). When higher resolution is required for flood modelling more localised aerial LiDAR should be considered.

2.3.2 – Aerial LiDAR

Aerial LiDAR is another remote sensing tool that can be used for flood modelling. It works in much the same way as Satellite LiDAR with one major difference in that the LiDAR instruments aren't in space attached to satellites but are at a much lower altitude and typically attached to the underside of unmanned aerial vehicle (UAVs), small planes and helicopters.

Despite those differences aerial LiDAR still has the same advantages like getting multiple returns from laser/light emitted from the instrument as shown in Figure 2. This means that when surveying areas, some of the LiDAR pulses hit and return from the vegetation canopy and some from the surface of the ground, with others returning from anywhere in between the two (Wasser, 2024). The multiple return from LiDAR means it's possible to interpolate Earth's surface with greater accuracy which can result in highly accurate DTMs because of the ability to remove some Earth's features such as vegetation (Renslow *et al*., 2000). Aerial LiDAR also has one advantage over satellite in that it's much closer to earth which means a much higher resolution of captured data, however this also means that it does have a lower capture footprint.

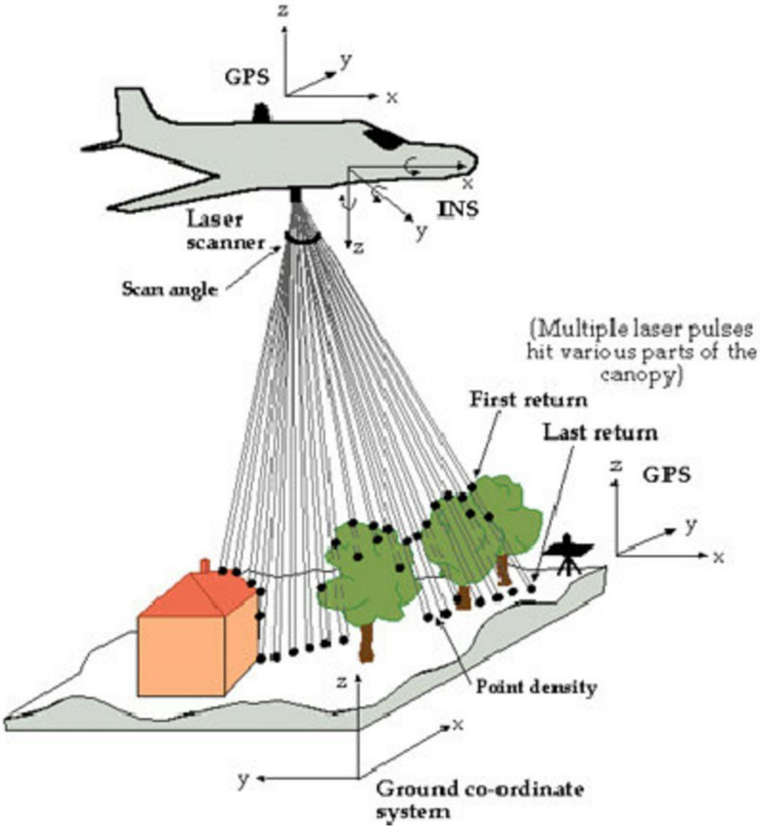

Figure 2 - Airborne LiDAR showing multiple lasers and returns (Dowman, 2004)

With greater flexibility such as being able to design a flight plan for optimal capturing conditions and the manoeuvrability of small aircraft (Saylam, 2009), aerial LiDAR is a powerful tool for acquiring high-res local topographical data. The dense point clouds that can be captured and generated from aerial LiDAR instruments can represent local terrain with a high degree of accuracy. This is because of the high-resolution sensors along with onboard equipment that records XYZ position, aircraft roll and altitude that can correct any LiDAR returns that may be skewed due to flight motion. This results in aerial LiDAR having some of the highest levels of vertical accuracy compared to mobile terrestrial LiDAR and UAV Photogrammetric Capture (Khanal *et al.*, 2020).

The optimal flight plan and conditions along with high spatial resolution and vertical accuracy can result in detailed dense point cloud derived digital elevation models (DEMs). These DEM's can assist with flood modelling by capturing river channels and floodplains along with other areas of interest that can affect river flooding like urban and woodland areas. Capturing the river channel can be used in hydraulic modelling to try and predict flood extent (Kabite, 2017) while mapping floodplains can assess potential flood risk by identifying areas that could be prone to inundation (Muhadi *et al.*, 2020).

Despite the positives of aerial LiDAR there are some drawbacks and one of these is the potential lack of coverage of data. In Scotland, as of 31st October 2024 only 40% of land has been captured by LiDAR (Scottish Government, 2024) with this data being captured over 5 phases between 2011-2022. For comparison, this compares to England (Environment Agency, 2024a) and Wales (Welsh Government, 2023) who have both achieved near full national aerial LiDAR coverage.

A Guardian article quoted an anonymous Scottish Government spokesperson in May 2023 who stated that Scotland was exploring repeated LiDAR scans of Scotland's land surface (Greenfield, 2023). However, in response to a personal letter sent on 02/10/2024 to Member of Scottish Parliament (MSP) Gillian Martin (Acting Cabinet Secretary for Net Zero and Energy), the Scottish Government concluded that there are no commitments and that the Scottish Government is continuing to consider "the feasibility and financial viability of a national capture programme" (Scottish Government, 2024b). Where there are LiDAR data blackspots, then an alternative to aerial LiDAR is photogrammetry.

2.3.3 – Photogrammetry

Photogrammetry is a 150-year-old passive remote sensing technique that is able to obtain, measure and interpret information on the properties of surfaces and objects. When first developed photogrammetry was a purely analogue and optical-mechanical technique, however with advancements of technology photogrammetry is now almost entirely digital and computer-aided (Aber *et al*., 2010).

Photogrammetry works by taking overlapping photographs of Earth's surface or an object. These photographs can be acquired by satellite imagery (space photogrammetry) or from lower altitude aircraft such as a plane or UAV with camera lenses fitted to the underbody of that flying vehicle (aerial photogrammetry) (Schenk, 2005) with processing done by specialised applications like Metashape (Agisoft, n.d).

Metashape is created by software company Agisoft and the application is able to process (red, green and blue) RGB, thermal and multispectral images by utilising high power computer hardware and algorithms along with manual post-processing (Agisoft, 2020). Metshape is used by the United States Geological Service (Over, *et al*., 2021) and a 2015 paper by the Federation of International Surveyors concluded that while no algorithms can be perfect for all conditions, it's possible to generate high-resolution DEMs from UAV images in Metashape (Bhandari *et al.*, 2015).

When Metashape has processed the raw data, DEMs can be exported for flood modelling. From the DEM a DSM can be created which is an elevation model including tops of all surfaces such as buildings and vegetation. A DTM can also be created from the DEM which is a model of just Earths bare surface free of all nonground surfaces with buildings and vegetation removed (Zhou, 2017).

There are pros and cons of Photogrammetry when compared to LiDAR such as lower costs. However, LiDAR may be more accurate due to having no dependency on light and being able to penetrate vegetation (Jouav, 2024). Similarly, there are pros and cons of satellite derived photogrammetry and aerial photogrammetry. With satellite derived photogrammetry, images may be readily available which could be faster and more cost-effective but may be lower resolution with images out of date and obscured by weather and lighting conditions (DJI Enterprise, 2021). In these circumstances, localised aerial photogrammetry via UAV might be preferred.

2.3.4 – Unmanned Aerial Vehicles

UAV technology has advanced quite rapidly in recently with UAV's becoming smaller, lighter and more affordable making them more accessible. With different remote sensing add-ons available for drones like GPS modules and high-resolution digital cameras, UAVs can be the go-to solution for filling the gap where there is a lack of LiDAR coverage and satellite derived photogrammetry is also unavailable or inadequate.

Quadcopter UAVs, such as the DJI Mavic 2 Pro has 31 minutes of flight time and wind resistance of 29-38kph and comes equipped with GPS & Glonass, a 1" CMOS sensor with 20MP and manual ISO. Weighing 907g (DJI, 2018) it can be flown by anyone with a Civil Aviation Authority (CAA) Operator and Flyer ID and within the restrictions of subcategories A2 or A3 (see Table 1) (CAA, 2024). With the specification of UAVs and remote sensing instruments available, one study concluded that UAV-derived DEMs could be an alternative to LiDAR DEM, striking a compromise between accuracy and cost (Annis *et al.*, 2020) potentially making UAV-photogrammetry a vital tool for assisting with localised flood modelling.

Table 1 - UAV rules and requirements for flying in open category (CAA, 2023)

Operation		UAS		UAS Operator	Remote Pilot
Subcategory	**Operating Area**	**Class**	**Speed**	**Registration**	**Competency**
All	-Max height 120m -No dropping of articles of carrying dangerous goods -Must be able to see UAV at all times -Airspace restrictions apply -Be aware of temporary restrictions			Minimum age 18	
A1	Fly over uninvolved people but no crowds	Built privately or placed on market before 01/01/2026	Up to 250g flying weight	If camera equipped	-Read operation instructions
	No intentional flights over uninvolved persons	A1 Transitional (not after 01/01/2026)	250g – 500g flying weight	Yes	-Read operation instructions -Online training and test -Self-practical training -A2 CofC Theory Test
A2	No closer than 50m horizontally from uninvolved persons	A2 Transitional (not after 01/01/2026)	Up to 2kg flying weight	Yes	-Read operation instructions -Online training and test -Self-practical training -A2 CofC Theory Test
A3	-No uninvolved people within area of flight (50m+ separation required) -No flight within 150m horizontally of residential/commercial/ industrial/recreational areas.	Built privately or placed on market before 01/01/2026	Up to 25kg flying weight	Yes	-Read operation instructions -Online training and test

2.4 Flood Modelling

The raw data derived from remote sensing requires processing for flood modelling and several applications can assist with this depending on the original data source. Datasets from aerial LiDAR such as mosaic, LAS or terrain can be processed, analysed and mapped to create highly accurate shapefiles, DEMs and visualisations via Geographic Information System (GIS) applications (IBM, 2023) such as QGIS and ArcGIS.

QGIS is a free and open-source programme supported and used by organisations such as Zurich University (QGIS, n.d). QGIS with imported flood simulation results from modelling software like HEC-RAS, along with Ordnance Survey maps will allow for accurate mapping of areas of inundation (floodplains) (Cimpianu *et al*., 2019). ArcGIS, while offering similar functionality of QGIS is a licensed and paid for suite of widely used geospatial tools by ESRI and has additional in-built functionality such as Flood Simulation (Esri, 2024a).

Flood Simulation is available as part of the licensed paid-for application ArcGIS Pro. The latest version of the software (v3.4) includes a new integrated GPU-based 2D flood modelling tool (Esri, 2024a) . Hydraulic modelling uses computational power and mathematics to simulate how water flows through open channels (Yeong, 2016). ArcGIS Pro 1D flood simulation has been used to successfully map floodplains along the Swat River (Pakistan) (Ullah *et al.*, 2024), however, despite this, ESRI state in their own technical papers that ArcGIS Pro tools cannot handle all flow regimes and conditions and are designed to complement and not replace existing modelling tools (Esri, 2024b) like HEC-RAS.

HEC-RAS (Hydrologic Engineering Centre-River Analysis System) is a free to use flood modelling computer application created by US Army Corps of Engineers (USACE, 2024a). It differs to ArcGIS Pro as when combined with GIS data such as DEMs derived from LiDAR or Photogrammetry, HEC-RAS allows both 1D and 2D and steady flow and unsteady flow calculations. As such, HEC-RAS is a highly precise tool, used by both public and private organisations (Zainal and Abu Talib, 2024).

Due to the effectiveness of the computer application, HEC-RAS modelling has been used for hundreds of studies globally to assist with the implementation of NFM techniques (Hill *et al.*, 2023) including the Upper Calder Valley in the UK (Ferguson *et al*., 2019), Australia (Earl *et al.*, 2023), Zambia (Umer *et al.*, 2025), Indonesia (Supratman *et al.*, 2024) and Türkiye (Supratman *et al.*, 2024). HEC-RAS has also been used for studies comparing photogrammetry and LiDAR in Tanzania (Sakala, 2020) Northern Virginia (Zahirieh, 2019) and Atlanta (Ballow, 2016a) in USA

3 – Study Site Area

The study site (Figure 3) is an approximate 2.5km section of the River Devon between the towns of Tillicoultry and Dollar in Clackmannanshire, Scotland.

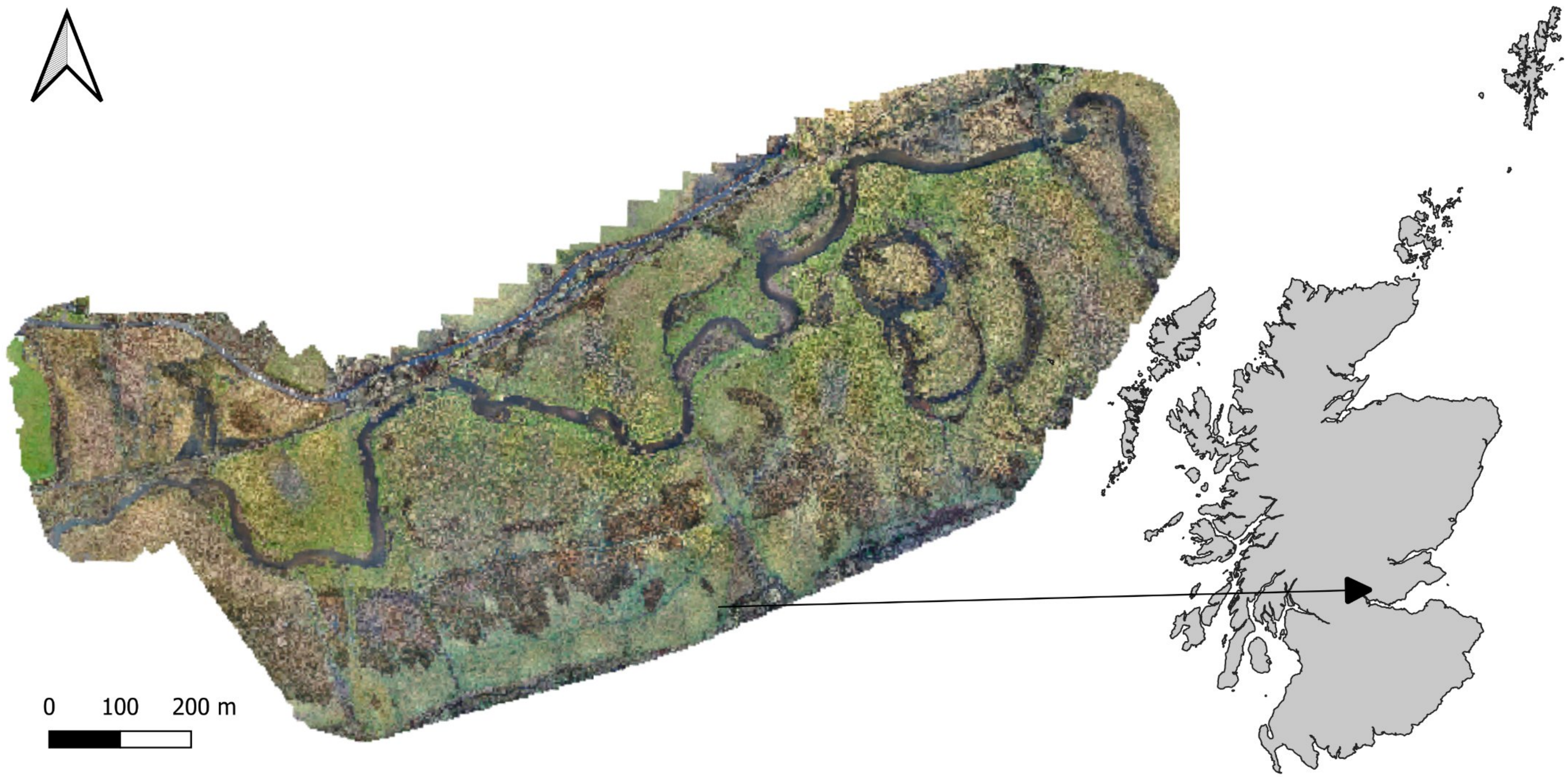

Figure 3 - Aerial photograph of study side (River Devon) (Forth Rivers Trust, 2024)

Land cover (Figure 4) - arable and horticulture, with broadleaved woodland towards the edges of the site. (NRFA, n.d).

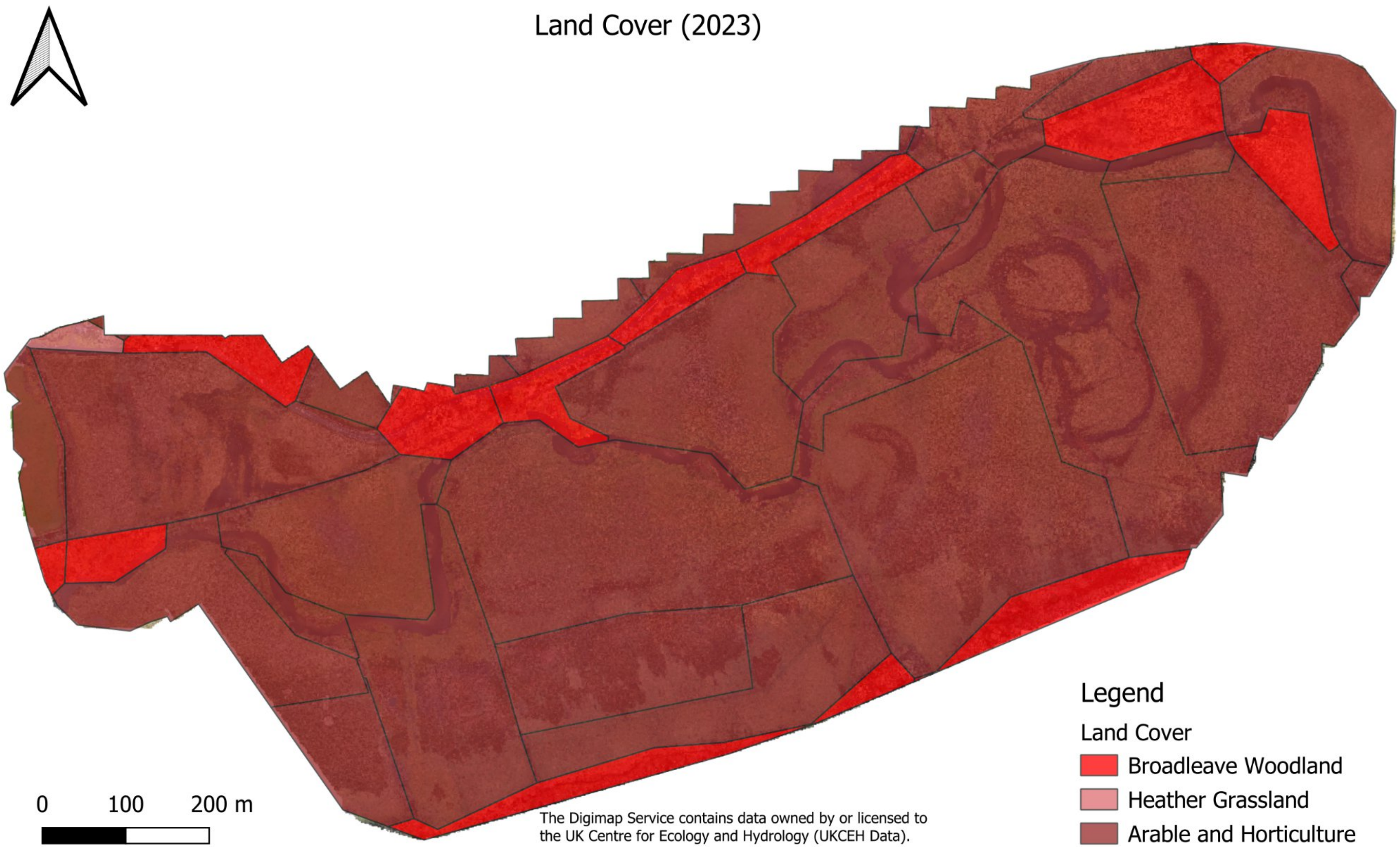

Figure 4 - Land cover of the study area (UKCEH, 2023)

4 – Aims & Objectives

Aim

The primary aim of this project is to conduct an evaluation of varied flood modelling techniques along a section of the River Devon to determine the effectiveness of SfM-UAV derived DEMs and different flood modelling applications. This could be used to assist Forth Rivers Trust with future implementation of natural flood management systems within the Forth River catchment.

Objectives

The aim will be met by the following objectives:

1. Replicate a flood model based on the method of the existing commercially produced report (2D HEC-RAS with SEPA LiDAR data) and compare results to that from the commercial report.

2. Using same data as Objective 1, conduct a 1D flood model (HEC-RAS) and compare results to the 2D model from Objective 1.

3. Using photogrammetry, convert Forth Rivers Trust drone image data to a DTM/DSM file, and conduct both 1D and 2D models (HEC-RAS) and compare outputs to the results of Objectives 1 & 2.

4. Conduct an ArcGIS Pro flood simulation using both SEPA LiDAR and photogrammetry derived DEM and compare to 2D models results from Objectives 2 and 3.

5. Create a comprehensive method to enable Forth Rivers Trust to apply the method on future study sites within the Forth Rivers catchment area.

5 – Preparatory Methods and Results

5.1 – Ground Control Point Collection

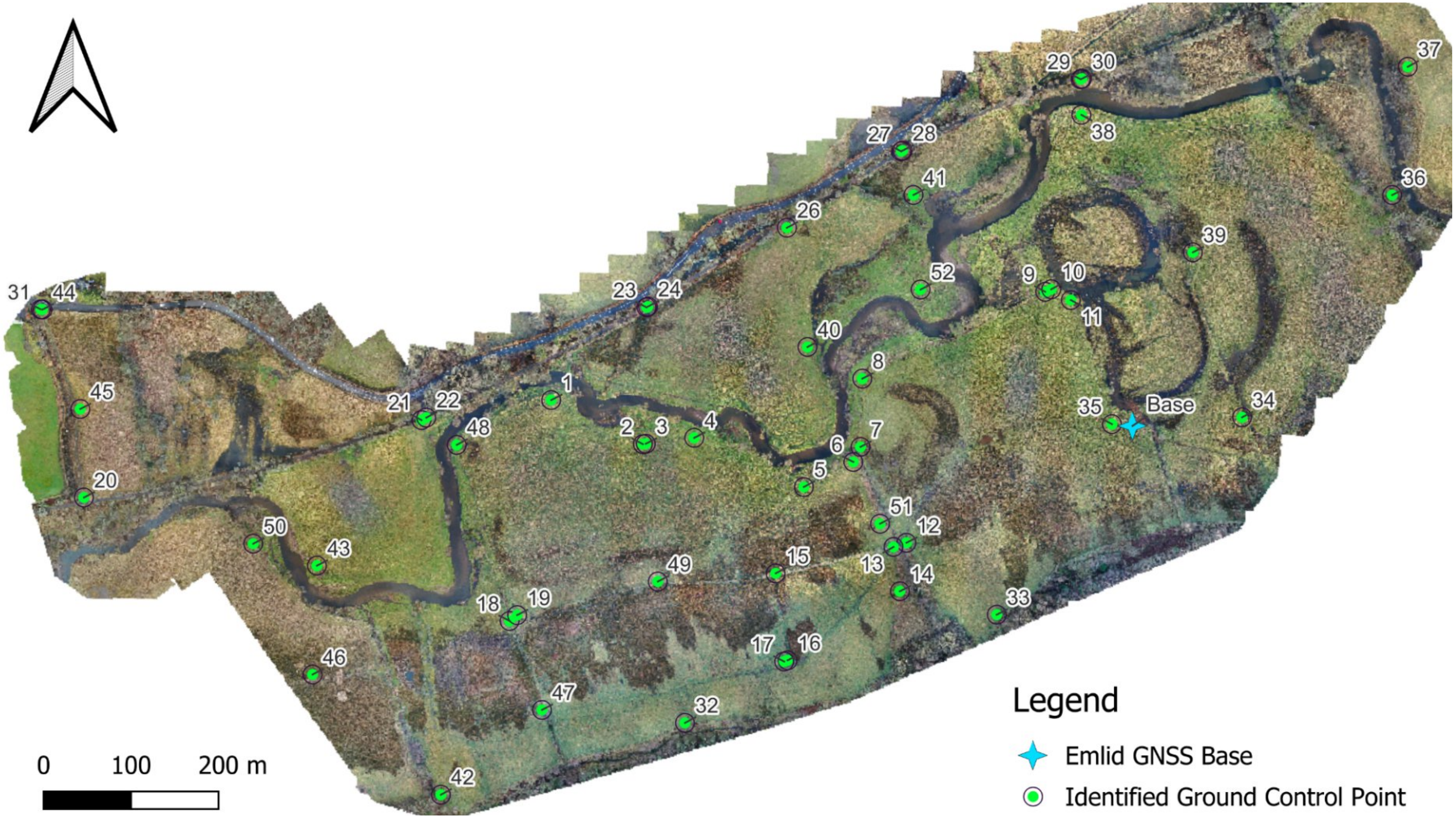

Figure 5 - Study site showing the location of identified ground control points

5.1.1 – Methods

Ground control points (GCP) are specific and identifiable points on Earth's surface with known co-ordinates and are used to improve reliability and accuracy of spatial data. They are vital in Photogrammetry because they provide reference points which helps ensure the structure-from-motion (SfM) models aligns more closely with the real-world (Yodono *et al.,* 2020). This is vital because GPS sensors, such as the one within the DJI Mavic 2 Pro quadcopter used to capture the aerial images of the study site, are typically accurate to around 4 metres depending on the environment and conditions (US Government, 2022).

For the collection of GCP a desk study was conducted to identify 50 potential points as shown in Figure 5. A site visit was undertaken and using a configured Emlid RS+ GNSS base and receiver (Figure 6) , the co-ordinates of each ground control point was collected. These were stored on the GNSS equipment then exported in CSV formatted for future geo-referencing within Metashape that can be seen in section 5.2. More detailed information outlining expanded methods for GCP collection can be found in Appendix 3.

Figure 6 - Emlid RS+ GNSS base (left) and receiver (right)

5.1.2 – Results

Figure 7 shows the results from the GCP collection field study. 50 points were identified prior to the visit with 44 GCP successfully collected on the day. Reasons for missing ground control points: Points 31, 44, 45 and 46 - receiver being out of range due to distance to the Emlid GNSS base. Point 36 out of range to Emlid GNSS base due to dense tree lines affecting the signal with GCP 18 not being collected and marked down as miscellaneous.

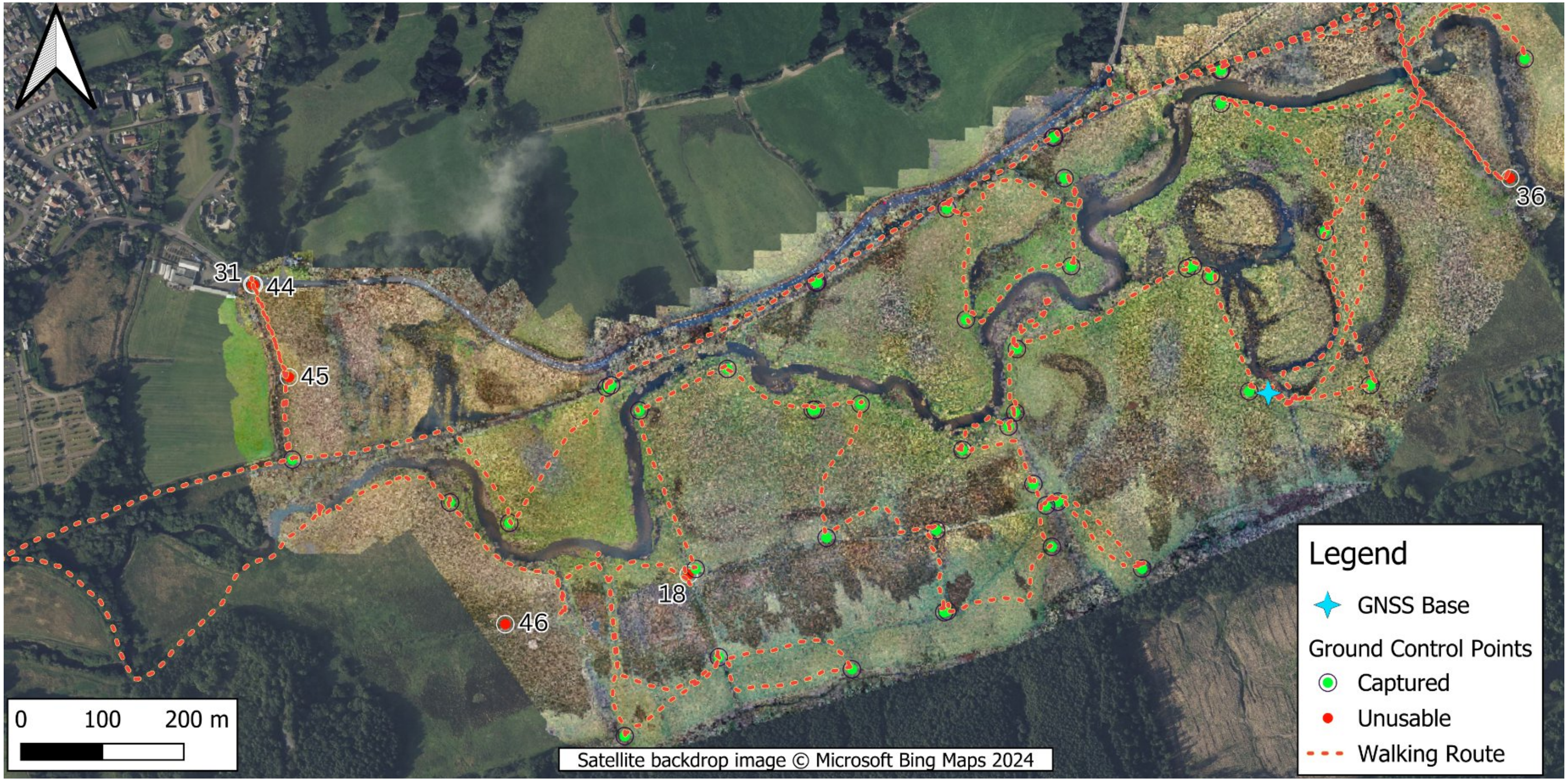

Figure 7 - Results from ground control point collection field work

5.2 – Photogrammetry UAV-SfM data post processing

5.2.1 – Methods

The process of georeferencing within the Metashape application (Figure 8) is to increase the accuracy of captured data such as aerial images, to ensure that the finished 3D model is as closely aligned to real-world as possible. This was achieved by anchoring the captured GCP then using optimisation and transformation tools and algorithms within Metashape to reduce errors in photograph alignment, while improving accuracy on aligning everything to the proper co-ordinate system with a method similar used on a project on at Proctor Creek in Atlanta, USA (Ballow, 2016b). As well as this, another key aspect of UAV data post processing is the creation of dense point cloud and digital surface models and subsequently being able to filter out vegetation, buildings and vehicles to create a digital terrain model (Polat *et al*., 2023).

This section was completed following the steps outlined in the Structure From Motion Workflow Document by USGS (Over *et al.*, 2021). While the document stated that it's for processing coastal imagery using Metashape v1.6, it can be applied to inland imagery and is valid for Metashape v2.1. At each key step of the workflow, the Metashape Workspace was duplicated and re-named appropriately to keep track of changes and avoid losing work due to human-error or file corruption. Expanded methods, including input parameters and screenshots related directly to this project can be seen in Appendix 4.

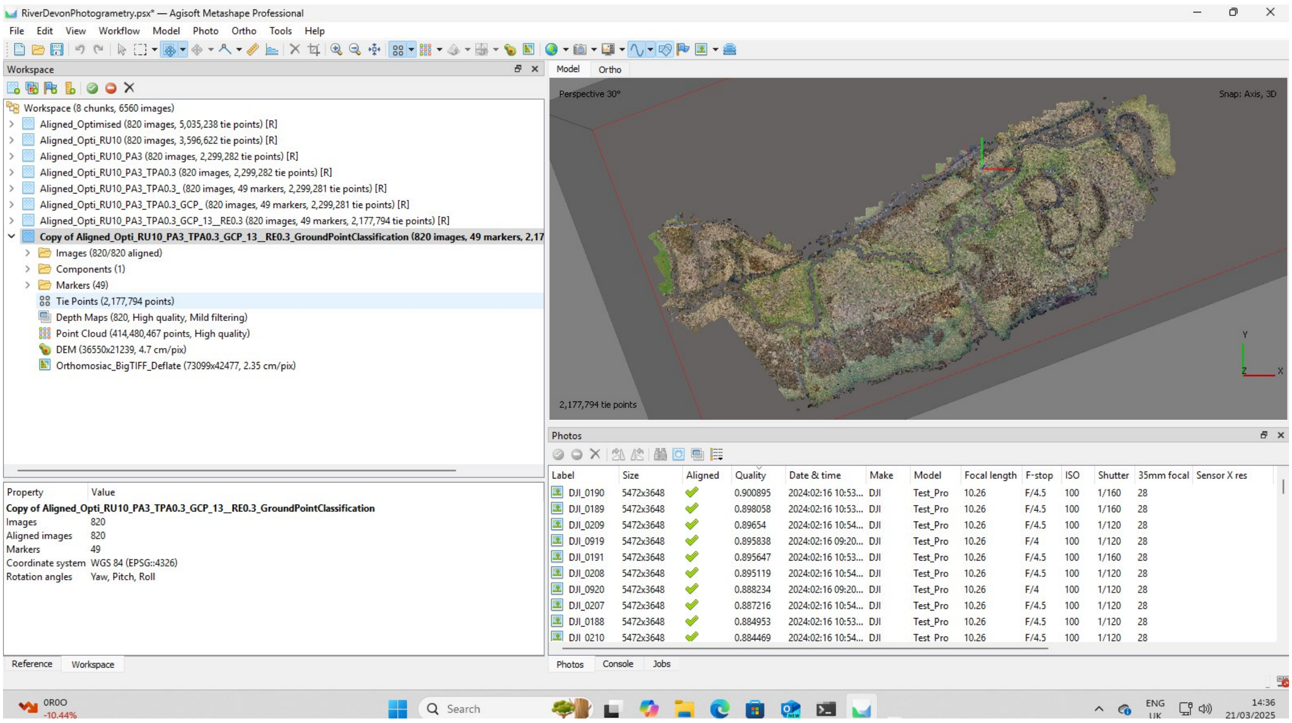

Figure 8 - Metashape workspace, layout and dense point cloud created for this project

5.2.2 – Results

After utilising 13 of 46 ground control points as checkpoints (6, 16, 18, 20, 23, 27, 28, 29, 36, 38, 46, 47 and 50) for camera optimisation, and completing all other steps outlined in Section 5.2.1, Table 2 shows the accuracy levels of the finished model within Metashape, while Figure 9 shows a 3D visualisation of the point dense cloud that was derived from Forth Rivers Trust UAV camera images.

Table 2 – Model error and accuracy results from Metashape

Total Error	Longitude Error (m)	Latitude Error (m)	Altitude Error (m)	Error (m)
Control Points	0.419	0.183	0.329	0.564
Check Points	0.338	0.285	0.759	0.878

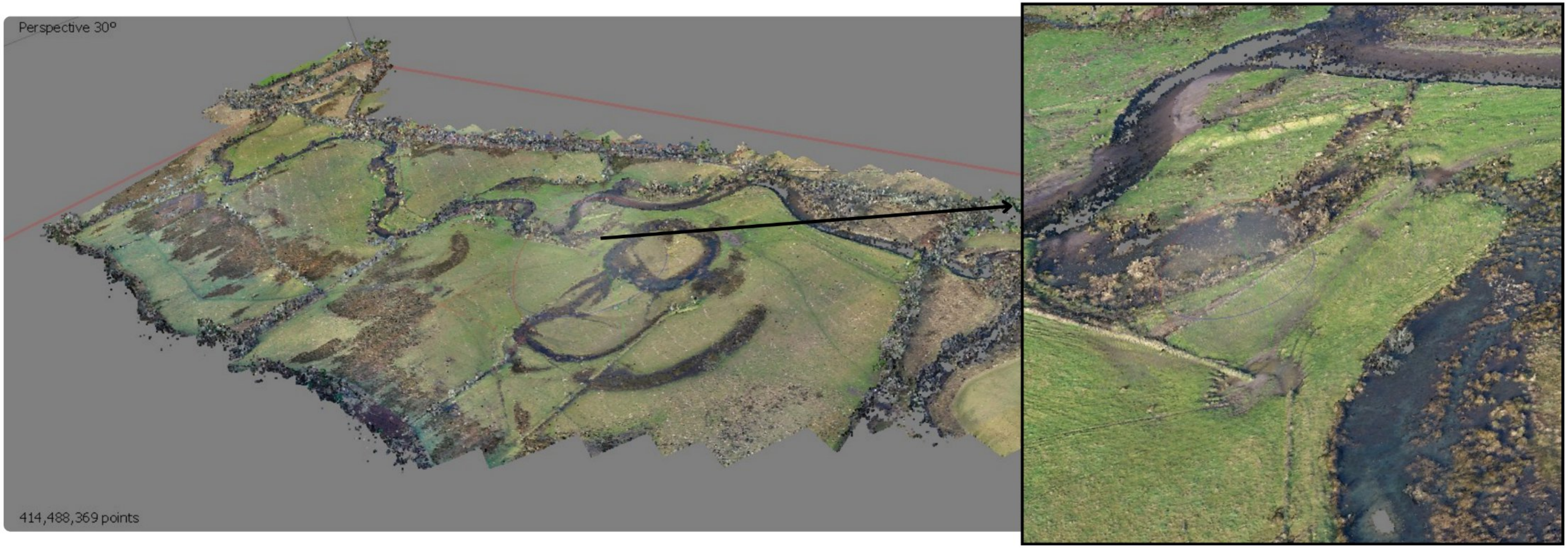

Figure 9 - Photogrammetry derived point dense cloud 3D visualisation

Figure 10 shows a DSM that was derived from the Photogrammetry processes outlined in section 5.2.1 showing the meandering of the river and elevation differences of the study site. As a digital surface model, it captures all over features such as tree's, bushes and fence lines.

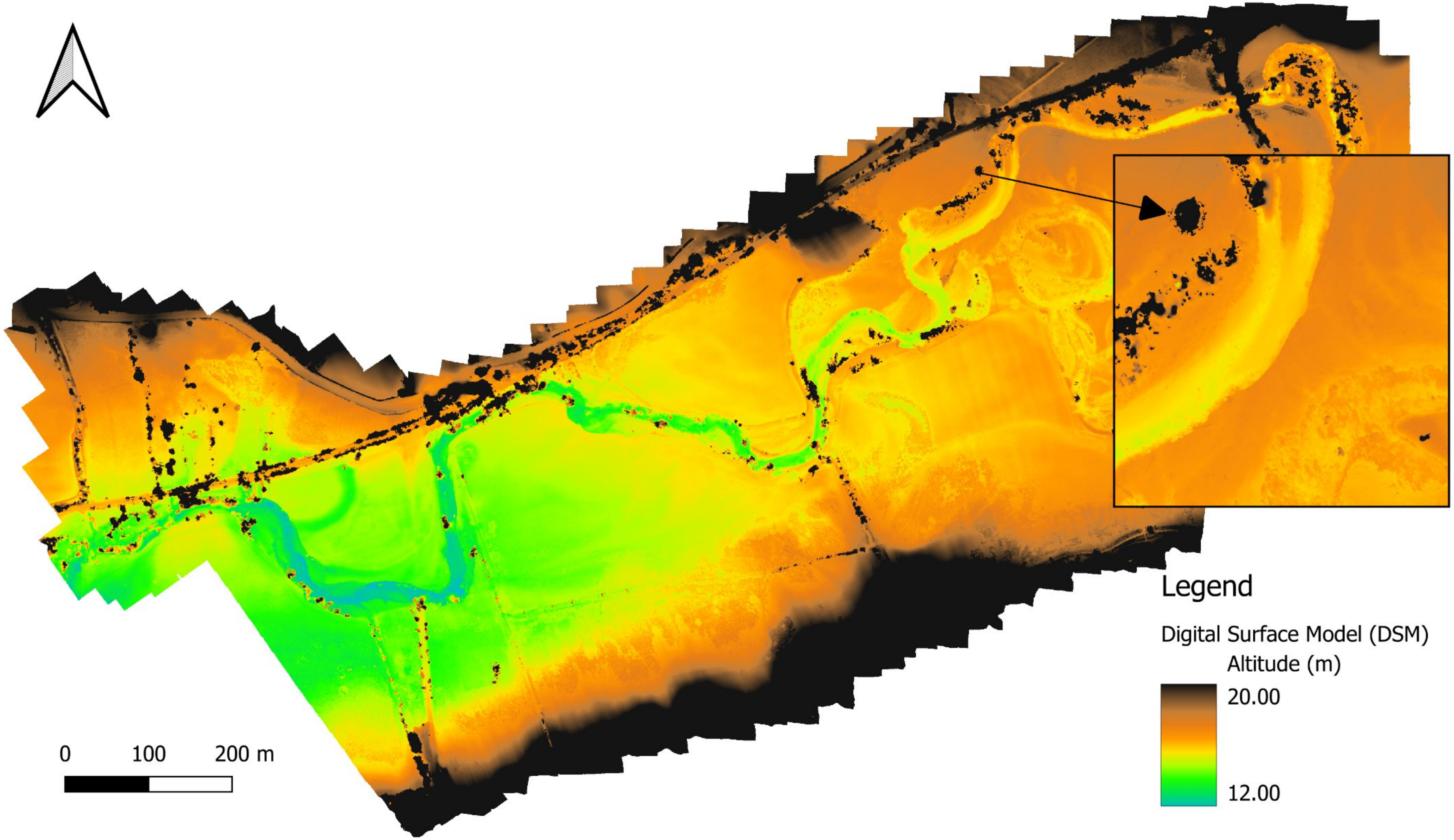

Figure 10 - Photogrammetry derived DSM of study site area

Figure 11 shows a DTM that was derived from the DSM in Figure 10. Being a digital terrain model, it is a representation of Earth's surface showing the River Devon and terrain with features such as vegetation and fence lines removed.

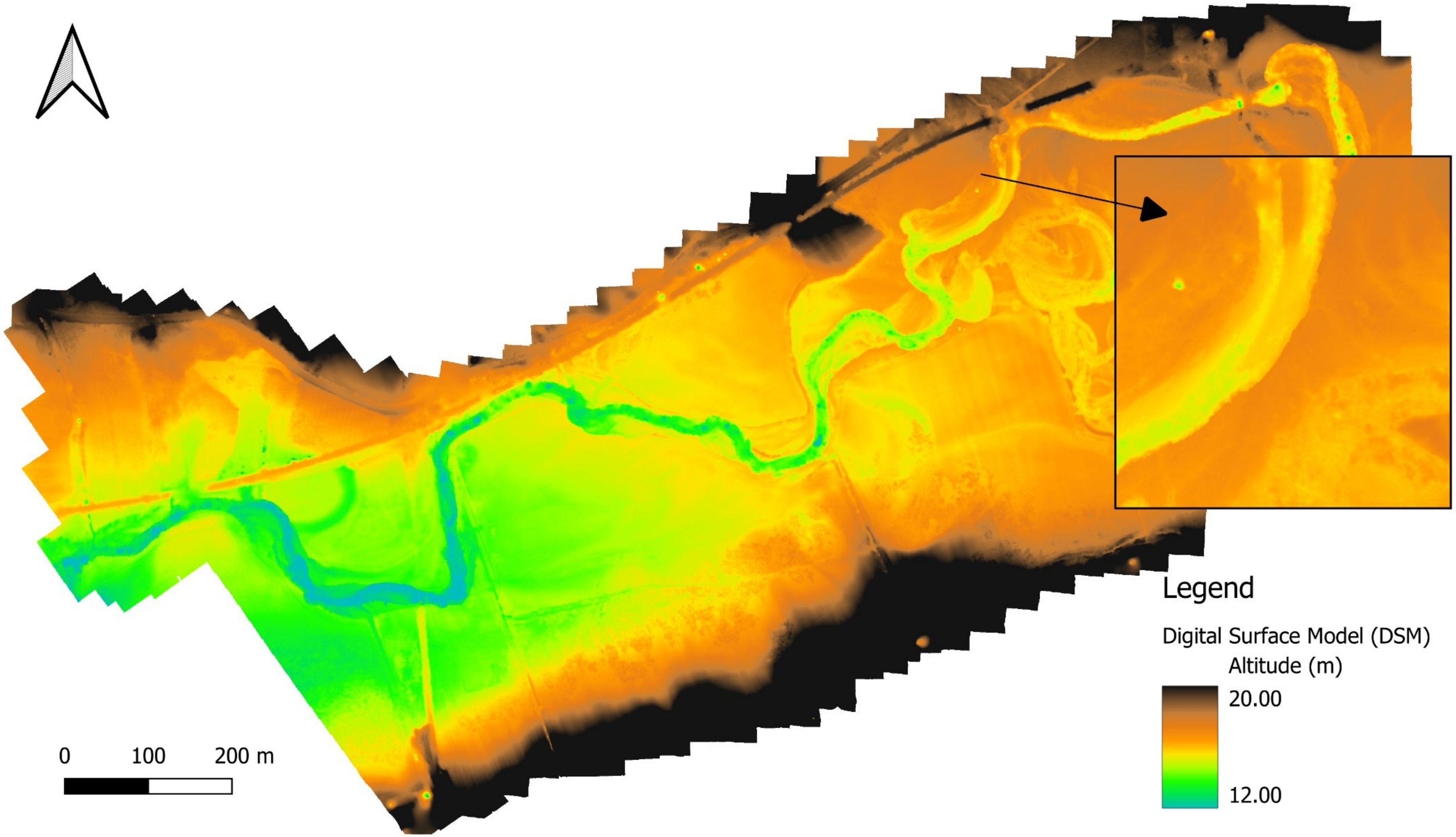

Figure 11 - Photogrammetry derived DTM of study area

Figure 12 shows some differences between the FRT DSM, and the finished DSM derived from the Photogrammetry processing conducted in section 5.2. Number 1 shows a lot of artefacts in the data in the potential floodplains in the FRT DSM that have been removed in the DSM created in this project. Number 2 shows these similar artefacts in the FRT DSM in the stream channel, with a lot of these removed in the project DSM.

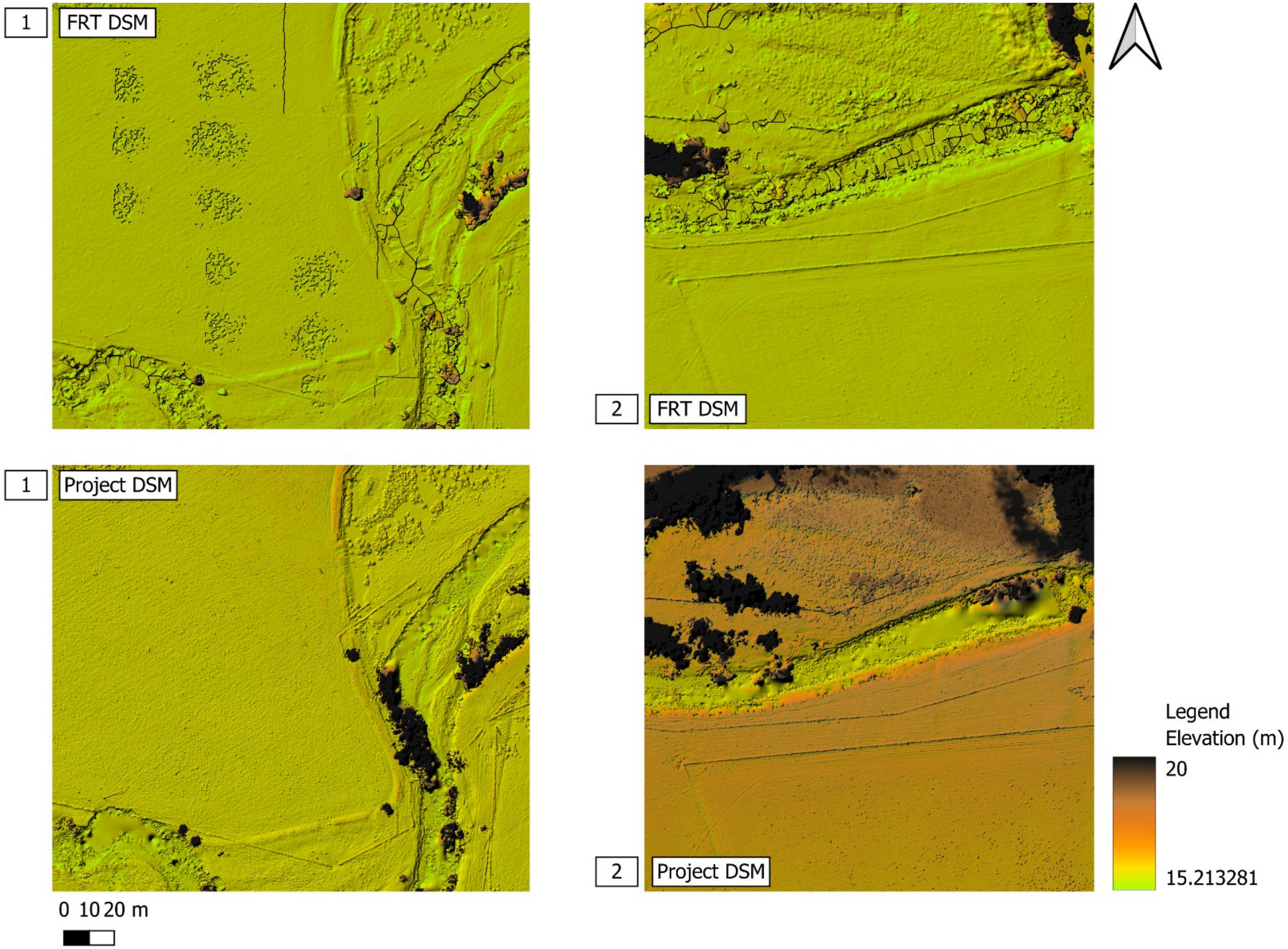

Figure 12 - Differences in quality between FRT and project DSMs

5.3 – DEM editing in QGIS using Serval plug-in

5.3.1 – Methods

Before the flood simulation a thorough examination of DTM's was conducted. Artefacts and anomalies in the data were identified and fixed with the bridge deck also removed as shown in Figure 14. This was an important step to ensure a higher level of accuracy and realism for the flood simulations as the applications won't identify the bridge as a bridge. Instead, it will use terrain and elevation data and identify the bridge as a wall thus not allowing water to enter through which greatly alter the flood model and simulation results.

As Figure 13 shows, for the exact same point there is a difference of over 3.5 metres in elevation for when the bridge existed and subsequently removed. The removal of the bridge and artefacts fixes will allow water to flow through the channel with greater levels of accuracy.

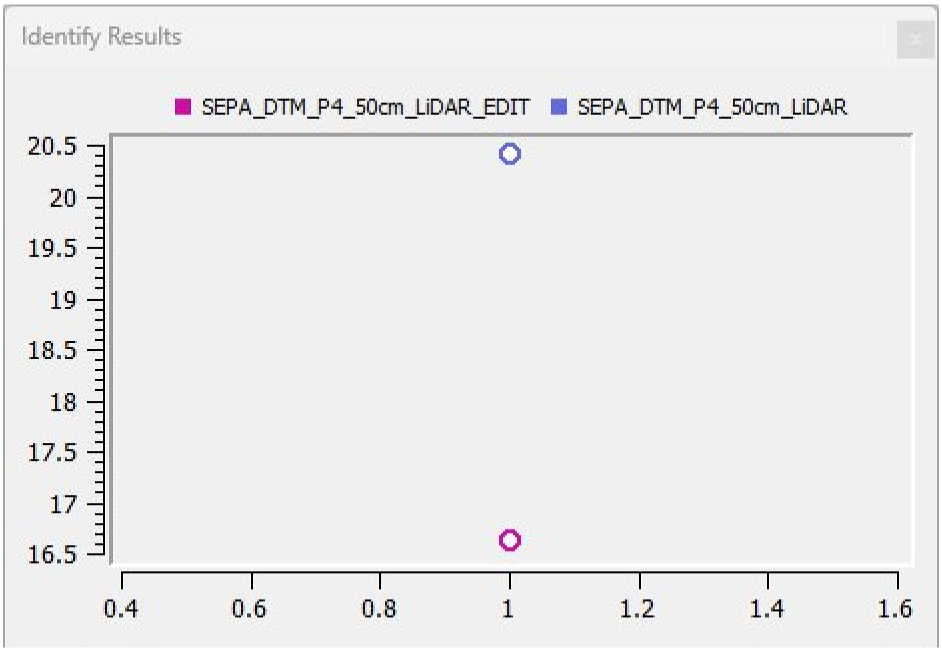

Figure 13 - Blue dot showing elevation of bridge area before removal, purple dot showing elevation data after bridge removal

The DEM amendments outlined in this section was done using QGIS v3.34.12 and installing Serval v3.32.0 plug-in. Serval plugin is a raster editing tool that allows the editing of raster imagery (Pasiok *et al.,* 2023). A full step-by-step method with screenshots relating directly to this project can be found in Appendix 5.

5.3.2 – Results

Figure 14 shows an example section of the LiDAR derived DTM before the bridge removal and missing data fix and after the bridge removal and data fix.

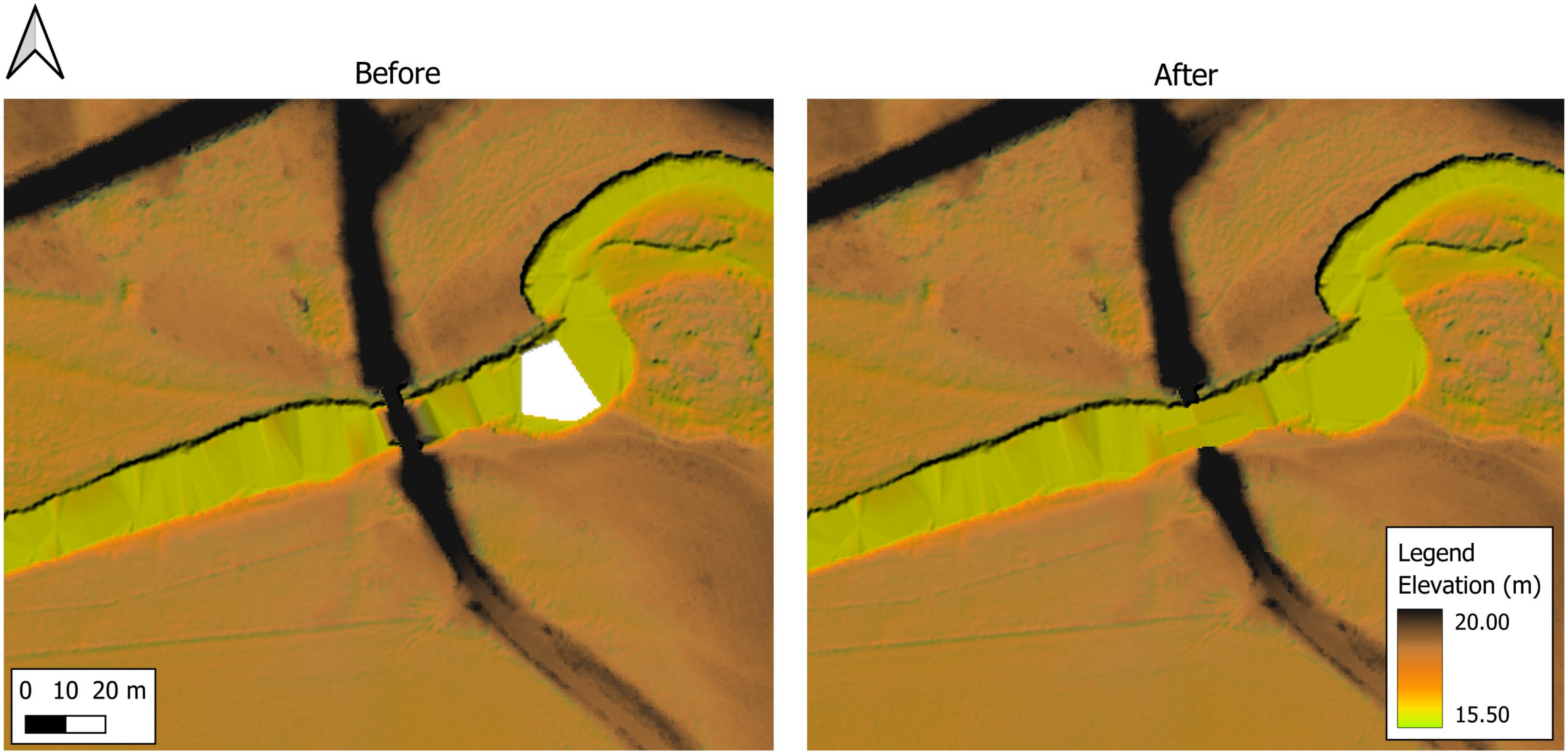
Before
After
0 10 20 m
Legend
Elevation (m)
20.00
15.50

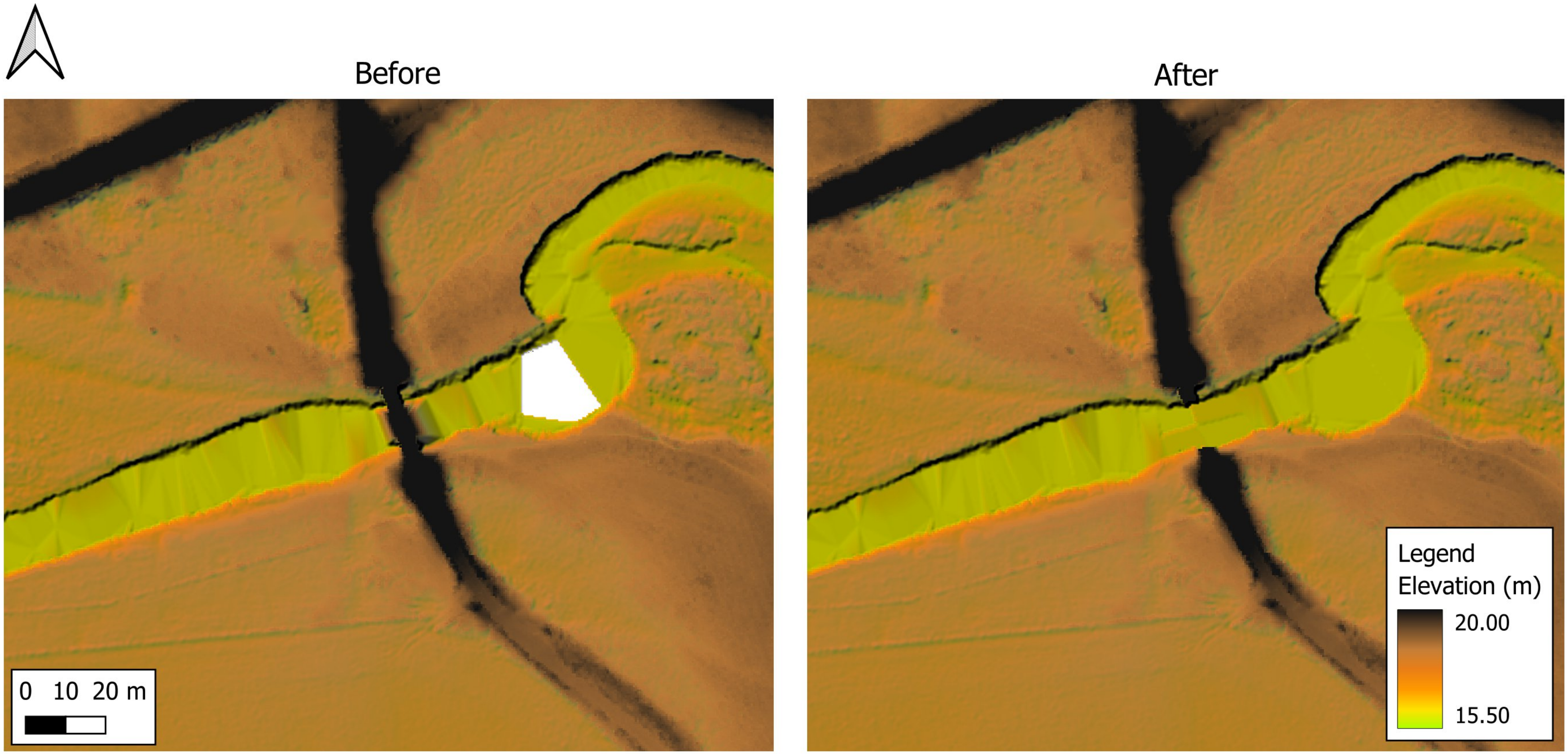

Figure 14 - Example section of the LiDAR derived DTM showing before and after of raster editing

5.4 – Finalised Workflow

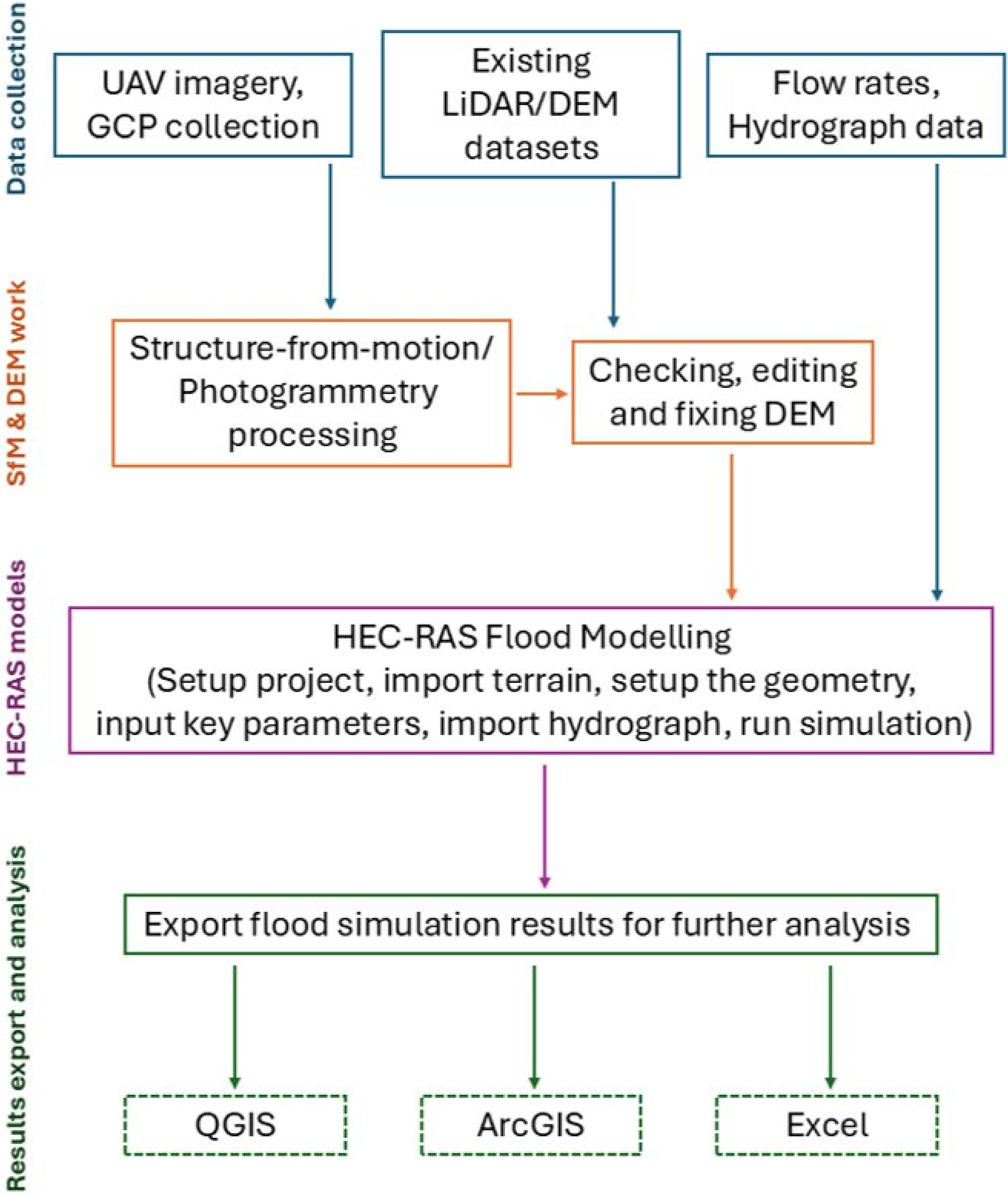

Figure – Workflow outlining main steps completed in this study

6 - HEC-RAS 2D model (unsteady flow) - Testing

6.1 – Methods

All 2D HEC-RAS models with unsteady flow were completed on HEC-RAS v6.6 and following an official “Creating a Simple 2D Model with HEC-RAS” (Ackerman, 2021) workshop. The LiDAR DTM (Scotland-DTM-50cm-Phase 4) was downloaded from Digimap with the Photogrammetry DTM derived from section 5.2 of this report. Full hydrograph data can be seen in Appendix 1.

With no unsteady hydrograph data, this was created manually within HEC-RAS increasing or reducing flow rates after every test model until the peak flow downstream was close to the values provided in the Dynamic Rivers report and was done for all 3 flood events (100, 20 and 2 year). Manning’s ‘N’ values used for this project were taken from the Dynamic Rivers report (Williamson, 2024).

Model Register can be seen in Appendix 2 and step-by-step instructions, screenshots and input parameters directly related to this part of the project can be seen in Appendix 6.

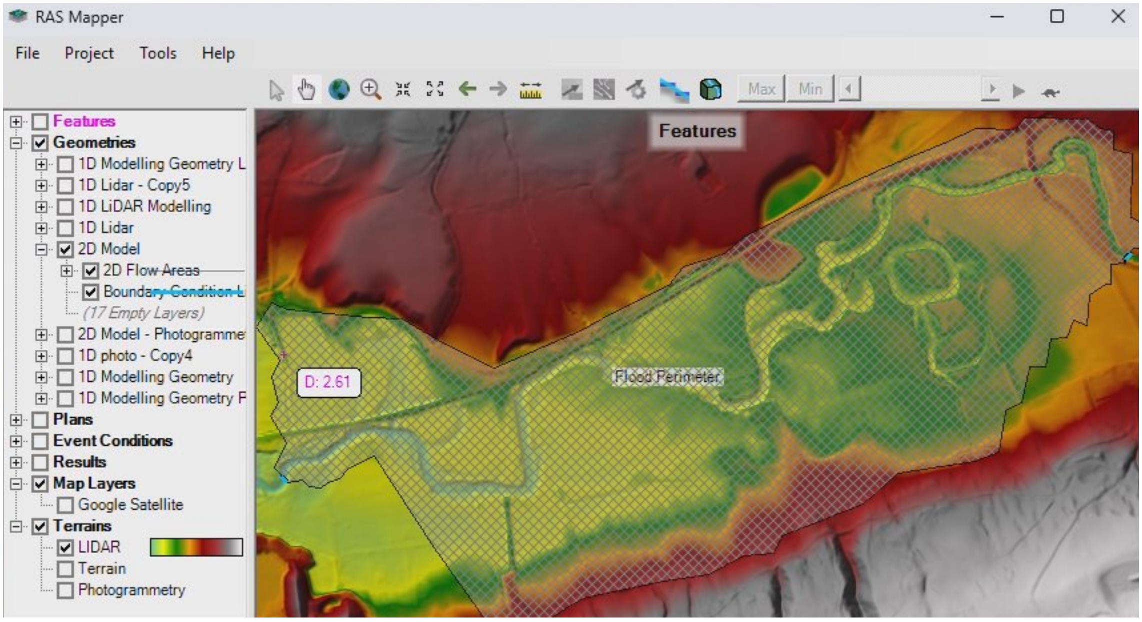

Figure 15 - 2D geometry and LiDAR terrain within RAS Mapper in HEC-RAS

6.2 – Dynamic Rivers report replication – Results

The first HEC-RAS model ran was an attempt to replicate some of the flood modelling from the Dynamics Rivers report on the same stretch on the River Devon using main input parameters listed in Table 3.

Table 3 - Main inputs used within for 2D unsteady model

DEM (Model no.)	Cell size (m)	Number of cells	'N' Value	Flow (flood)	Run-time (mins)
LiDAR (L0015)	1 x 1	770,856	0.06	Unsteady (100 year)	~123
LiDAR (L0017)	1 x 1	770,856	0.06	Unsteady (20 year)	~92
LiDAR (L0018)	1 x 1	770,856	0.06	Unsteady (2 year)	~73

For all 3 flood events, Figure 16 shows the results of the model of water surface elevation (WSE), which is the height of the water surface above a specified referenced datum with Figure 17 showing the actual depth of flood and channel water. Both WSE and depth are vital for mapping and analysing flood plains as well as understanding hydraulic behaviours and potential flood risks (FEMA, 2019).

Figure 18 has been included into just this section only and shows the shear stress of the 3 flood models ran. Shear stress in the context of HEC-RAS is the force of water and sediment exerted upon the stream channel bed and/or walls and is vital for predicting bank and bed erosion (Johnson *et al*., 2017).

The final figure in this section is peak flow rates measured downstream which can be seen on Figure 19 for 100-year, 20-year and 2-year flood events. Downstream flow rates peaked at 141.81 m^3/s, 86.04 m^3/s and 50.16 m^3/s respectively compared to around 149 m^3/s, 80 m^3/s and 47 m^3/s from the Dynamic Rivers report (Williamson, 2024).

The time to run each model was longer than anticipated with the 100-year flood simulation taking over 2 hours to complete, therefore further tests on cell sizes was conducted.

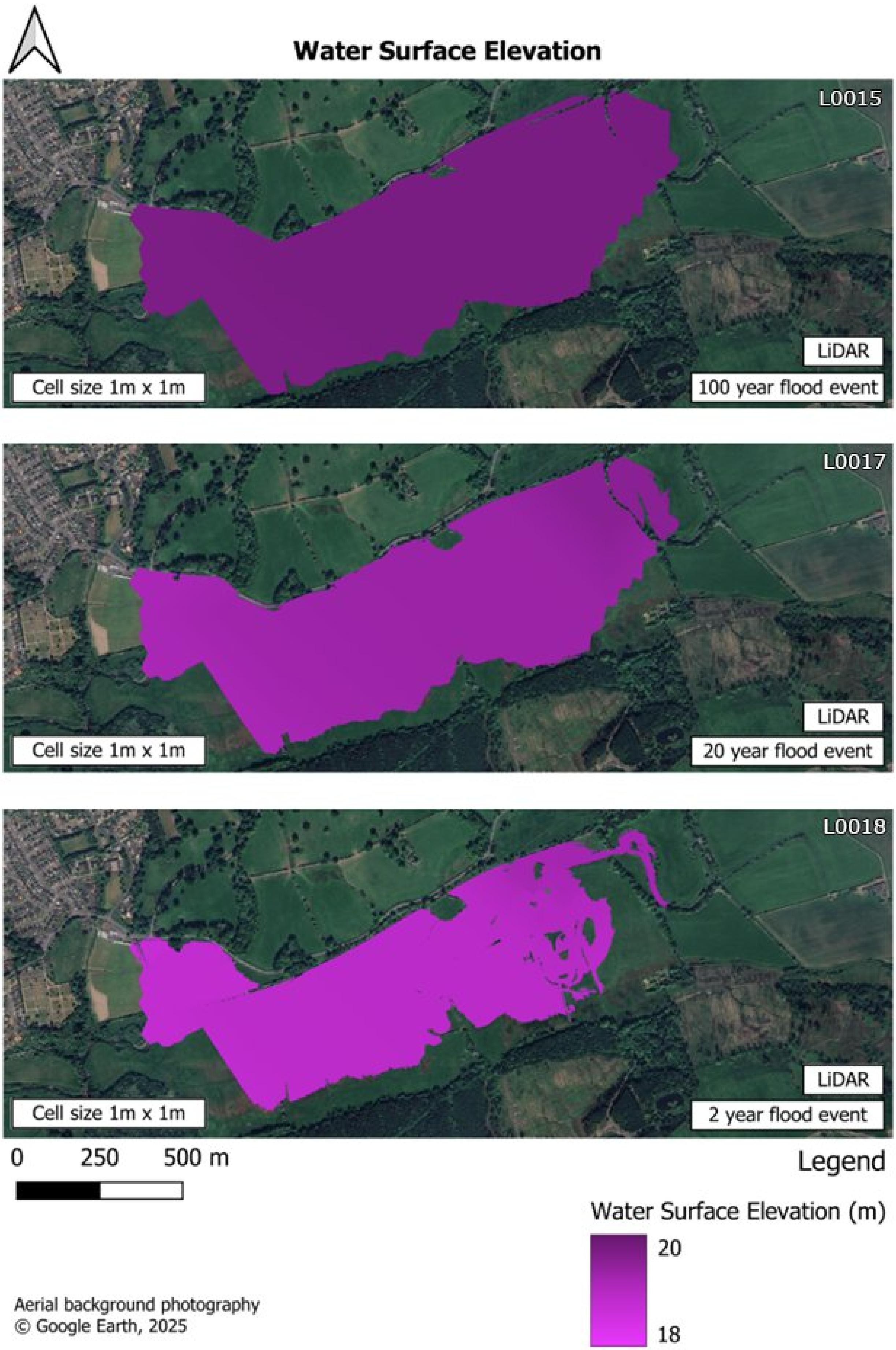

Figure 16 - WSE for 100, 20 and 2 year flood events (LiDAR data, 1x1m cell)

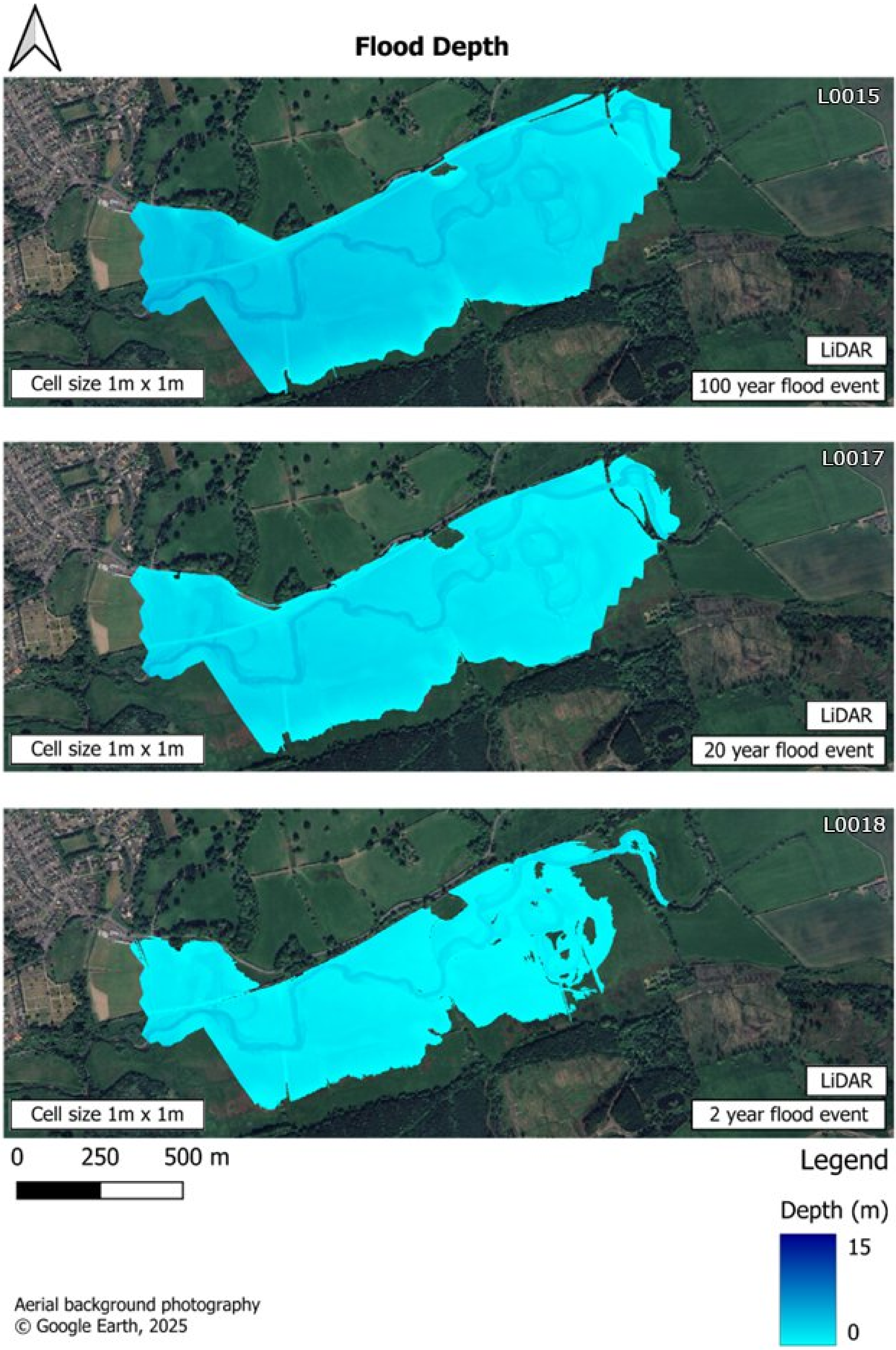

Figure 17 - Depth for 100, 20 and 2 year flood events ran using LiDAR data (LiDAR data, 1x1m cell)

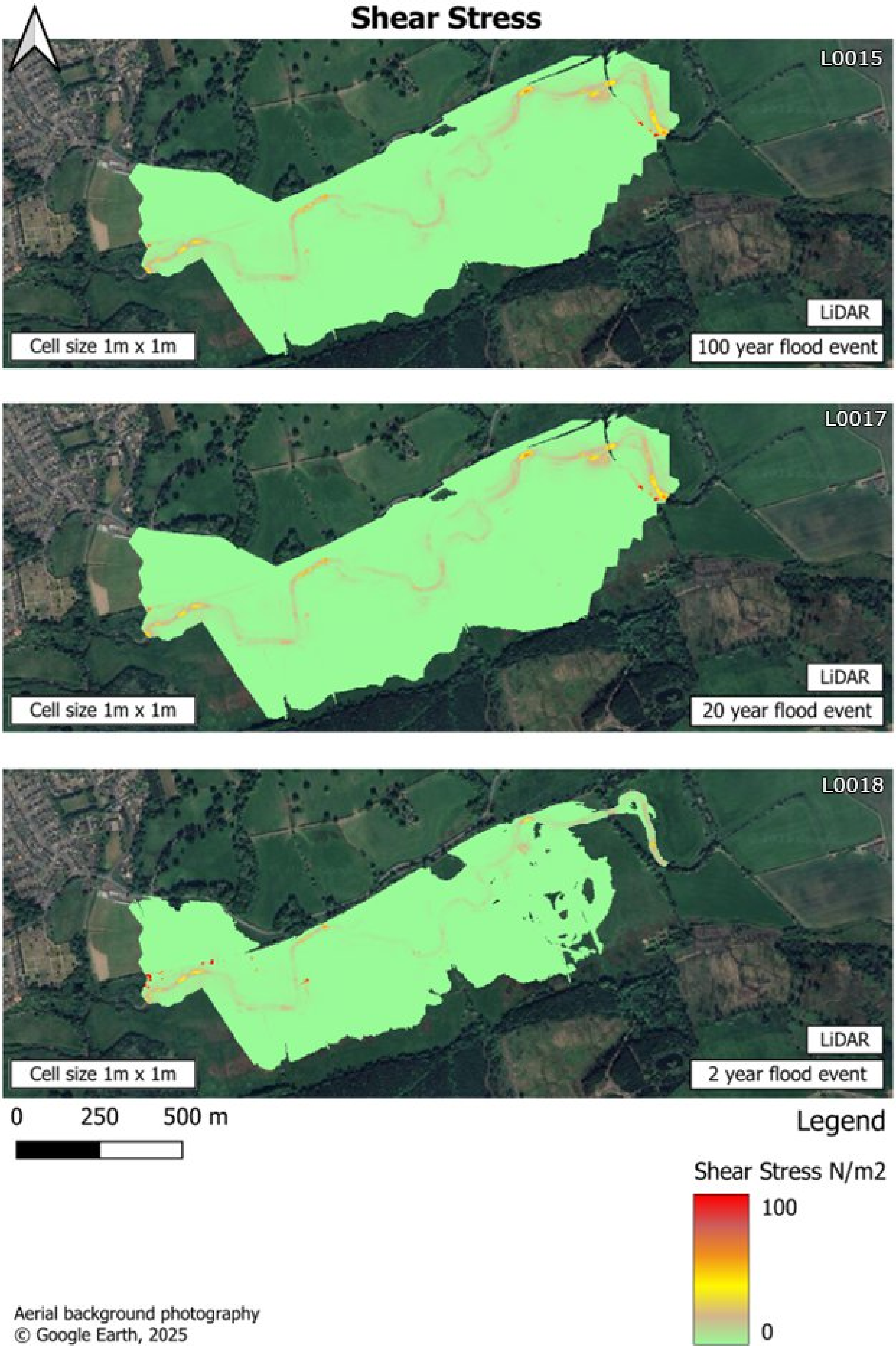

Figure 18 - Shear stress for 100, 20 and 2 year flood events using LiDAR (LiDAR data, 1x1m cell)

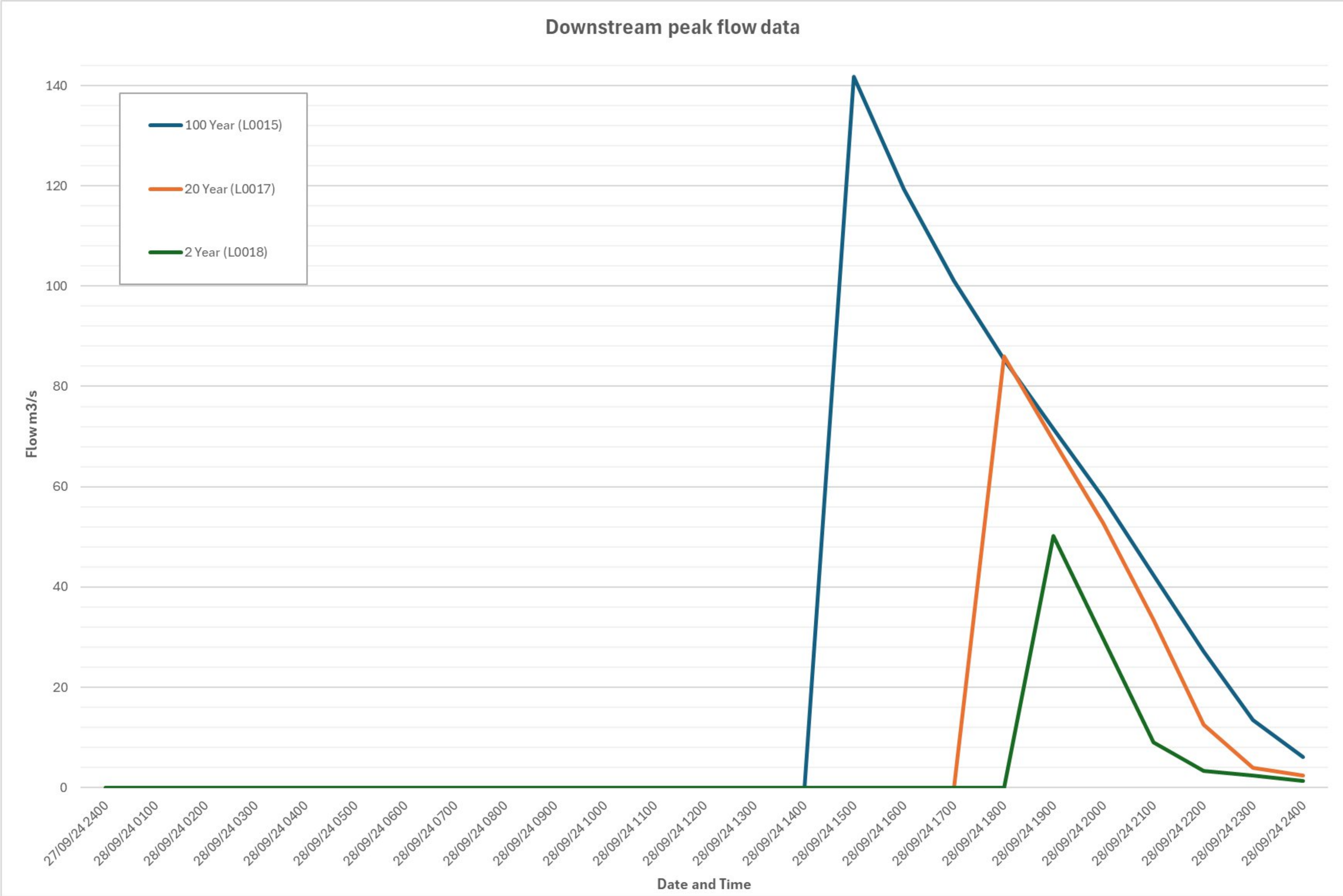

Figure 19 - Line graph showing peak flow for all flood scenarios, measured downstream

6.3 – Mesh cell size and 'N' value comparison - Tests and Results

Due to the length of the flood simulation run-times for modelling conducted in section 6.1, further experimentation of mesh cell size for the flood perimeter, manning N value and computation interval was done. The computation interval for all models was increased from 30 seconds to 1 minute (*except for L0015 from section 6.1 which remained at 30 seconds) with all other main inputs listed in Table 4.

Table 4 - Inputs for cell size testing and comparison (2D unsteady flow)

DEM (Model no.)	Cell size (m)	Number of cells	'N' Value	Flow (flood)	Run-time (mins)
LiDAR (L0001)	10 x 10	7611	0.06	Unsteady (100 year)	~0.5
LiDAR (L0002)	5 x 5	30,652	0.06	Unsteady (100 year)	~1.75
LiDAR (L0003)	3 x 3	85,410	0.06	Unsteady (100 year)	~6.5
LiDAR (L0004)	2 x 2	192,437	0.06	Unsteady (100 year)	~15
LiDAR (L0015)*	1 x 1	770,856	0.06	Unsteady (100 year)	~123
LiDAR (L0006)	2 x 2	192,437	0.045	Unsteady (100 year)	~15
LiDAR (L0007)	2 x 2	192,437	0.05	Unsteady (100 year)	~13
LiDAR (L0008)	2 x 2	192,437	0.08	Unsteady (100 year)	~12.5

Figure 20 visually demonstrates how different cell sizes in flood models can drastically change results by showing a clear difference in flood extent and depth. This can be seen again in Figure 21 which shows these differences in water surface elevation results.

The line graph (Figure 22) confirms this again, showing how the different cell sizes in a 2D model can alter the shape of the flood hydrograph with a 10x10m cell size flow peaking downstream at just 36 m^3/s compared to 142 m^3/s for a 2x2m mesh cell.

While 3x3m, 5x5m and 10x10m simulations ran around 2-30 times quicker than the 2x2m model, the differences in outputs compared to the section 6.1 model were too vast to consider them viable. One interesting point to note is that there just around 5% difference in peak flow shown in Figure 22 between 1x1m and 2x2m cell size, despite the latter being around 8 times quicker to complete.

An additional line graph (Figure 23) has also been included showing how different Manning's 'N' roughness values can alter the flood shape. Recorded downstream, while the time of the peak flow remains consistent for all values, applying an 'N' value of 0.008 to the model shows the peak flow to be just 114.13 m^3/s compared to 150.47 m^3/s for the correct N value of 0.006. Similarly, applying lower N values of 0.045 and 0.05 to the model increases peak flow to 198.98 m^3/s and 180.18 m^3/s.

Figure 20 showing large differences in extent of flood and depth of water between different cell sizes.

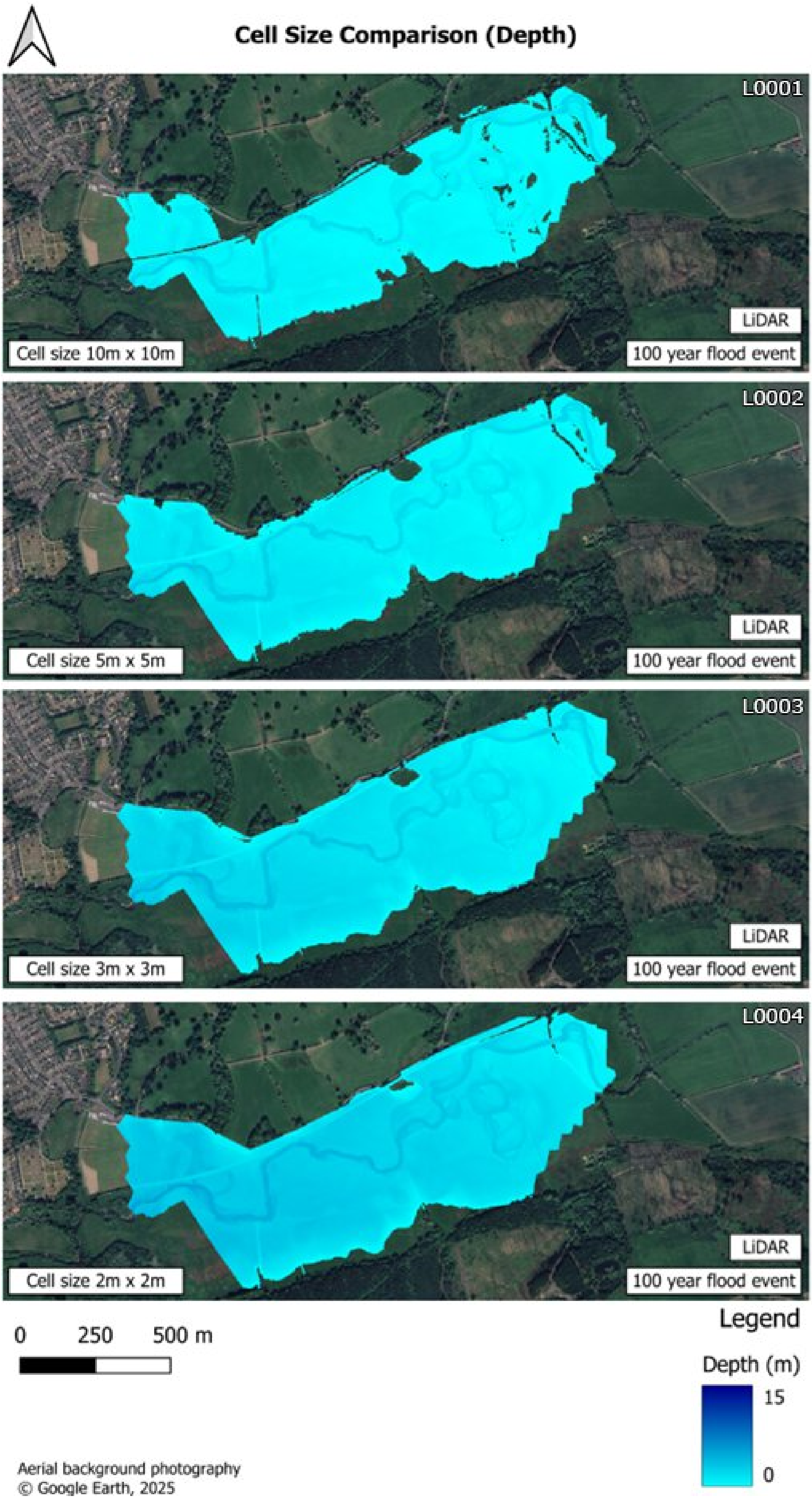

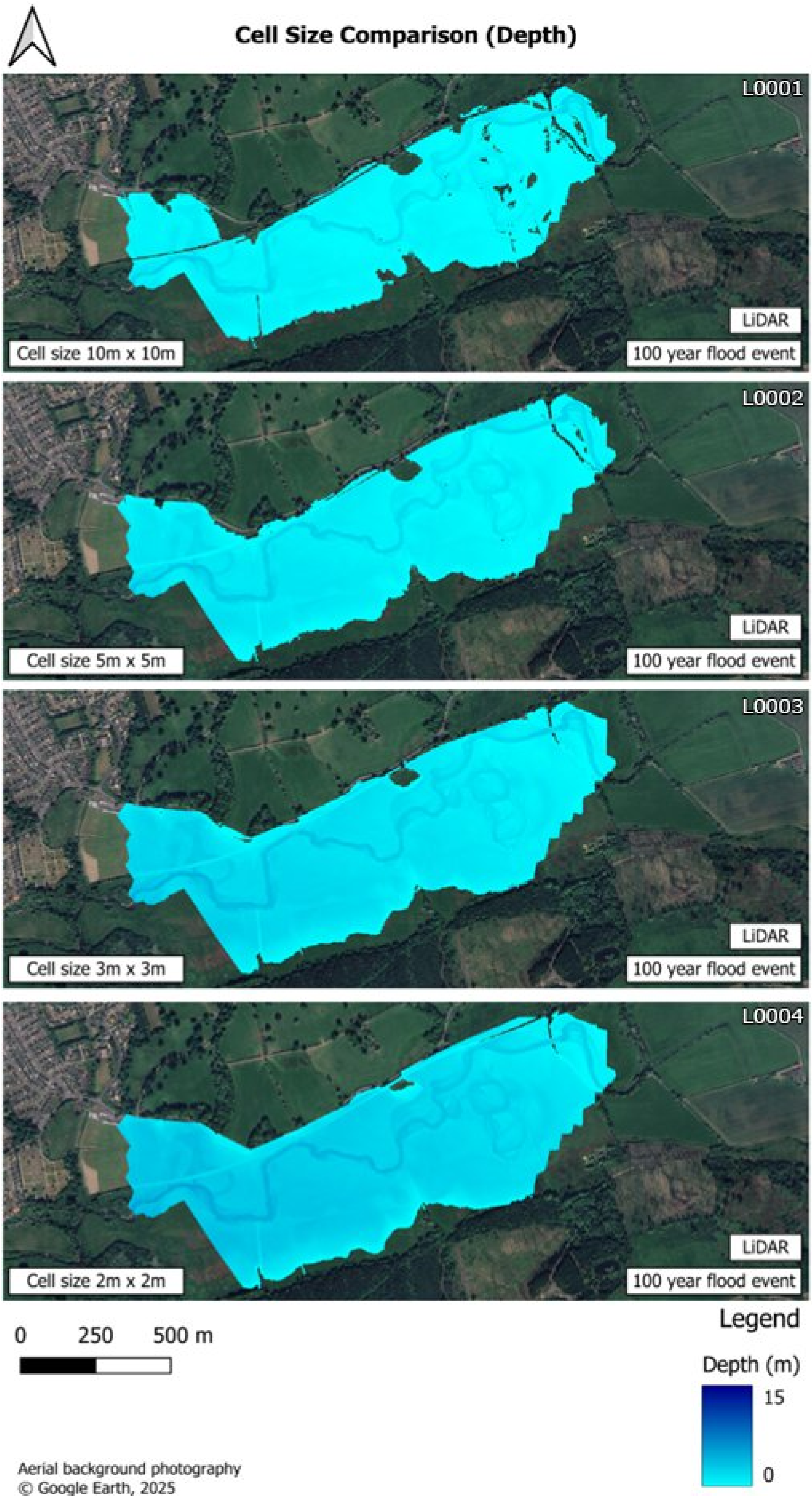

Figure 20 - 2D mesh different cell size comparison showing flood depth using 100-year flood hydrograph

Continuation of showing large differences between water surface elevation. L0001 (10x10m) at the top left of flooded area has an WSE of 15.60m compared to 20m for L0004 (2x2m) for the same area.

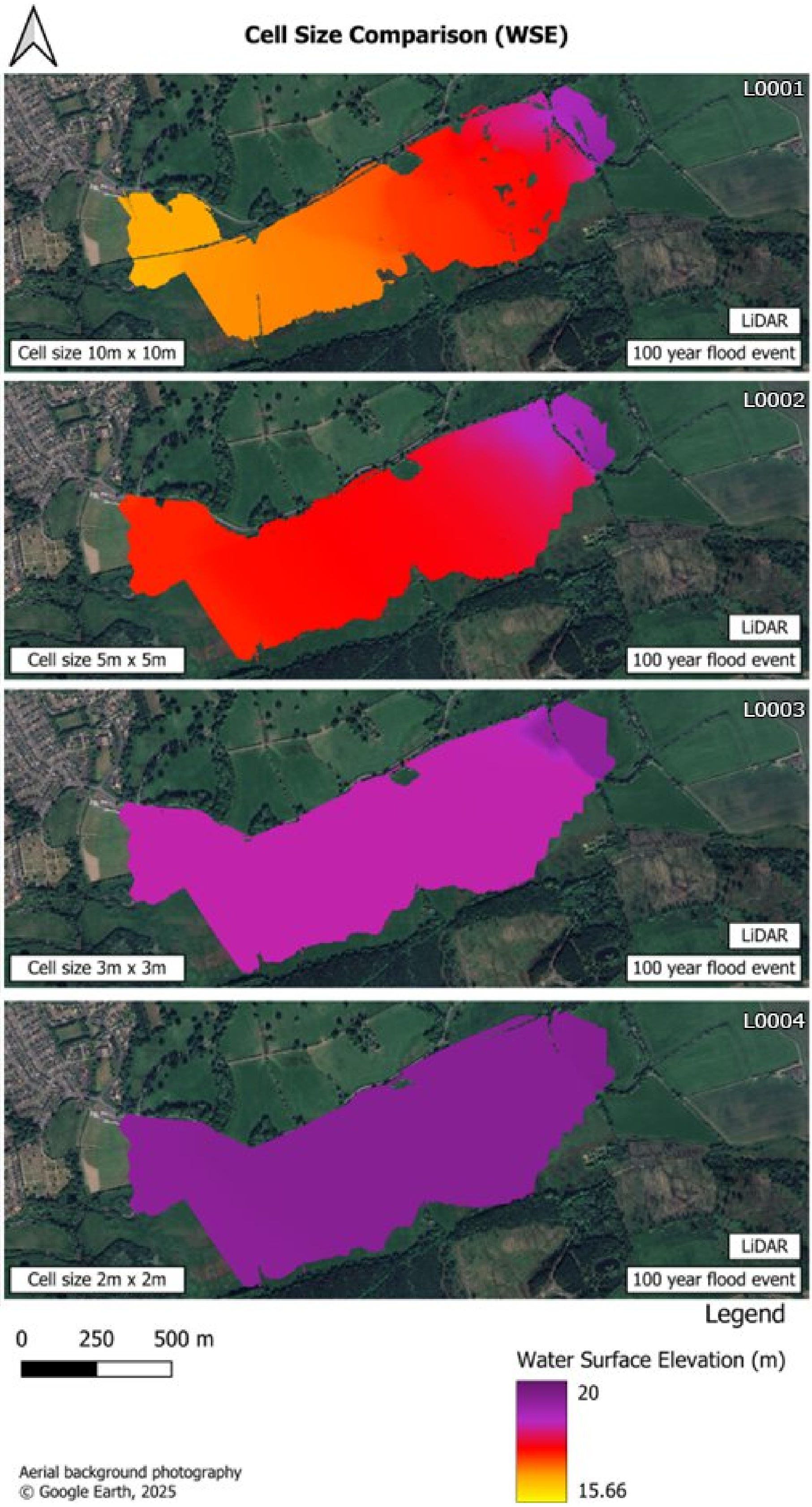

Figure 21 - 2D mesh different cell size comparison showing flood WSE using 100-year flood hydrograph

Line graph demonstrating how different cell sizes can alter the shape of a flood, despite all models and simulations ran in this section using the same hydrograph flow data and DEM.

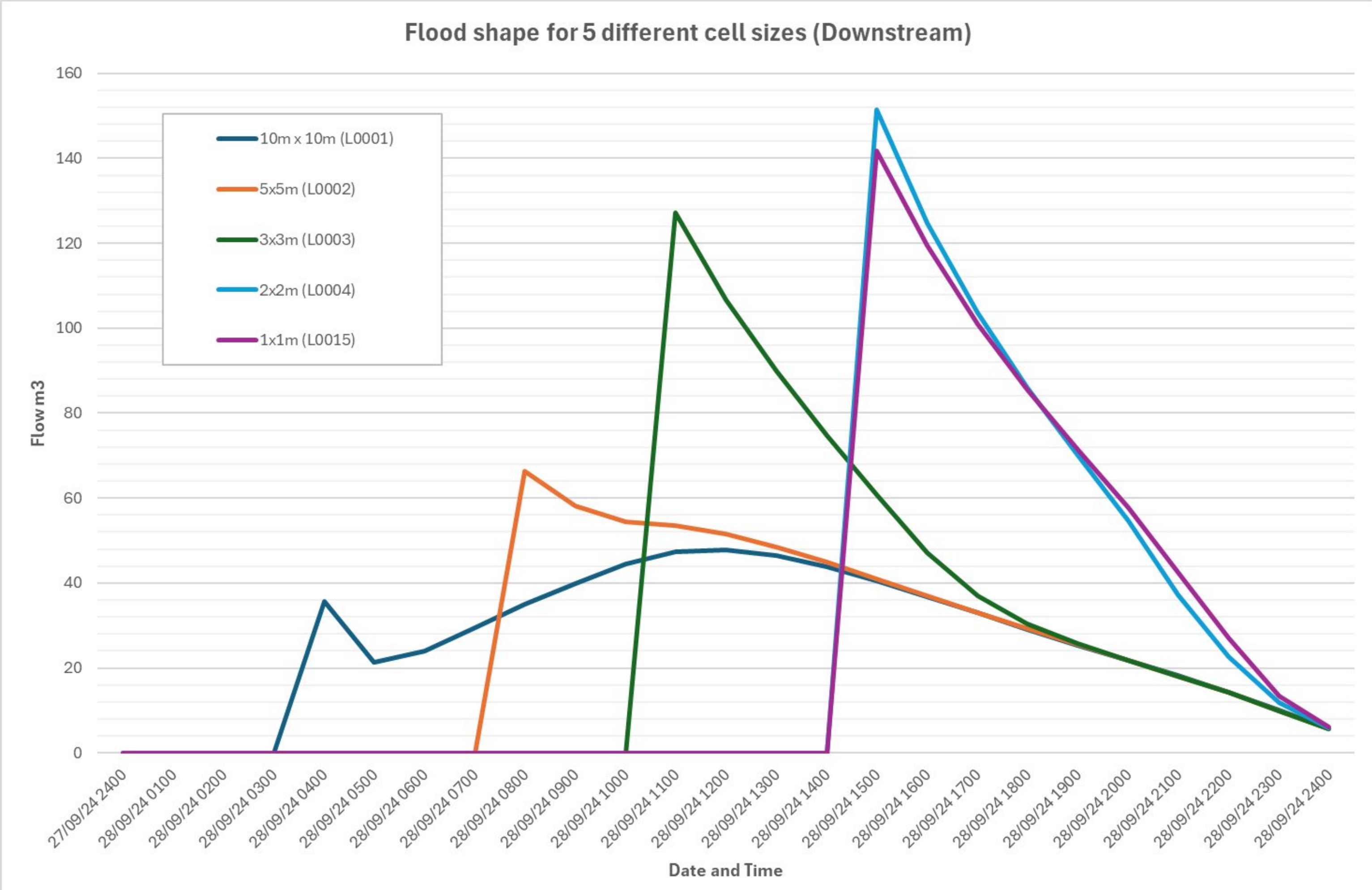

Figure 22 – Downstream measurements showing how different mesh cell sizes can greatly alter results

Line graph showing the importance of assigning the correct Manning's 'N' values to models with a 40% difference in downstream peak flow between the lowest (0.045) and highest (0.08) N values applied.

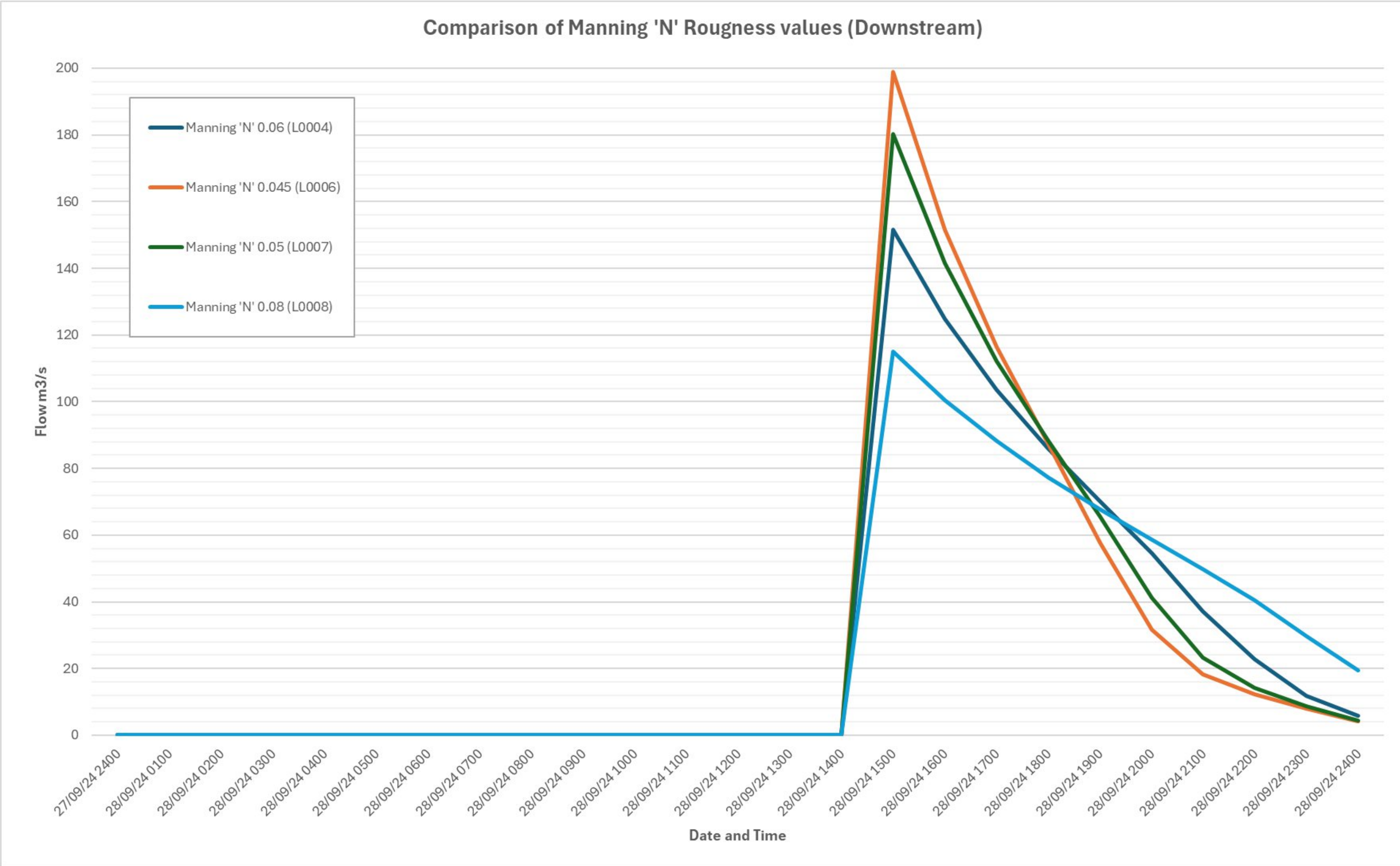

Figure 23 – Downstream measurements demonstrating how altering manning N value can greatly affect results

7 – Simple 2D model (unsteady flow)

LiDAR v Photogrammetry

The methods for this section have been outlined in Section 6.1 with full step-by-step instructions in Appendix 6.

7.1 - 100 year flood – Results

The main inputs used for the 100-year model and simulation can be seen in Table 5.

Table 5 – Main inputs for 2D model with 100-year flood unsteady flow

100 year flood					
DEM (Model no.)	**Cell size (m)**	**Number of cells**	**'N' Value**	**Flow (flood)**	**Run-time (mins)**
LiDAR (L0014)	2 x 2	192,437	0.06	Unsteady (100 year)	~15
Photogrammetry (P0001)	2 x 2	192,437	0.06	Unsteady (100 year)	~17

The first model ran was a 100-year flood extent on the DTM's derived from both LiDAR and Photogrammetry. Figure 24 shows the water surface elevation with Figure 25 showing flooding depth for a 100-year flood. Table 6 contains numerical results and percentage differences between the two terrains' used and that the differences are quite small for all metrics except maximum flood depth that has 46% difference.

Table 6 - Results of 2D (unsteady flow) 100 year flood

100 Year Flood						
DTM	**Downstream Max Flow (m^3/s)**	**Downstream Volume 1000 (m^3)**	**Total Area Flooded (m^2)**	**Volume (WSE) (m^3)**	**Minimum Depth (m)**	**Maximum Depth (m)**
LiDAR (L0014)	151.52	2394.45	716,299.75	13,905,945.90	0.001	5.615
Photogrammetry (P0001)	161.51	2437.42	693,989.00	13,128,424.87	0.001	9.022
Difference between Photogrammetry and LiDAR models						
	6.38%	1.77%	3.16%	5.59%	0%	46.5%

Figure 34 shows while the spread of the flood is very similar, there is around a 2m difference in WSE.

Figure 24 - 2D (unsteady) model comparing WSE results for 100-year flood

Figure 25 shows similarly, fairly even flood area but with the Photogrammetry model showing greater depth of flood water, particularly in the bottom left.

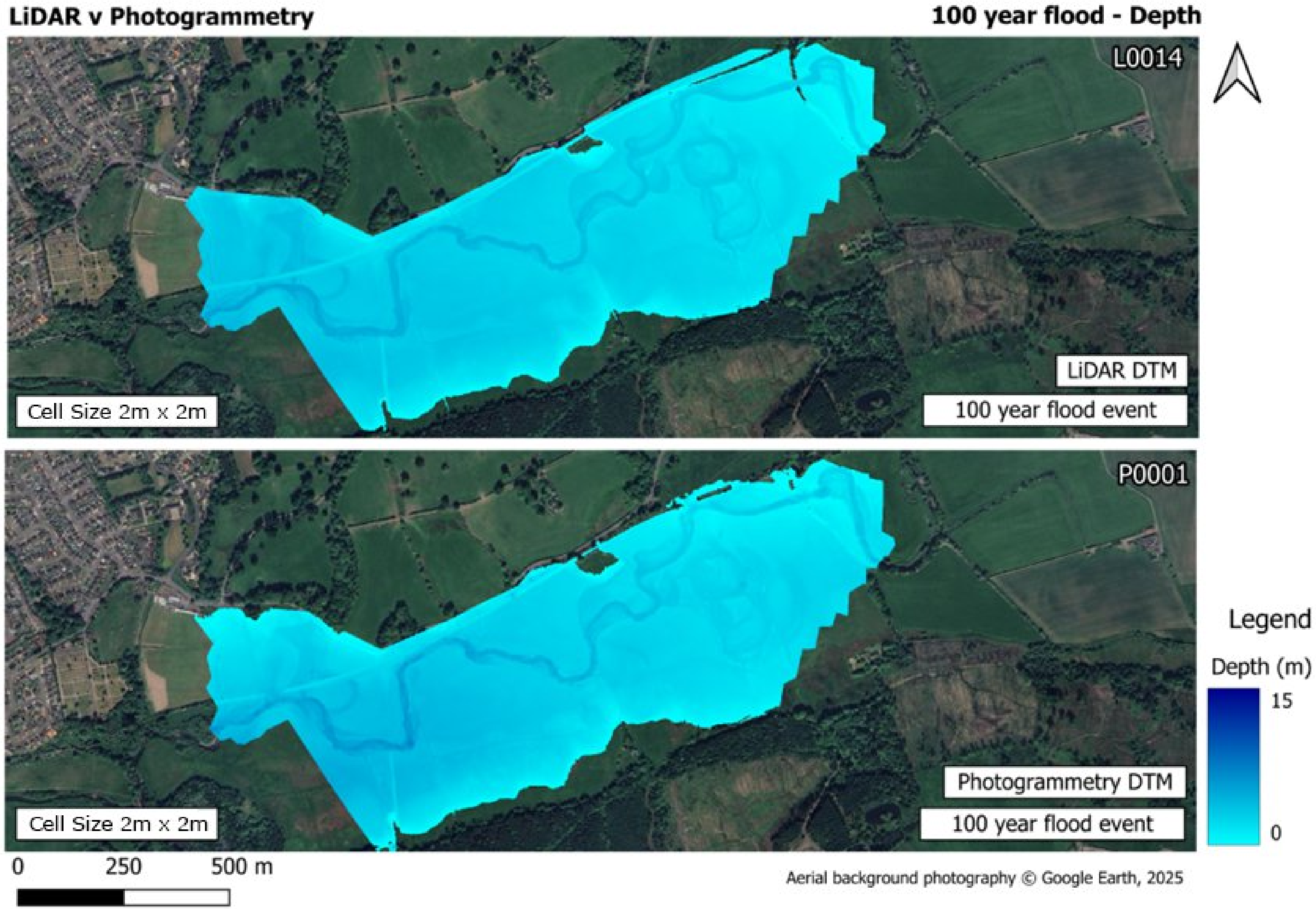

Figure 25 - 2D (unsteady) model comparing depth results for 100-year flood

7.2 - 20 year flood – Results

The main input parameters used for the 20-year model and simulation can be seen in Table 7.

Table 7 - Main inputs for 2D model with 20-year flood unsteady flow

20 year flood					
DEM (Model no.)	**Cell size (m)**	**Number of cells**	**'N' Value**	**Flow (flood)**	**Run-time (mins)**
LiDAR (L0014)	2 x 2	192,437	0.06	Unsteady (20 year)	~15
Photogrammetry (P0001)	2 x 2	192,437	0.06	Unsteady (20 year)	~17

The second batch of models ran in this section was still using the same LiDAR and Photogrammetry derived DTMs but using the 20-year flood extent hydrograph. WSE (Figure 26) and Depth (Figure 27) maps are included as well as well as the numerical results in Table 8 showing the difference between the LiDAR and Photogrammetry models, and shows that despite maximum downstream flow and volume decreasing for the Photogrammetry model, maximum depth continues to increase.

Table 8 - Results of 2D (unsteady flow) 20 year flood

20 Year Flood						
DTM	**Downstream Max Flow (m^3/s)**	**Downstream Volume 1000 (m^3)**	**Total Area Flooded (m^2)**	**Volume (WSE) (m^3)**	**Minimum Depth (m)**	**Maximum Depth (m)**
LiDAR (L0009)	89.08	913.91	669,708.50	12,299,491.75	0.001	4.266
Photogrammetry (P0002)	70.33	687.90	608,354.75	10,707,091.69	0.001	12.657
Difference between Photogrammetry and LiDAR models						
	23.52%	28.21%	9.60%	13.84%	0%	99.16

20 Year Flood						
DTM	**Downstream Max Flow (m^3/s)**	**Downstream Volume 1000 (m^3)**	**Total Area Flooded (m^2)**	**Volume (WSE) (m^3)**	**Minimum Depth (m)**	**Maximum Depth (m)**
LiDAR (L0009)	89.08	913.91	669,708.50	12,299,491.75	0.001	4.266
Photogrammetry (P0002)	70.33	687.90	608,354.75	10,707,091.69	0.001	12.657
Difference between Photogrammetry and LiDAR models						
	23.52%	28.21%	9.60%	13.84%	0%	99.16

Figure 32 shows there is greater differences in water surface elevation. LiDAR terrain WSE is greater and fluctuates over the floodplains while the photogrammetry DTM is lower and consistent across the entire flooded area.

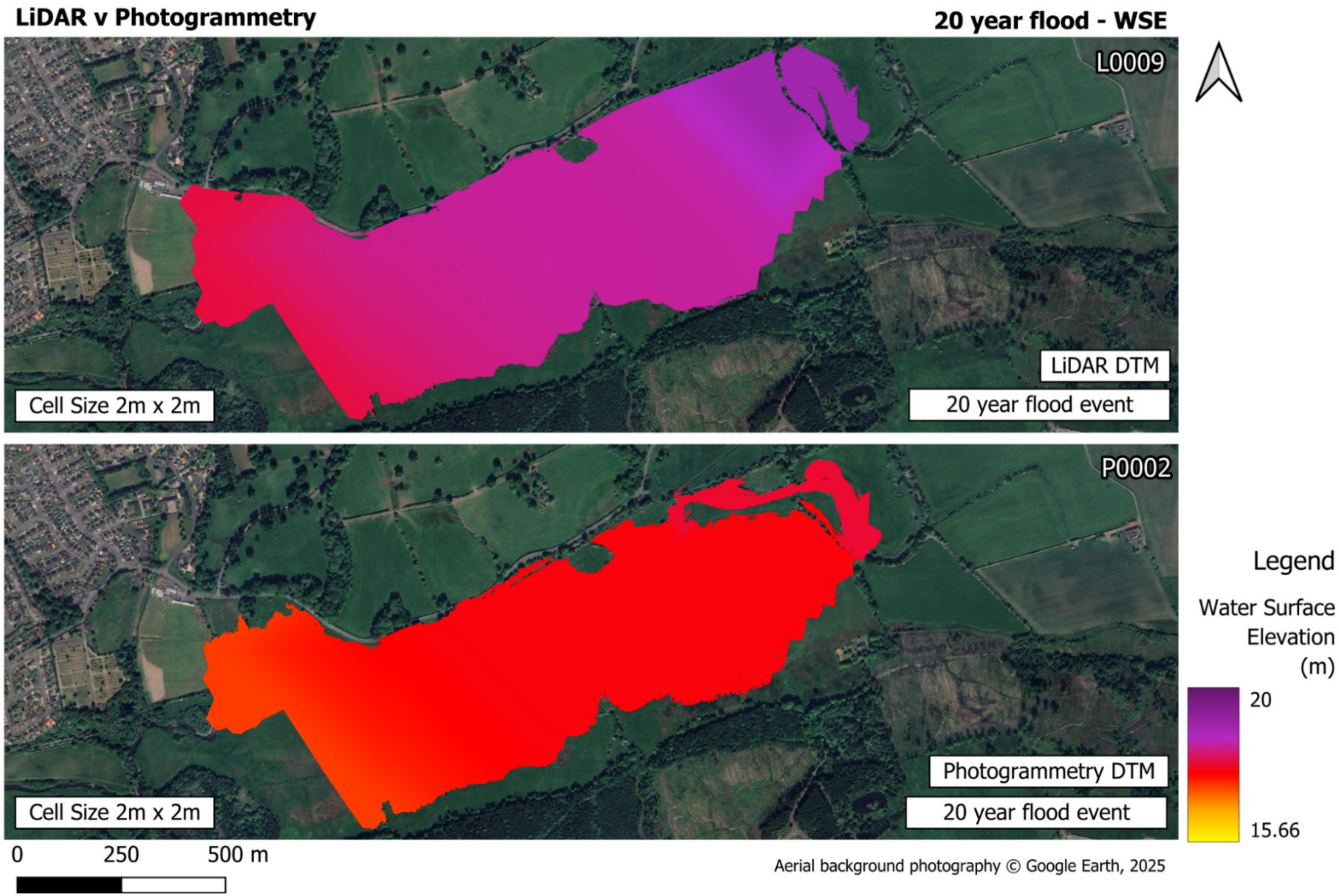

Figure 26 - 2D (unsteady) comparing WSE results for 20-year flood

While it's harder to see differences in flood depth, Figure 27 shows some subtle differences in flood depth.

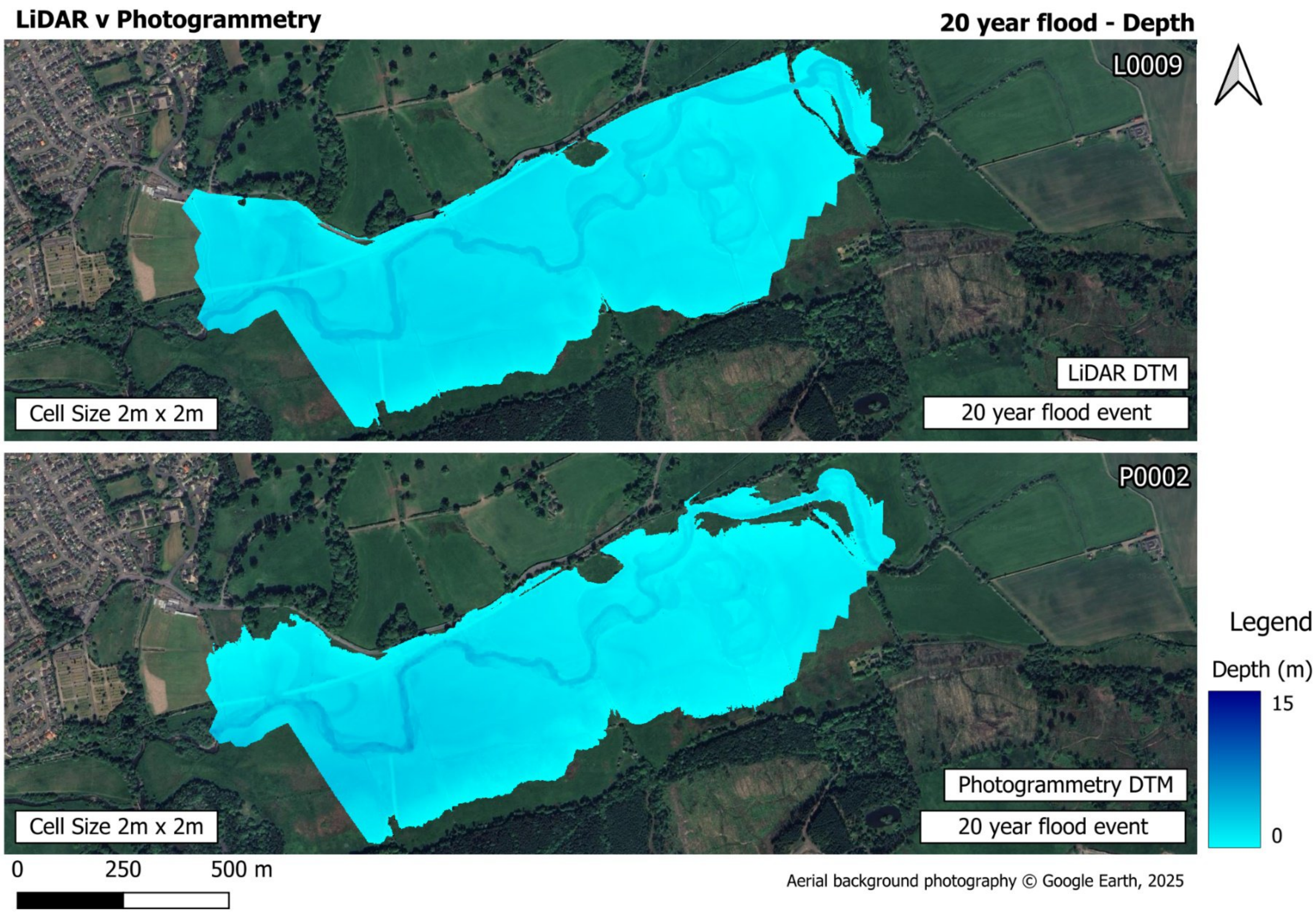

Figure 27 - 2D (unsteady) model comparing depth results for 20-year flood

7.3 - 2 year flood – Results

The main input used for the 2-year model and simulation can be seen in Table 9.

Table 9 - Main inputs for 2D model with 2-year flood unsteady flow

2 year flood					
DEM (Model no.)	**Cell size (m)**	**Number of cells**	**'N' Value**	**Flow (flood)**	**Run-time (mins)**
LiDAR (L0010)	2 x 2	192,437	0.06	Unsteady (2 year)	~9.75
Photogrammetry (P0003)	2 x 2	192,437	0.06	Unsteady (2 year)	~10.5

The third and last set of models ran in this section was using a 2-year flood event. Figures 28 and 29 shows the WSE and depth of the floods and shows some clear differences in the spread of the flooded area, WSE and depth.

Numerical outputs from this model can be seen in Table 10 which continues to show that there are differences in all metrics between the models, and continues to show that despite having less volume and flooded area, the Photogrammetry model continues to have far greater depth of flood compared to the LiDAR model which would be unexpected.

Table 10 - Results of 2D (unsteady flow) 2 year flood

2 Year Flood						
DTM	**Downstream Max Flow (m^3/s)**	**Downstream Volume 1000 (m^3)**	**Total Area Flooded (m^2)**	**Volume (WSE) (m^3)**	**Minimum Depth (m)**	**Maximum Depth (m)**
LiDAR (L00010)	51.78	344.68	533,210.00	9,253,811.81	0.0009	3.405
Photogrammetry (P0003)	31.31	229.39	478,786.75	8,013,504.71	0.0009	6.426
Difference between Photogrammetry and LiDAR models						
	49.27%	40.16%	10.75%	14.36%	0%	61.45%

Figure 28 shows differences of flood spread and up to 2m water surface elevation differences

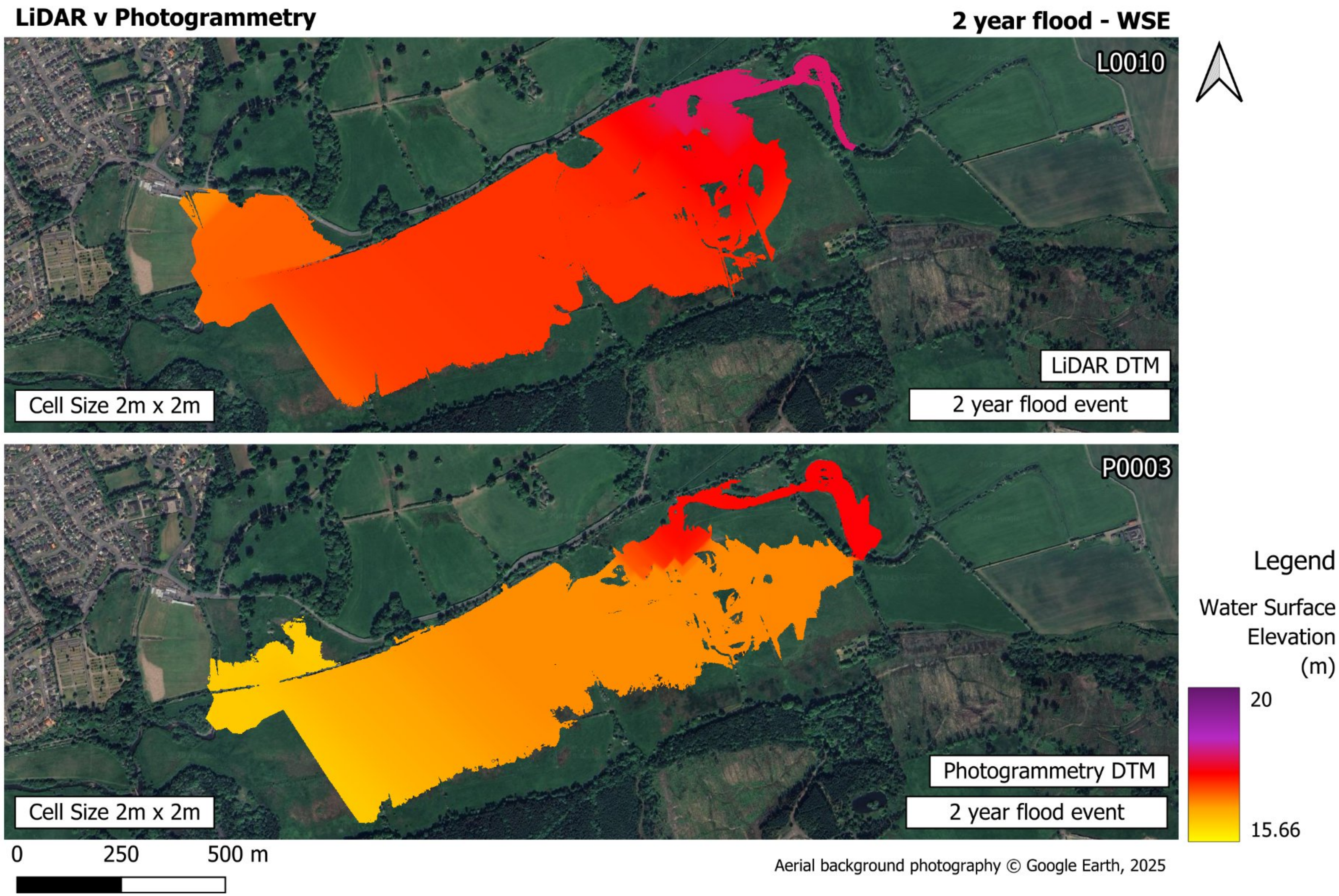

Figure 28 - 2D (unsteady) model comparing WSE results for 2-year flood

Figure 29 shows differences in flood spread and Photogrammetry model having greater depth

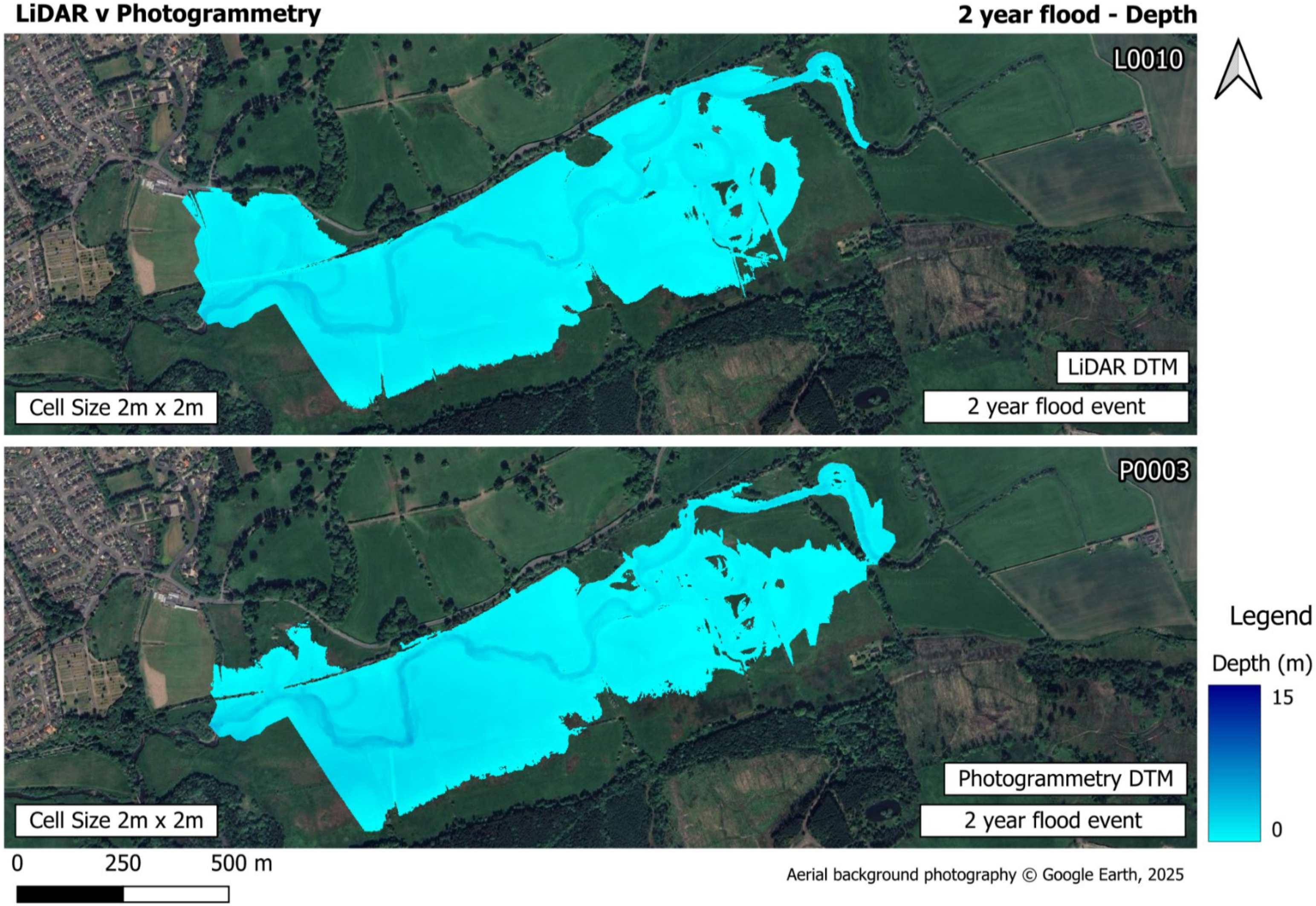

Figure 29 - 2D (unsteady) model comparing depth results for 2-year flood

Figure 30 shows the shape of the floods and peak flow (downstream) for all models conducted in this section.

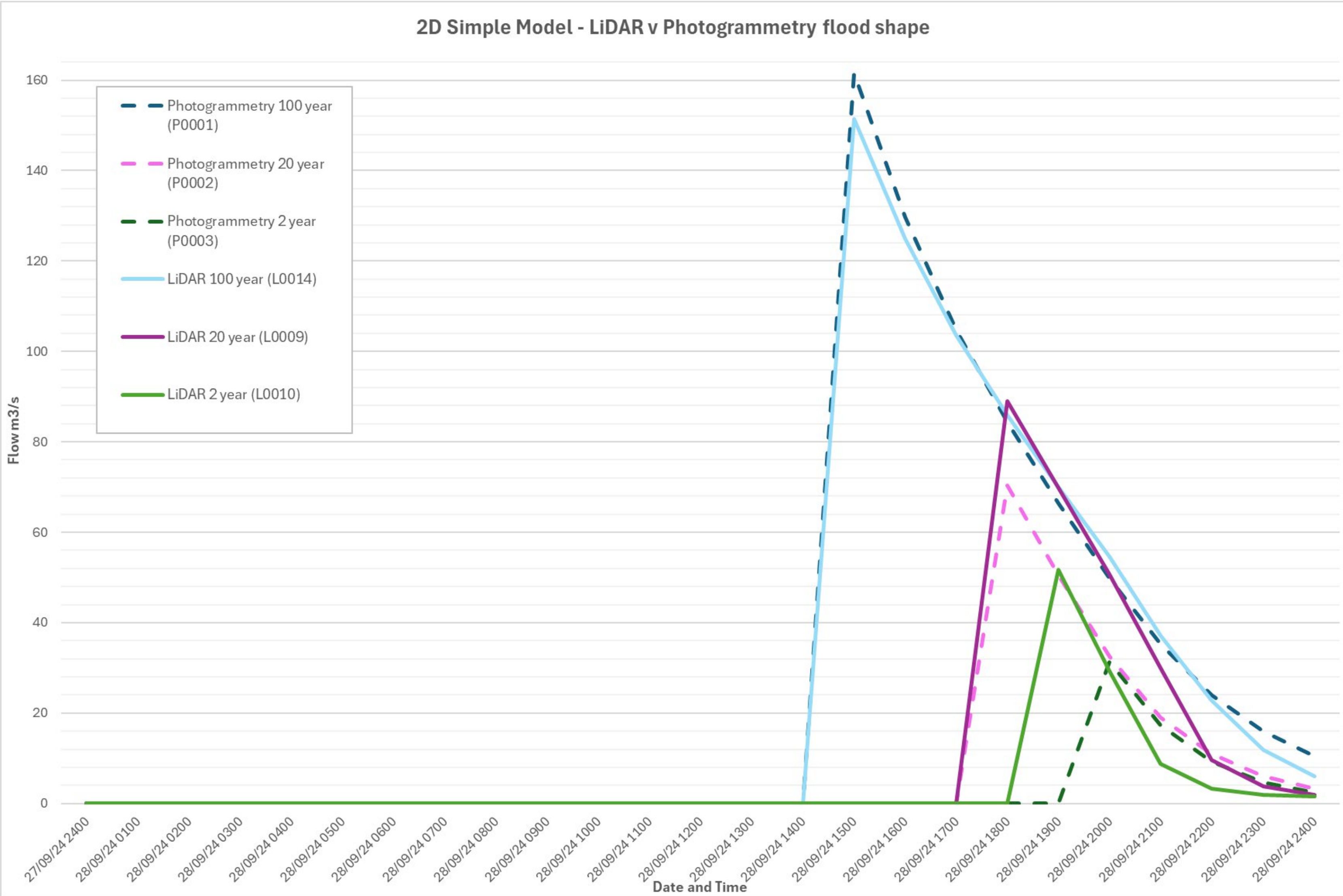

Figure 30 - Downstream flood shape for different DTM's and 3 different flood extent

8 – Simple 1D model (steady flow)

LiDAR v Photogrammetry

8.1 - Methods

All 1D HEC-RAS models shown in this section were completed on HEC-RAS v6.6 combining both official HEC-RAS “1D Steady Flow” tutorial (USACE, n.d a) and a Purdue University exercise “1D HEC-RAS Model Development using RAS-Mapper” (Dey *et al*., 2020). The LiDAR DTM (Scotland-DTM-50cm-Phase 4) was downloaded from Digimap with the Photogrammetry DTM derived from section 5.2 of this report. Steady flow data for flood events and Mannings ‘N’ values were taken from the Dynamic Rivers report (Williamson, 2024).

A model register can be found in Appendix 2. Further step-by-step instructions, screenshots and input parameters directly related to this section can be seen in Appendix 7.

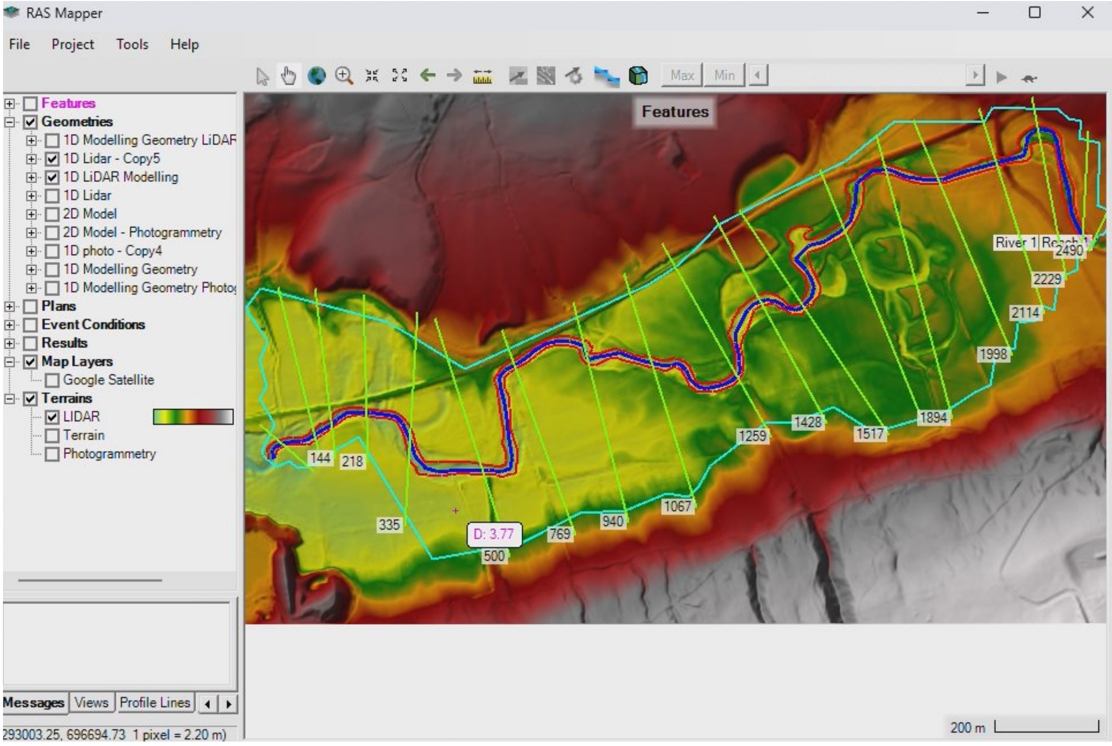

Figure 31 - 1D geometry against the LiDAR terrain within RAS Mapper, HEC-RAS

8.2 - 100 year flood – Results

The main input parameters used for the 100-year model and simulation can be seen in Table 11

Table 11 - Main inputs for 1D model with 100-year flood steady flow

100 year flood			
DEM (Model no.)	**'N' Value**	**Flow (flood)**	**Run-time (mins)**
LiDAR (L0019)	Banks 0.06 - Channel 0.045	Steady (151.6 m^3/s)	~0.5
Photogrammetry (P0004)	Banks 0.06 - Channel 0.045	Steady (151.6 m^3/s)	~0.5

The first model ran in this section was a 1D model with a steady flow of 151.6 m^3/s (100 year flood). Figures 32 and 33 shows the water surface elevation (WSE) and maximum flood depth respectively and shows that visually there is little difference in flooded area and water surface elevation. This is confirmed in the numerical outputs in Table 12 which shows that the differences are minimal, however it does show again, like the 2D model, that the flood depth is substantially greater in the Photogrammetry model compared to the LiDAR model.

Table 12 - Results of 1D (steady flow) 100 year flood

100 Year Flood (151.6 m^3/s)						
DTM	**Total Area Flooded (m^2)**	**Volume (WSE) (m^3)**	**WSE Mean (m)**	**Minimum Depth (m)**	**Maximum Depth (m)**	**Depth Mean (m)**
LiDAR (L0019)	613,156.5	10,799,730.25	17.613	0.001	5.615	0.877
Photogrammetry (P0004)	612,262.0	10,780,153.72	17.607	0.001	9.022	1.506
Difference between Photogrammetry and LiDAR models						
	0.15%	0.18%	0.03%	0%	46.55%	52.79%

Figure 32 showing there is little difference in spread of flood and WSE between the two models.

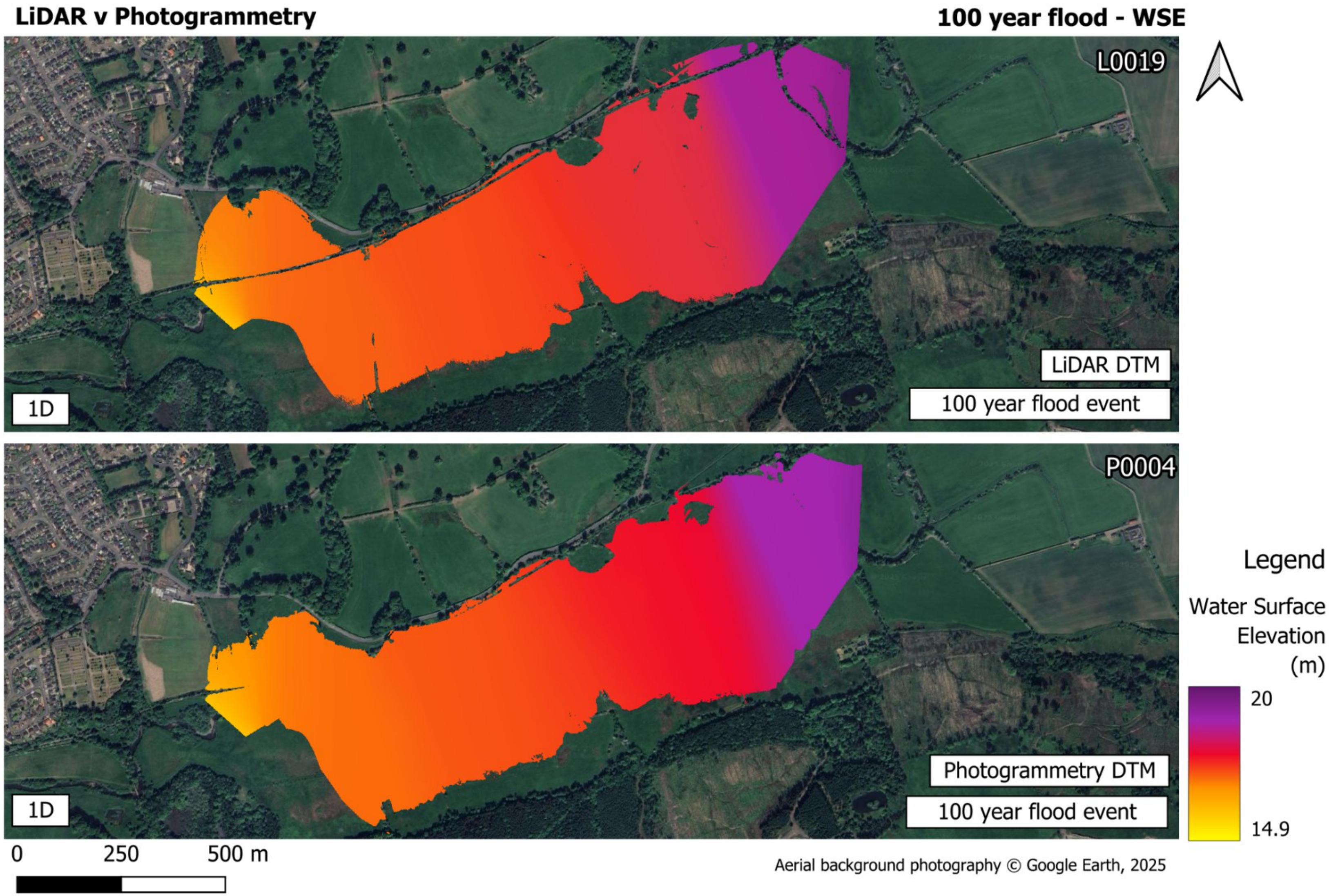

Figure 32 - 1D simple model (steady flow) comparing WSE results for 100-year flood

Figure 33 showing there is a larger difference in flood depth between the models, particularly the centre right and far bottom left being slightly darker in the Photogrammetry model, showing greater depth of water.

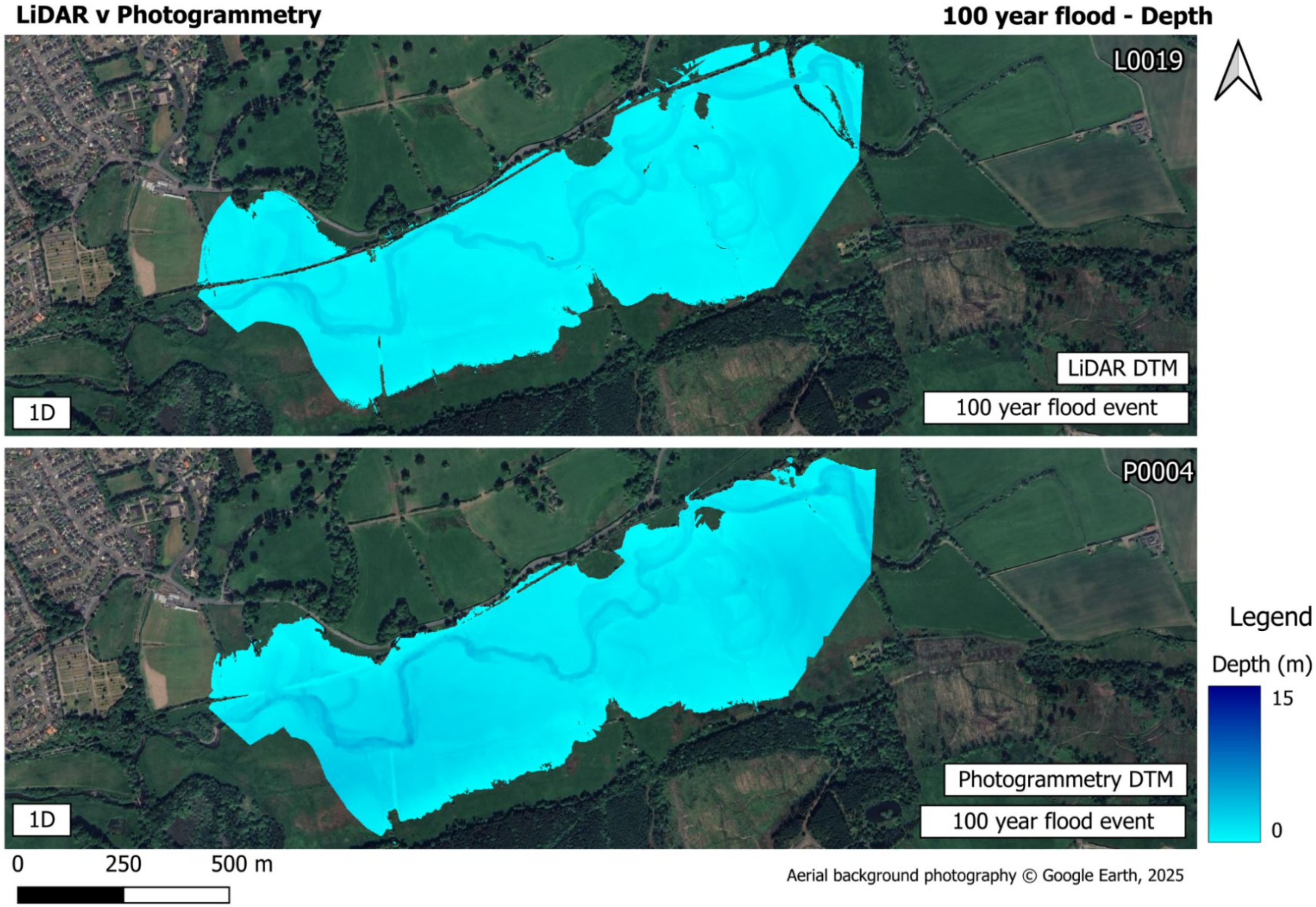

Figure 33 - 1D simple model (steady flow) comparing depth results for 100-year flood

8.3 - 20 year flood – Results

The main inputs used for the 20-year model and simulation can be seen in Table 13

Table 13 - Main inputs for 1D model with 20-year flood steady flow

20 year flood			
DEM (Model no.)	**'N' Value**	**Flow (flood)**	**Run-time (mins)**
LiDAR (L0020)	Banks 0.06 - Channel 0.045	Steady (79.8 m^3/s)	~0.5
Photogrammetry (P0005)	Banks 0.06 - Channel 0.045	Steady (79.8 m^3/s)	~0.5

The next model ran in this section was a 1D model with a steady flow of 79.8 m^3/s (20 year flood). Figure 34 is an illustration of WSE showing that despite there being a difference in the spread of flood, there's little difference in the actual elevation of water.

Figure 35 continues to show the difference in spread of flood water, but also shows the differences in depth of water.

Table 14 shows these results in numerical format and any differences in percentage between the HEC-RAS model ran using LiDAR DTM as terrain and a model ran using Photogrammetry derived DTM as terrain. It shows that compared to the 2D unsteady model, the differences are a lot smaller for most outputs but are continuously high for maximum flood depth.

Table 14 - Results of 1D (steady flow) 20 year flood

20 Year Flood (79.8 m^3/s)						
DTM	**Total Area Flooded (m^2)**	**Volume (WSE) (m^3)**	**WSE Mean (m)**	**Minimum Depth (m)**	**Maximum Depth (m)**	**Depth Mean (m)**
LiDAR (L0020)	546,853.00	9,432,028.75	17.247	0.0010	2.729	0.593
Photogrammetry (P0005)	570,739.75	9,850,486.47	17.259	0.0009	5.658	1.236
Difference between Photogrammetry and LiDAR models						
	4.27%	4.34%	0.06%	10%	69.84%	70.31%

Figure 34 shows that while there are differences in spread of flood between the models, water surface elevation remains similar.

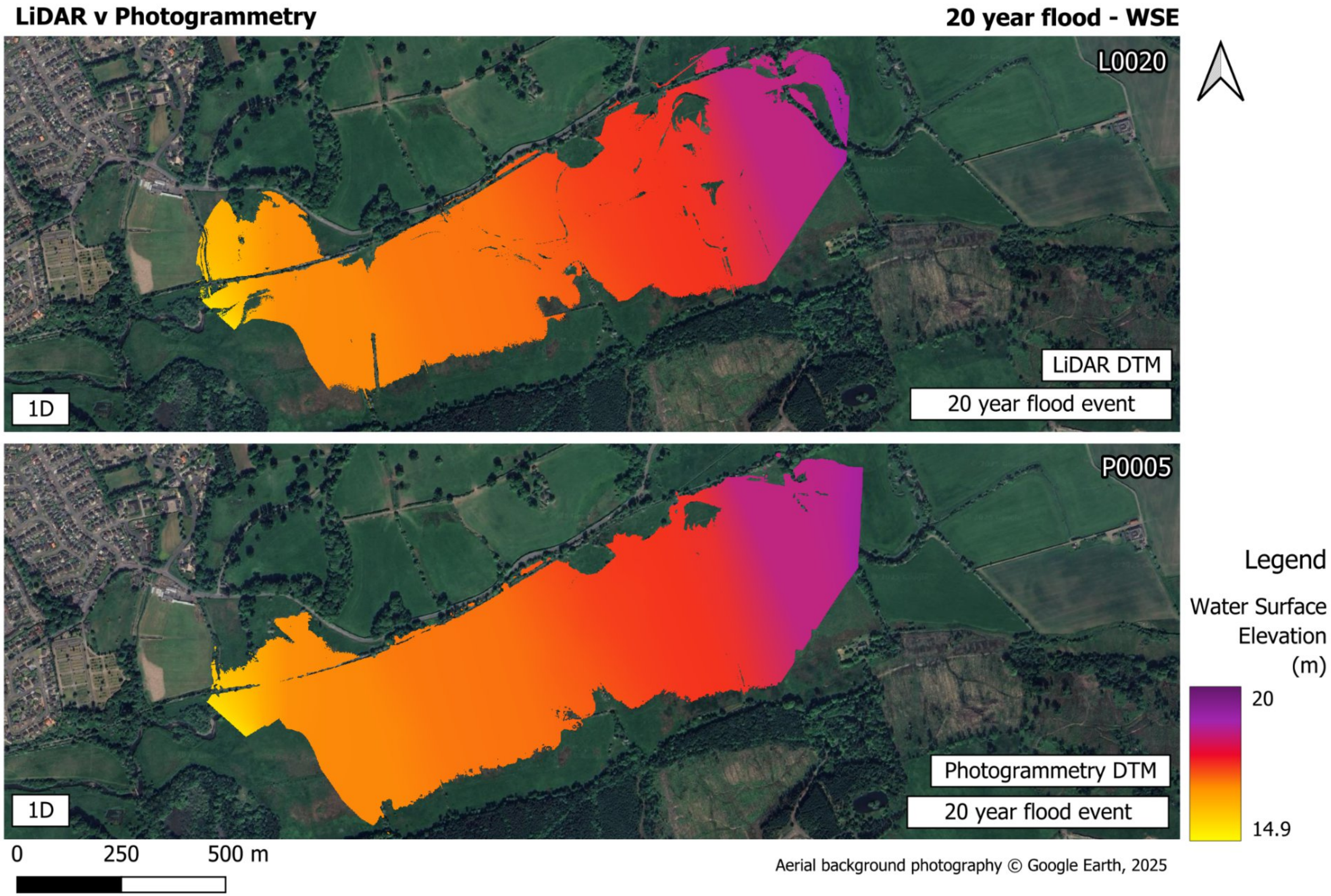

Figure 34 - 1D simple model (steady flow) comparing WSE results for 20-year flood

Figure 35 shows greater differences in both extent of flood and dept of flood water, evident by the darker shades of blue in the photogrammetry model.

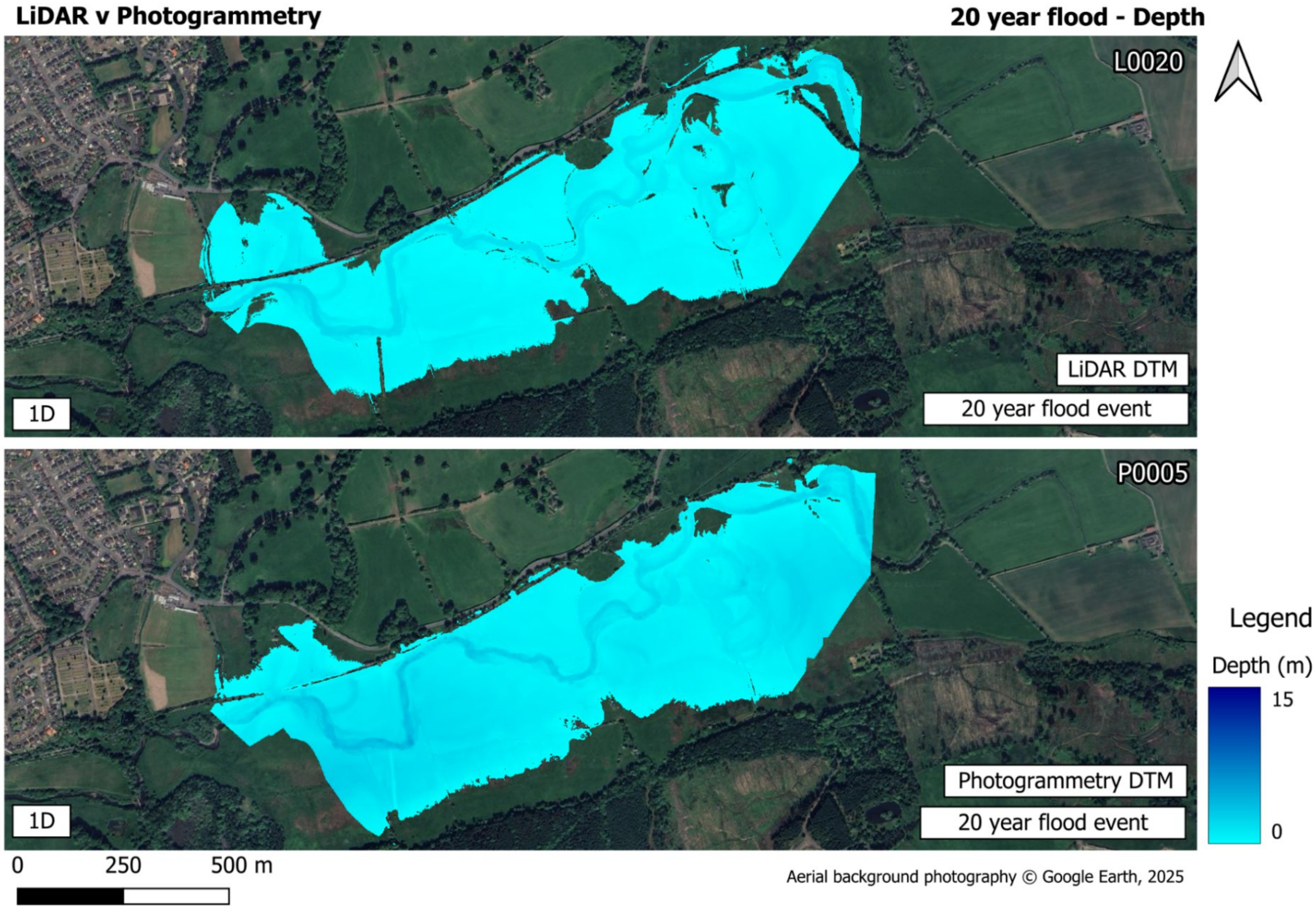

Figure 35 - 1D simple model (steady flow) comparing depth results for 20-year flood

8.4 - 2 year flood – Results

The main input parameters used for the 2-year model and simulation can be seen in Table 15.

Table 15 - Main inputs for 1D model with 2-year flood steady flow

2 year flood			
DEM (Model no.)	**'N' Value**	**Flow (flood)**	**Run-time (mins)**
LiDAR (L0021)	Banks 0.06 - Channel 0.045	Steady (48 m^3/s)	~0.5
Photogrammetry (P0006)	Banks 0.06 - Channel 0.045	Steady (48 m^3/s)	~0.5

The final HEC-RAS models created and flood simulations ran for this project was a 1D model with a steady flow of 48m^3/s (2 year flood). Numerical results and percentage differences can be seen in Table 16 and are continuing the pattern that the lower hydrograph flow rate see's increases in differences in the flood simulation outputs, similar to 2D model (Section 7)

An example of this, shown in Table 16 is the differences between total flooded area and volume of water for the different terrains. For the 100 year flood simulation it was 0.15% and 0.18%. For the 20 year flood it was 4.27% and 4.34% but for the 2 year flood it jumps up quite substantially to 21.55% and 21.29%. Differences in flood depth remain high throughout but again increase with lower flow rate.

Table 16 - Results of 1D (steady flow) 2 year flood

2 Year Flood (48 m^3/s)						
DTM	**Total Area Flooded (m^2)**	**Volume (WSE) (m^3)**	**WSE Mean (m)**	**Minimum Depth (m)**	**Maximum Depth (m)**	**Depth Mean (m)**
LiDAR (L0021)	431,534.75	7,362,619.17	17.061	0.0010	2.341	0.593
Photogrammetry (P0006)	535,779.25	9,117,201.86	17.016	0.0009	5.307	1.236
Difference between Photogrammetry and LiDAR models						
	21.55%	21.29%	0.26%	10%	77.56%	70.31%

2 Year Flood (48 m^3/s)						
DTM	**Total Area Flooded (m^2)**	**Volume (WSE) (m^3)**	**WSE Mean (m)**	**Minimum Depth (m)**	**Maximum Depth (m)**	**Depth Mean (m)**
LiDAR (L0021)	431,534.75	7,362,619.17	17.061	0.0010	2.341	0.593
Photogrammetry (P0006)	535,779.25	9,117,201.86	17.016	0.0009	5.307	1.236
Difference between Photogrammetry and LiDAR models						
	21.55%	21.29%	0.26%	10%	77.56%	70.31%

Illustrations showing WSE and maximum flood depth can be seen in Figures 36 and 37 respectively, with both figures clearly showing large differences in the flooded areas. Bar graphs showing Total Flooded Area (Figure 38) and Maximum Flood Depth (Figure 39) have also been included in this section to further show the differences between model and simulations ran against LiDAR and Photogrammetry DTM terrains.

Figure 36 shows that while water surface elevation may be consistent, there are large differences between the total area flooded.

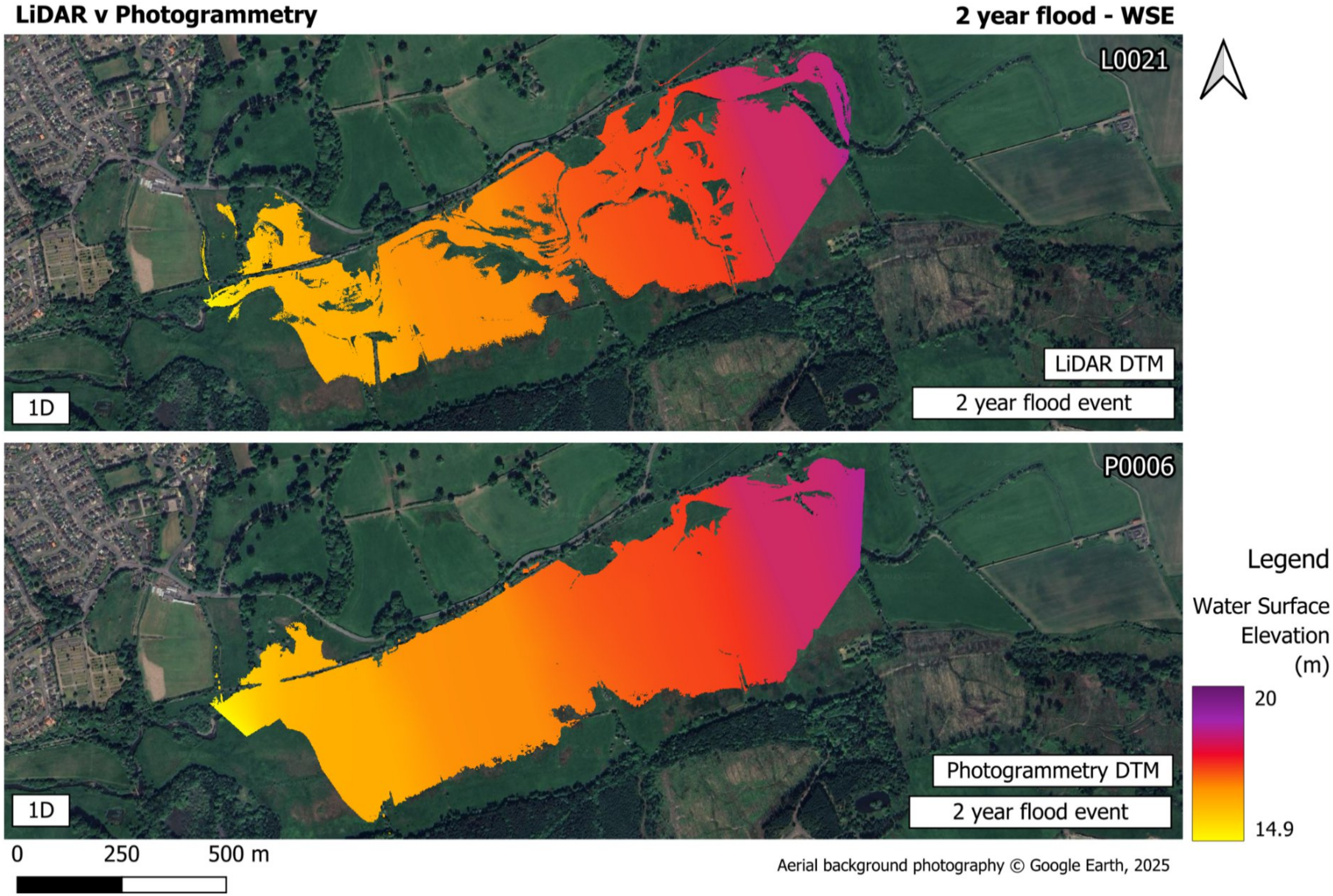

Figure 36 - 1D simple model (steady flow) comparing WSE results for 2-year flood

Figure 37 also shows differences in flooded area but also continues to highlight the differences in depth of water.

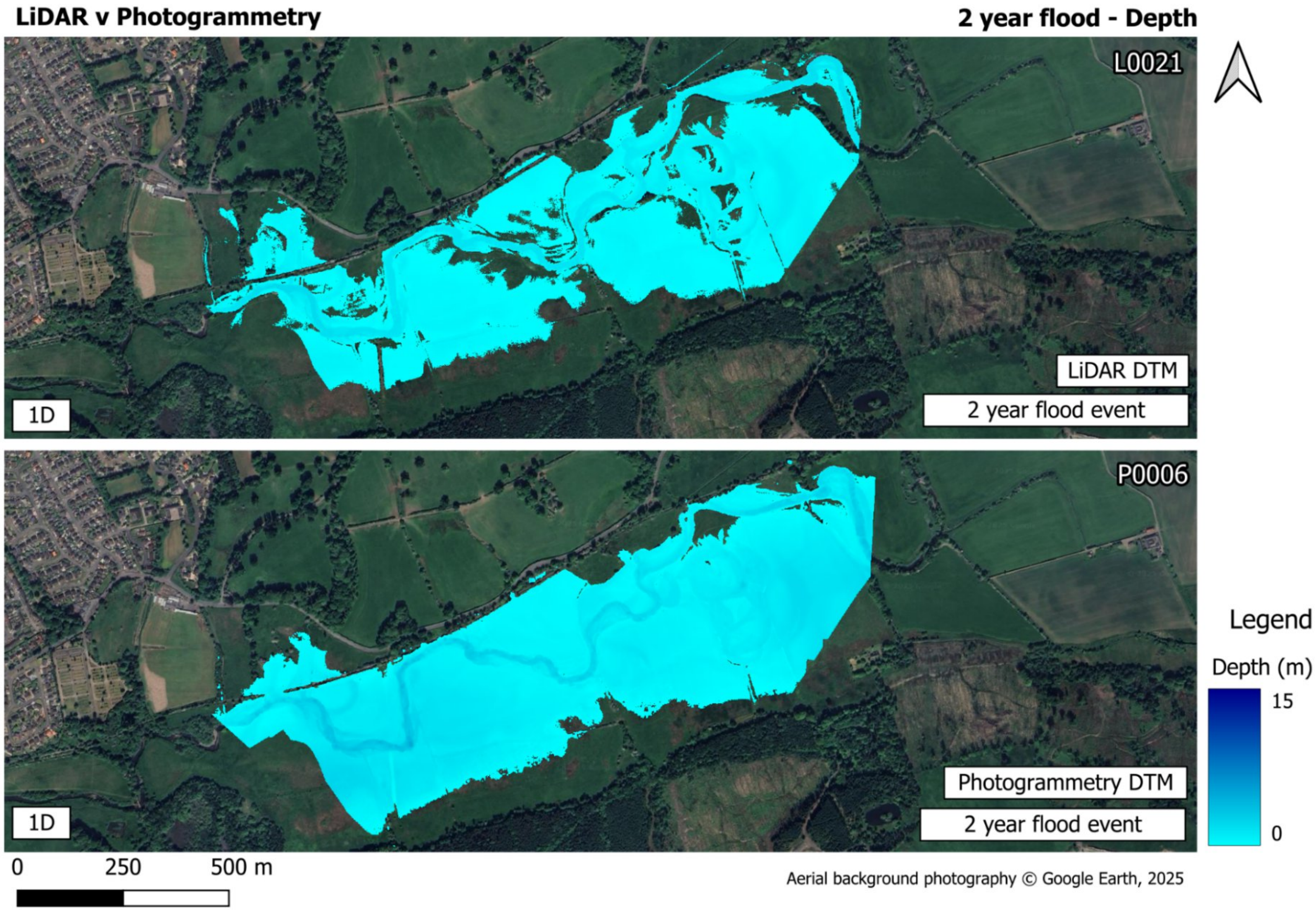

Figure 37 - 1D simple model (steady flow) comparing depth results for 2-year flood

Figures 38 and 39 show that while the hydrograph/flow can affect the differences in total flooded area, for differences between flood water depth remains high regardless of flow rate.

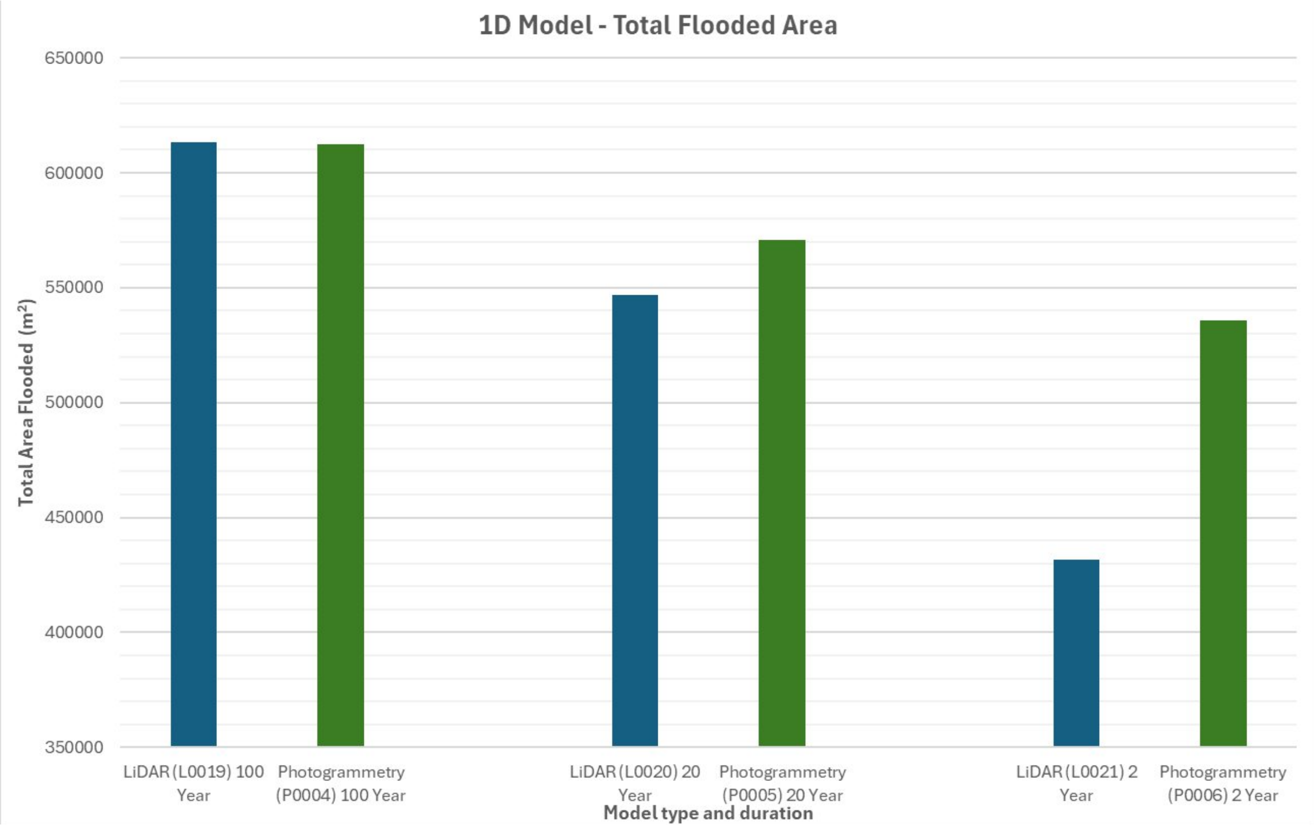

Figure 38 - Bar graph showing the differences in the total area flooded for different flood area for all models

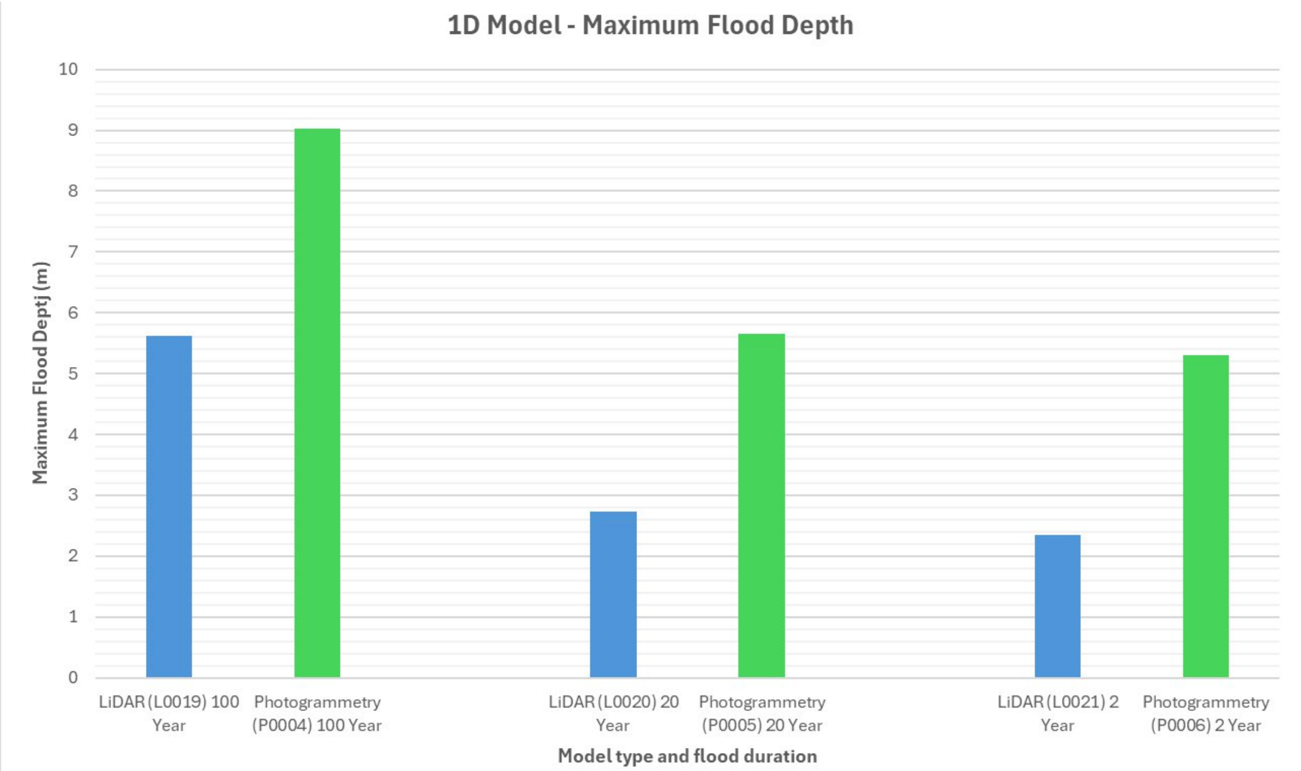

Figure 39 - Bar graph showing the differences in the maximum flood depths for all models

9 - ArcGIS Pro flood simulation (unsteady flow) LiDAR v Photogrammetry

9.1 – Methods

All 2D models created and ran as shown in this section done using the Flood Simulation tool within ArcGIS Pro v3.4, utilising official Esri ArcGIS “Create a flood simulation scenario” (Esri, n.d) and other documentation available from here. The LiDAR DTM (Scotland-DTM-50cm-Phase 4) was downloaded from Digimap with the Photogrammetry DTM derived from section 5.2 of this report. Exact flow data can be found in Appendix 1.

Further step-by-step instructions, screenshots and input parameters directly related to this part of the project can be seen in Appendix 8 with a model register available in Appendix 2.

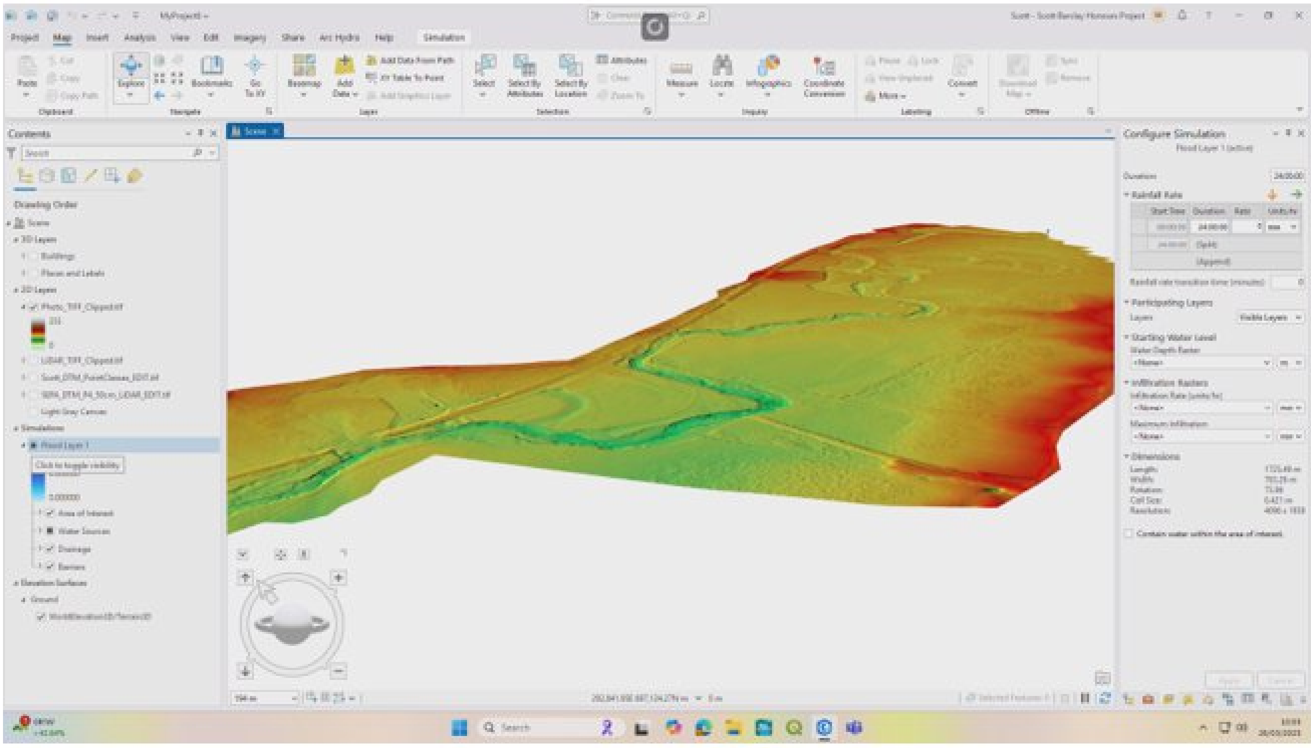

Figure – Terrain and Flood Simulation tool within ArcGIS

9.2 – 100 year flood – Results

The main inputs used for the 100-year model and simulation can be seen in Table 17

Table 17 - Main inputs for ArcGIS 2D model with 100-year flood unsteady flow

100 year flood				
DEM (Model no.)	**Cell size (m)**	**'N' Value**	**Flow (flood)**	**Run-time (mins)**
LiDAR (L0022)	0.421	N/A	Unsteady (100 year)	~39*
Photogrammetry (P0007)	0.421	N/A	Unsteady (100 year)	~40*

*plus the same again for each model for results export

The final set of models created and ran were done entirely within ArcGIS Pro 3.4. The first simulation was using the 100-year unsteady flow hydrograph on DTMs derived from both LiDAR and Photogrammetry. Figure 40 shows little differences in depths between the two DTMs (Note that it wasn't possible to extract water surface elevation from these models). Table 18 contains numerical outputs showing some peculiar results with minimum depths having a negative number which is unexpected.

Table 18 - Results of 2D (unsteady flow) ArcGIS simulation for 100 year flood

100 Year Flood			
DTM	**Minimum Depth (m)**	**Maximum Depth (m)**	**Mean Depth (m)**
LiDAR (L0022)	-2.354	5.84	3.094
Photogrammetry (P0007)	-2.197	5.744	3.095

Figure 40 shows near identical flooded area and depths for models ran on the two different terrains.

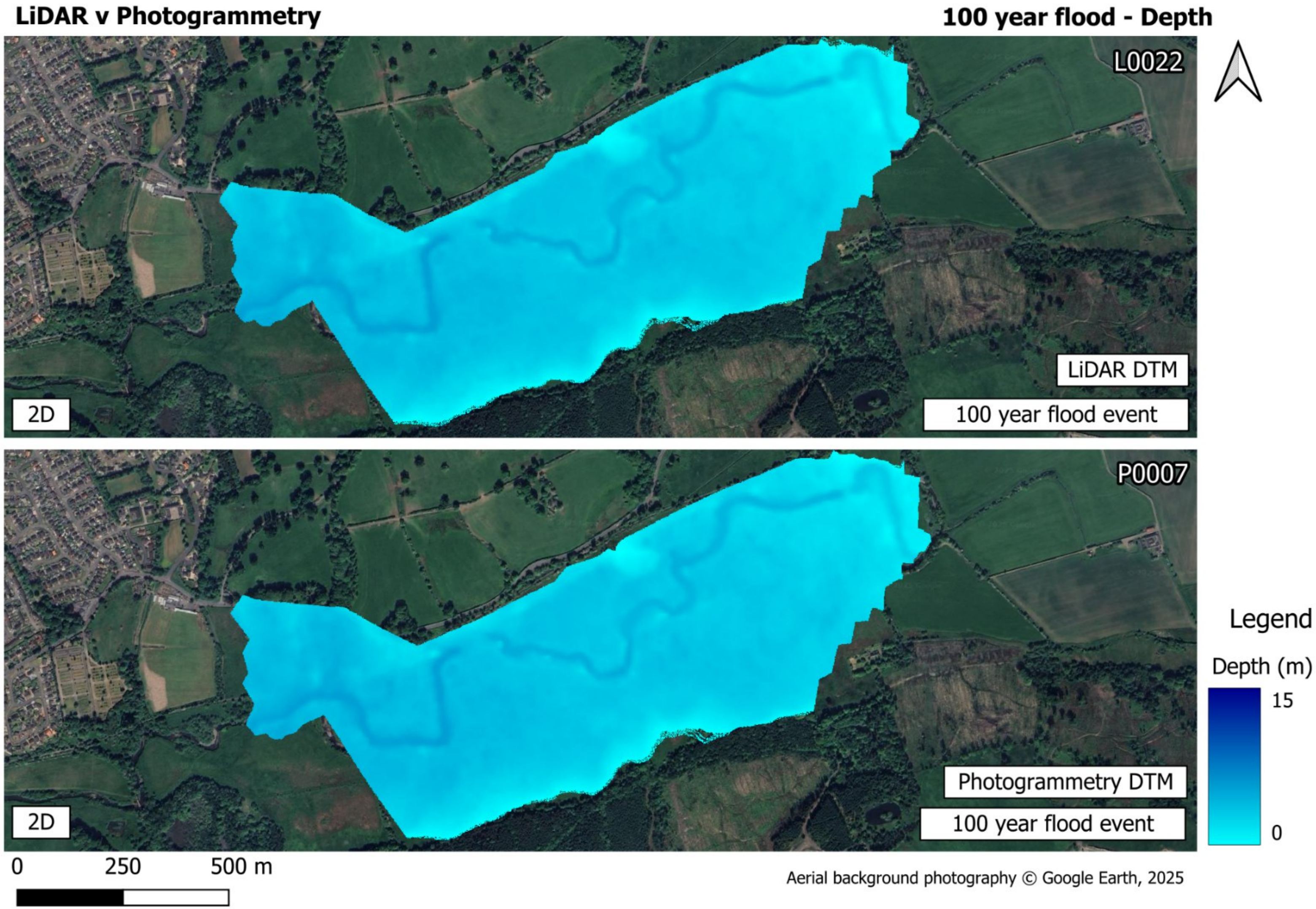

Figure 40 - 2D simulation in ArGIS Pro comparing depth results for 100-year flood

9.3 – 20 year flood – Results

The main inputs used for the 100-year model and simulation can be seen in Table 19.

Table 19 - Main inputs ArcGIS 2D model with 100-year flood unsteady flow

20 year flood				
DEM (Model no.)	**Cell size (m)**	**'N' Value**	**Flow (flood)**	**Run-time (mins)**
LiDAR (L0023)	0.421	N/A	Unsteady (20 year)	~41*
Photogrammetry (P0008)	0.421	N/A	Unsteady (20 year)	~42*

*plus the same time again for results export.

The second batch of models created and simulations ran in this section was still using the same DTMs but using the 20-year unsteady flow hydrograph. Figure 41 shows the water depth and flooded area and again shows little difference in water depth, which is unexpected given the differences in results from previous HEC-RAS simulations. There is a difference in flooded area but this is also completely unexpected as part of the flooded area is actually out with the boundary used for all models.

The numerical results shown in Table 20 also shows little differences in maximum flood depth but has a larger difference between minimum depth, but again has both of these as a negative number which was not expected and made little sense, because if there was shallow flood water, the number should be zero or close to zero as seen in the HEC-RAS models.

Table 20 - Results of 2D (unsteady flow) ArcGIS simulation for 20 year flood

20 Year Flood			
DTM	**Minimum Depth (m)**	**Maximum Depth (m)**	**Mean Depth (m)**
LiDAR (L0023)	-8.316	3.677	1.283
Photogrammetry (P0008)	-1.282	3.660	1.320

Figure 41 shows little difference in depth of flood but greater difference in area flooded area. The section highlighted red in the LiDAR result is actually out the flood area boundary, and this area hasn't been flooded in any previous or future models at all in this project.

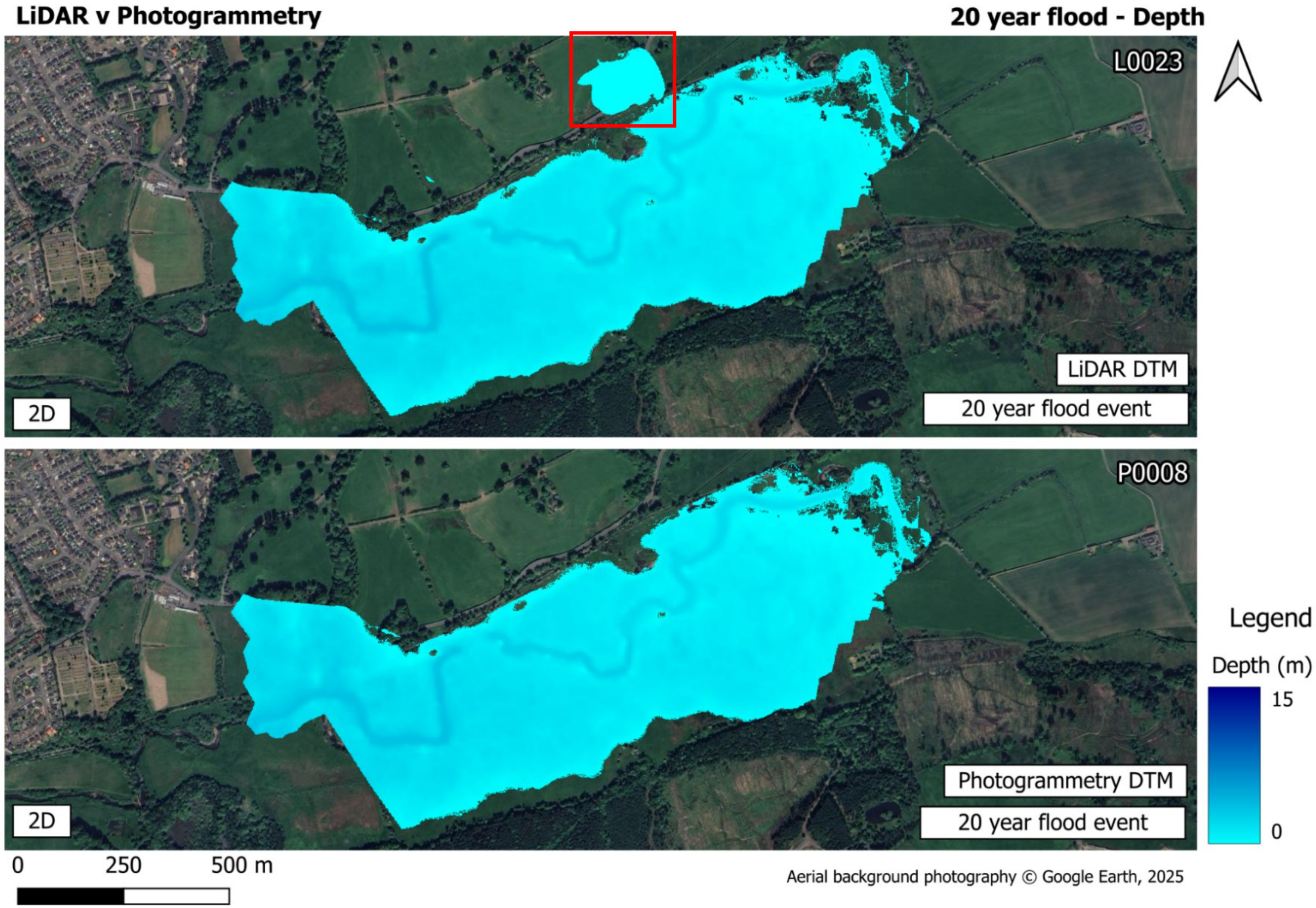

Figure 41 - 2D simulation in ArGIS Pro comparing depth results for 20-year flood

9.4 – 2 year flood – Results

Table 21 - Main inputs for ArcGIS 2D model with 2-year flood unsteady flow

2 year flood				
DEM (Model no.)	**Cell size (m)**	**'N' Value**	**Flow (flood)**	**Run-time (mins)**
LiDAR (L0024)	0.421	N/A	Unsteady (2 year)	~41*
Photogrammetry (P0009)	0.421	N/A	Unsteady (2 year)	~41*

*plus the same time again for results export

The third and last set of models created was still 2D unsteady flow in ArcGIS Pro, using the Photogrammetry and LiDAR derived DTMs but running the 2-year flood hydrograph. Visually, Figure 42 continues to show that as per the other results in this section there is little to no difference in maximum flood depth, and similar to the 100 year simulation ran on ArcGIS there is little to no difference in flood extent.

Table 22 contains the numerical data extracted from the results and again confirms that there is little difference in maximum flood depth. Table X also continues to show that minimum depth is a negative number like the 100 and 20 year simulations, which again is completely unexpected.

Table 22 - Results of 2D (unsteady flow) ArcGIS simulation for 2-year flood

2 Year Flood			
DTM	**Minimum Depth (m)**	**Maximum Depth (m)**	**Mean Depth (m)**
LiDAR (L0024)	-1.336	2.748	0.653
Photogrammetry (P0009)	-9.365	2.731	0.652

Given the peculiarities in the results for all models ran in section 10 using the Flood Simulation tool within ArcGIS Pro, there is a reluctance to recommend this as a viable flood modelling tool (See section 11.3 for further discussion).

Figure 42 is a continuation of unexpected results within this section, with LiDAR and Photogrammetry flooded area and flood water depth being near identical.

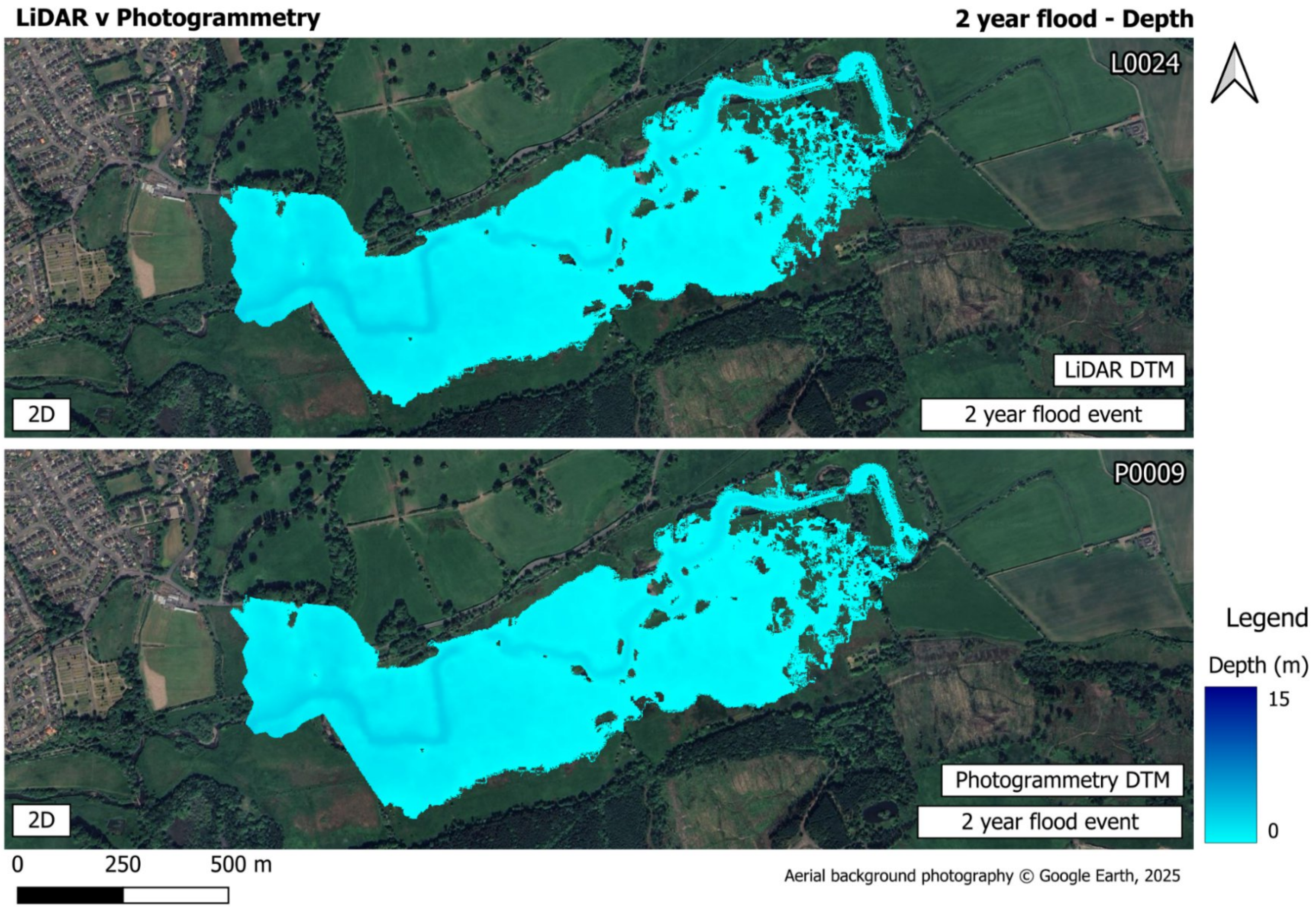

Figure 42 - 2D simulation in ArGIS Pro comparing depth results for 2-year flood for LiDAR and Photogrammetry derived DTM's

10 – Post simulation analysis

An analysis of all the results from both HEC-RAS and ArcGIS pro was conducted in QGIS v3.34. This was achieved by exporting the result TIFFs from the two modelling applications and importing them into a new QGIS project. The Raster Analysis tools were used to extract required information before manually exporting this to Excel for further more in-depth analysis.

Finished maps that can be seen throughout sections 7-10 were created using the Print Layout feature in QGIS. Further step-by-step instructions directly related to this part of the project can be seen in Appendix 9.

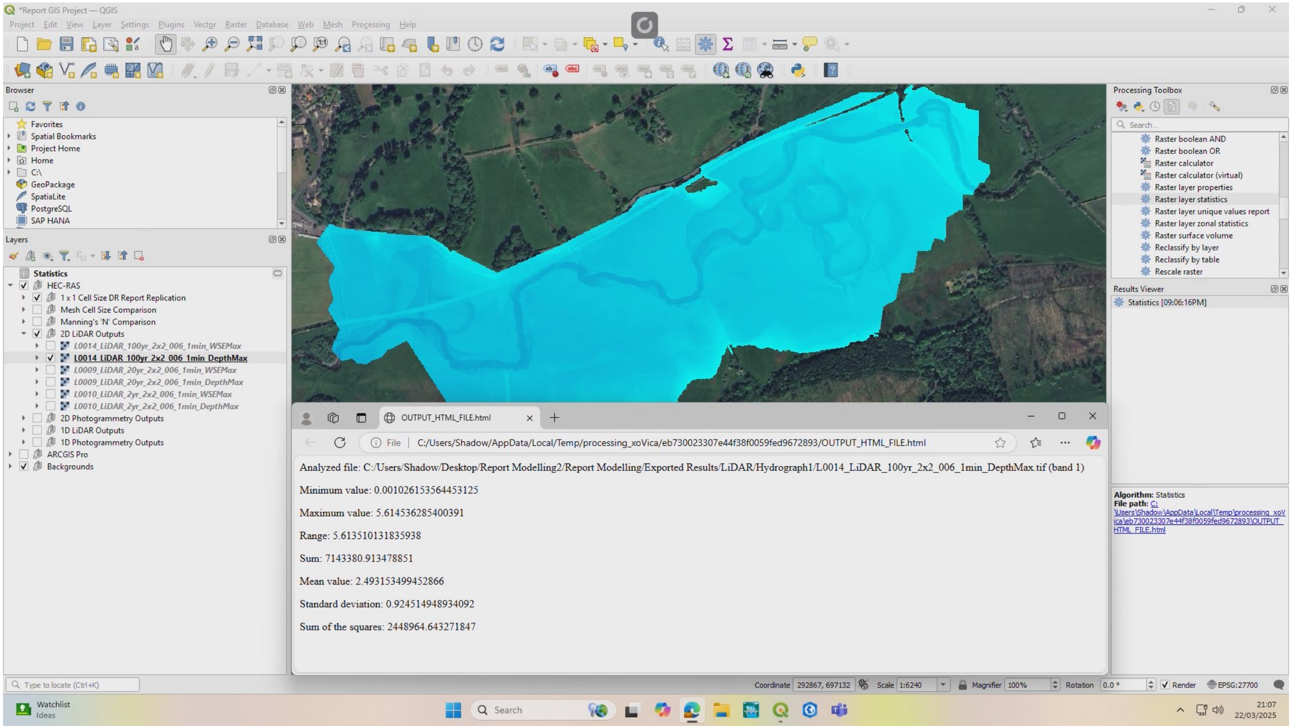

Figure 43 - QGIS project and an example of a raster analysis

11 – Discussion

11.1 – HEC-RAS 2D unsteady flow

11.1.1 - Report replication (1x1m cell size, LiDAR DEM)

An evaluation of flood modelling techniques was conducted on a stretch of the River Devon in the chosen study area. The first flood simulations ran was a 2D model (unsteady flow) using LiDAR data in an attempt to replicate some of results from the existing Dynamic Rivers report. An unsteady flow hydrograph means flow characteristics (velocity, discharge and water level) of that regime can change with time (Ponce, 2005), whereas with steady flow the conditions may change from point to point within the stream system, but not change with time (Loughborough University, 2002). A 2D mesh was used which allows simulated water to realistically flow across 2D areas (floodplains).

Mesh size, manning N roughness values and other input parameters were obtained from the Dynamic Rivers report, but it was at this point the project encountered its first problem which was hydrograph data. To obtain flow data for their models, the original Dynamic Rivers report used the following computer applications (Williamson, 2024) from WHS:

- Ref2H (WHS, 2025b).
- WINFAP (WHS, 2025c).
- LowFlows (WHS, 2025a).

While these are acceptable methods as outlined in guidance by SEPA (SEPA, 2022), DEFRA and the EA (DEFRA, 2023), due to licencing costs the applications were unobtainable for this project. As such, the hydrographs for this project were created manually and aren't entirely comparable with real world conditions. Another problem encountered was lack of measurable data within the original report with finished maps lacking legends and scale bars, meaning there was little data to compare the findings from this project too, however despite that, 3 models were completed, one for each flood event, using a smaller 1m cell size and 30 second computation intervals with the final results shown above in Section 6.2.

11.1.2 – Cell/Mesh size comparison

While smaller mesh cell sizes and lower computation intervals can result in more accurate modelling, as found in previous studies (Yalcin, 2020), smaller mesh sizes can greatly increase the running time of flood simulations (Ongdas *et al.*, 2020). Therefore, using the LiDAR DEM, a comparison of cell sizes (10x10m, 5x5, 3x3m and 2x2m) was conducted to ascertain any differences in simulation run times and outputs, using the data from section 6.2 as a benchmark.

The results show the flood shape and peak flowrate downstream for 5 different cell sizes while Figures 20-21 shows the differences via completed maps. While the 10m x 10m and 5m x 5m models took 29 seconds and 1 minute 48 seconds respectively to run, compared to 45 minutes for the 1m x 1m model, there are large differences in the flood shape and peak flow downstream. A 3m x 3m cell size was created with the simulation completing in 6m 34 seconds. While the differences between this model and 1m x 1m are smaller, the shape of the flood was still different and peak flow measured just 124 m^3/s compared to almost 142 m^3/s for 1x1m model.

Therefore, a further model was created using a 2m x 2m cell size and as shown in Figure 22, the shape of the flood is almost identical with peak flow within around 6% of the 1m x 1m model. Finishing in 14m 48 seconds, less than a third of the time for 1m x 1m model, it was decided this would be the cell size to use while conducting Manning's N value comparison.

11.1.3 – "N-value" comparison

Manning's 'N' co-efficient can be defined as a parameter used to quantify roughness and/or frictional resistance of a water channels surface that could impact water flow efficiency in an open channel (Whatmore *et al*., 2010). While the Manning 'N' values of 0.045, 0.05, 0.06 and 0.08 used in this section were obtained from the Dynamic Rivers report (Williamson, 2024), in future projects they can be obtained from HEC-RAS using a land cover layer as outlined in the HEC-RAS 2D user manual (USACE, n.d b).

The results confirm the importance of applying the correct n-value to a model due to the large variation of peak flow downstream using the LiDAR dataset. Lower N-values of 0.045 and 0.05 resulted in faster water flow of 200 m^3/s and 180 m^3/s respectively while a higher value of 0.08 resulted in slower water flow of around 117 m^3/s. With optimum cell size (2x2m) and N-value (0.06) established a comparison of models between LiDAR and Photogrammetry derived DEMs was then conducted.

11.1.4 – LiDAR v Photogrammetry

The first model ran in this series was using the 100 year flood event hydrograph with the purpose of determining any differences in outputs from models using the LiDAR derived DTM from SEPA, and that obtained from the Photogrammetry processes outlined in section 5.2. There are some minor differences in the spread of the flood with the LiDAR simulation showing slightly more flooded area. This is confirmed in Table 6 that shows while the Photogrammetry has 6% greater downstream maximum flow rate and 1.7% more volume, it has 3% less flooded areas and water 5.59% less surface water extent to the LiDAR model.

The next model ran was using the 20-year flood hydrograph using the exact same inputs and DEMs as above. The results in this simulation show greater differences which can been seen in water surface extent and flood water depth. These differences are confirmed in Table 8 that show while water surface extent and volume is lower in the Photogrammetry model, flood depth has increased which is an unexpected result.

The last model created for this section was using the 2-year hydrograph (with all other inputs remaining the same). The results show clear differences in flood depth, area flooded and water surface elevation from the LiDAR DTM model and Photogrammetry DTM model. These differences can be seen in Table 10 showing a continuation of the pattern of larger differences in all metrics between LiDAR and Photogrammetry results, with downstream maximum flow and volume for Photogrammetry model being 49% and 40% less, but again, despite this the Photogrammetry model has much greater depth of flood water by 3 metres.

While some of the results were initially unexpected, some of the results are in-line with a previous study in Tanzania, that also found a variation of differences in outputs from models ran against a LiDAR and Photogrammetry DTMs. The study found that despite the Photogrammetry DTM maximum water surface elevation being less than the LiDAR maximum WSE, maximum flood depth was around 50% greater (Sakala, 2020), similar to the results in this section of the study. This could be because of differences in DTM resolutions and artefacts within the Photogrammetry data (Further analysis would need completed before confirming this).

11.2 – HEC-RAS 1D steady flow

LiDAR v Photogrammetry

The final models created and ran in HEC-RAS was a continuation of using the LiDAR derived DTM and Photogrammetry derived DTM but using 1D model and steady flow state. 1D modelling uses hand-drawn bank lines, centrelines and cross-sections to perform calculations (Sánchez, 2022) with a journal article finding that the preference for 1D or 2D can depend upon the location, shape and meandering of a river (Arash *et al.*, 2023).

The results for the 1D model using the100-year flood hydrograph are similar to the 2D model, in that the flooded area is similar and result differences are small (<1%) for all outputs except maximum flood depths, with the Photogrammetry model having far greater flood depth again. The differences increase slightly for the 20 year flood with the Photogrammetry model having 4% greater total for both area flooded and volume (WSE), this compares to photogrammetry model having 9% and 13% less total flooded area and volume (WSE), so the differences between the 1D and 2D models was unexpected.

The final model in this section was using the 2 year flood data. The volume (WSE) is 21% greater for the photogrammetry model compared to LiDAR, this is a complete contrast to the 2D model that had photogrammetry volume (WSE) being 14% less than the LiDAR model. Similarly the total flooded area for the photogrammetry model is 21% greater for 1D, but 10% less for the 2D model confirming again the variation and inconsistencies of results produced except for maximum flood depth which was consistently higher for Photogrammetry throughout.

While the vast differences in flood depth for all 3 models are unexpected, some of the findings are in-line with a 2016 study comparing aerial LiDAR and SfM-UAV flood modelling. For 3 study sides in Northern Virginia (USA), it was found that depending on the flowrate there was a 28-50% difference in floodplain areas for site 1, a 28-50% difference in mapped floodplain areas for site 2 with a 1-70% difference in site 3 (Zahirieh, 2019) with no pattern to the results. The conclusion from this study was that the differences can be partly attributed to the in-consistent differences in elevation of vegetated and grassland areas between the results from photogrammetry processes and LiDAR datasets (Sakala, 2020).

11.3 – ArcGIS Flood Simulation 2D unsteady flow

LiDAR v Photogrammetry

6 models were conducted using ArcGIS Pro against the 3 flood event hydrographs for both LiDAR and Photogrammetry DTMs. The initial plan was to run 1D models using ArcMap however that tool is discontinued for new customers. Therefore all models were 2D with no ability to input other values such as 'N' value, and slope in the Flood Simulation tool. It should also be noted that it wasn't possible to export water surface elevation and downstream flow rate from this tool for post simulation analysis.

For consistency the first model ran was the 100-year flood hydrograph and the results for this were unexpected given how close the results within ArcGIS were but how different they were to HEC-RAS. From Table 18 it shows the maximum flood depth to be 5.84m and 5.74m for LiDAR and Photogrammetry respectively, which compares to 5.615 and 9.022 for the HEC-RAS model. For the ArcGIS 20 year flood model the maximum depth was 3.677 for LiDAR and 3.660 for Photogrammetry (Table 22) comparing to 4.266 and 12.657 for HEC-RAS.

A final model was run for both LiDAR and Photogrammetry DTMs and the two results within ArcGIS against the different terrains were near identical, LiDAR maximum depth being 2.748 and Photogrammetry being 2.731. This compares to maximum depths of 4.266 and 12.657 for the 2D HEC-RAS models. Another unexpected and peculiar result was that for every single model ran in this section the minimum depth of flood water was a negative number.

Given the peculiarity of the minimum depth being a negative number, and little difference in results for models conducted within ArcGIS Pro, yet hugely different results for ArcGIS models compared to HEC-RAS models, there would be a reluctance to recommend ArcGIS Pro Flood Simulation as a credible modelling tool. While the tool is simple to use, its simplicity is also its downfall as it doesn't allow the same inputs (N-values, slopes) or export of results for analysis as HEC-RAS.

There are also other limitations in that cell sizes and resolutions are pre-determined by ArcGIS Pro and it doesn't allow areas longer than 14.3 km so can't be used for large river stretches and/or catchment modelling (ESRI, n.d b), unlike HEC-RAS which has no hard limit and the river/area/catchment size and is down to computer processing power. Another problem encountered with ArcGIS Pro flood simulation is the inability to import hydrograph data, this had to be typed in manually for all models which was time-consuming, compared to HEC-RAS that will allow imports and copy/pasting of flow values. While HEC-RAS models may take longer for initial setup, it allows greater editing and adding of data, and depending on the geometry can be quicker to run.

One observation when reading the official literature on Flood Simulation was that every graphic used to showcase the tool, in every official webpage (ESRI, n.d c) , press release or technical paper (ESRI, 2024) was a small-scale simulation in an urban area using in-built ESRI maps, with ESRI themselves concluding that this tool doesn't handle complex conditions and flow regimes, and that the Flood Simulation tool shouldn't replace existing modelling applications (ESRI, 2024) . This was also confirmed in an official webinar that also stated the Flood Simulation tool isn't engineer grade with and that the result accuracy for Flood Simulation is a lot less than HEC-RAS (Figure 44).

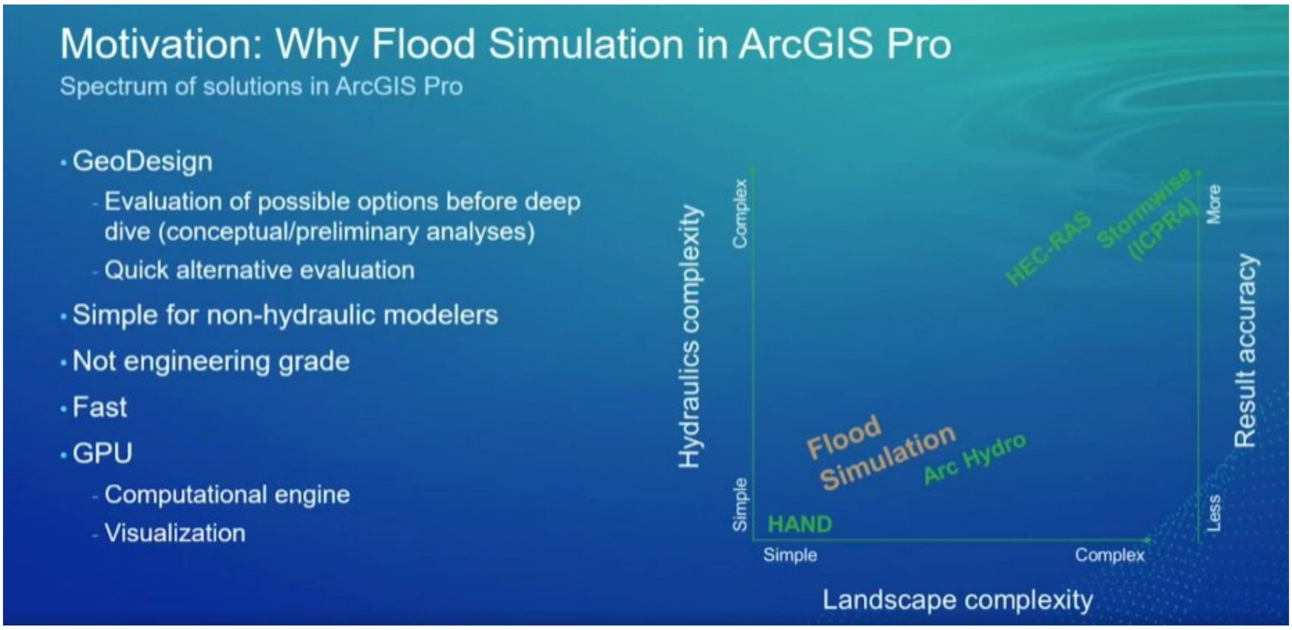

Figure 44 - ArcGIS Pro Flood Simulation webinar showing differences between it and HEC-RAS (Patti, 2024)

Future Considerations

While Photogrammetry could be viable for paved/urban areas, a study for the Msimbaza river basin (Tanzania) found that differences between Photogrammetry and LiDAR can be attributed to the in-consistent differences in elevation in the dense point clouds and DEMs of vegetated and grassland areas that didn't exist in flat and paved areas (Sakala, 2020). A further study at Proctor Creek (USA) also found similar, UAV data collection and SfM/Photogrammetry processes can be greatly affected by natural conditions such as moving water and areas of high vegetation (Ballow, 2016b).

A recommendation in an attempt to reduce the differences between LiDAR and Photogrammetry would be to reduce flight height to increase image overlap and include strategically placed GCPs with camera calibration to increase accuracy (Deliry *et al*., 2021). If the differences in results are still too large, an alternative could be commercial grade UAV with dedicated photogrammetry camera or LiDAR lens which is as accurate as aerial LiDAR in small areas of vegetation (Kucharczyk *et al*., 2018). This could be achieved via a standalone DJI Matrice 350 RTK (A) and either Zenmuse L2 LiDAR lens (B) or a Zenmuse P1 Photogrammetry camera (C) shown in Figure 45.

Figure 45 - Professional grade DJI UAV and accessories

Conclusion

An evaluation of different flood modelling techniques to ascertain any differences between flood simulations ran on LiDAR and Photogrammetry DTMs on two main applications HEC-RAS and ArcGIS Pro was conducted. The study shows that from the results there are large differences between HEC-RAS and ArcGIS Pro Flood Simulation tools, with this confirmed via a range of official documentation from ArcGIS Pro creator ESRI. While the Flood Simulation can be easier and quicker to setup it does have severe limitations such as small maximum river and catchment size and limited hydrograph/flow capabilities, therefore the project can conclude ArcGIS Pro Flood Simulation should not be considered a viable alternative to HEC-RAS which while being more complex, does have far greater accuracy in results.

Simulations were run to establish any differences in the outputs from 1D and 2D models between LiDAR derived DTM and Photogrammetry DTM. While a direct comparison can't be made between the 1D and 2D results due to the differences in flows (2D using unsteady and 1D using steady flow) the study finds that if computation processing power and time allows it then typically a 2D model will give more accurate results over 1D due to being better able to capture complex channels, terrain and floodplains. However it's worth noting that the model setup can be more complex and time-consuming with the simulation run-time also being far greater for 2D over 1D.

For 1D and 2D models ran using the different terrains derived from the LiDAR dataset and Photogrammetry processes, the differences in outputs for all models was to vast and inconsistent to consider Photogrammetry DTM at this stage to be a viable alternative to LiDAR DTM and recommends further research to be done. This could be because how LiDAR can remove vegetation better resulting in a cleaner DTM compared to Photogrammetry, shown in Figure 45b. This conclusion was reached due to the differences in downstream flowrate, volume, total flooded area, water surface elevation and depth for all models conducting, with some differences in results being 60-70% between the two terrains.

Figure 45b showing a satellite image of bankside over hanging trees and how LiDAR removes vegetation better than Photogrammetry, by showing how clearly defined the river channel is in the LiDAR DEM compared to blurred river banks in the Photogrammetry DTM

Figure 45b - Satellite imagery showing river bankside vegetation and how LiDAR and Photogrammetry removes it differently for exact same river section.

References

Aber, J.S., Marzolff, I. and Ries, J.B. (2010) ‘Chapter 3 - Photogrammetry’, in J.S. Aber, I. Marzolff, and J.B. Ries (eds) *Small-Format Aerial Photography*. Amsterdam: Elsevier, pp. 23–39. Available at: https://doi.org/https://doi.org/10.1016/B978-0-444-53260-2.10003-1.

Acharya, T.D. and Yang, I. (2015) ‘Exploring landsat 8’, *International Journal of IT, Engineering and Applied Sciences Research (IJIEASR)*, 4(4), pp. 4–10.

Ackerman (2021) *Creating a Simple 2D Model with HEC-RAS*. Available at: https://www.hec.usace.army.mil/confluence/rasdocs/rastraining/files/6.6/217581145/217581219/1/1729725839088/Workshop+-+Creating+a+2D+Model.pdf (Accessed: 26 February 2025).

Agisoft (2020) *Agisoft Metashape User Manual Professional Edition, Version 1.6*. Available at: https://www.agisoft.com/pdf/metashape-pro_1_6_en.pdf (Accessed: 8 January 2025).

Agisoft (no date) *About*. Available at: https://www.agisoft.com/about/ (Accessed: 29 January 2025).

Amani, M. *et al.* (2022) ‘Remote Sensing Systems for Ocean: A Review (Part 1: Passive Systems)’, *IEEE Journal of Selected Topics in Applied Earth Observations and Remote Sensing*, 15, pp. 210–234. Available at: https://doi.org/10.1109/JSTARS.2021.3130789.

Annis, A. *et al.* (2020) ‘UAV-DEMs for Small-Scale Flood Hazard Mapping’, *Water*, 12(6). Available at: https://doi.org/10.3390/w12061717.

Arash, A.M. and Yasi, M. (2023) ‘The assessment for selection and correction of RS-based DEMs and 1D and 2D HEC-RAS models for flood mapping in different river types’, *Journal of Flood Risk Management*, 16(1), p. e12871. Available at: https://doi.org/https://doi.org/10.1111/jfr3.12871.

Avila-Aceves, E. *et al.* (2023) ‘Geospatial modelling of floods: a literature review’, *Stochastic Environmental Research and Risk Assessment*, 37(11), pp. 4109–4128. Available at: https://doi.org/10.1007/s00477-023-02505-1.

Ballow, W. (2016a) ‘The Evaluation of Measuring Stream Channel Morphology using Unmanned Aerial System-Based Structure-From-Motion Photogrammetry’.

Ballow, W. (2016b) ‘The Evaluation of Measuring Stream Channel Morphology using Unmanned Aerial System-Based Structure-From-Motion Photogrammetry’.

Bauska, T. (2022) *Ice cores and climate change*. Available at: https://www.bas.ac.uk/data/our-data/publication/ice-cores-and-climate-change/ (Accessed: 14 November 2024).

Bhandari, B. *et al.* (2015) ‘Generation of high resolution DSM using UAV images’, in *FIG working week*, pp. 17–21.

Breen, M.J., Kebede, A.S. and König, C.S. (2022) 'The Safe Development Paradox in Flood Risk Management: A Critical Review', *Sustainability*, 14(24). Available at: https://doi.org/10.3390/su142416955.

British Geological Survey (2019) *What causes the Earth's climate to change?* Available at: https://www.bgs.ac.uk/discovering-geology/climate-change/what-causes-the-earths-climate-to-change/#:~:text=Geological%20records%20show%20that%20there,carbon%20dioxide%20(CO2). (Accessed: 14 November 2024).

CAA (2023) *CAP2012: Drone Rules: REQUIREMENTS FOR FLYING IN THE OPEN CATEGORY*. Available at: https://www.caa.co.uk/our-work/publications/documents/content/cap2012/ (Accessed: 29 January 2025).

CAA (2024) *The Drone and Model Aircraft Code*. Available at: https://register-drones.caa.co.uk/drone-code/getting-what-you-need-to-fly (Accessed: 8 January 2025).

Calvin, K. *et al.* (2023) *IPCC, 2023: Climate Change 2023: Synthesis Report. Contribution of Working Groups I, II and III to the Sixth Assessment Report of the Intergovernmental Panel on Climate Change [Core Writing Team, H. Lee and J. Romero (eds.)]. IPCC, Geneva, Switzerland.* Geneva. Available at: https://doi.org/10.59327/IPCC/AR6-9789291691647.

Chiu, Y.-Y., Raina, N. and Chen, H.-E. (2022) 'Evolution of Flood Defense Strategies: Toward Nature-Based Solutions', *Environments*, 9(1). Available at: https://doi.org/10.3390/environments9010002.

Chu, J. (2024) *New AI tool generates realistic satellite images of future flooding*, *MIT News*.

Cimpianu, C.I. and Mihu-Pintilie, A. (2019) 'Open Source flood mapping tools—QGIS, RIVER GIS and HEC-RAS', *Acta Geobot*, 6, pp. 35–41.

CIWEM (2022) *Natural Flood Management*. Available at: https://www.ciwem.org/assets/pdf/Policy/Policy%20Position%20Statement/Natural%20Flood%20Management%20PPS%20FINAL_compressed%20(1).pdf (Accessed: 12 November 2024).

Davis, A.B. *et al.* (1999) 'Off-beam lidar: an emerging technique in cloud remote sensing based on radiative green-function theory in the diffusion domain', *Physics and Chemistry of the Earth, Part B: Hydrology, Oceans and Atmosphere*, 24(3), pp. 177–185. Available at: https://doi.org/https://doi.org/10.1016/S1464-1909(98)00034-3.

DEFRA (2023) 'River modelling: technical standards and assessment'. Available at: https://www.gov.uk/government/publications/river-modelling-technical-standards-and-assessment (Accessed: 20 March 2025).

Deliry, S.I. and Avdan, U. (2021) 'Accuracy of Unmanned Aerial Systems Photogrammetry and

Structure from Motion in Surveying and Mapping: A Review', *Journal of the Indian Society of Remote Sensing*, 49(8), pp. 1997–2017. Available at: https://doi.org/10.1007/s12524-021-01366-x.

Dey, S. and Merwade, V. (2020) '1D HEC-RAS Model Development using RAS-Mapper', *Lyles School of Civil Engineering, Purdue University* [Preprint].

Dilmore Robert and Zhang, L. (2018) 'Greenhouse Gases and Their Role in Climate Change', in V. Romanov (ed.) *Greenhouse Gases and Clay Minerals: Enlightening Down-to-Earth Road Map to Basic Science of Clay-Greenhouse Gas Interfaces*. Cham: Springer International Publishing, pp. 15–32. Available at: https://doi.org/10.1007/978-3-319-12661-6_2.

DJI (2018) *MAVIC 2 Specs*. Available at: https://www.dji.com/uk/mavic-2/info (Accessed: 8 January 2025).

DJI Enterprise (2021) *Why aerial photogrammetry is the proper technique for surveying jobs*.

Dowman, I. (2004) 'Integration of LiDAR and IFSAR for mapping', *International Archives of Photogrammetry and Remote Sensing*, 35.

Earl, E. *et al.* (2023) 'Spatially Optimising Natural Flood Management Approaches across Catchments', in *HWRS2023: Hydrology & Water Resources Symposium*. Sydney: Engineers Australia. Available at: https://search.informit.org/doi/10.3316/informit.T2024051500006491344292804.

Environment Agency (2024a) *National LIDAR Programme*. Available at: https://www.data.gov.uk/dataset/f0db0249-f17b-4036-9e65-309148c97ce4/national-lidar-programme (Accessed: 7 January 2025).

Environment Agency (2024b) *Natural flood management programme*. Available at: https://www.gov.uk/guidance/natural-flood-management-programme#full-publication-update-history (Accessed: 12 November 2024).

Esri (2024a) *Flood Simulation Capabilities in ArcGIS Pro – Webinar Q&A*. Available at: https://community.esri.com/t5/water-resources-documents/webinar-resources-flood-simulation-capabilities-in/ta-p/1500132 (Accessed: 9 January 2025).

Esri (2024b) 'Flood Simulation in ArcGIS Pro 3.3'. Available at: https://www.esri.com/content/dam/esrisites/en-us/media/technical-papers/flood-simulation-arcgis-pro-3.3.pdf (Accessed: 9 January 2025).

ESRI (2024) *Flood Simulation in ArcGIS Pro 3.4*.

ESRI (no date a) *ArcGIS Overview*. Available at: https://www.esri.com/en-us/arcgis/products/arcgis-online/overview (Accessed: 22 October 2024).

Esri (no date) *Create a flood simulation scenario*. Available at: https://pro.arcgis.com/en/pro-app/latest/help/mapping/simulation/create-a-flood-simulation-scenario.htm (Accessed: 19 March 2025).

ESRI (no date b) *Create a flood simulation scenario*. Available at: https://pro.arcgis.com/en/pro-app/latest/help/mapping/simulation/create-a-flood-simulation-scenario.htm#:~:text=Note:,the%20Flood%20Simulation%20Cache%20heading.&text=in%20the%20Active%20group%20of%20the%20Simulation%20tab. (Accessed: 24 March 2025).

ESRI (no date c) *Flood Simulation*, *2024*. Available at: https://pro.arcgis.com/en/pro-app/latest/help/mapping/simulation/simulation-in-arcgis-pro.htm (Accessed: 24 March 2025).

FEMA (2019) *Water Surface Elevation Grids*, *RiskMAP*.

Ferguson, C. and Fenner, R. (2019) ‘Coupling dynamic top model and HEC-RAS to evaluate catchment scale natural flood management in the upper Calder’.

Greenfield, P. (2023) *Scotland considers annual laser scan to monitor health of forest and peatlands*, *The Guardian*.

Gupta, S.D. (2018) ‘Active and Passive Remote Sensing’.

Hall, J. *et al.* (2014) ‘Understanding flood regime changes in Europe: a state-of-the-art assessment’, *Hydrology and Earth System Sciences*, 18(7), pp. 2735–2772. Available at: https://doi.org/10.5194/hess-18-2735-2014.

Hashimoto, K. (2019) ‘Global Temperature and Atmospheric Carbon Dioxide Concentration’, in *Global Carbon Dioxide Recycling: For Global Sustainable Development by Renewable Energy*. Singapore: Springer Singapore, pp. 5–17. Available at: https://doi.org/10.1007/978-981-13-8584-1_3.

Hill, B. *et al.* (2023) ‘A systematic review of natural flood management modelling: Approaches, limitations, and potential solutions’, *Journal of Flood Risk Management*, 16(3), p. e12899. Available at: https://doi.org/https://doi.org/10.1111/jfr3.12899.

Hoskins, W.G. (1955) ‘The Making of the English Landscape’. Hodder Stoughton.

Huntington, T.G. (2006) ‘Evidence for intensification of the global water cycle: Review and synthesis’, *Journal of Hydrology*, 319(1), pp. 83–95. Available at: https://doi.org/https://doi.org/10.1016/j.jhydrol.2005.07.003.

IBM (2023) *Examples and uses of GIS*.

James M. Buttle Diana M. Allen, D.C.B.D.M.H.D.L.P.J.W.P.S.S.A.S.-H. and Whitfield, P.H. (2016) ‘Flood processes in Canada: Regional and special aspects’, *Canadian Water Resources Journal / Revue canadienne des ressources hydriques*, 41(1–2), pp. 7–30. Available at: https://doi.org/10.1080/07011784.2015.1131629.

Johnson, E.D. and Cowen, E.A. (2017) ‘Estimating bed shear stress from remotely measured surface turbulent dissipation fields in open channel flows’, *Water Resources Research*, 53(3), pp. 1982–1996. Available at: https://doi.org/https://doi.org/10.1002/2016WR018898.

Jouav (2024) *LiDAR vs. Photogrammetry: The Ultimate Showdown for 3D Mapping (2024)*. Available at: https://www.jouav.com/blog/lidar-vs-photogrammetry.html (Accessed: 8 January 2025).

Kabite, G. (2017) ‘LiDAR DEM Data for Flood Mapping and Assessment; Opportunities and Challenges: A Review’, *Journal of Remote Sensing & GIS*, 06. Available at: https://doi.org/10.4172/2469-4134.1000211.

Kew, S.M.M.R.C.P.J.M.E.V.M.A.A.P.J.L.F.C.O.C.B.P.I.B.C.P.S.O.F.W.E.B.L.T.E.S.R.M.A. (2024) *Autumn and Winter storms over UK and Ireland are becoming wetter due to climate change*.

Khanal, M. *et al.* (2020) ‘Accuracy Comparison of Aerial Lidar, Mobile-Terrestrial Lidar, and UAV Photogrammetric Capture Data Elevations over Different Terrain Types’, *Infrastructures*, 5(8). Available at: https://doi.org/10.3390/infrastructures5080065.

Kucharczyk, M., Hugenholtz, C.H. and Zou, X. (2018) ‘UAV–LiDAR accuracy in vegetated terrain’, *Journal of Unmanned Vehicle Systems*, 6(4), pp. 212–234. Available at: https://doi.org/10.1139/juvs-2017-0030.

Lee, J. *et al.* (2020) ‘Water-related disasters and their health impacts: A global review’, *Progress in Disaster Science*, 8, p. 100123. Available at: https://doi.org/https://doi.org/10.1016/j.pdisas.2020.100123.

Leitão, J. (2016) *Effects of merging Digital Elevation Models on flood modelling results*.

Loughborough University (2002) *3. Fluid Dynamics*. Available at: https://learn.lboro.ac.uk/pluginfile.php/504741/mod_resource/content/1/Fluid_Mechanics_3.pdf (Accessed: 20 March 2025).

Moreira, A. *et al.* (2013) ‘A tutorial on synthetic aperture radar’, *IEEE Geoscience and Remote Sensing Magazine*, 1(1), pp. 6–43. Available at: https://doi.org/10.1109/MGRS.2013.2248301.

Muhadi, N.A. *et al.* (2020) ‘The Use of LiDAR-Derived DEM in Flood Applications: A Review’, *Remote. Sens.*, 12, p. 2308. Available at: https://api.semanticscholar.org/CorpusID:220872853.

Munawar, H.S., Hammad, A.W.A. and Waller, S.T. (2022) ‘Remote Sensing Methods for Flood Prediction: A Review’, *Sensors*, 22(3). Available at: https://doi.org/10.3390/s22030960.

NASA (2015) *Landsat Benefited U.S. Economy by $1.8 Billion in 2011*.

NASA (2021) *Active Instruments*.

NRFA (no date) *18002 - Devon at Glenochil*. Available at: https://nrfa.ceh.ac.uk/data/station/spatial/18002 (Accessed: 9 January 2025).

Ongdas, N. *et al.* (2020) 'Application of HEC-RAS (2D) for Flood Hazard Maps Generation for Yesil (Ishim) River in Kazakhstan', *Water*, 12(10). Available at: https://doi.org/10.3390/w12102672.

Over, J.-S.R. *et al.* (2021) *Processing coastal imagery with Agisoft Metashape Professional Edition, version 1.6—Structure from motion workflow documentation*. US Geological Survey. Available at: https://essay.utwente.nl/85192/1/85192_Sakala.pdf#page=67.10 (Accessed: 21 March 2025).

Pasiok, R. and Giudiceandrea, A. (2023) *Serval*. Available at: https://github.com/lutraconsulting/serval/tree/master (Accessed: 24 January 2025).

Patti, V. (2024) *Flood Simulation Capabilities in ArcGIS Pro*.

Polat, N., Memduhoğlu, A. and Kaya, Y. (2023) 'Evaluating the ground point classification performance of Agisoft Metashape Software', *7th Intercontinental Geoinformation Days* [Preprint]. Available at: https://publish.mersin.edu.tr/index.php/igd/article/view/1461 (Accessed: 21 March 2025).

Ponce, M. (Professor) (2005) *STEADY VS UNSTEADY FLOW WITH HEC-RAS*. Available at: https://ponce.sdsu.edu/legacy_tales_steady_unsteady_hec_ras.html#:~:text=The%20model%20calculates%20discharges%20and,the%20variabilities%20of%20the%20flow. (Accessed: 20 March 2025).

Purseglove, J. (1988) *Taming the flood: a history and natural history of rivers and wetlands*. Oxford University Press Oxford.

QGIS (no date) *Members and Donors* . Available at: https://www.qgis.org/funding/membership/members/ (Accessed: 9 January 2025).

Ranasinghe, R. (2022) 'Climate change 2021: Summary for all'.

Renslow, M., Greenfield, P. and Guay, T. (2000) 'Evaluation of multi-return LIDAR for forestry applications', *US Department of Agriculture Forest Service-Engineering, Remote Sensing Applications. http://www. ndep. gov/USDAFS/LIDAR. pdf [Consulta: 12 de marzo de 2009]* [Preprint].

Sakala, K. (2020) *Compare UAV laser and image data for flood modelling*. University of Twente.

Sánchez, A. (2022) *1D vs 2D Unsteady Flow Modeling*. Available at: https://www.hec.usace.army.mil/confluence/rasdocs/rastraining/files/6.6/217581413/217581482/1/1729729905823/2.9+1D+vs+2D+Modeling.pdf (Accessed: 20 March 2025).

Saylam, K. (2009) 'Quality assurance of lidar systems–mission planning', in *ASPRS 2009 Annual*

Conference, pp. 9–13.

SCHANZE, J. (2006) 'FLOOD RISK MANAGEMENT – A BASIC FRAMEWORK', in E. and M.J. Schanze Jochen and Zeman (ed.) *Flood Risk Management: Hazards, Vulnerability and Mitigation Measures*. Dordrecht: Springer Netherlands, pp. 1–20.

Schenk, T. (2005) 'Introduction to photogrammetry', *The Ohio State University, Columbus*, 106(1), p. 1.

Scottish Government (2024a) 'Our Reference: 202400434963'. Edinburgh.

Scottish Government (2024b) 'Our Reference: 202400434963'. Edinburgh.

SEPA (2016) *Natural Flood Management Handbook*. Available at: https://www.sepa.org.uk/media/163560/sepa-natural-flood-management-handbook1.pdf (Accessed: 12 November 2024).

SEPA (2022) *Technical Flood Risk Guidance for Stakeholders*. Available at: https://www.sepa.org.uk/media/162602/ss-nfr-p-002-technical-flood-risk-guidance-for-stakeholders.pdf (Accessed: 20 March 2025).

Snyder, C.W., Mastrandrea, M.D. and Schneider, S.H. (2011) 'The Complex Dyanmics of the Climate System: Constraints on our Knowledge, Policy Implications and the Necessity of Systems Thinking', in C. Hooker (ed.) *Philosophy of Complex Systems*. Amsterdam: North-Holland (Handbook of the Philosophy of Science), pp. 467–505. Available at: https://doi.org/https://doi.org/10.1016/B978-0-444-52076-0.50017-1.

Supratman, M. *et al.* (2024) 'Flood Hazard Assessment Due to Changes in Land Use and Cover', *Civil Engineering Journal*, 10, pp. 3874–3891. Available at: https://doi.org/10.28991/CEJ-2024-010-12-04.

Thaler, T. *et al.* (2023) 'Natural flood management: Opportunities to implement nature-based solutions on privately owned land', *WIREs Water*, 10(3), p. e1637. Available at: https://doi.org/https://doi.org/10.1002/wat2.1637.

Tweed Forum (2022) *Eddleston Water 2021 Report* . Available at: https://tweedforum.org/wp-content/uploads/2023/02/Eddleston-Water-2021-Report.pdf (Accessed: 12 November 2024).

Ullah, M.I. *et al.* (2024) 'Advanced floodplain mapping: HEC-RAS and ArcGIS pro application on Swat River', *Journal of Umm Al-Qura University for Engineering and Architecture*, 15(3), pp. 245–258. Available at: https://doi.org/10.1007/s43995-024-00054-4.

Umer, Y. *et al.* (2025) 'Nature-Based Solutions for River Restoration and Flow Management: The Case of Kitwe City, Zambia', in Dr.C. Guo (ed.) *River Basin Management*. Rijeka: IntechOpen. Available at: https://doi.org/10.5772/intechopen.1007632.

University of Reading (2019) *What is Natural Flood Management?*

US Army Corps of Engineers (2024a) *HEC-RAS 6.6*.

US Army Corps of Engineers (2024b) *HEC-RAS FEATURES*. Available at: https://www.hec.usace.army.mil/software/hec-ras/features.aspx (Accessed: 9 January 2025).

US Government (2022) *GPS Accuracy*.

USACE (no date a) *1D Steady Flow*. Available at: https://www.hec.usace.army.mil/confluence/rasdocs/hgt/latest/tutorials/1d-steady-flow (Accessed: 28 February 2025).

USACE (no date b) 'Creating Land Cover, Manning's n values, and % Impervious Layers'. Available at: https://www.hec.usace.army.mil/confluence/rasdocs/r2dum/latest/developing-a-terrain-model-and-geospatial-layers/creating-land-cover-mannings-n-values-and-impervious-layers (Accessed: 20 March 2025).

Vitousek, S. *et al.* (2017) 'Doubling of coastal flooding frequency within decades due to sea-level rise', *Scientific Reports*, 7(1), p. 1399. Available at: https://doi.org/10.1038/s41598-017-01362-7.

Wandinger, U. (2005) 'Introduction to lidar', in *Lidar: range-resolved optical remote sensing of the atmosphere*. Springer, pp. 1–18.

Wasser, L. (2024) *The Basics of LiDAR - Light Detection and Ranging - Remote Sensing*, *NEON Science*. Available at: https://www.neonscience.org/resources/learning-hub/tutorials/lidar-basics#:~:text=How%20Light%20Energy%20Is%20Used,from%20one%20pulse%20of%20light. (Accessed: 29 January 2025).

Welsh Government (2023) *LiDAR viewer*. Available at: https://datamap.gov.wales/maps/lidar-viewer/ (Accessed: 7 January 2025).

Werritty, A. (2006) 'Sustainable flood management: oxymoron or new paradigm?', *Area*, 38(1), pp. 16–23. Available at: https://doi.org/https://doi.org/10.1111/j.1475-4762.2006.00658.x.

Whatmore, S.J. and Landström, C. (2010) 'Manning's N: Putting roughness to work', *How well do facts travel*, pp. 111–135.

WHS (2025a) *LowFlows2*. Available at: https://www.hydrosolutions.co.uk/software/lowflows2/ (Accessed: 20 March 2025).

WHS (2025b) *ReFH 2*. Available at: https://www.hydrosolutions.co.uk/software/refh-2/ (Accessed: 20 March 2025).

WHS (2025c) *WINFAP 5*.

Williamson, R. (2024) *River Devon Restoration Optioneering & Design FINAL Report*.

Wingfield, T. *et al.* (2019) ‘Natural Flood Management: Beyond the evidence debate’, *Area*, 51(4), pp. 743–751. Available at: https://doi.org/https://doi.org/10.1111/area.12535.

Wu, X. *et al.* (2023) ‘A Near-Real-Time Flood Detection Method Based on Deep Learning and SAR Images’, *Remote Sensing*, 15(8). Available at: https://doi.org/10.3390/rs15082046.

Yalcin, E. (2020) ‘Assessing the impact of topography and land cover data resolutions on two-dimensional HEC-RAS hydrodynamic model simulations for urban flood hazard analysis’, *Natural Hazards*, 101(3), pp. 995–1017. Available at: https://doi.org/10.1007/s11069-020-03906-z.

Yeong, A. (2016) *Q2(a) Differentiate between hydrologic model and hydraulic model*. Available at: https://www.academia.edu/24385764/Q2_a_Differentiate_between_hydrologic_model_and_hydraulic_model (Accessed: 9 January 2025).

Yodono Garcia, M. and Oliveira, H. (2020) ‘THE INFLUENCE OF GROUND CONTROL POINTS CONFIGURATION AND CAMERA CALIBRATION FOR DTM AND ORTHOMOSAIC GENERATION USING IMAGERY OBTAINED FROM A LOW-COST UAV’, *ISPRS Annals of Photogrammetry, Remote Sensing and Spatial Information Sciences*, V-1–2020, pp. 239–244. Available at: https://doi.org/10.5194/isprs-annals-V-1-2020-239-2020.

Zahirieh, S. (2019) *A comparison of hydraulic modeling results between unmanned aerial vehicle with structure-from-motion and LIDAR produced digital elevation models*. Available at: https://mars.gmu.edu/items/0d904f46-9717-4a78-9456-24e9ef7a5cfe (Accessed: 25 March 2025).

Zainal, N.N. and Abu Talib, S.H. (2024) ‘Review paper on applications of the HEC-RAS model for flooding, agriculture, and water quality simulation’, *Water Practice and Technology*, 19(7), pp. 2883–2900. Available at: https://doi.org/10.2166/wpt.2024.173.

Zhou, Q. (2017) ‘Digital Elevation Model and Digital Surface Model’, in *International Encyclopedia of Geography*. John Wiley & Sons, Ltd, pp. 1–17. Available at: https://doi.org/https://doi.org/10.1002/9781118786352.wbieg0768.

Appendix

Appendix 1 – Hydograph and Flow Rates

Table 23 - Hydograph and flow data for unsteady and steady models

2D Unsteady Flow	**100 year flood**	**20 year flood**	**2 year flood**
Model Date/Time	**Flow (m3/s)**	**Flow (m3/s)**	**Flow (m3/s)**
27/09/24 2400	0	0	0
28/09/24 0100	5.445	0.7	0.4
28/09/24 0200	10.889	2.1	0.8
28/09/24 0300	16.333	5.6	1.4
28/09/24 0400	21.778	6	1.6
28/09/24 0500	27.222	10	2
28/09/24 0600	32.667	12.6	2.4
28/09/24 0700	38.111	16.1	2.8
28/09/24 0800	43.555	16.8	3.5
28/09/24 0900	49	17	4.2
28/09/24 1000	54	17.85	4.9
28/09/24 1100	49	18	7
28/09/24 1200	45.231	17.5	8.4
28/09/24 1300	41.462	17.5	8.5
28/09/24 1400	37.692	16.8	9.2
28/09/24 1500	33.923	15.992	8.5
28/09/24 1600	30.154	14.216	8
28/09/24 1700	26.384	10.5	7
28/09/24 1800	22.616	9.1	5.25
28/09/24 1900	18.846	6.3	4.55
28/09/24 2000	15.077	4.9	3.15
28/09/24 2100	11.308	2.8	1.68
28/09/24 2200	7.538	2.1	1.4
28/09/24 2300	3.77	0.7	0.4
28/09/24 2400	0	0	0
1D Unsteady Flow	**100 year flood**	**20 year flood**	**2 year flood**
	Flow (m3/s)	**Flow (m3/s)**	**Flow (m3/s)**
	151.6	79.8	48

Appendix 2 – Model Register

Model	Application	1D / 2D	Data	Cell Size	No of Cells	Mannings 'n' Roughness	Slope	Computation Interval	Flow	Flood Extent
L0001	HEC-RAS	2D	LiDAR	10x10	7611	0.06	0.001164	1 minute	Unsteady	100yr
L0002	HEC-RAS	2D	LiDAR	5x5	30652	0.06	0.001164	1 minute	Unsteady	100yr
L0003	HEC-RAS	2D	LiDAR	3x3	[illegible]	0.06	0.001164	1 minute	Unsteady	100yr
L0004	HEC-RAS	2D	LiDAR	2x2	[illegible]	0.06	0.001164	1 minute	Unsteady	100yr
L0005	HEC-RAS	2D	LiDAR	1x1	[illegible]	0.06	0.001164	1 minute	Unsteady	100yr
L0006	HEC-RAS	2D	LiDAR	2x2	[illegible]	0.045	0.001164	1 minute	Unsteady	100yr
L0007	HEC-RAS	2D	LiDAR	2x2	[illegible]	0.05	0.001164	1 minute	Unsteady	100yr
[illegible]	HEC-RAS	2D	LiDAR	2x2	[illegible]	[illegible]	0.001164	1 minute	Unsteady	100yr
[illegible]	HEC-RAS	2D	LiDAR	2x2	[illegible]	0.06	0.001164	1 minute	Unsteady	20yr
L0010	HEC-RAS	2D	LiDAR	2x2	[illegible]	0.06	0.001164	1 minute	Unsteady	2yr
L0011	HEC-RAS	2D	LiDAR	2x2	[illegible]	0.06	0.001164	3 minutes	Unsteady	100yr
L0012	HEC-RAS	2D	LiDAR	2x2	[illegible]	0.06	0.001164	2 minutes	Unsteady	100yr
L0013	HEC-RAS	2D	LiDAR	2x2	[illegible]	0.06	0.001164	0.5 minutes	Unsteady	100yr
L0014	HEC-RAS	2D	LiDAR	2x2	[illegible]	0.06	0.001164	1 minute	Unsteady	100yr
L0015	HEC-RAS	2D	LiDAR	1x1	[illegible]	0.06	0.001164	0.5 minutes	Unsteady	100yr
L0016	HEC-RAS	2D	LiDAR	2x2	[illegible]	0.06	0.001164	0.5 minutes	Unsteady	100yr
L0017	HEC-RAS	2D	LiDAR	1x1	[illegible]	0.06	0.001164	0.5 minutes	Unsteady	20yr
[illegible]	HEC-RAS	2D	LiDAR	1x1	[illegible]	0.06	0.001164	0.5 minutes	Unsteady	2yr
P0001	HEC-RAS	2D	Photogrammetry	2x2	[illegible]	0.06	[illegible]	1 minutute	Unsteady	100yr
P0002	HEC-RAS	2D	Photogrammetry	2x2	[illegible]	0.06	[illegible]	1 minutute	Unsteady	20yr
P0003	HEC-RAS	2D	Photogrammetry	2x2	[illegible]	0.06	[illegible]	1 minutute	Unsteady	2yr
[illegible]	HEC-RAS	1D	LiDAR	N/A	N/A	0.06 | 0.45 | 0.06	0.001164	N/A	Steady	100yr (151.6 m3/s)
L0020	HEC-RAS	1D	LiDAR	N/A	N/A	0.06 | 0.45 | 0.06	0.001164	N/A	Steady	20yr ([illegible] m3/s)
L0021	HEC-RAS	1D	LiDAR	N/A	N/A	0.06 | 0.45 | 0.06	0.001164	N/A	Steady	2yr ([illegible] m3/s)
P0004	HEC-RAS	1D	Photogrammetry	N/A	N/A	0.06 | 0.45 | 0.06	0.001164	N/A	Steady	100yr (151.6 m3/s)
P0005	HEC-RAS	1D	Photogrammetry	N/A	N/A	0.06 | 0.45 | 0.06	0.001164	N/A	Steady	20yr ([illegible] m3/s)
P0006	HEC-RAS	1D	Photogrammetry	N/A	N/A	0.06 | 0.45 | 0.06	0.001164	N/A	Steady	2yr ([illegible] m3/s)
L0022	ArcGIS Pro	2D	LiDAR	0.405m	N/A	N/A	N/A	N/A	Unsteady	100yr
L0023	ArcGIS Pro	2D	LiDAR	0.405m	N/A	N/A	N/A	N/A	Unsteady	20yr
L0024	ArcGIS Pro	2D	LiDAR	0.405m	N/A	N/A	N/A	N/A	Unsteady	2yr
P0007	ArcGIS Pro	2D	Photogrammetry	0.405m	N/A	N/A	N/A	N/A	Unsteady	100yr
[illegible]	ArcGIS Pro	2D	Photogrammetry	0.405m	N/A	N/A	N/A	N/A	Unsteady	20yr
[illegible]	ArcGIS Pro	2D	Photogrammetry	0.405m	N/A	N/A	N/A	N/A	Unsteady	2yr

Model	Downstream Maximum Flow (cms)	Downstream Volume 1000 (m3)	Total Area Flooded (m2)	WSE Volume (m3)	WSE Minimum (m)	WSE Maximum (m)	WSE Mean (m)	Depth Minimum (m)	Depth Maximum (m)	Depth Mean (m)	Time to run
L0001	47.1	[illegible]	[illegible]	[illegible]	[illegible]	[illegible]	17.24	[illegible]	[illegible]	0.612	[illegible]
L0002	66.24	[illegible]	[illegible]	11252271.2	[illegible]	[illegible]	17.762	[illegible]	[illegible]	1.035	[illegible]
L0003	127.15	[illegible]	[illegible]	[illegible]	17.34	[illegible]	[illegible]	0.001	4.702	[illegible]	[illegible]
L0004	151.52	[illegible]	[illegible]	[illegible]	[illegible]	[illegible]	[illegible]	0.001	5.614	[illegible]	[illegible]
L0005	No data	No data	No data	No data	No data	No data	No data	No data	No data	No data	45m 12s
L0006	[illegible]	2462.62	716237.75	[illegible]	[illegible]	[illegible]	[illegible]	[illegible]	[illegible]	[illegible]	15m 01s
L0007	[illegible]	[illegible]	716253.75	[illegible]	[illegible]	[illegible]	[illegible]	0.001	5.611	[illegible]	[illegible]
[illegible]	[illegible]	[illegible]	[illegible]	[illegible]	[illegible]	[illegible]	[illegible]	0.001	5.616	[illegible]	[illegible]
[illegible]	[illegible]	[illegible]	[illegible]	[illegible]	[illegible]	[illegible]	[illegible]	0.001	4.266	1.572	11m 00s
L0010	[illegible]	[illegible]	533210	[illegible]	[illegible]	[illegible]	17.354	[illegible]	3.405	[illegible]	[illegible]
L0011	No data	No data	No data	No data	No data	No data	No data	No data	No data	No data	2m 33s
L0012	No data	No data	No data	No data	No data	No data	No data	No data	No data	No data	5m 20s
L0013	[illegible]	[illegible]	No data	No data	No data	No data	No data	No data	No data	No data	[illegible]
L0014	151.52	[illegible]	[illegible]	[illegible]	[illegible]	[illegible]	[illegible]	0.001	5.615	[illegible]	[illegible]
L0015	[illegible]	[illegible]	716523	[illegible]	[illegible]	[illegible]	[illegible]	0.001	5.625	[illegible]	2hrs 03m
L0016	[illegible]	[illegible]	No data	No data	No data	No data	No data	No data	No data	No data	30m 41s
L0017	[illegible]	[illegible]	[illegible]	[illegible]	[illegible]	[illegible]	[illegible]	0.001	4.273	1.576	1hr 32m
[illegible]	50.16	342.64	532557.5	[illegible]	[illegible]	[illegible]	17.355	[illegible]	3.403	[illegible]	1hr 13m
P0001	161.51	2437.42	[illegible]	[illegible]	[illegible]	[illegible]	[illegible]	0.001	[illegible]	2.605	[illegible]
P0002	70.33	[illegible]	[illegible]	[illegible]	[illegible]	[illegible]	17.6	0.001	12.657	[illegible]	12m 35s
P0003	31.31	[illegible]	[illegible]	[illegible]	16.077	17.65	16.737	[illegible]	6.426	[illegible]	10m 26s
[illegible]	No data	No data	613156.5	[illegible]	[illegible]	[illegible]	17.613	0.001	3.11	[illegible]	1s
L0020	No data	No data	[illegible]	[illegible]	[illegible]	[illegible]	17.247	[illegible]	[illegible]	[illegible]	1s
L0021	No data	No data	431534.75	[illegible]	[illegible]	[illegible]	17.061	[illegible]	2.341	0.452	1s
P0004	No data	No data	612262	[illegible]	[illegible]	[illegible]	17.607	[illegible]	6.061	1.506	1s
P0005	No data	No data	[illegible]	[illegible]	[illegible]	[illegible]	[illegible]	0.001	[illegible]	1.236	1s
P0006	No data	No data	[illegible]	[illegible]	[illegible]	[illegible]	17.016	0.001	5.307	1.046	1s
L0022	No data	No data	No data	No data	No data	No data	No data	-2.354	[illegible]	[illegible]	[illegible]
L0023	No data	No data	No data	No data	No data	No data	No data	[illegible]	3.677	[illegible]	42m
L0024	No data	No data	No data	No data	No data	No data	No data	-1.336	[illegible]	0.653	41m
P0007	No data	No data	No data	No data	No data	No data	No data	[illegible]	5.744	[illegible]	40m
[illegible]	No data	No data	No data	No data	No data	No data	No data	[illegible]	3.6	1.32	41m
[illegible]	No data	No data	No data	No data	No data	No data	No data	[illegible]	2.731	0.652	41m

An excel copy of the register can be opened from here > Compelted%20model%20register.xlsx

Appendix 3 – Ground Control Points (Expanded from Section 5.1)

Using the aerial image provided by FRT that was captured from a UAV, and utilising QGIS, a desk study of the site was conducted to identify 50 potential ground control points as seen on Figure 5. Chosen locations for ground control points were easily identifiable permanent and semi-permanent objects such as fence posts, gate posts and benches. Points were picked to ensure distribution of GCP throughout entire site, paying close attention to ensure edges of the chosen study area had an adequate number of ground control points, and that the ground control points weren't confined to just the centre of the study area.

With a new QGIS project, GCPs were marked and the attribute table updated to include additional fields that may be required on the day of the field visit. This project was then synced to the Mergin Map cloud then synced offline to mobile phone which was then used to locate and tick off collected GCP on the day. An example of Mergin Maps android application can be seen in Figure 46

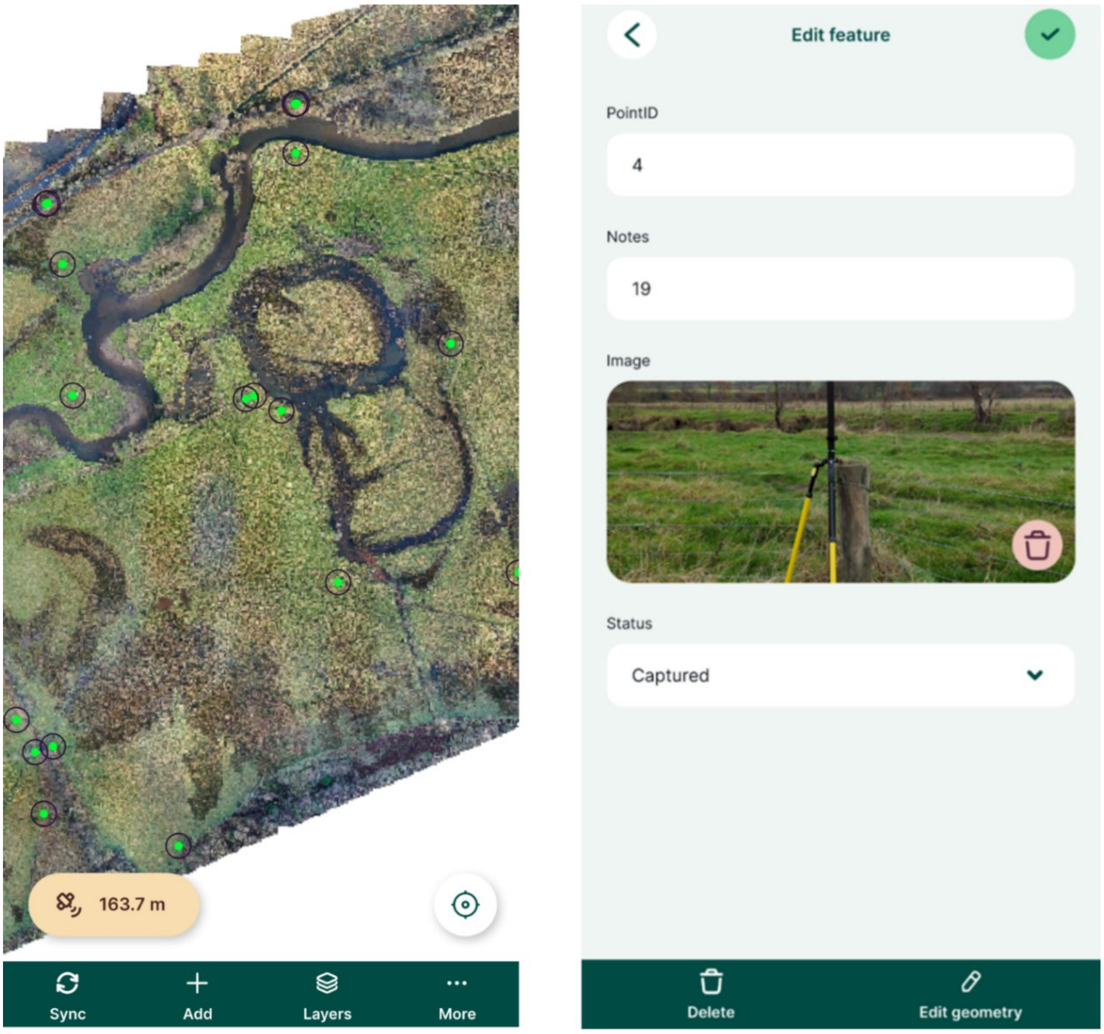

Figure 46 - Mergin Maps (Android) showing GCPs across whole site and individual feature settings

A dry day was picked for the field work to ensure maximum accuracy of the Global Navigation Satellite System (GNSS) equipment. The location of the Emlid RS+ GNSS base, depicted by the blue cross in Figure 5, was chosen due to centralised and accessible location and slightly higher ground. Utilising the telescopic legs and built-in spirit level on the SECO 5301 tripod, the Emlid base was levelled with the height of the base measured with the built-in tape measure as shown in Figure 47. Any relevant information was entered into the Emlid Android application once a successful connection to the base was established.

Figure 47 - Emlid RS+ GNSS base mounted on SECO 5301 tripod showing inbuilt tape measure

With the base correctly setup and a connection established between the base and receiver, the X & Y co-ordinates of each ground control point were collected, going in an anticlockwise direction from the Emlid base. A photograph was taken and uploaded of the Emlid receiver for each ground control point from either a north or south location (Ochil hills in the background meant the camera was facing North shown in Figure 48, Melloch or Lawmuir Woods in the background meant camera was facing South as shown in Figure 49). This was done to assist with orientation when doing the future Metashape post-processing work.

Figure 48 - Emlid GNSS receiver capturing GCP 01 with Ochil Hills in background

Figure 49 - Emlid GNSS receiver capturing GCP 49 with Melloch Woods in background

Appendix 4 – Metashape (Expanded from section 5.2)

Project setup, Photo Import and Photo Alignment

1) New Metashape project created with Co-ordinate System kept as default (WGS 84 ESPG::4326). Aerial photos of study area imported and aligned with following settings:

-Accuracy: High,
-Pair selection: Reference,
-Key point limit: 60,000,
-Tie point limit: 0,
-Everything else: default.

Camera Calibration tool was then used to extract information like pixel size, shutter speed and ISO which can be seen in Figure 50.

2) The quality of each individual aerial photograph was checked using “Estimate Image Quality” for all images. (Note: image quality result of 1 is best, with USGS recommending anything under 0.7 being removed if photo overlap allows so.) Example of results can be seen in Figure 50.

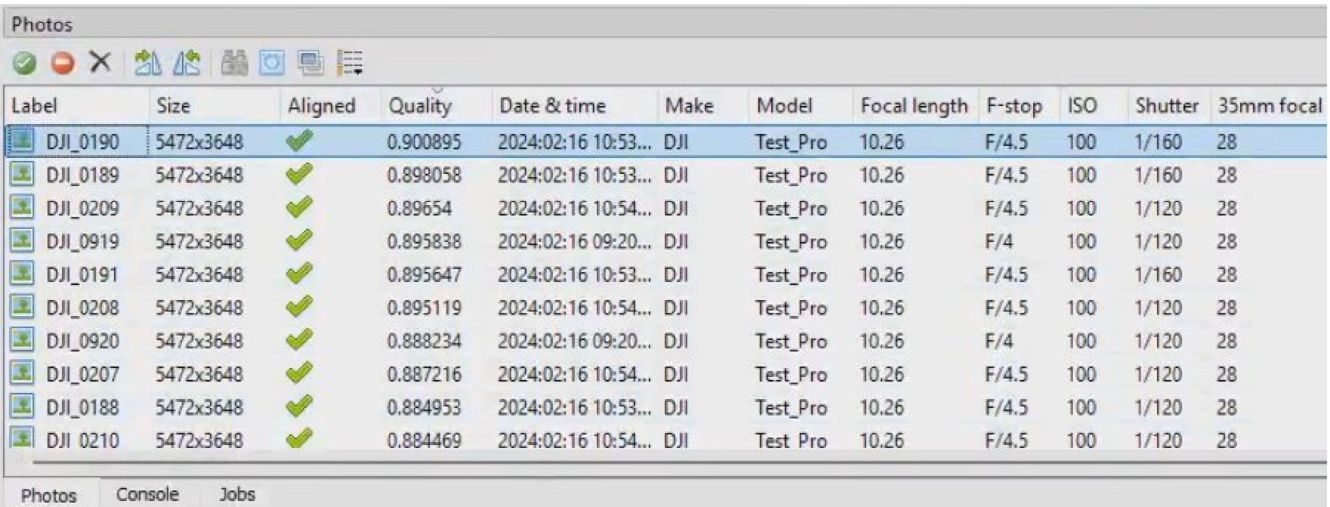
Photos

Label	Size	Aligned	Quality	Date & time	Make	Model	Focal length	F-stop	ISO	Shutter	35mm focal
DJI_0190	5472x3648	✓	0.900895	2024:02:16 10:53...	DJI	Test_Pro	10.26	F/4.5	100	1/160	28
DJI_0189	5472x3648	✓	0.898058	2024:02:16 10:53...	DJI	Test_Pro	10.26	F/4.5	100	1/160	28
DJI_0209	5472x3648	✓	0.89654	2024:02:16 10:54...	DJI	Test_Pro	10.26	F/4.5	100	1/120	28
DJI_0919	5472x3648	✓	0.895838	2024:02:16 09:20...	DJI	Test_Pro	10.26	F/4	100	1/120	28
DJI_0191	5472x3648	✓	0.895647	2024:02:16 10:53...	DJI	Test_Pro	10.26	F/4.5	100	1/160	28
DJI_0208	5472x3648	✓	0.895119	2024:02:16 10:54...	DJI	Test_Pro	10.26	F/4.5	100	1/120	28
DJI_0920	5472x3648	✓	0.888234	2024:02:16 09:20...	DJI	Test_Pro	10.26	F/4	100	1/120	28
DJI_0207	5472x3648	✓	0.887216	2024:02:16 10:54...	DJI	Test_Pro	10.26	F/4.5	100	1/120	28
DJI_0188	5472x3648	✓	0.884953	2024:02:16 10:53...	DJI	Test_Pro	10.26	F/4.5	100	1/120	28
DJI_0210	5472x3648	✓	0.884469	2024:02:16 10:54...	DJI	Test_Pro	10.26	F/4.5	100	1/120	28

Photos Console Jobs

Figure 50 - Examples of extracted EXIF information and estimated image quality

Optimising Photo Alignment

1) Optimising photo alignment was done to correct camera lens distortion using following settings: Camera accuracy (m): 10 with all other options left as default (Camera accuracy (deg): 2, Marker accuracy (m): 0.10, Scale bar accuracy (m): 0.001, Marker accuracy (pix): 0.1, Tie point accuracy (pix): 1)

2) “Optimise Camera Alignment” was completed and the following options were selected: f, cx cy, k1, k2, k3, p1 and p2. After Optimization completed the results can be checked by clicking on the Reference tab and looking at the Projections and Error (pix) column. (Note: USGS best practice recommends that the number of Projections doesn’t go below 100 and the goal for error (pixel) is 0.3 or below). A selection of photographs and results shown in Reference can be seen in Figure 51.

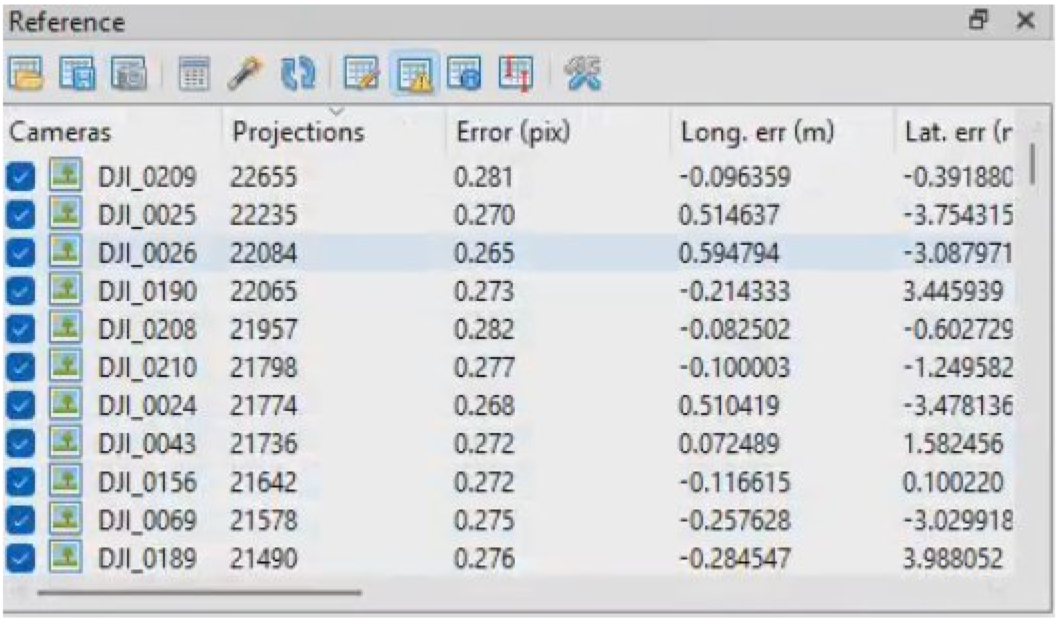

Cameras	Projections	Error (pix)	Long. err (m)	Lat. err (r
DJI_0209	22655	0.281	-0.096359	-0.391880
DJI_0025	22235	0.270	0.514637	-3.754315
DJI_0026	22084	0.265	0.594794	-3.087971
DJI_0190	22065	0.273	-0.214333	3.445939
DJI_0208	21957	0.282	-0.082502	-0.602729
DJI_0210	21798	0.277	-0.100003	-1.249582
DJI_0024	21774	0.268	0.510419	-3.478136
DJI_0043	21736	0.272	0.072489	1.582456
DJI_0156	21642	0.272	-0.116615	0.100220
DJI_0069	21578	0.275	-0.257628	-3.029918
DJI_0189	21490	0.276	-0.284547	3.988052

Figure 51 - Reference tab, projections and error (pix) examples

Error Reduction

1) Error reduction was done to removes bad points due to poor geometry, pixel matching and pixel residual errors. Geometry - From “Model”, “Gradual Selection” was selected with “Reconstruction Uncertainty” selected from the dropdown box. After this process completed, 10 was entered as the Level before clicking OK. Selected points were deleted and image optimisation was re-ran (Section 6.2.2).

2) Pixel Matching Errors - From “Model”, “Gradual Selection” was selected with “Projection Accuracy” selected from the dropdown box. 3.0 was entered as the Level before clicking OK. Selected points were deleted and image optimisation was re-ran (Section 6.2.2).

3) Pixel Residual Errors – “Reference Settings” was selected after right clicking the latest Workspace. Marker accuracy (pix) was set to 0.5 and Tie point accuracy (pix) set to 0.3. Image

optimisation re-ran.

Control Points (Markers)

1) GCPs collected from the field work (Section 6.1) were imported into the Metashape project by right-clicking on the Workspace and selecting “Import Reference” with the following settings:
-Coordinate System – WGS 84 (EPSG::4326)
-Delimiter set to Tab.
-Columns: Label: column 3, Longitude: column 4, Latitude: column 5 and Altitude: column 6.

2) GCP locations were manually corrected by using “Filter Photos By Markers” then manually moving the GCP to correct location. Figure 52 shows the GCP before and Figure 53 shows the after manual correction. This was repeated for all 49 markers and 820 photographs.

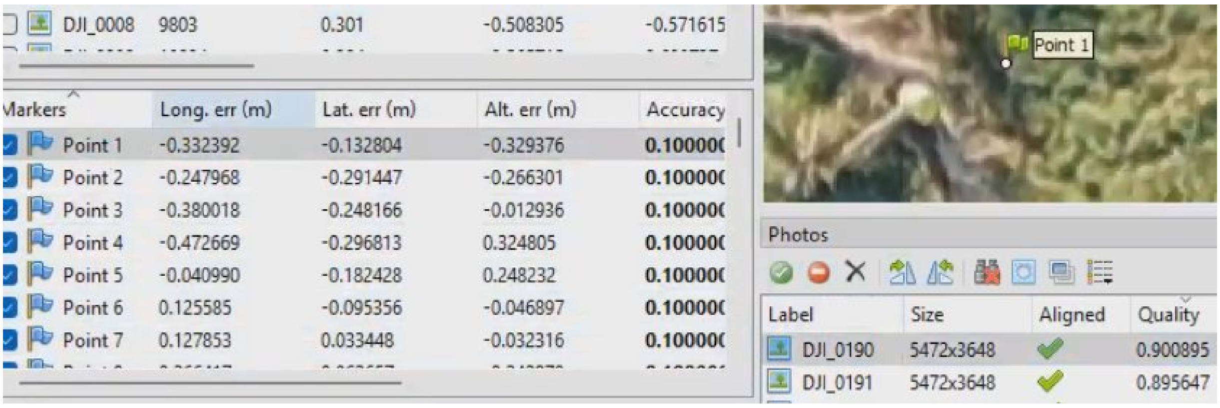

Figure 52 - Manually moving Point 1 to correct location (before)

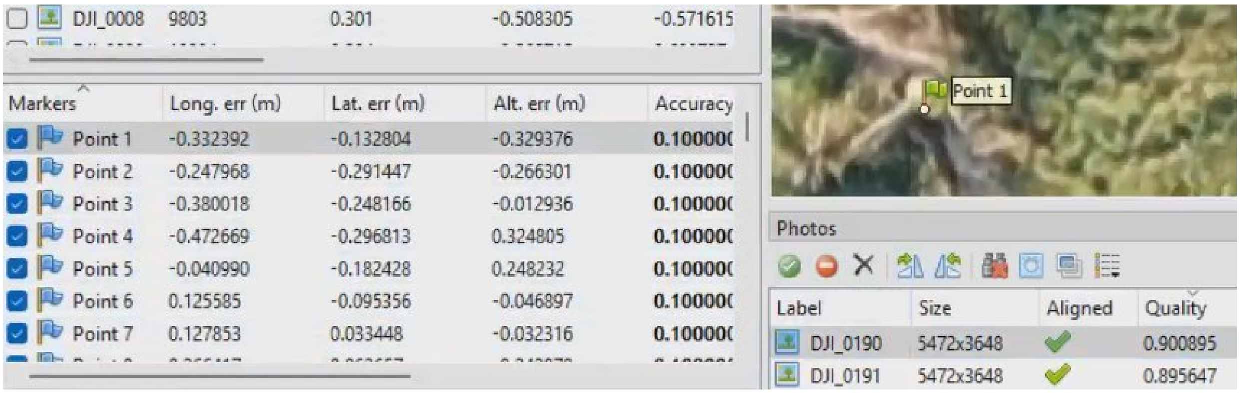

Figure 53 - Manually moving Point 1 to correct location (after)

3) “Optimize Camera Alignment” tool was then ran using default settings. Once completed the results were sorted by Error (pix). 13 ground control points were selected (6, 16, 18, 20, 23, 27, 28, 29, 36, 38, 46, 47, 50) striking a balance between their location within the study area aiming for a wide spread, Error (pix) being preferably under or as close to 5.0 and Error (m) being as close to 0.5. “Optimize Camera Alignment” tool was ran again using default settings.

4) “Gradual Selection” tool was opened, “Reprojection Error” was selected from the Criterion dropdown and the Level set to 0.3. After completion the highlighted points were deleted and the “Optimize Camera Alignment” tool was ran again using default settings. These steps were repeated a further 4 times.

5) “Classify Ground Points” was ran with the following Parameters used: Max Angle (^{o}): 10.0, Max Distance (m): 1, Max Terrain Slope (deg): 10.0, Cell Size (m) 22.

Building Dense Point Cloud, DEM and Orthomosaic

1) “Build Point Cloud” was ran with following settings: Quality set to High from the dropdown box and Depth Filtering kept as Mild (default).

2) “Build DEM” was ran with following settings: Point Classes changed from All to Created (never classified) and Ground. After completion DSM was exported (Coordinate System changed to ESPG::27700 with all other options remaining as the default.)

3) “Build DEM” was ran with following settings: Point Classes changed from All to only Ground. After completion DTM was exported (Coordinate System changed to ESPG::27700 with all other options remaining as the default.)

4) “Build Orthomosaic” was ran. Projection was changed to ESPG::27700 with all other options remaining as the default. After completion Orthomosaic was exported.

Appendix 5 – DEM fixes/amendments (Expanded from Section 5.3)

1) The Serval plug-in automatically edits and overwrites the DEM file without prompting to save. Before starting this process, its good practice to copy the original DEM file and work on the copy. Serval plug-in was installed and a new QGIS project was created (CRS set to ESPG:27700) with the DEM copy imported (CRS set to ESPG:27700 and Symbology set to Hillshade).

2) Artefacts in the data that needed fixed were identified and fixed by selecting the Select Raster Cells by Polygon tool shown in Figure 54.

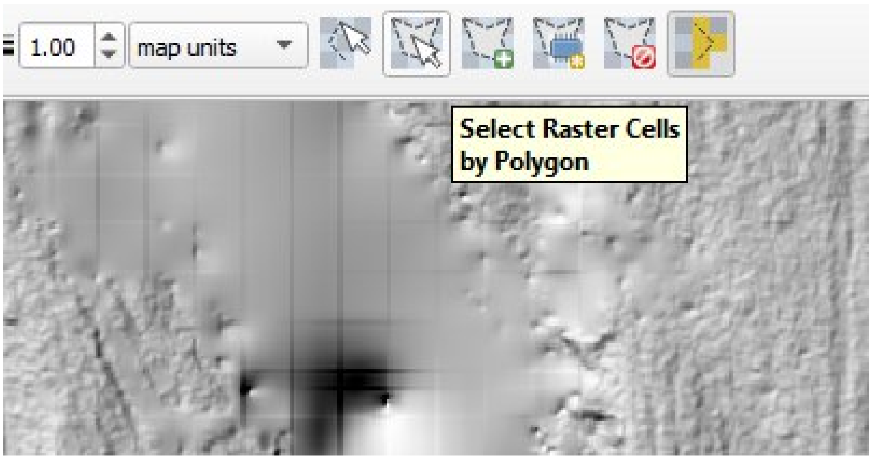

Figure 54 - Screenshot showing an artefact example and Serval toolbar

With the Polygon tool selected a Polygon was drawn round the artefact and the Raster Probe tool was selected shown in Figure 55

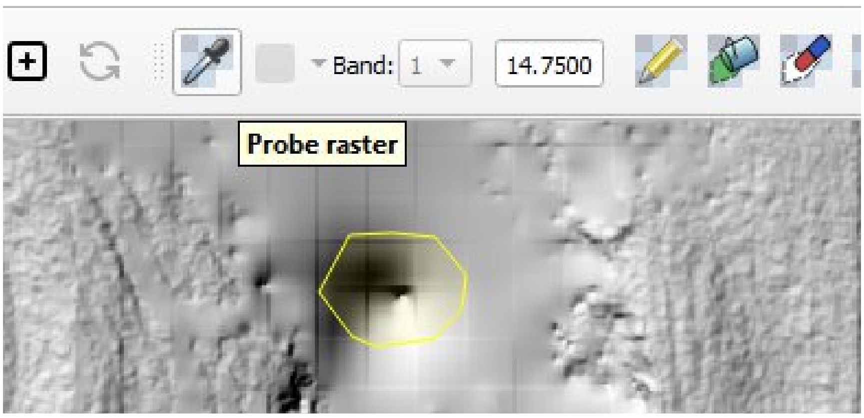

Figure 55 - Screenshot polygon around artefact and Serval Raster Probe tool

The Probe tool was used to identify the height of the area surrounding the Polygon with this entered into the text-field in the Serval tool bar then clicking Apply Value to Selection button (see Figure 56)

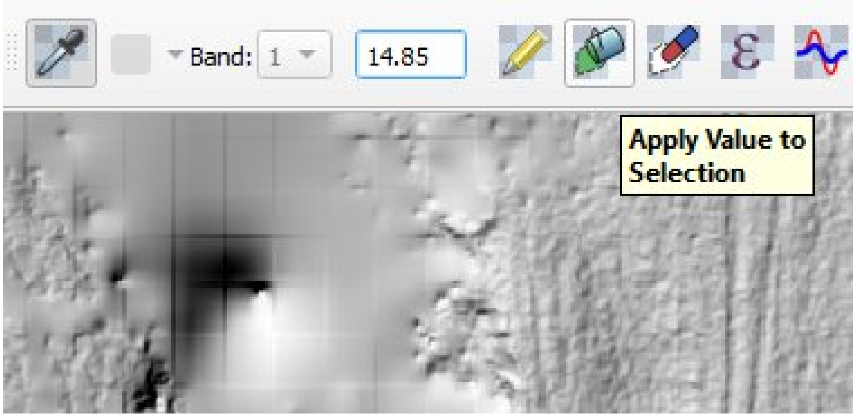

Figure 56 - Text-field for new height data and Apply button in Serval toolbar

3) The above steps were then repeated for all other artefacts including removing the bridge deck and in-filling the missing data from LiDAR set. While there is no official guidance on the number of polygons needed to be drawn, more polygons should result in more accurate data. Some small artefacts can be correctly with 1-4 polygons while larger amendments like bridge deck removal (Figure 57) and missing data correction (Figure 58) used 12 and 18 polygons as respectively.

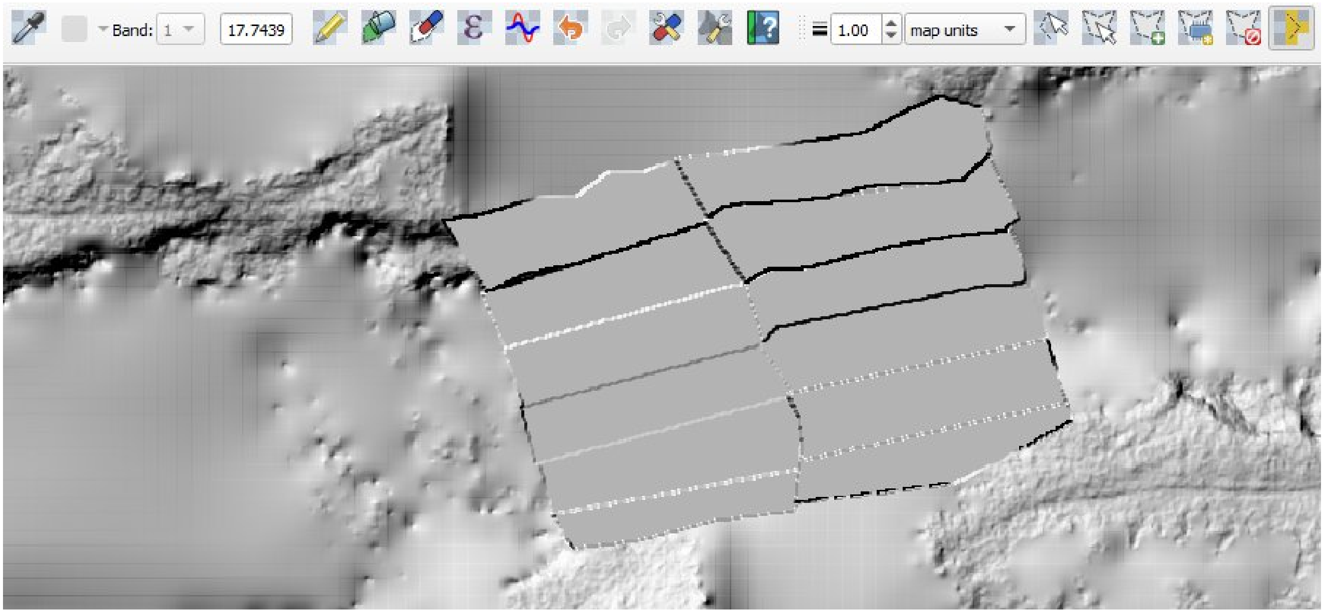

Figure 57 - Bridge deck removal by drawing 12 separate polygons with 12 separate height values

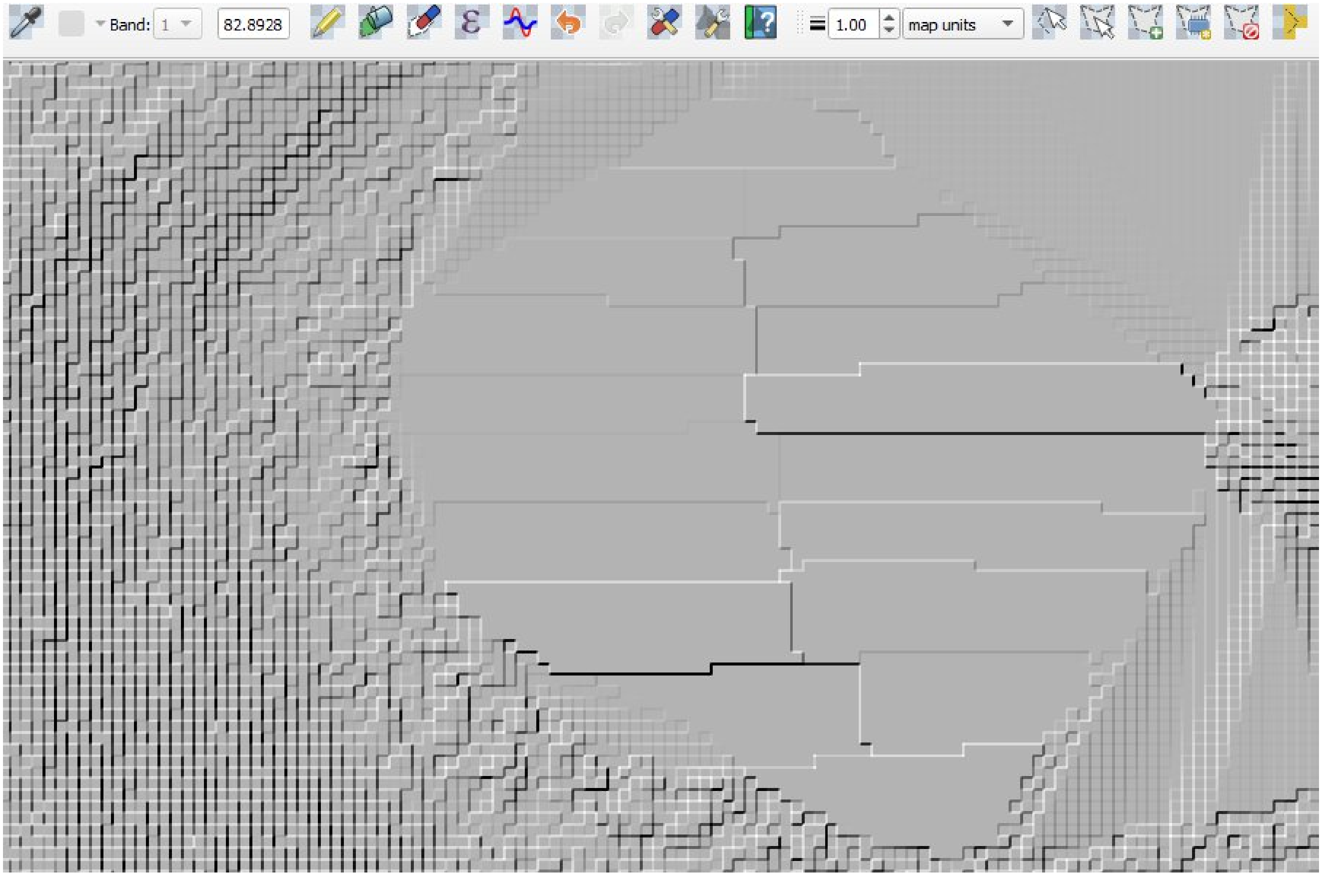

Figure 58 - Missing LiDAR amended by drawing 82 separate polygons with 1 separate height values

Appendix 6 – HEC-RAS 2D unsteady model (Expanded from section 6.1)

1 – Project Setup

A new directory was created using File Explorer that contained the correct projection file downloaded from here and all DEMs that were planning on being used for 2D models. Sub-directories were created for different modelling types (2D LiDAR, 2D Photogrammetry, 1D Models etc) and HEC-RAS was opened and a new project created and saved in the correct modelling type directory shown in Figure 59.

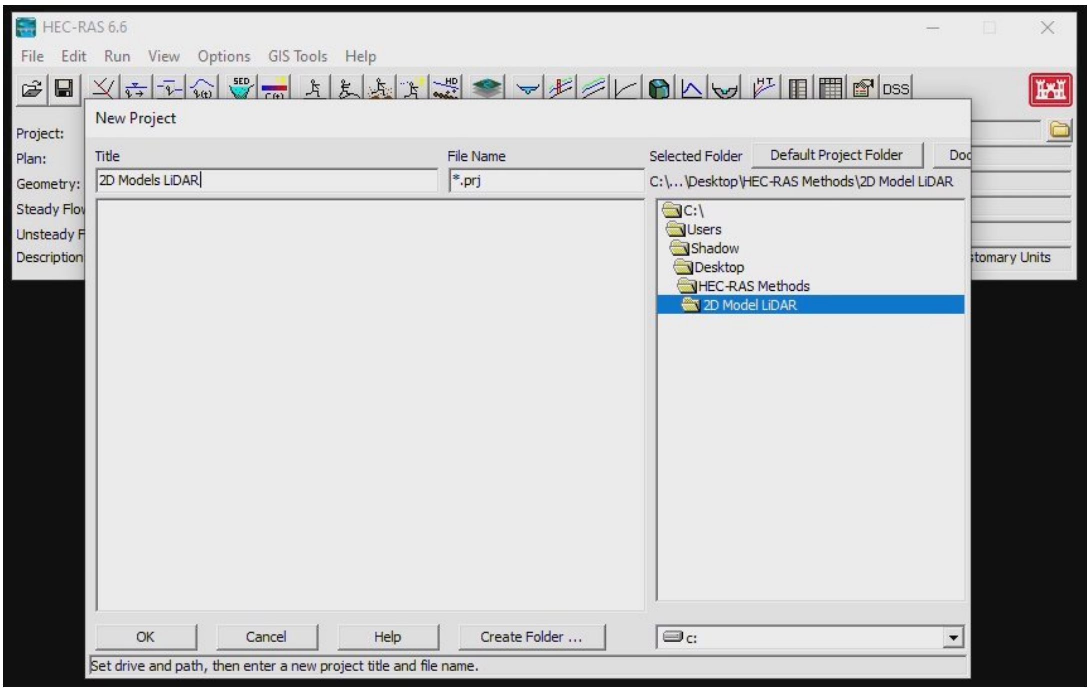

Figure 59 - New project creation within HEC-RAS

All units in the application will default to US/imperial but were changed by selecting “Options” then “Unit System”. Metric units and select as default were confirmed. “RAS Mapper” was opened and the projection file was imported and applied from “Project” then “Set Projection” (Figure 60)

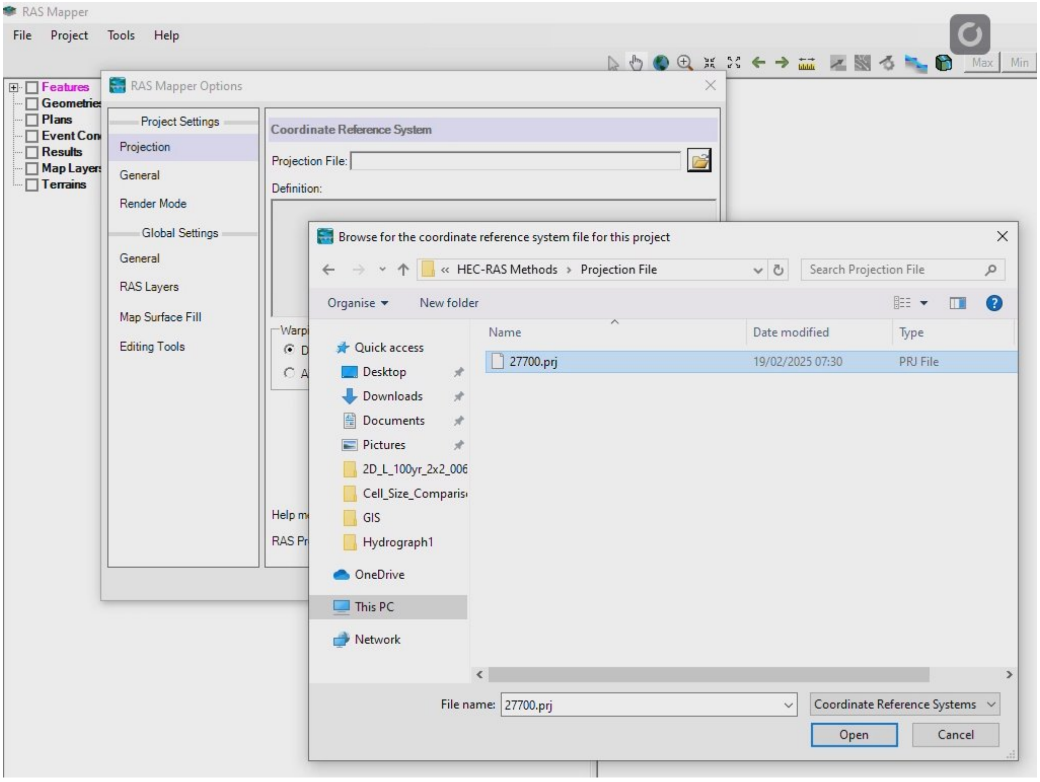

Figure 60 - Setting projection within HEC-RAS project

2 - Adding Terrain

In RAS Mapper the LiDAR DTM was imported by right clicking "Terrain" and selecting "Create a new RAS terrain". DTM was selected by clicking the + symbol and locating the correct DEM file before clicking "Create" as shown in Figure 61.

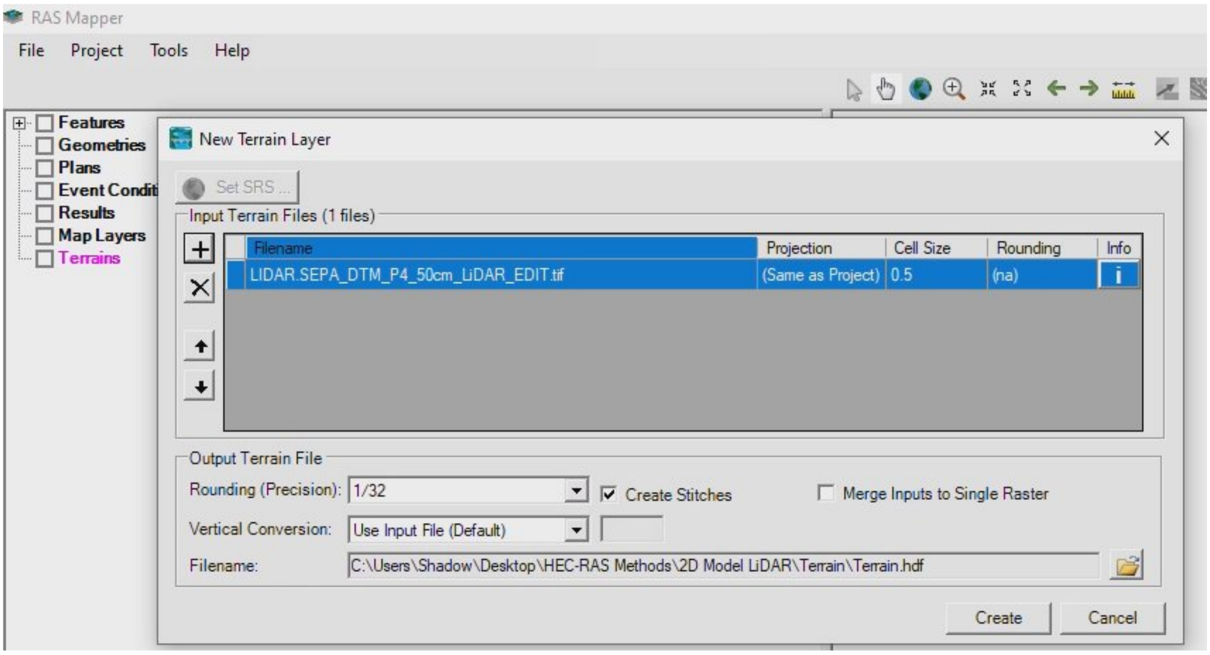

Figure 61 - Creating a new terrain file

The Create Terrain process should run and complete automatically (speed dependant on computer specs and size of DEM). This process was replicated and the Photogrammetry DTM was added (this can be removed, but was needed for the Geometry section and 1D models later).

Figure 62 shows a satellite imagery layer being added by right clicking “Map Layers”, “Add Web Imagery”, and selecting “Google Satellite”. The DEMs and Google Satellite layers were all shown in RAS Mapper.

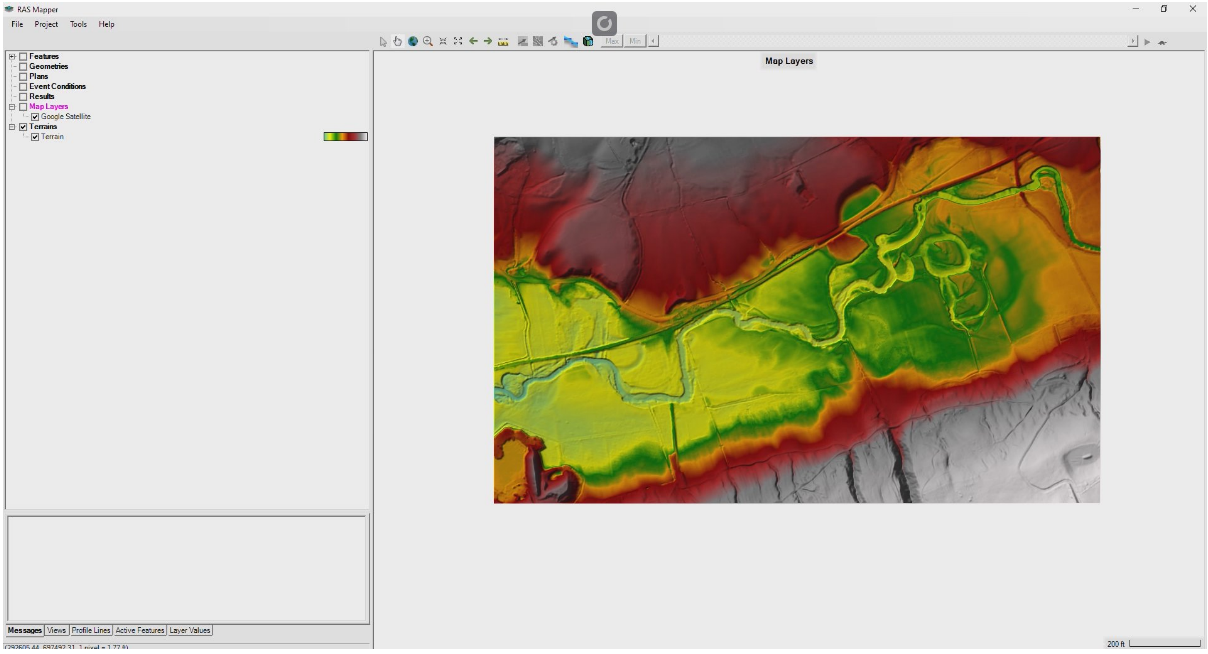

Figure 62 - Adding a satellite background layer within RAS Mapper

3 – New Geometries

With projection set and correct layers added and imported, the flow areas were created by right clicking on “Geometries” and “Create New Geometry”, a name was entered “Devon Flood Study Area” before clicking OK.

3.1 – New Perimeter

The new geometry (“Devon Flood Study Area”) was right clicked before selecting “Edit Geometry”. 2D Flow Areas was expanded and Perimeter ticked. (Note: because the photogrammetry derived DTM area was smaller than the LiDAR DTM area, drawing flood permitter was done against the Photogrammetry derived DTM, to ensure that all geometries for both DEM types were identical and consistent and within both DEM boundaries). When drawing the permitter, it was ensured no lines go in the “white section” and the permitter stayed within the DTM terrain shown in Figure 63.

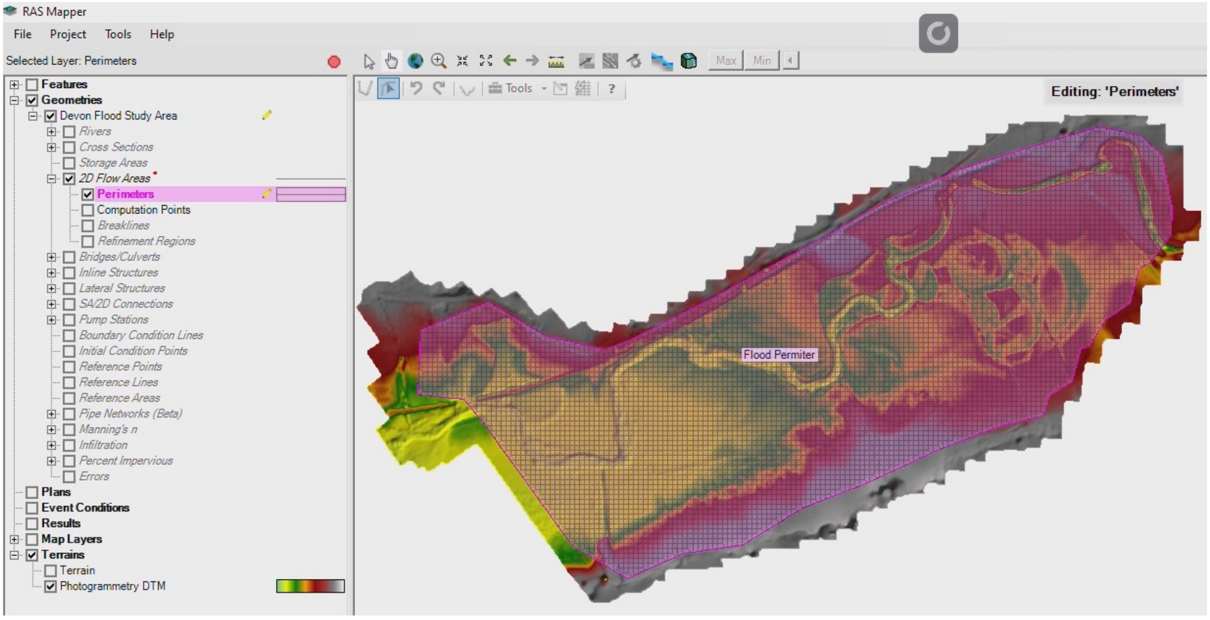

Figure 63 - Creating a new geometry for 2D model

After the permitter was drawn the “2D Flow Area Editor” opened, this tool allows editing of Point Spacing (cell size) and Manning’s N Value. A value can be entered into the DX and DY section of point spacing (in this example 10 and 10 was used) and default N value kept. “Generate Computation Points” and “Compute Property Tables” were both ran (Figure 64)

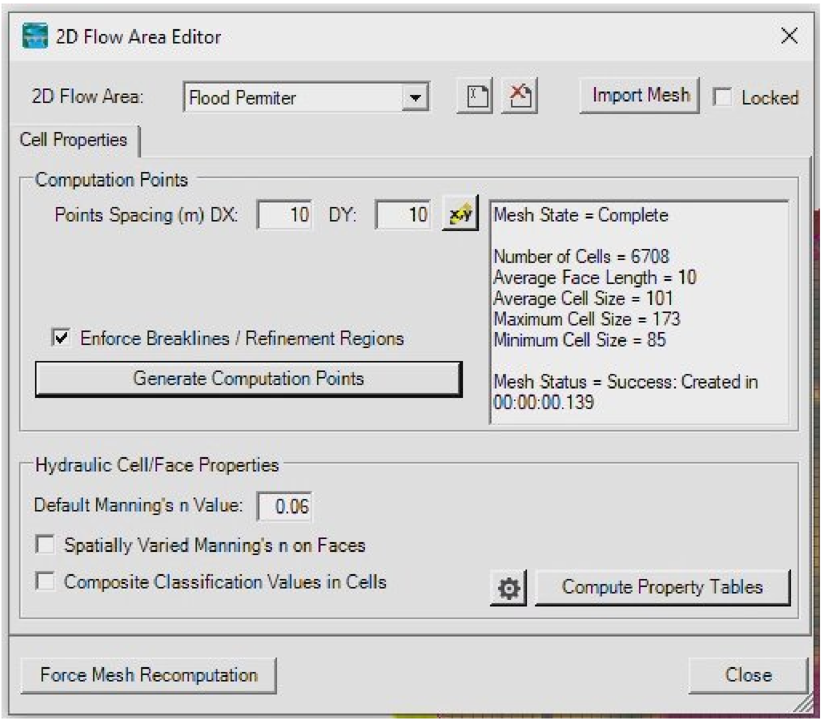

Figure 64 - 2D Flow Area Editor within HEC-RAS showing cell size and mesh setup

Before doing the next steps, under “2D Flow Area”, “Computation Points” were selected and the LiDAR terrain was re-selected with the Photogrammetry terrain deselected. RAS Mapper then looked Figure 65.

Note: At this point, the Perimeter layer was exported as a shapefile (Right clicked “Perimeter” under “2D Flow Area” and selected Export as “Shapefile” before giving a name. This was used in future projects.)

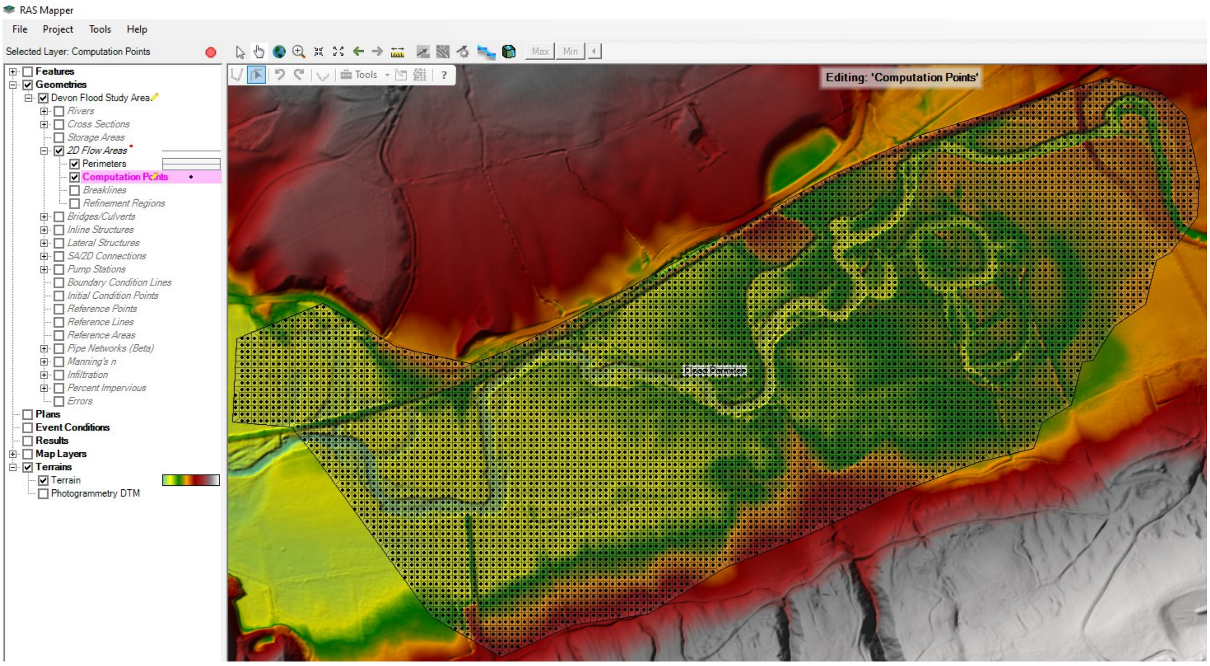

Figure 65 - Example of how RAS Mapper should look with flood perimeter correctly setup

4 Flow Data Connections

The final part within RAS Mapper (at this stage) was adding “Boundary Condition Lines”. As shown in Figure 66. Starting upstream with “Boundary Conditions” selected, zoom tool was used and a BC line drawn just on the outside of with the BC named “Upstream”. This was then replicated downstream, with the BC named “downstream” (Note, this is where the Google Satellite layer became useful to help identify the river banks)

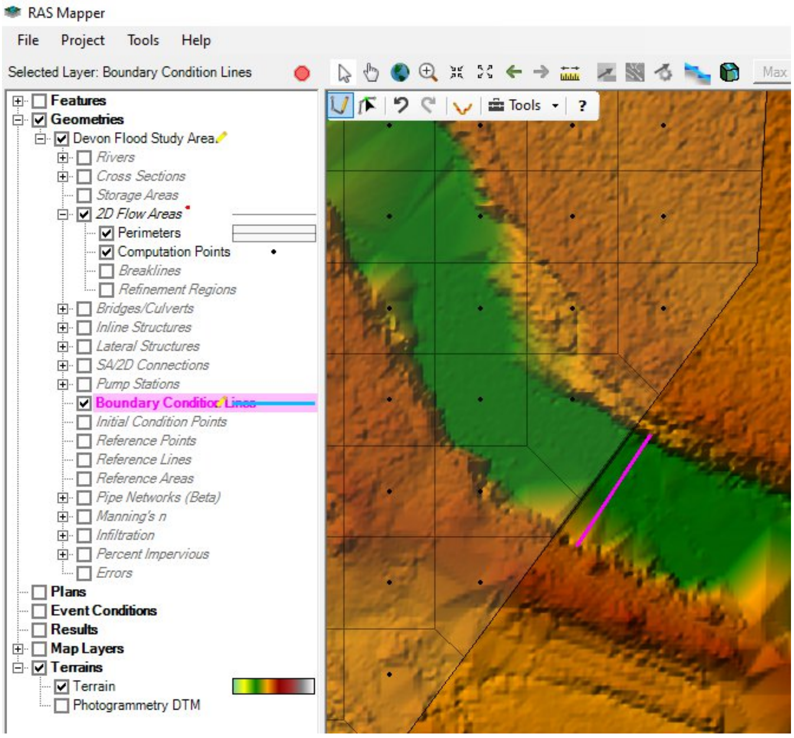

Figure 66 - Manually creating boundary conditions in 2D geometry

Editing in RAS Mapper was stopped by right clicking the geometry “Devon Study Area” and selecting the “Stop Editing”. All changes in RAS Mapper were then saved by selecting “File and Save”.

4.1 – Measuring Slope

With only the LiDAR terrain selected, the ruler tool was used and a line was drawn from downstream to upstream in the centre of the river banks to find the Slope which was then displayed in the “Ruler” window. This was written down and used later.

5 - Geometry Verification

To verify Geometry, “Geometric Data” was selected from the “Edit” menu in HEC-RAS. In the Geometric Data window “File and Open” was selected. “Devon Study Area” was selected before clicking OK (Figure 67)

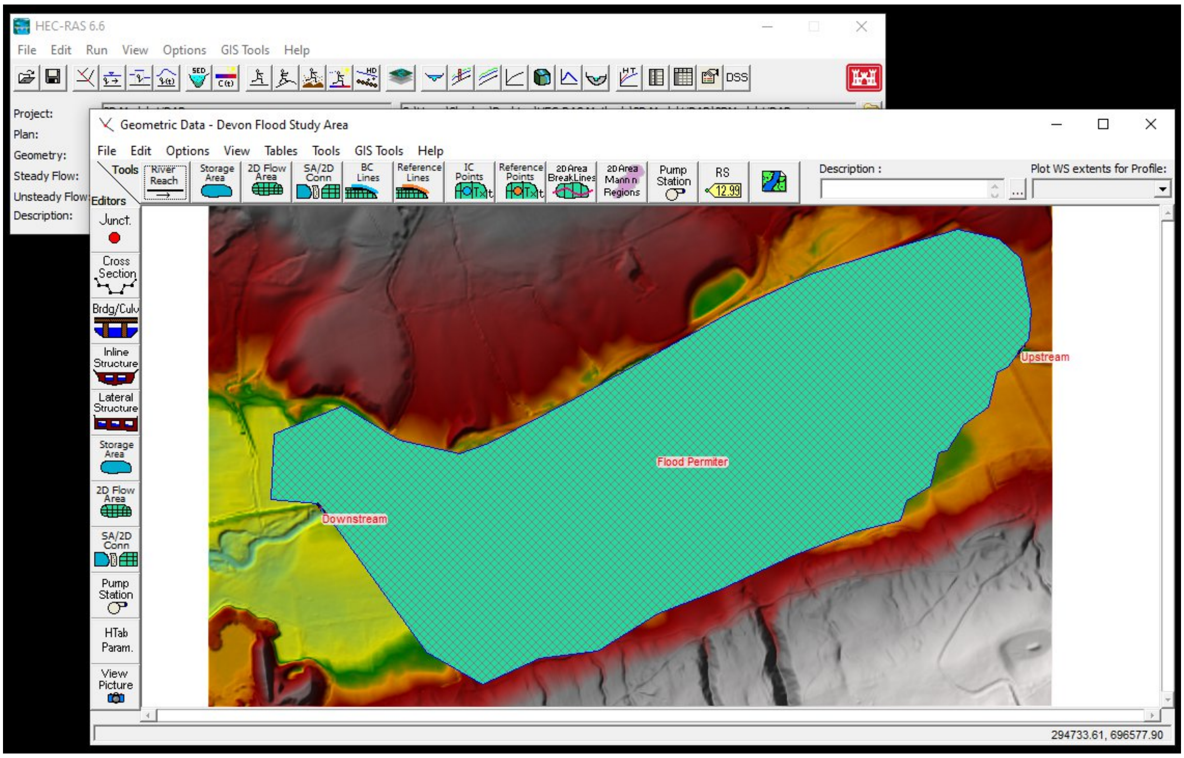

Figure 67 - Verifying geometric data within HEC-RAS

With no errors identified the “Geometric Data window was closed.

6 - Unsteady Flow Data

From the main HEC-RAS window “Unsteady Flow Data” was selected from the “Edit” option. In this new window, “Downstream” boundary condition was selected before clicking on “Normal Depth”. The slope which was worked out from section 4.1 was entered before clicking OK shown in Figure 68

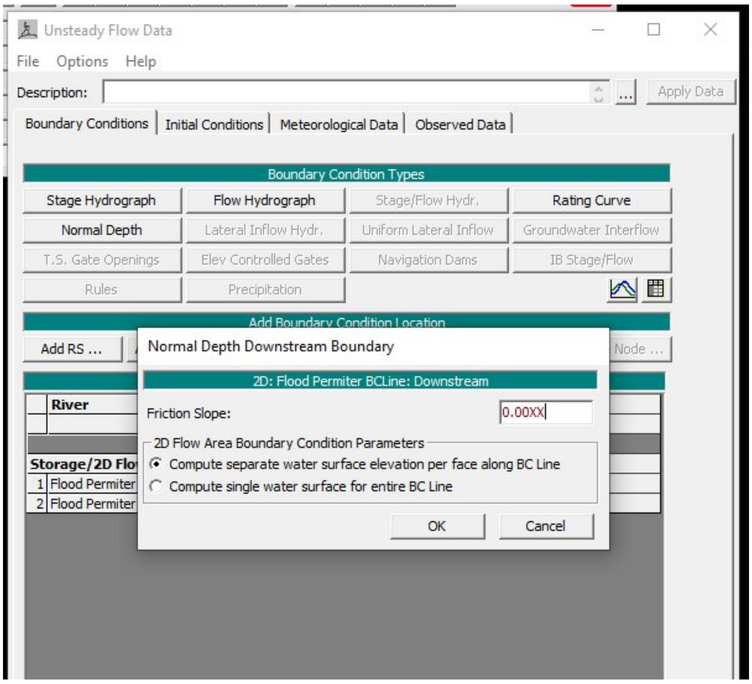

Figure 68 - Setting up unsteady flow in HEC-RAS

Still in the "Unsteady Flow Data" window, the "Upstream" boundary condition was selected before clicking on "Flow Hydrograph". The 100-year flow data was copy and pasted from the Model Register (Table X) with 0.001 entered as the EG Slope before clicking ok shown in Figure 69.

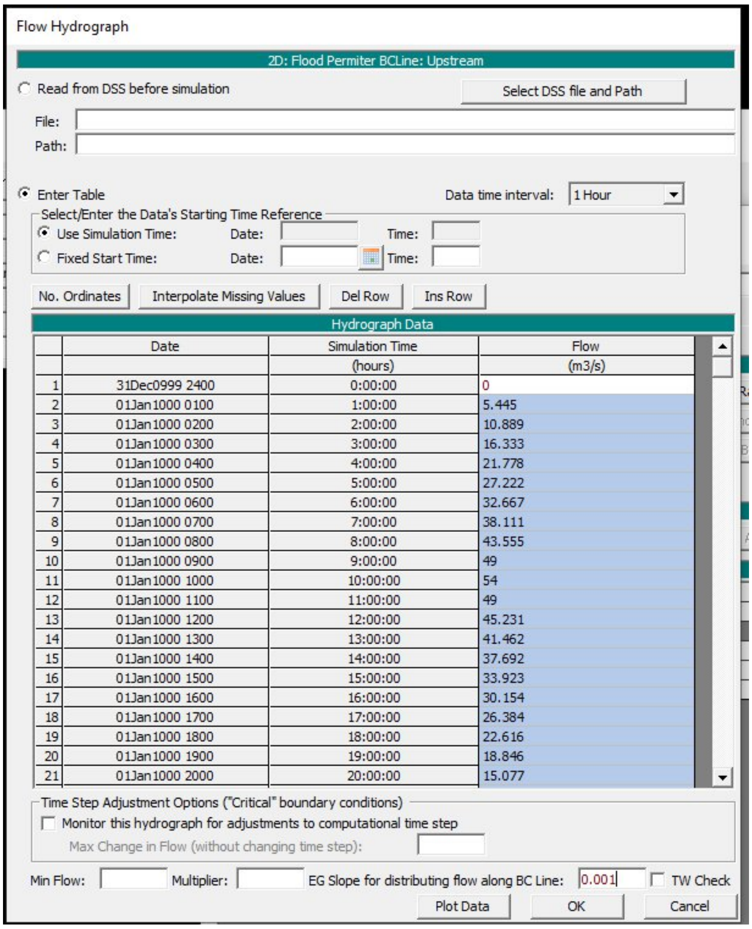

Figure 69 - Flow data input into flow hydrograph editor

The Hydrograph was saved as “100 year flood extent” by clicking “File” then “Save Unsteady Flow Data As” before giving the correct name. The steps in this section were then replicated for the 20 year and 2 year flood hydrographs.

7 – Running the simulation

The flood simulation was ran by clicking “Run” from the main HEC-RAS window then selecting “Unsteady Flow Analysis”. It was ensured the correct Geometry was selected “Devon Study Area” then before running the correct flow was selected that was created in section 6. Under “Programs to Run” the following options were selected:

-Geometry Preprocessor
-Unsteady Flow Simulation
-Post Processor
-Floodplain Mapping

Start and End date under “Simulation Time Window” can be entered (for this example, “todays” date was entered).

The “Computation Settings” were all kept as default, however in future models “Computation Interval” can be altered, but for this example was kept at the default of 1 minute. A plan description was entered and the plan was saved by clicking “File” then “Save Plan As” giving a unique name to this plan. After confirming all settings were correct the “Compute” button was pressed (See Figure 70)

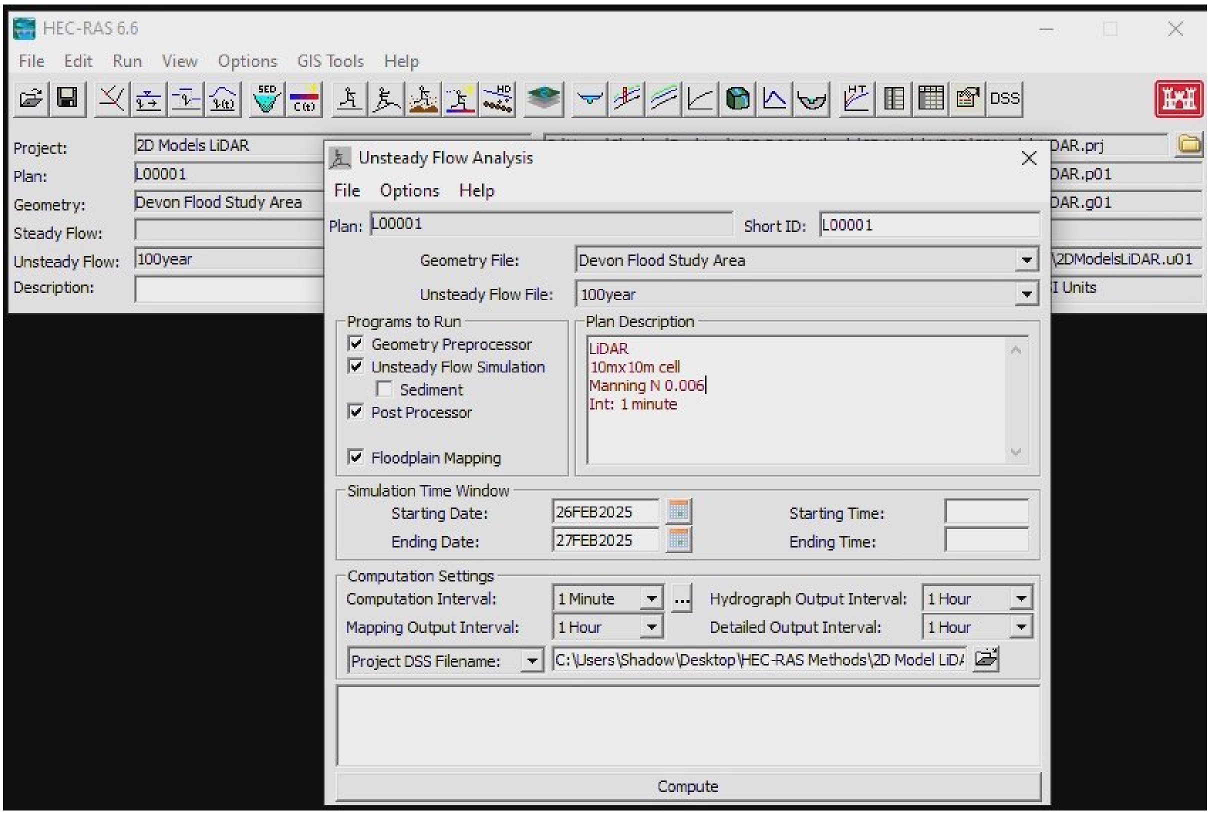

Figure 70 - Starting an unsteady flood simulation and analysis in HEC-RAS

The unsteady flow simulation will run and the speed of the simulation depends on the geometry such as area size and cell size, length of flood simulation and computation interval. When finished the following screen will appear (Figure 71) and the results can be viewed in RAS Mapper.

Note: to change hydrograph for simulation, follow the steps in this section, but select “20 year flood” or “2 year flood” from the “Unsteady Flow File”.

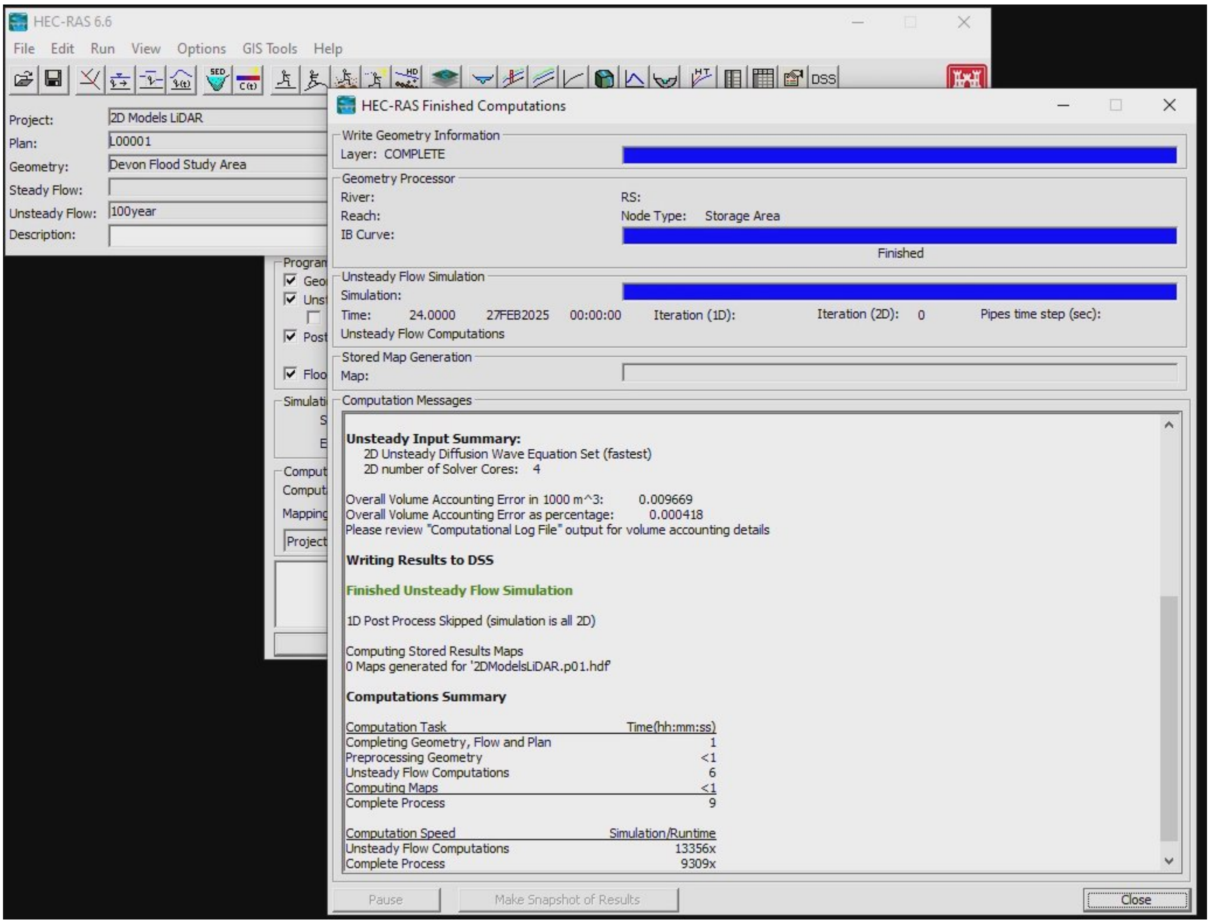

Figure 71 - HEC-RAS flood simulation complete with zero errors

8 - Results

After the above screen was displayed, the Finished Computations window can be closed and RAS Mapper re-opened (Figure 72). The simulation results can be viewed under “Results” in the left column. Flood simulation results can be viewed within RAS Mapper or exported for further analysis in a GIS application. This was done by right clicking what part of result it was decided to export “Depth” or “WSE” etc, “Export Layer” then “Export Raster”.

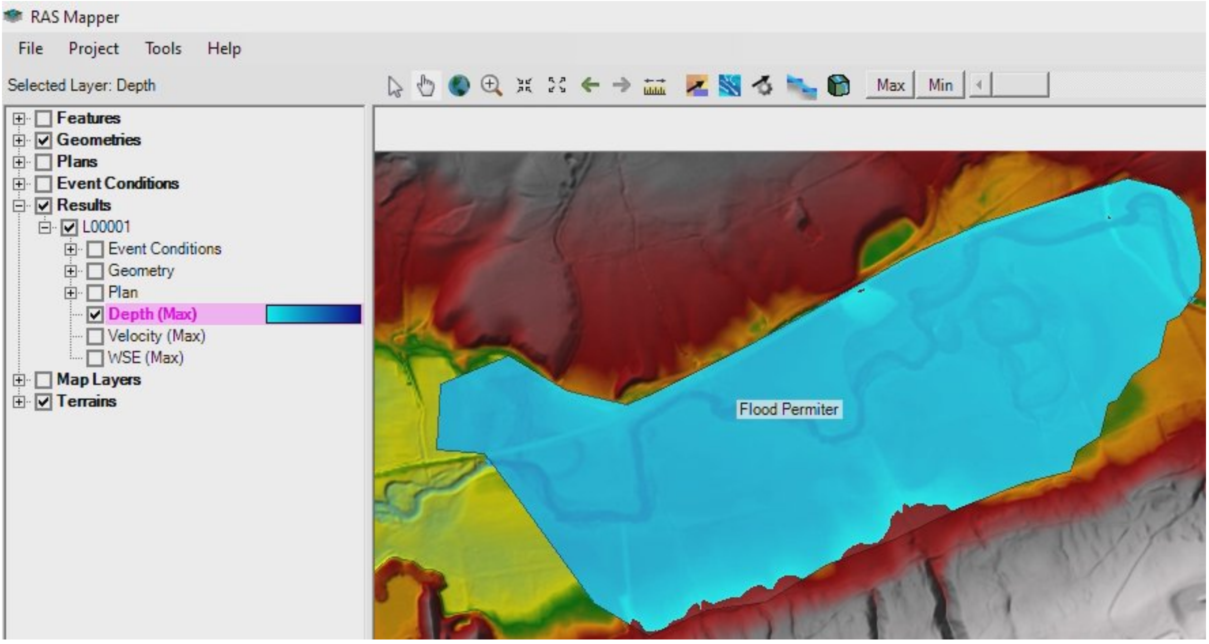

Figure 72 - Flood model results shown within RAS Mapper

Note: With RAS Mapper open, its possible to change computation and cell size for different flood simulations (Figure 71) The above was done using 10m x 10m (Section 3.1) but this was changed by going to “Geometries”, expanding “2D Flow Areas”, right clicking “Perimeter” and selecting “2D Flow Area Editor”. In this section cell size can be changed under “Computation Points” by entering new DX and DY values followed by “Generate Computation Points”. Manning N value can be changed under “Face Properties” followed by “Computer Property Tables”. Geometry can be saved and flood simulation ran or re-ran as per Section 7

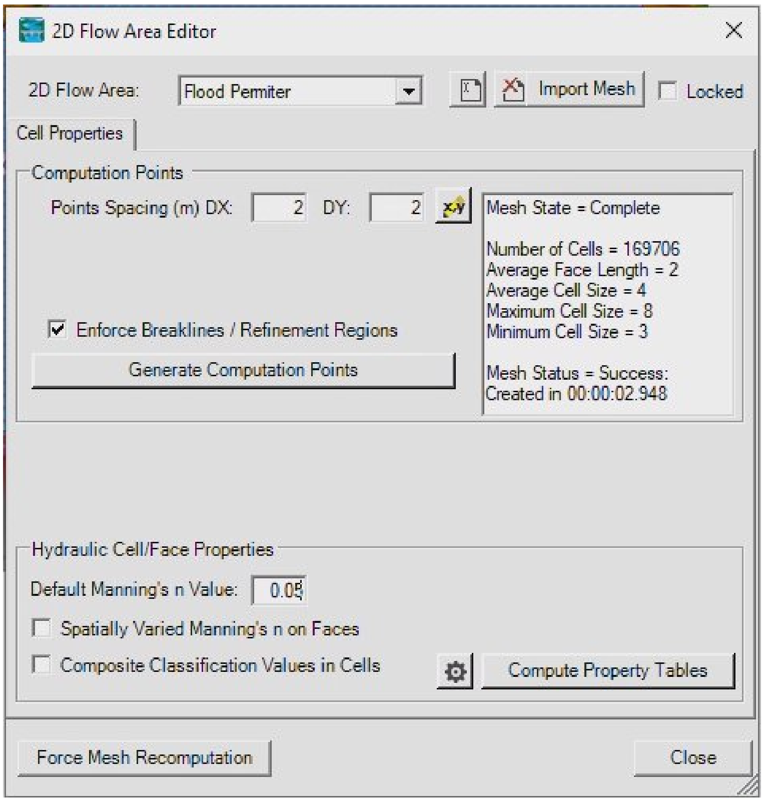

Figure 73 - 2D flow Area Editor within RAS Mapper to change cell and mesh size

The above section is the method section was used for 2D flood modelling using the LiDAR DTM. It should be possible to import the Photogrammetry DTM into this project however when it was tried there was several "Geometric error" messages appearing. Searching the HEC-RAS community pages online, this was quite common and it was recommended to create a new project for different terrains if this error was encountered.

To create a project for the Photogrammetry DTM, the above steps were replicated with the following key differences:

-In section 2, import and create the Photogrammetry DTM terrain and not LiDAR
-In section 3.1 above, instead of drawing a new perimeter, right click on perimeter under "2D Flow Areas" and import the shapefile that was exported under that same section.

Appendix 7 – HEC-RAS 1D steady model (Expanded from section 8.1)

The “2D Lidar” HEC-RAS project from Appendix 6 from earlier was opened up before entering into the RAS Mapper feature of HEC-RAS. In left column of RAS Mapper, “Geometries” was right clicked before entering a new geometry name “1D Modelling LiDAR”. In the “Manage Layer Associations” window under the “Terrain” column, it was double checked that the correct terrain layer was selected (LiDAR terrain layer in this example Figure 74).

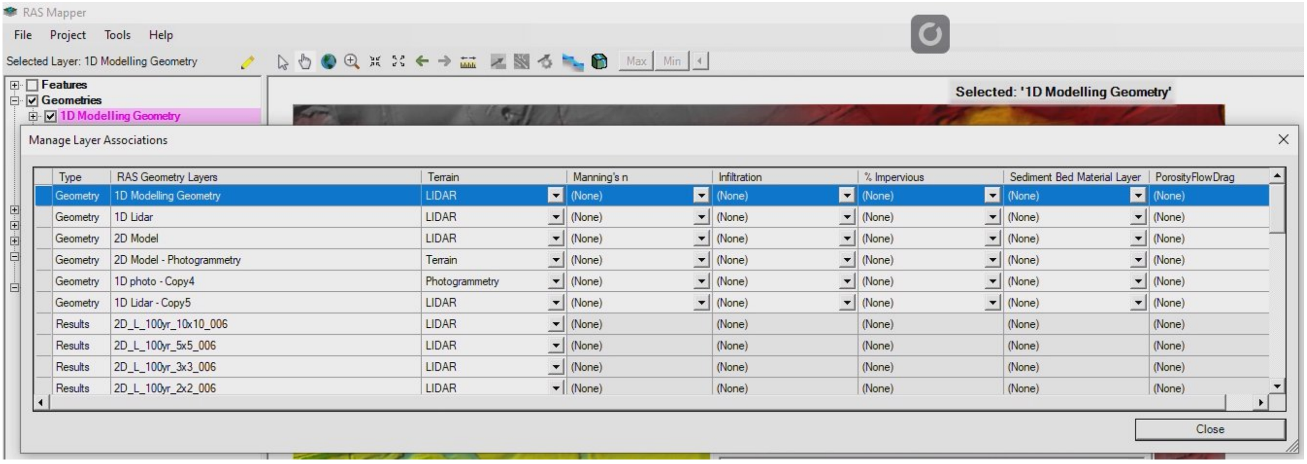

Figure 74 - Confirming correct terrain in HEC-RAS for 1D model

1 – River Centreline

“Rivers” under the new geometry “1D Modelling Geometry LiDAR” was right clicked before selecting “Edit”. Using the drawing tool in the toolbar, a centre line was drawn in the middle of the river channel for the entire length of the river starting upstream (Figure 75). (Note: Toggling between satellite layer and LiDAR terrain layer was done to help find river centre. Also toggling the 2D layer geometry from earlier (Appendix 6) to show the start and end of the river geometry. While this wasn’t part of project, it could be useful if wanting to directly compare 2D unsteady and 1D unsteady in future).

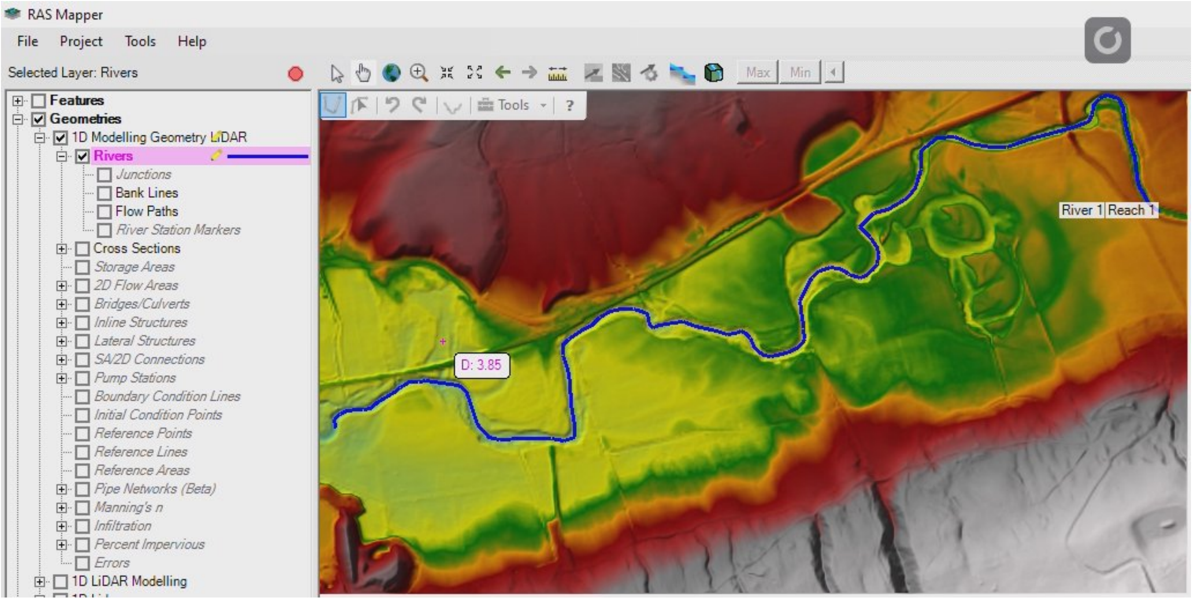

Figure 75 - Drawing river channel centreline in HEC-RAS

2 - Bankline's

Under the same Geometry, "Bank Lines" was ticked and the river bank lines were drawn. This was done in the same way section 1 "River Centreline", using the Drawing toolbar, drawing upstream to downstream (left bank first followed by right bank) and toggling and zoom in and out between different layers to help identify bank locations (Figure 76)

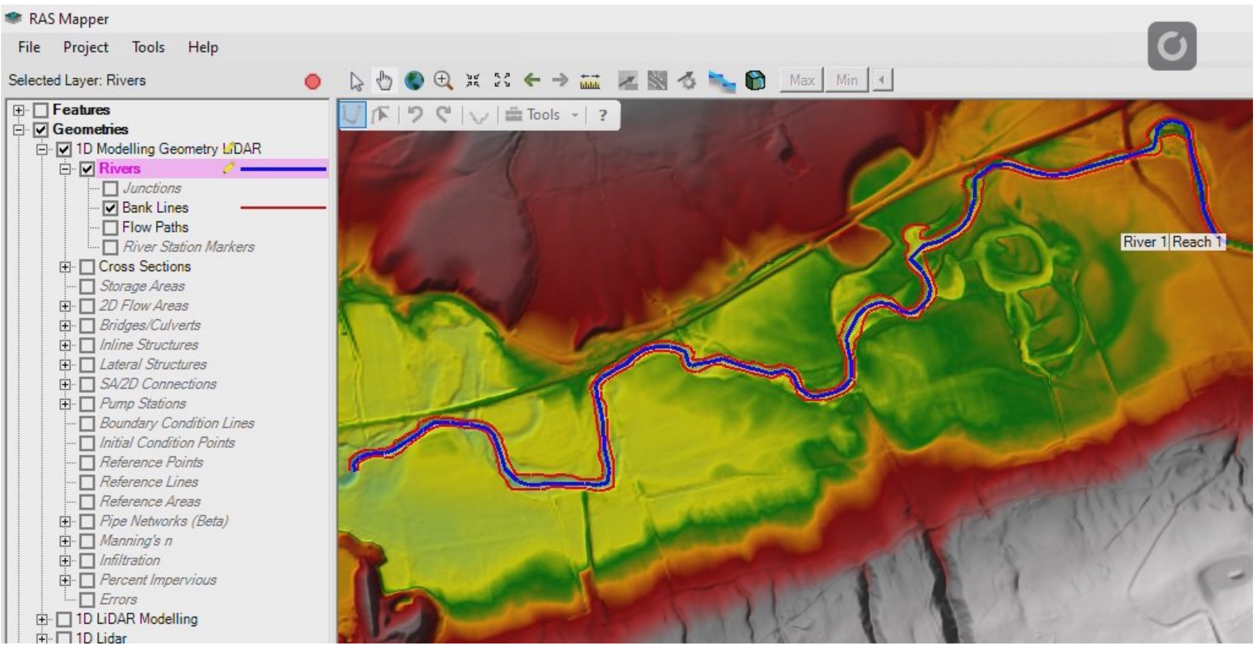

Figure 76 - Drawing bank lines in HEC-RAS for 1D model

3 – Flowpaths

Flowpaths were digitised using the same methods as section 1 and 2 in this appendix. Under the correct Geometry (1D Modelling Geometry LiDAR), "Flow Paths" was right clicked on before selecting "Edit Geometry". (Note: At this stage the 2D geometry from Appendix 6 was toggled on and off to ensure that the Flow Paths remained within the "2D Flow Areas" area. This was done to ensure the flowpaths stayed within the boundaries of both LiDAR terrain and Photogrammetry terrain). Flow Paths were drawn along the boundaries of the floodplain, using the Drawing toolbar, drawing upstream to downstream (left bank first followed by right bank) and toggling and zoom in and out between different layers to help identify boundary and floodplain locations. The flow paths were saved by right clicking "Flow Paths" then "Stop Editing".

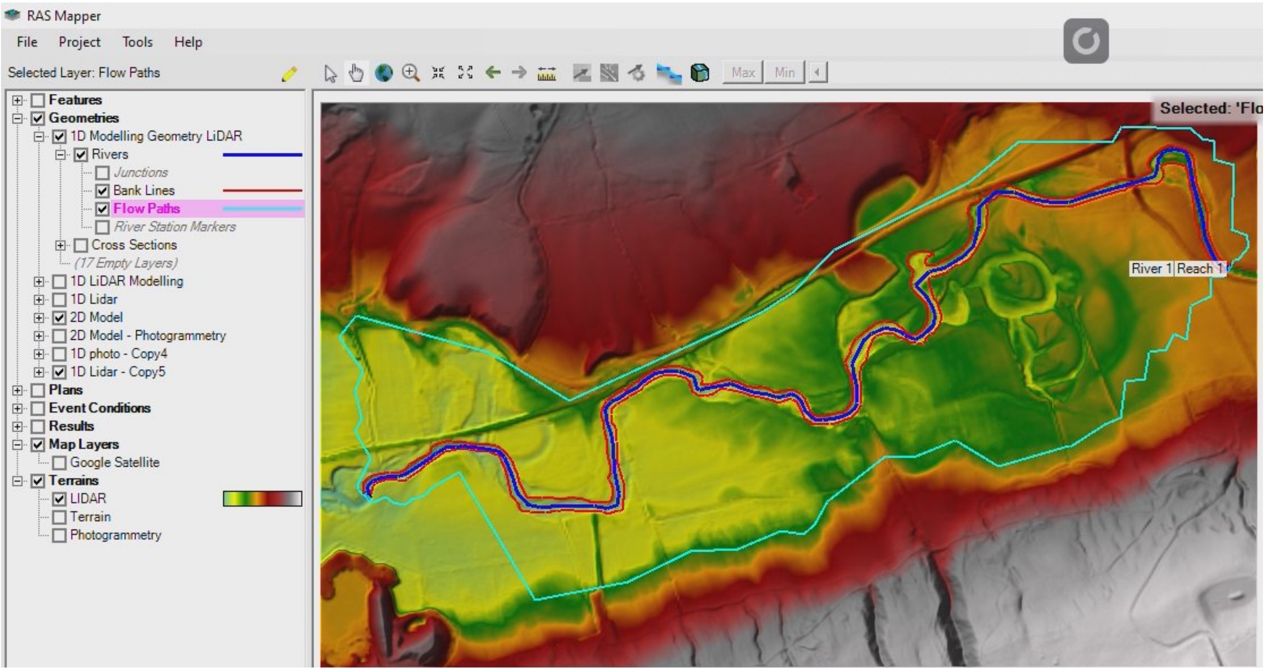

Figure 77 - Digitising flow paths within HEC-RAS for 1D model

4 – Cross-sections

To add in the cross sections, the "Cross Sections" tick button was selected before right clicking on "Cross Sections" and selecting "Edit Geometry". Using the Drawing Tool bar, cross sections were drawn roughly 75-100m width apart (Figure 78), starting from upstream to downstream. Cross sections were digitised perpendicular to the direction of flow ensuring that each cross section intersected the centre line, both bank lines and both flow paths once. Cross Sections were saved by right clicking on the geometry and clicking on the "Stop Editing" button.

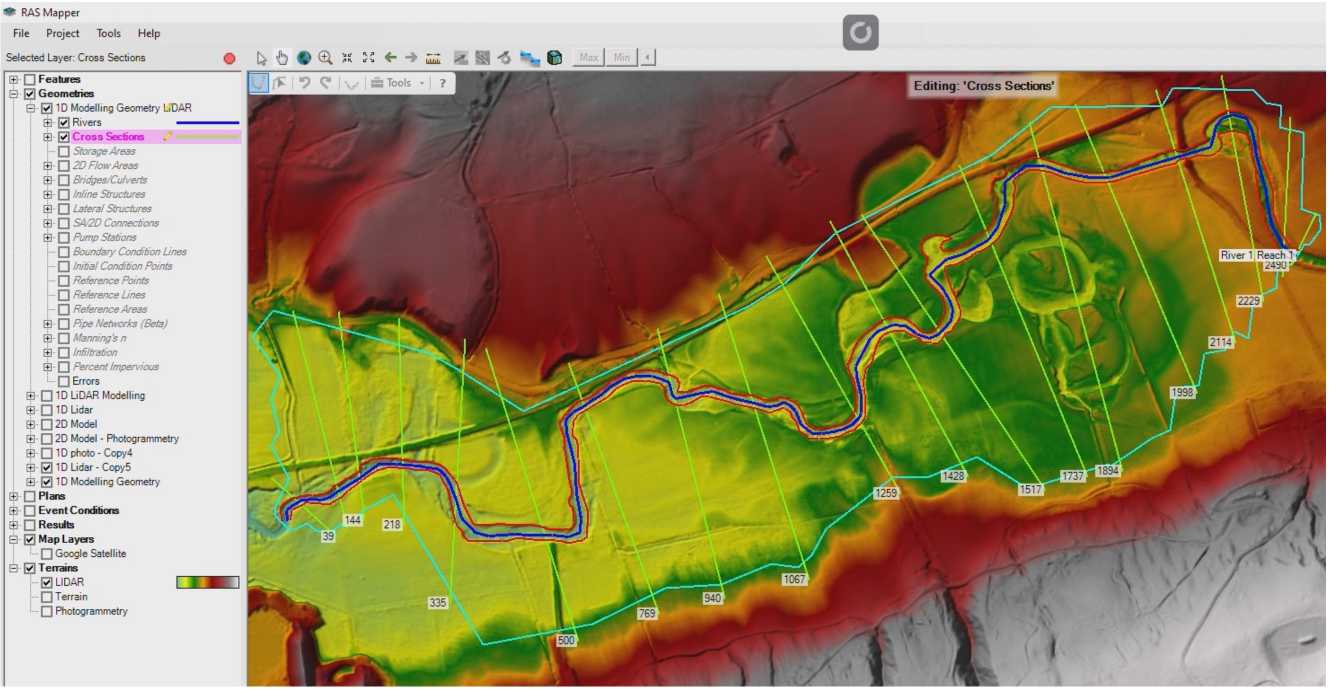

Figure 78 - Drawing cross sections within HEC-RAS

The final part within RAS Mapper at this stage was to update the cross sections by right clicking on "Cross Sections" and selecting "Update Cross Sections XX of XX) > All XS attributes (exl terrain) shown in Figure 79. Once this ran, editing of geometry was stopped and RAS Mapper exited by clicking "File" then Save" before closing RAS Mapper.

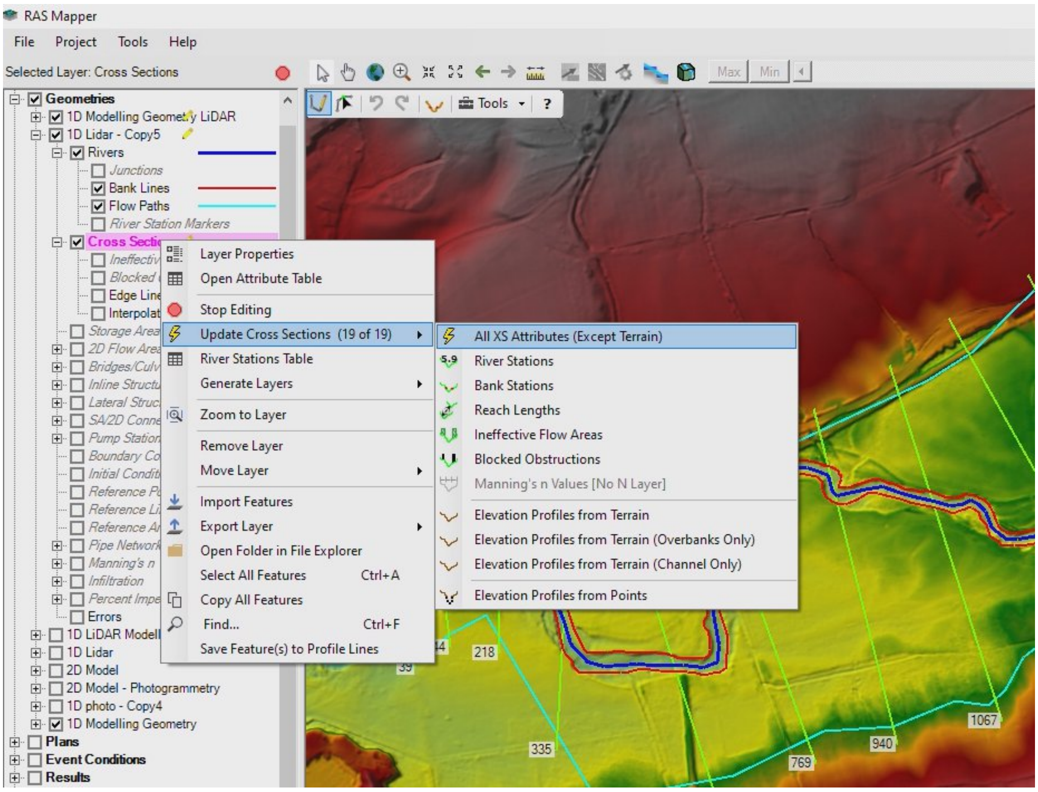

Figure 79 - Applying all model XS attributes

5 - Applying Mannings ‘N’ Values

Applying ‘N’ values to cross-sections was done by clicking on “Edit” in the main HEC-RAS window then “Geometric Data”. In the Geometric Data window, “File” then “Open Geometry Data” was selected before double clicking on the geometry that was just being worked on in RAS Mapper “1D Modelling Geometry LiDAR”.

When the geometry was finished loading “Tables” from the top menu bar was selected followed by “Manning’s N or K values (Horizontally varied)…”. In the table that opened 0.06 was entered for n#1 and n#3 columns (floodplains) and 0.045 for column n#2 (main channel) before clicking OK (See Figure 80) and saving this by clicking “File” then “Save Geometry Data”.

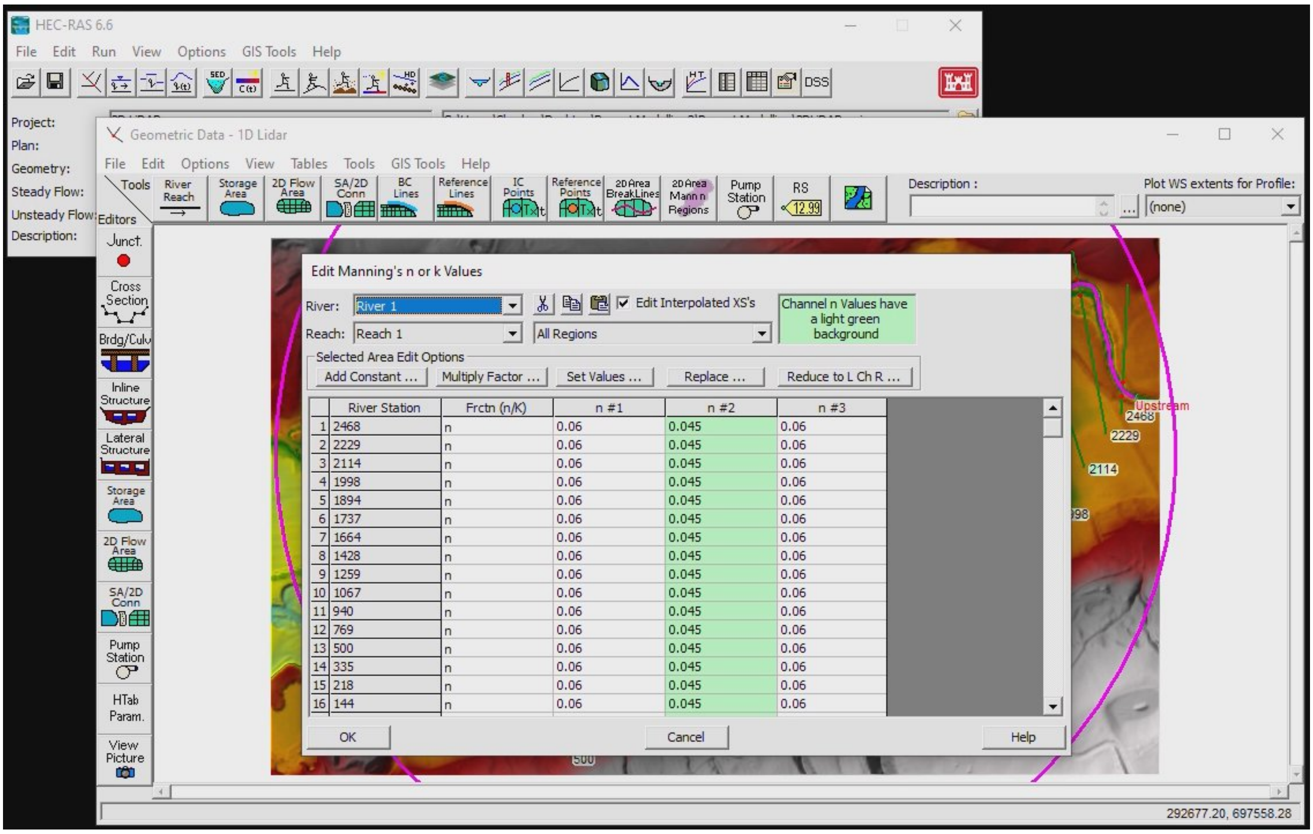

Figure 80 - Geometric data editor allowing editing of N values

6 – Duplicating Geometry Data for Photogrammetry Terrain

At this stage, all that was left to do was set up flow data before running the flood simulations. However, as this project was seeking to compare results from a LiDAR terrain and Photogrammetry derived terrain, the Photogrammetry geometry was set created. This was done by going back into “RAS Mapper” and right clicking the “1D Modelling Geometry LiDAR” geometry that was just created that was just created before clicking “Save Geometry As”. In the dialog box that appeared “1D Modelling Geometry Photogrammetry” was entered followed by OK.

A ”Manage Layer Associations” box automatically opened and for the “1D Modelling Geometry Photogrammetry” layer, under the “Terrain” column “Photogrammetry” was selected as shown in

Figure 81 (Note: this terrain layer was already added to RAS Mapper from the 2D steady flow model already discussed in Appendix 6).

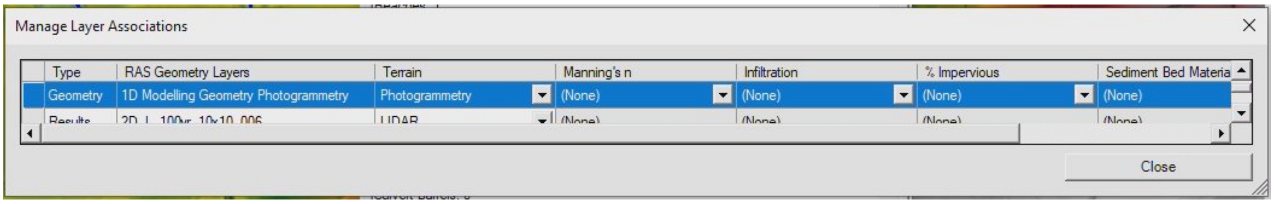

Figure 81 - Manage layer associations prompt in HEC-RAS

Section 5 "Applying Mannings 'N' Values" of this Appendix was repeated, however when opening geometry data "1D Modelling Geometry Photogrammetry" was selected.

7 – Creating Steady Flow Data

Back in the main HEC-RAS window "Edit" then "Steady Flow Data" was selected. In the steady flow window that appeared new flow data was created by clicking "File" followed by "New Flow Data" before entering a name "Steady flow 100yr flood".

"Reach Boundary Conditions…" was clicked followed by highlighting the "Downstream" column for the river/reach. "Normal depth" was selected and 0.002 before clicking OK (Figure 82)

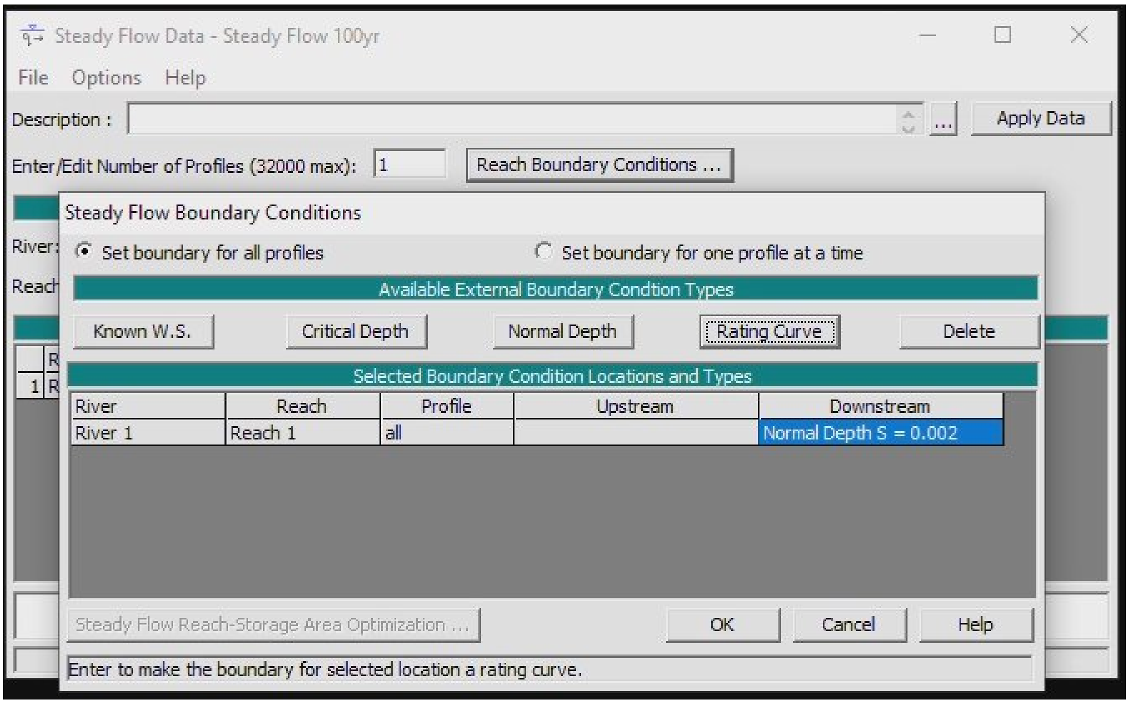

Figure 82 - Editing steady flow boundary conditions

Back in the main steady flow data window, PF 1 column was selected and the flow rate in m^3/s was entered for the 100 year flood extent – 151.6 before clicking "File" and "Save Flow Data". The steps in this section were repeated for the 20 year flood (79.8) and 2 year flood (48), re-saving each flow data with the new and correct name as shown in Figure 83.

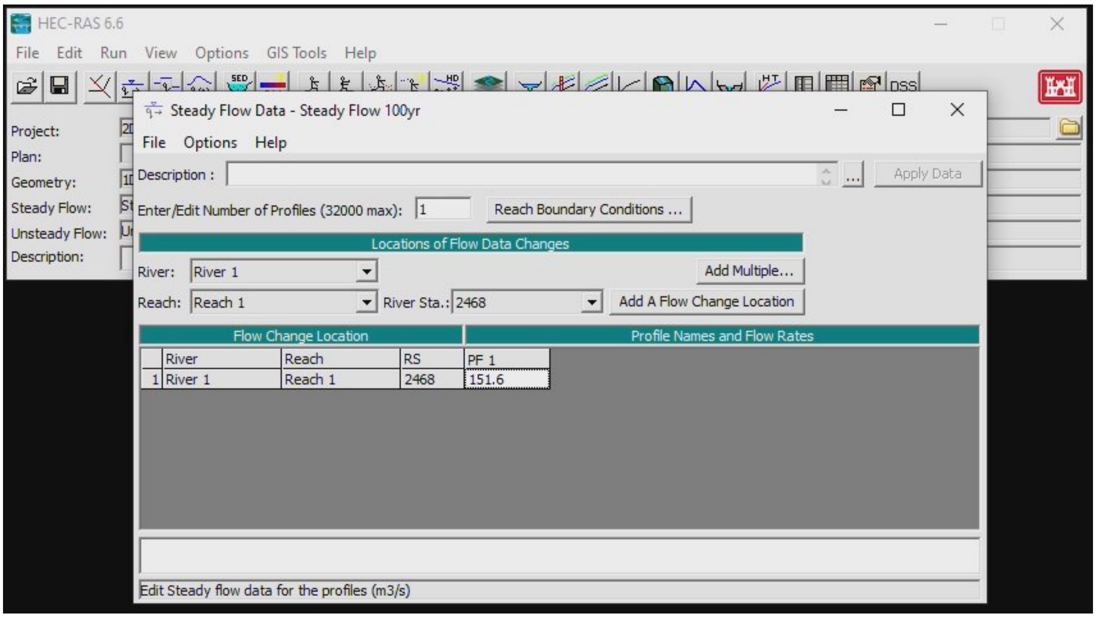

Figure 83 - Editing steady flow data for different flood events

8 – Running Flood Simulation

1D with steady flow simulations were ran by clicking “Run” then “Steady Flow Analysis” from the main HEC-RAS window. In the “Steady Flow Analysis” window that appeared, the LiDAR geometry file and 100 year steady flow data was selected from the dropdowns. “Flow Regime” was set to “Flood Critical” and “Floodplain Mapping” was selected before clicking saving this plan with a unique name then “Compute” button was pressed to start the simulation as shown in Figure 84. This step was repeated for the 20 year and 2 year flood flow file then for the Photogrammetry Geometry file and all 3 flood extents, ensuring each plan was saved with a unique name.

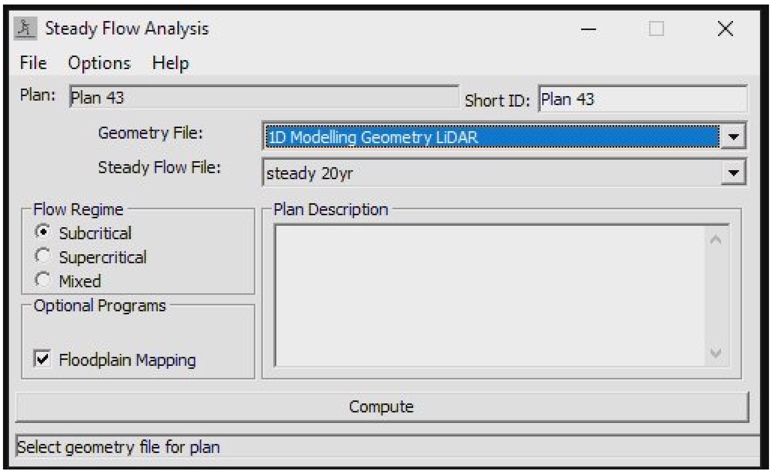

Figure 84 - Running a steady flow analysis in HEC-RAS

9 – Finished Results

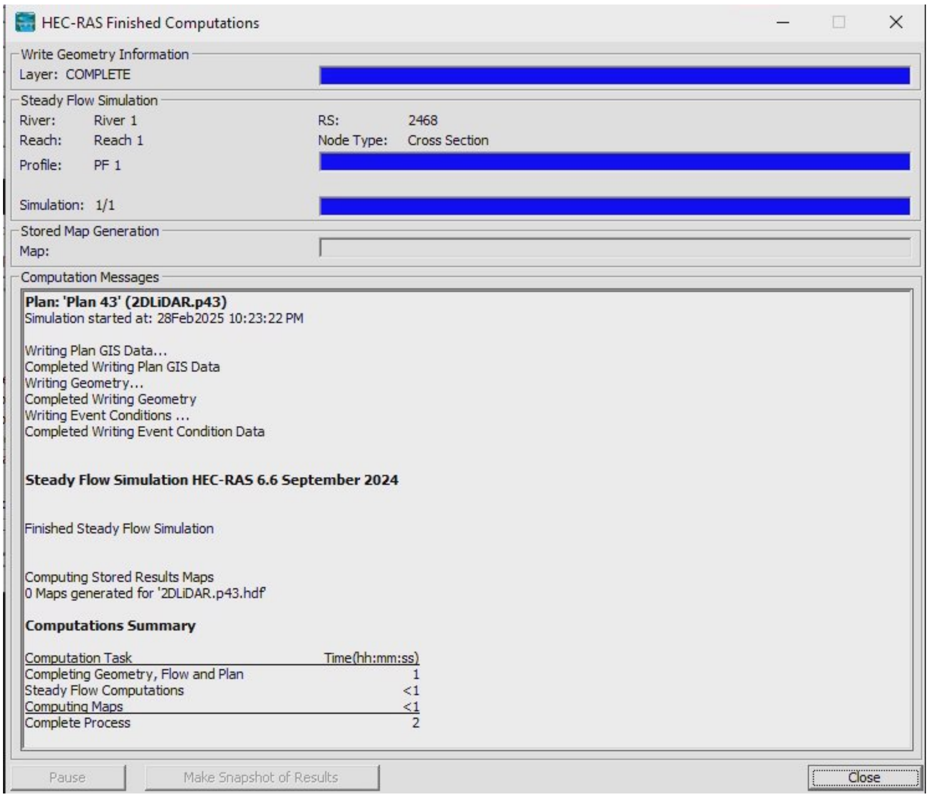

Figure 85 - Successfully completed 1D steady flow HEC-RAS simulation

After the simulation has complete, the “Finished Computations” window (Figure 85) can be closed and “RAS Mapper” re-opened. The simulation results can be viewed under “Results” in the left column. Flood simulation results can be viewed within RAS Mapper or exported for further analysis in a GIS application. This was done by right clicking what part of result it was decided to export “Depth” or “WSE” etc, followed by clicking “Export Layer” then “Export Raster” (Figure 86)

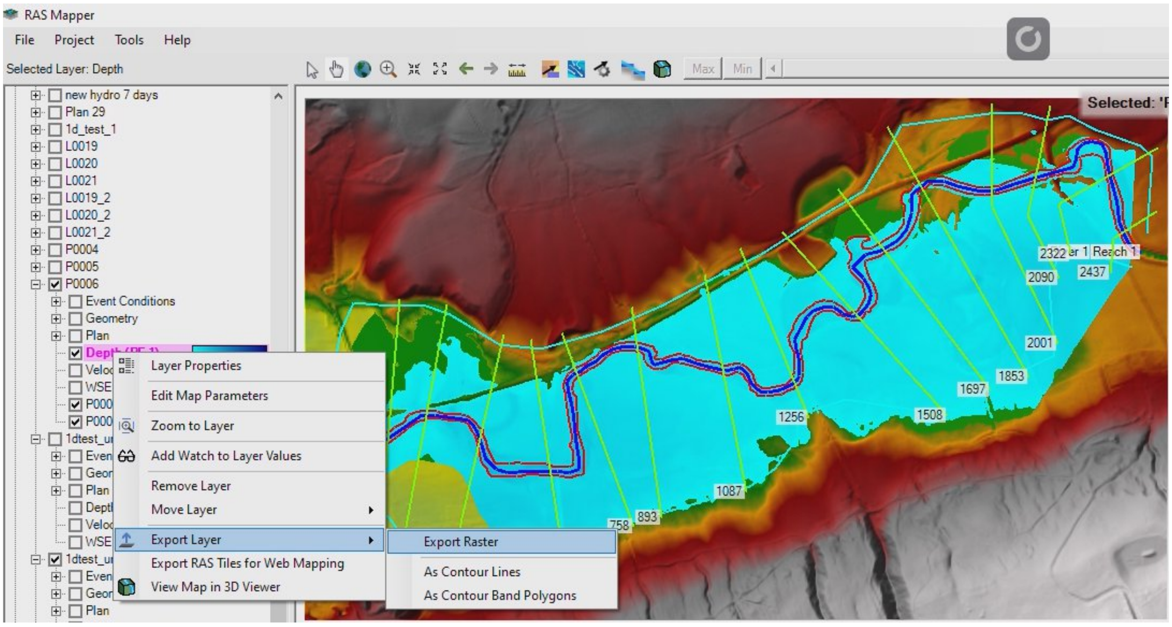

Figure 86 - Exporting results raster for further analysis within QGIS

Appendix 8 – ArcGIS Pro 2D unsteady model (Expanded from section 9.1)

1 – Project Setup

ArcGIS Pro was opened and new “Local Scene” was selected from the options menu as shown in Figure 87 before giving the new project a name and saved directory location.

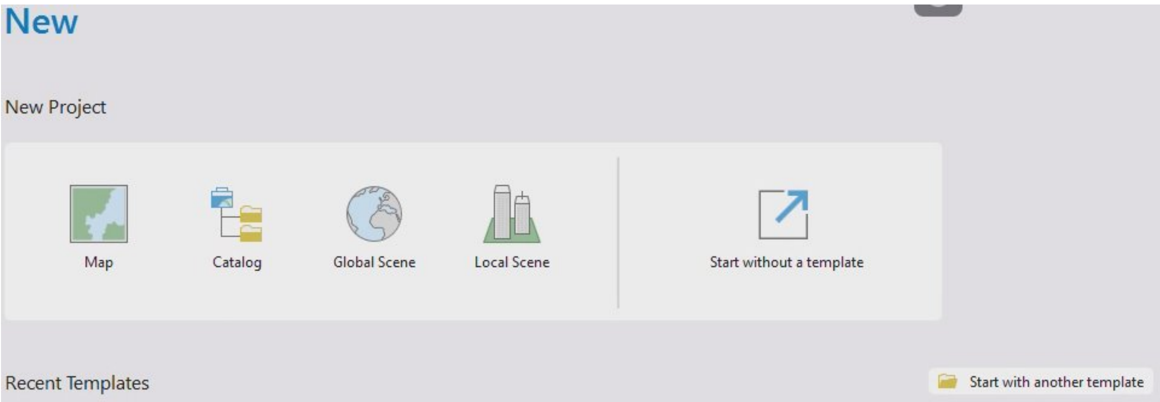

Figure 87 - Creation of a new project and local scene in ArcGIS

The “Map” tab was clicked before navigating to “Add Data > Browse” (Figure 88) and the two DEM’s (LiDAR DTM and Photogrammetry DTM) that were used in sections 6.2 – 6.5 were selected and opened.

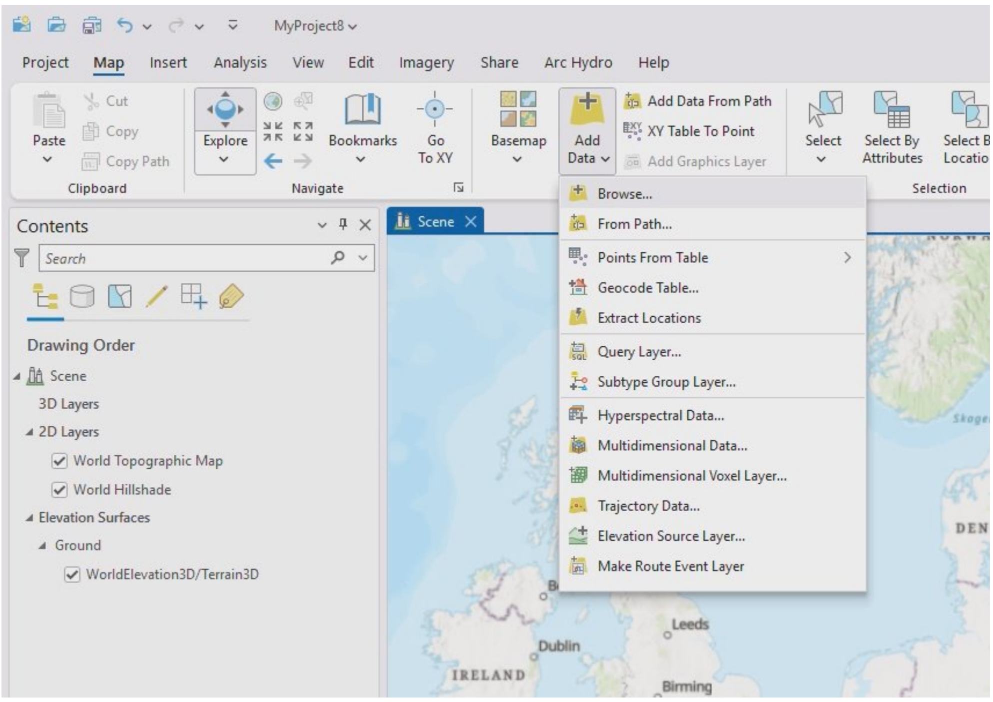

Figure 88 - Inserting LiDAR and Photogrammetry DTMs to the ArcGIS project

When the DEMs were imported correctly, they are shown within the left-hand side “Contents” section of the ArcGIS application as per Figure 89.

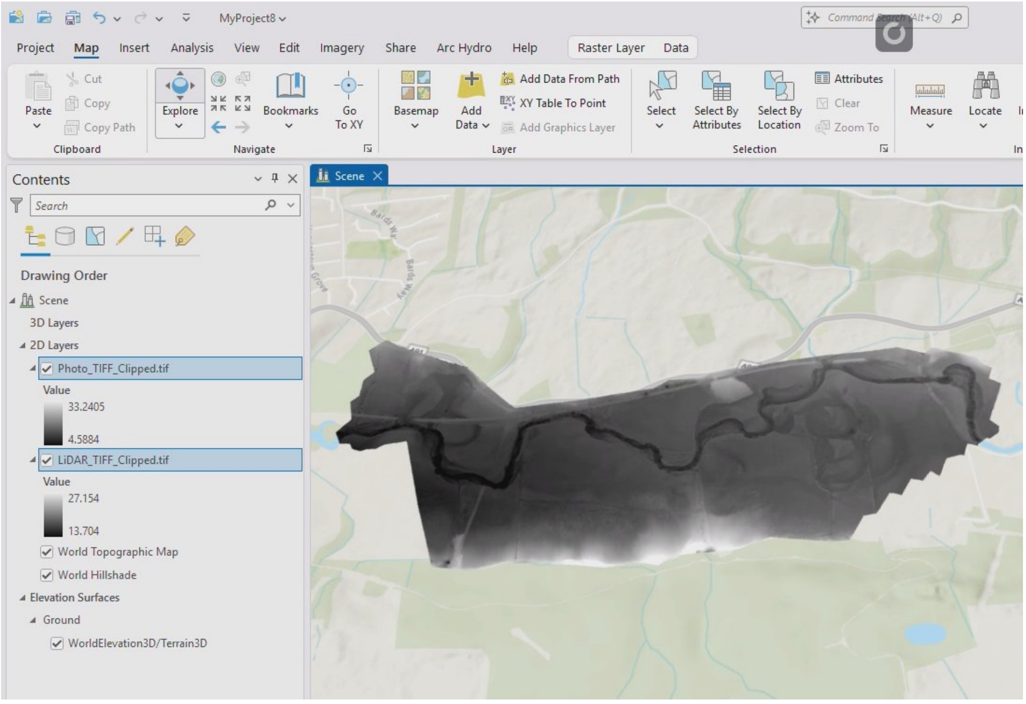

Figure 89 - Showing added DTMs within ArcGIS

For better eligibility the Symbology was changed on each of the new imported DEMs by right clicking on each individual layer and clicking on “Symbology”. In the Symbology processing window on the righthand side of the screen, from the “Primary symbology” dropdown, “Stretch” was replaced with “Shaded relief” (Figure 90).

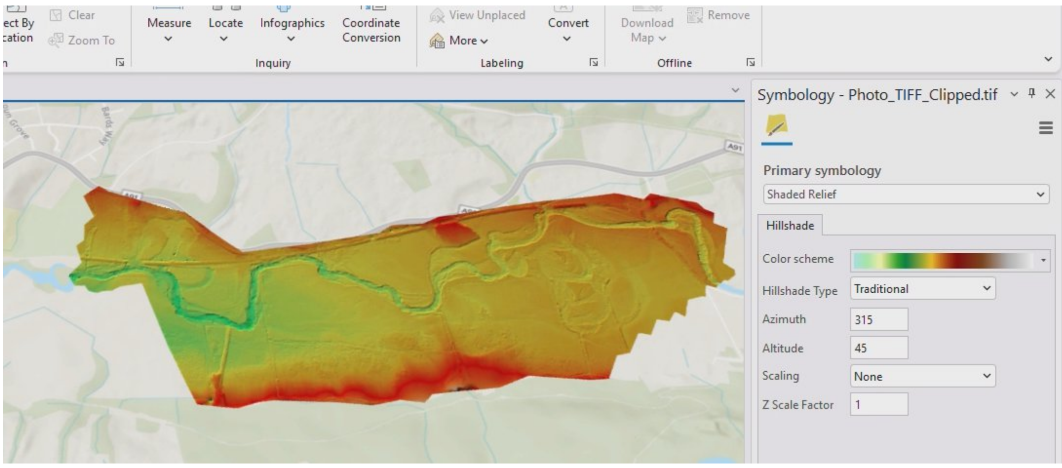

Figure 90 - Changing terrain symbology to shaded relief for greater eligibility

2 – Flood simulation preparation

To start a flood simulation the “Analysis” tab in the main menu bar was clicked on followed by “Simulation” and “Default” (Figure 91)

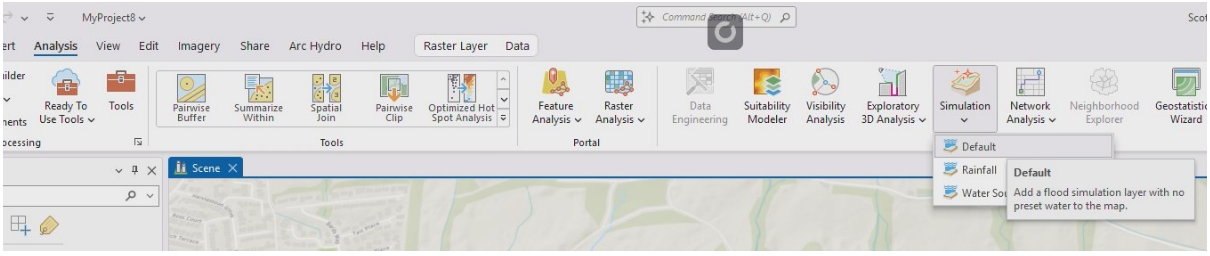

Figure 91 - Preparing a flood simulation model within ArcGIS

In the flood simulation area box that appeared central lower screen as shown in Figure 92 the 4th button from left “Area from selected layer” was selected.

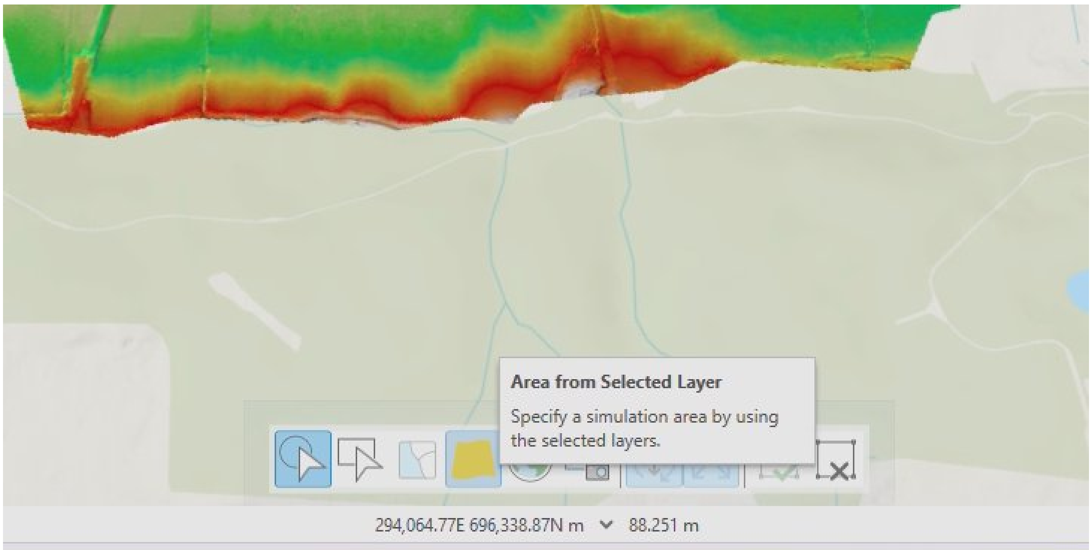

Figure 92 - Preparing (cont) for flood simulation in ArcGIS

The new “Simulation” tab that appeared in the top menu was selected followed by the “Water Source” button as shown in Figure 93.

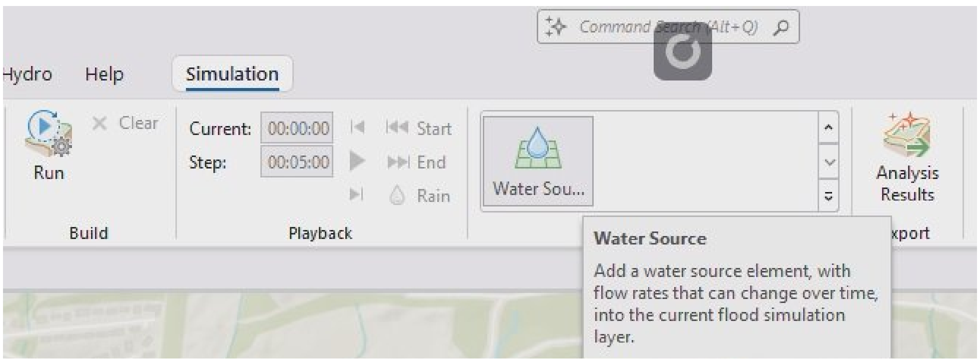

Figure 93 - Adding water source to ArcGIS flood simulation

Zooming into the middle of the River Devon at its furthest most upstream point, the water source point was dropped as shown below in Figure 94.

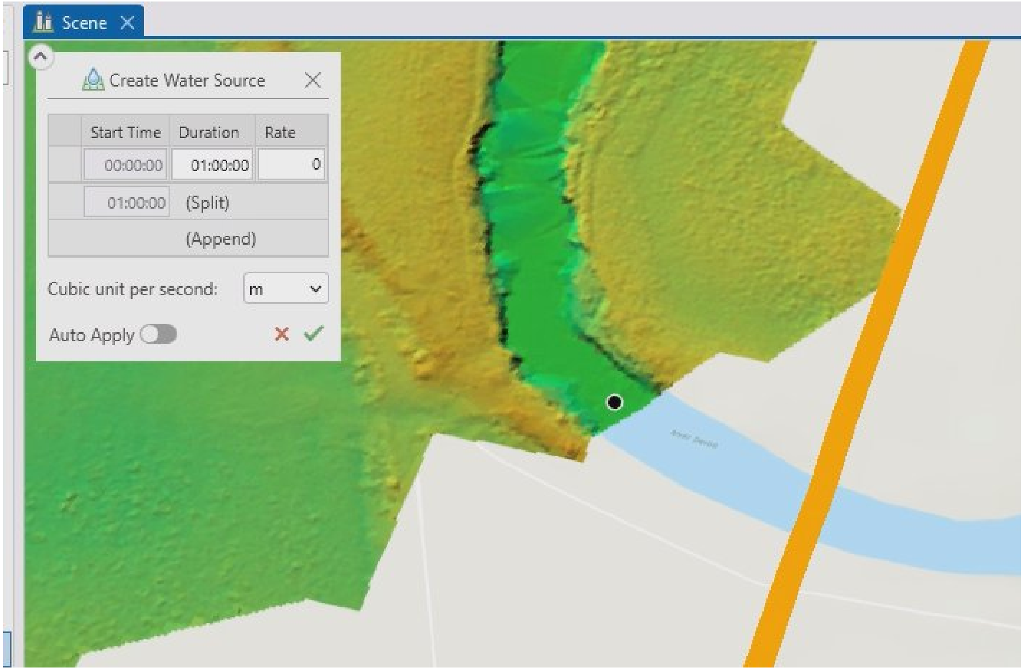

Figure 94 - Showing location of water source within the terrain

3 – Hydrograph/flow data

In the "Create Water Source" window that appeared that can be seen above in Figure 94, the "(Append) button was clicked 24 times with the 100 year flood hydrograph data from Appendix 1 manually entered into the window before clicking the green tick (Figure 95)

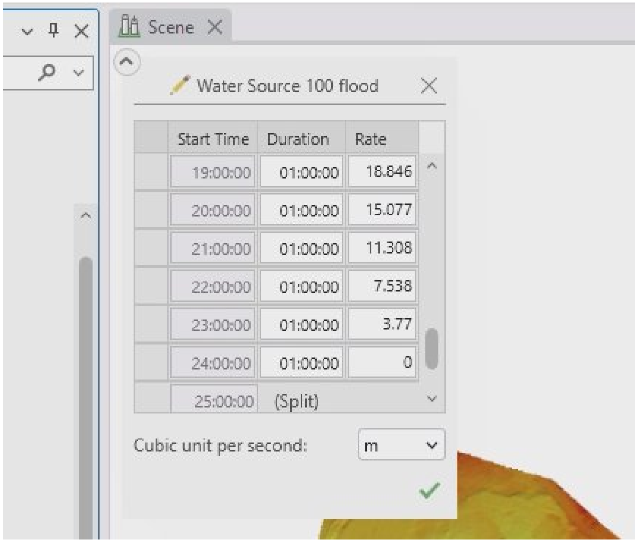

Figure 95 - Manually entering hydrograph data

In the left hand “Contents” column, “Water Sources” was expanded and “Water Source 1” was renamed to “100 year flood”. This was then duplicated, renamed to “20 year flood” with the 20 year hydrograph from Appendix 1 manually entered. This was then duplicated further with the duplication renamed to “2 year flood” and the hydrograph from Appendix X also manually entered. There were then 3 separate hydrographs showing under “Water Sources” (Figure 96)

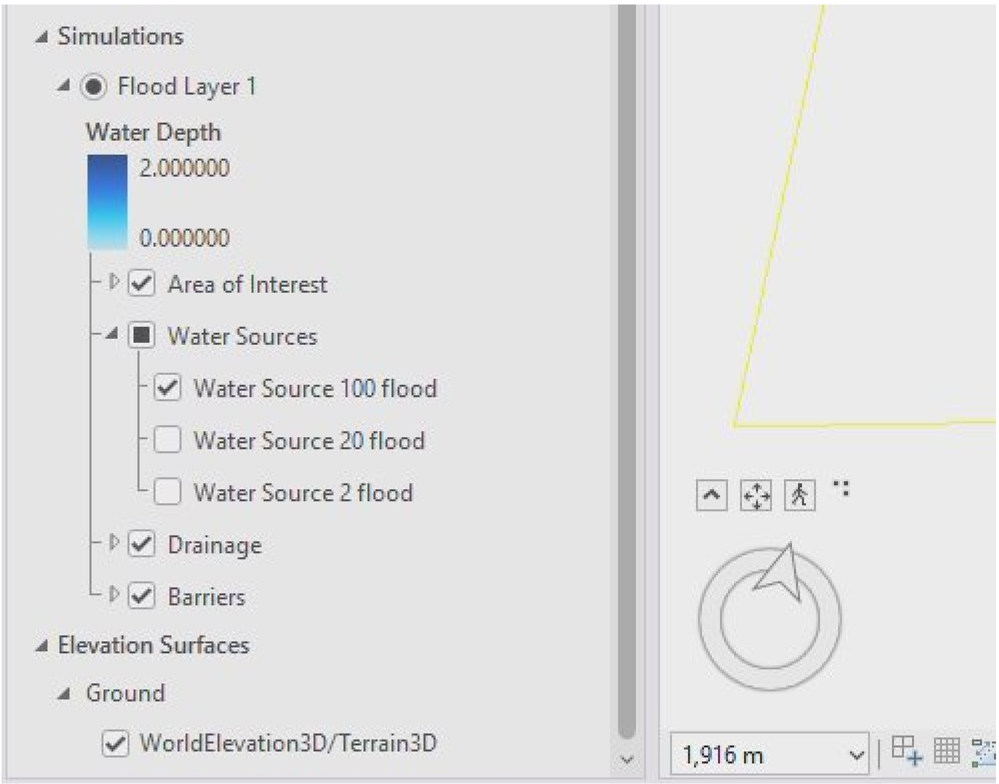

Figure 96 - Different hydrographs for different flood events in ArcGIS

4 – Simulation Run

A simulation was ran by selecting the correct hydrograph and DEM in the “Contents” section within ArcGIS Pro. 24:00:00 was entered into the “Duration” box in the top main menu bar before clicking on the “Run” button next to that as shown in Figure 97. The flood simulation would run and complete after around 40 minutes. This was replicated for all hydrographs and DEMs.

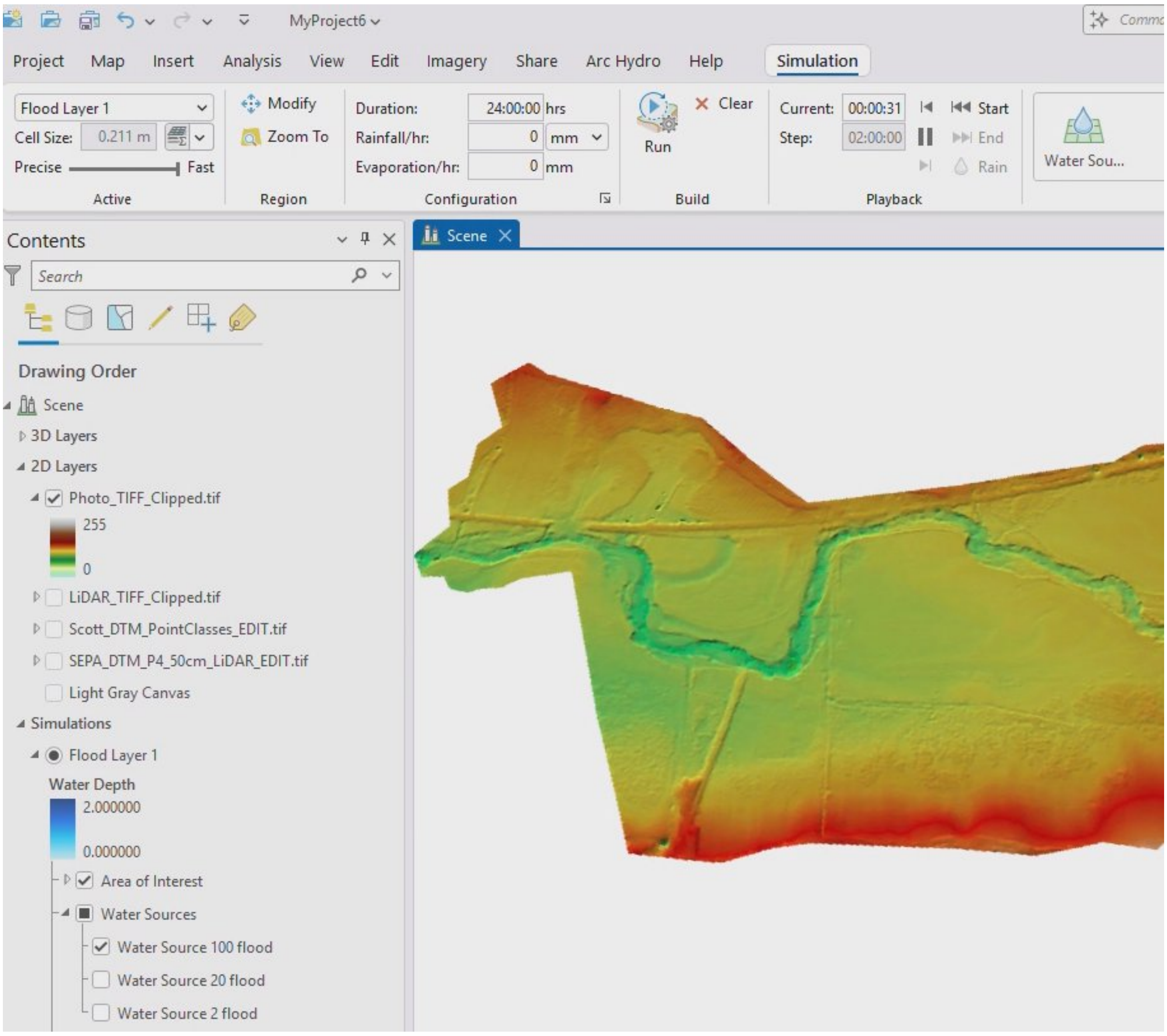

Figure 97 - Running a flood simulation in ArcGIS Pro

5 – Export Results

Results were exported by clicking on the “Analysis Results” button at the top right of the main menu bar. This opened the “Export Simulation” toolbox down the right hand side of the ArcGIS screen. A unique name was entered into the “Name prefix” box and correct export was selected in the “Location” box. “Vertical units” were kept as metres but “Format” changed to “Tiff”. Interval of exports was changed to “Time step” every 1 hour (in-line with HEC-RAS results) before clicking on the Export button, all shown within Figure 98. The TIFFs were then exported to chosen location and could then be imported into QGIS for further analysis as per section 6.6 of the main report.

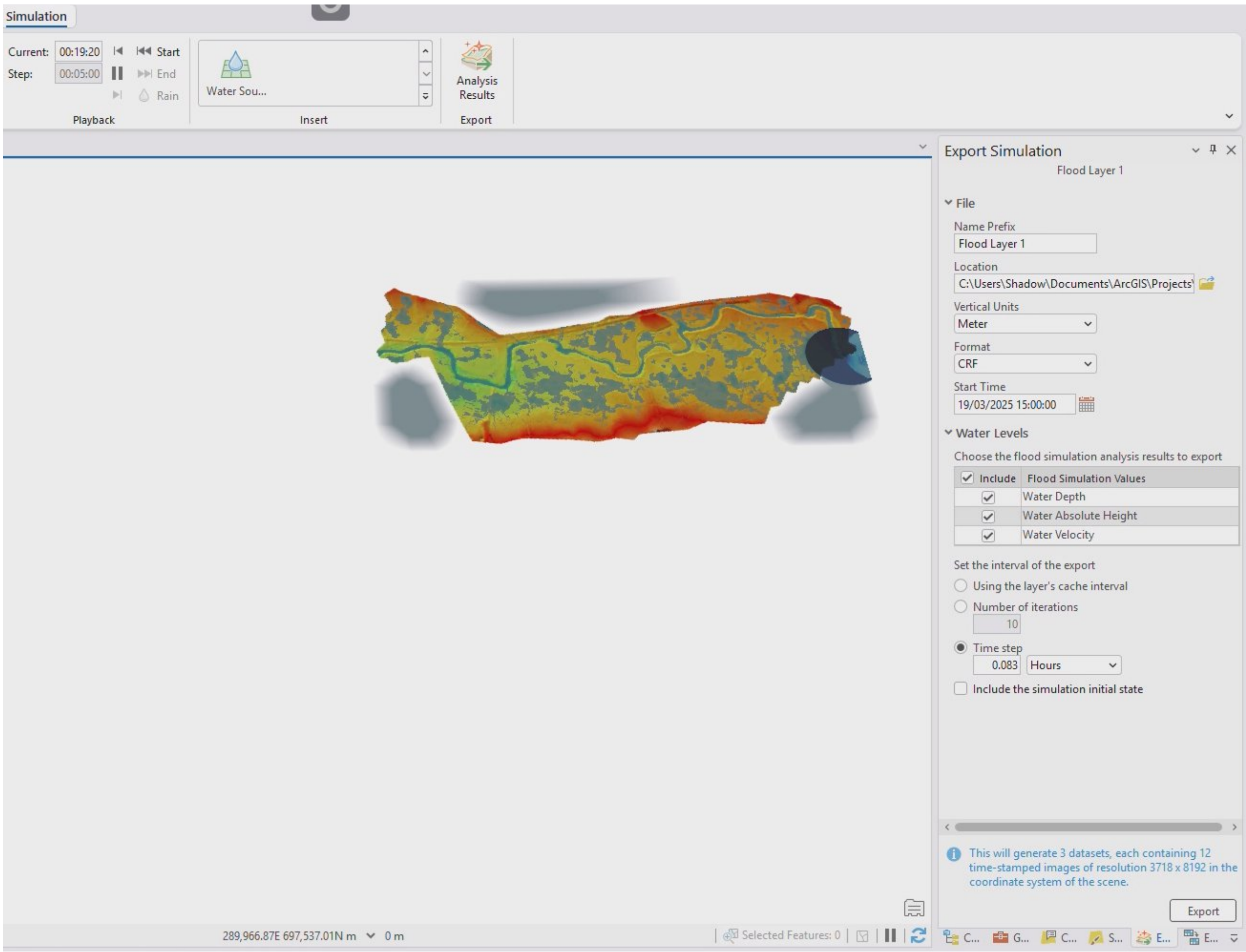

Figure 98 - Exporting raster results from ArcGIS for further analysis within QGIS

Appendix 9 – QGIS analysis and map creation (Expanded from section 10)

Raster Analysis

A new project was created within QGIS with the ESPG set to 27700. Processing toolbox was enabled by clicking “Processing” from the main menu bar followed by “Toolbox”, the toolbox then appeared on the right hand side of the main screen shown in Figure 99.

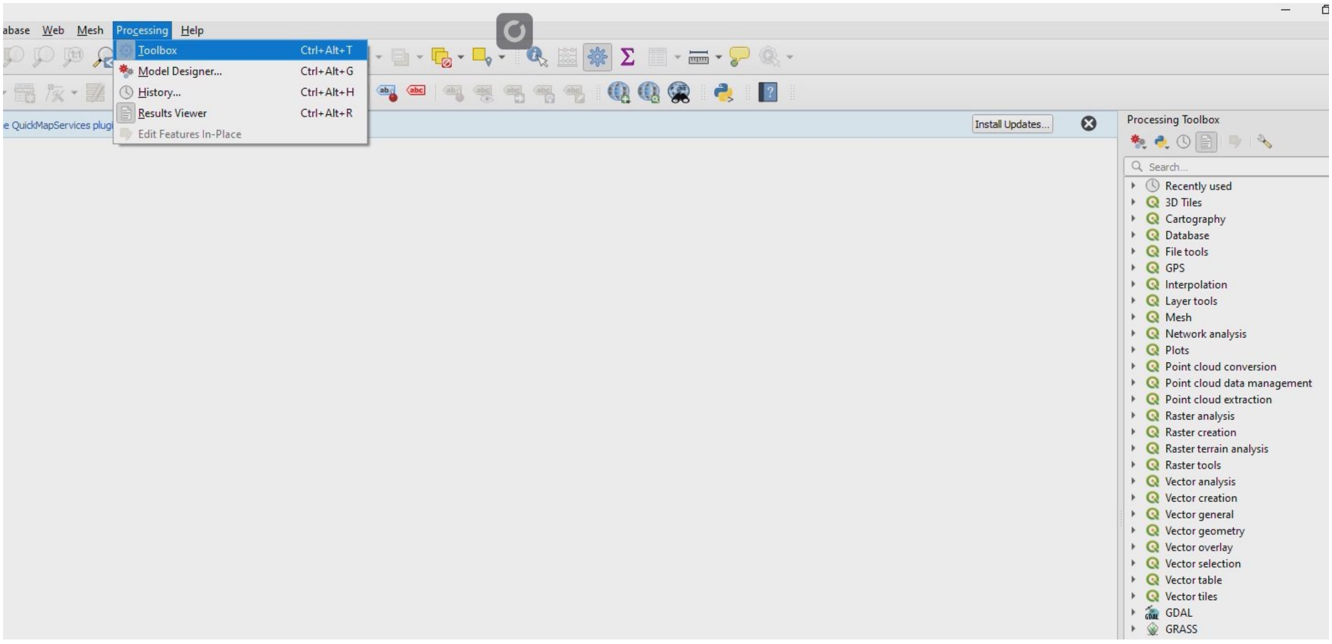

Figure 99 - Processing Toolbox enabled within QGIS for raster analysis

The exported flood simulation results from sections 6.4, 6.5 and 6.6 were imported into the newly created project, with the correct flood model name and placed in created “groups” for “good housekeeping” (Figure 100)

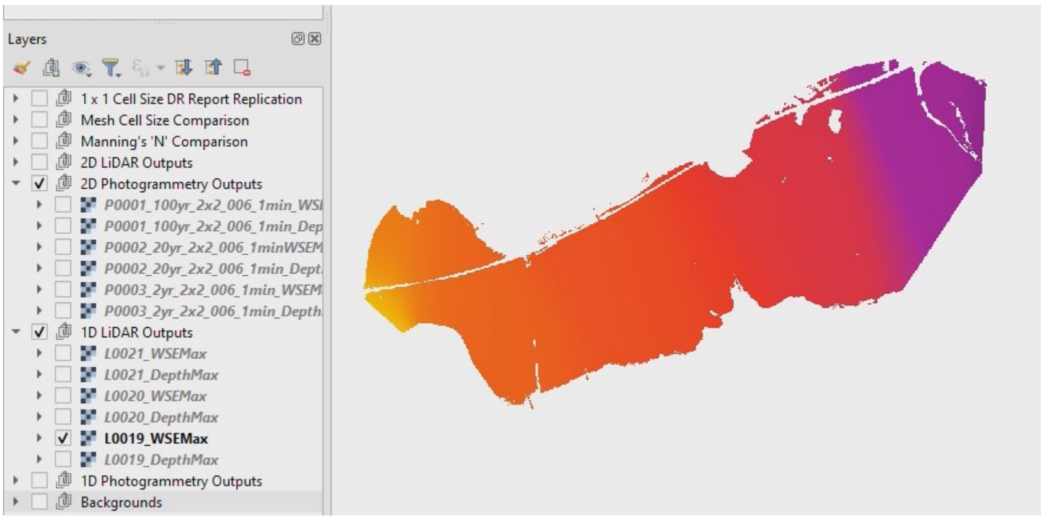

Figure 100 - Created groups, with imported results placed into correct category

Raster analysis was performed by selecting a flood simulation results layer from the “Layers” section, then running “Raster Layer Statistics” from the processing toolbox (Figure 101), selecting “Band 1 (gray)” from the Band number dropdown before clicking “Run”. “Surface Volume Report” (Figure 101) was then ran from processing toolbox, selecting “Count Only Above Base Level” before clicking “Run”.

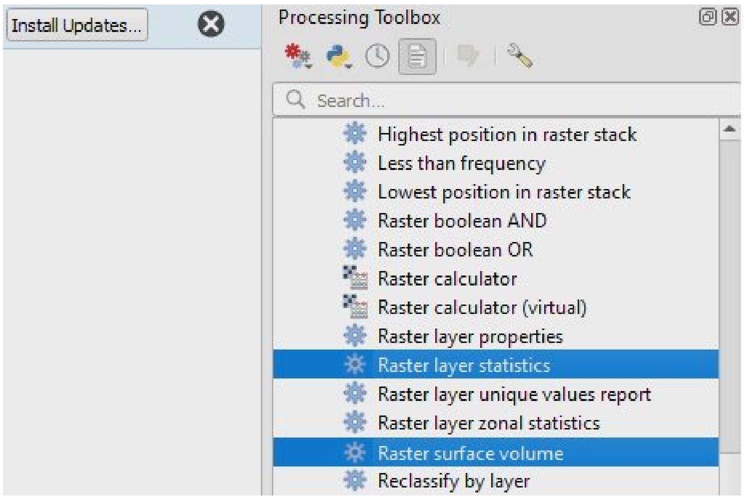

Figure 101 - Raster layer statistics and surface volume analysis options within QGIS processing toolbox

Exported results were seen via created HTML files from the “Results Viewer” window under the processing toolbox shown in Figure 102. The steps outlined in this section were repeated for all flood simulation result layers with the results for each layer copy and pasted into an Excel document.

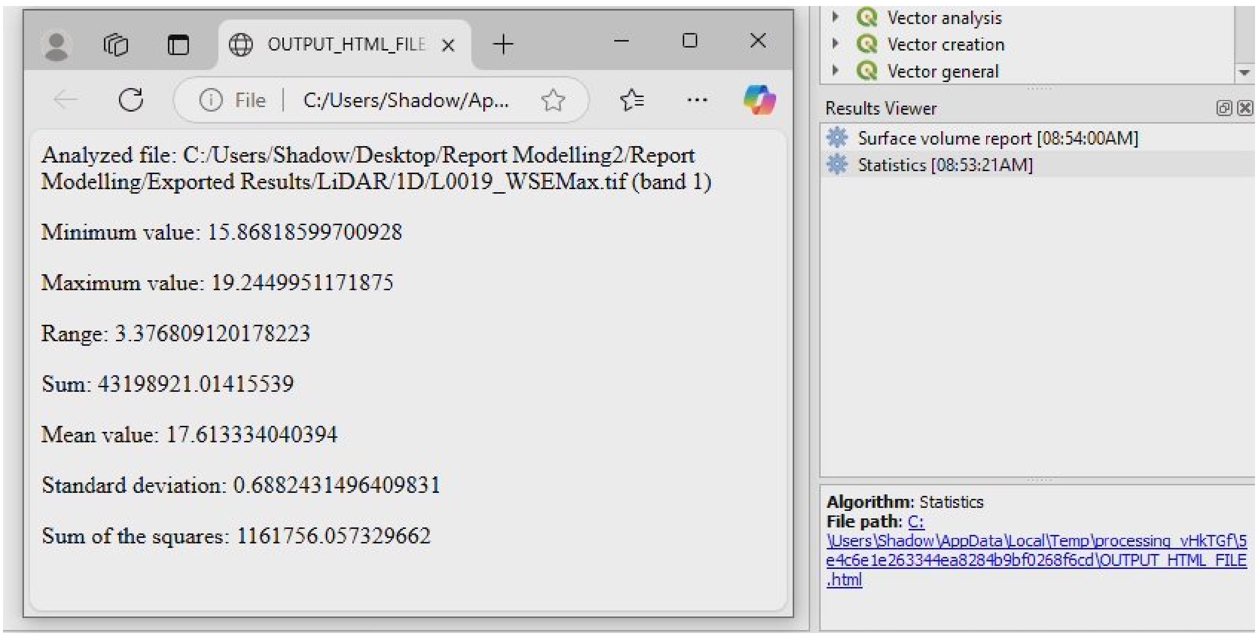

Figure 102 - Results viewer section and example of exported results in HTML format

Map creation

With no option to export symbology from HEC-RAS (RAS Mapper) to QGIS, the first thing that was required was to create new symbology in QGIS by replicating it from HEC-RAS. This was done by going into HEC-RAS then opening RAS Mapper. A flood simulation result was selected (Depth for this example) within the Results by right clicking on layer, followed by “Layer Properties” followed by clicking “Edit” within the “Surface” sub-section. The values and RGB colour codes shown in Figure 103 were noted down.

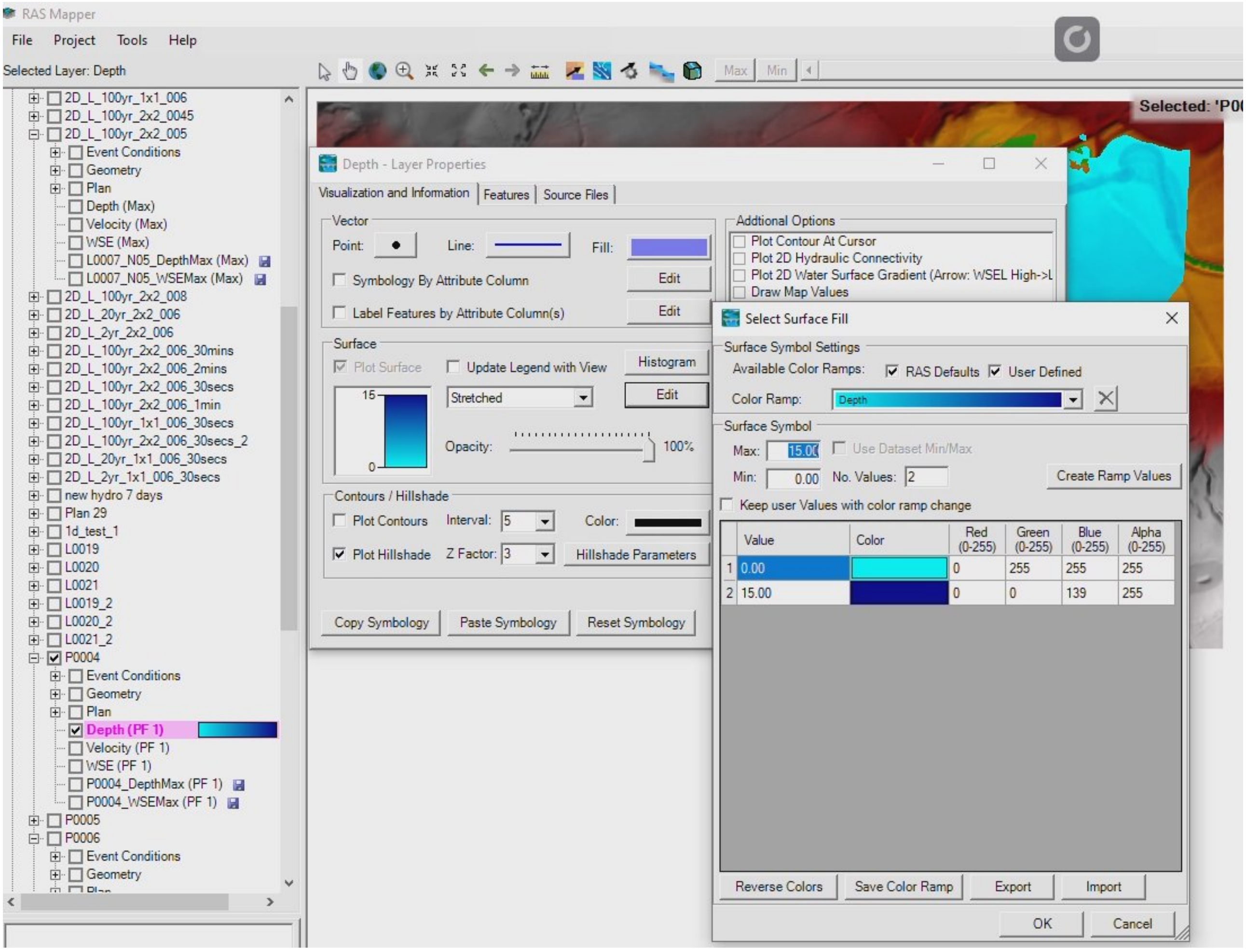

Figure 103 - HEC-RAS symbology values and RGB codes for Depth flood simulation results

In QGIS, an imported Depth flood simulation results layer was right clicked on before selecting “Properties” followed by “Symbology”. The following settings were applied which can be seen in Figure 104. Render type: Singleband pseudocolor, Mode: continuous, Label unit suffix: m, Label precision: 1, Classes: 2. Values and RGB codes, replicated from what was in HEC-RAS (Figure 103).

After the competition of this, layer symbology was copy and pasted to all Depth layers individually. The steps outlined in this process were then replicated for different layers such as Water Surface Extent. At this stage, satellite background maps were added from QuickMapServices plugin.

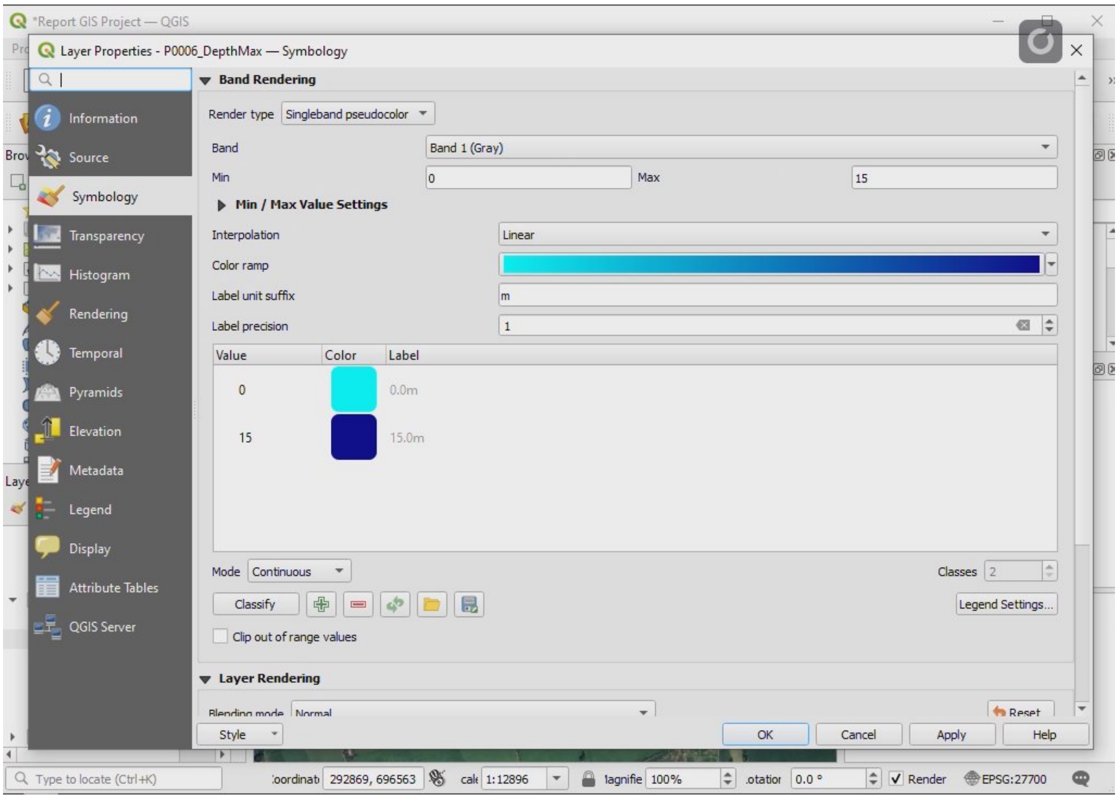

Figure 104 - Layer symbology settings within QGIS on a "Depth" flood simulation results layer

Final maps were created by clicking “File” and “New Print Layout”. North arrow, scalebar, legend and text boxes were added from “Add Item” menu. Items were placed into correct location by clicking and dragging (Figure 105). Finished maps were exported as PNGs with the layout was saved for future maps.

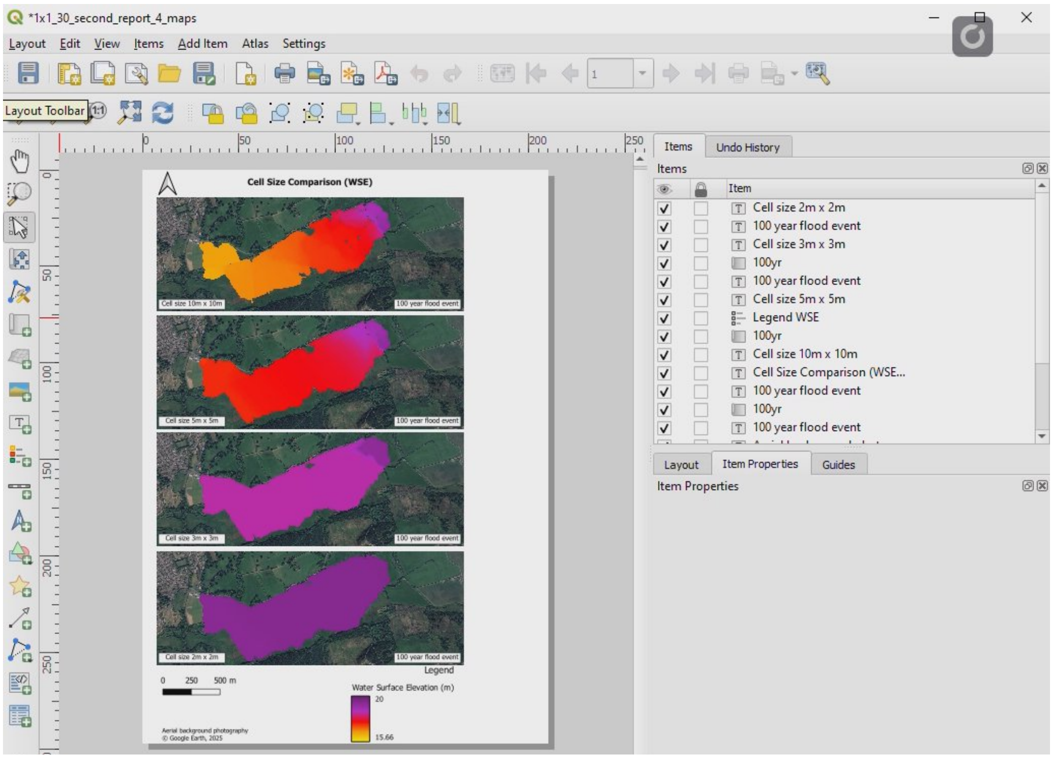

Figure 105 - QGIS "New print layout" showing different items added included in finished maps